

# Chapter 4

## Multi-scale modelling of dry granular flows

### 4.1 Introduction

In nature, instabilities of slopes or cliffs can manifest themselves in dramatic events involving sudden release of a large mass of soil. The prediction of these catastrophic events represents several challenges, one difficulty being our incomplete understanding of the granular flow dynamics (Rondon et al., 2011). Understanding the mechanics is of particular importance for risk assessment. Small scale laboratory experiments are usually unable to properly capture the dynamics of geophysical events. However, they can be useful to precisely study the physical mechanisms, which may play a crucial role in real flows (Iverson, 1997).

Conventionally, granular materials such as soils are modelled as a continuum. On a macroscopic scale, granular materials exhibit many collective phenomena and the use of continuum mechanics to describe the macroscopic behaviour can be justified. However on a grain-scale, the granular materials exhibit complex solid-like and/or fluid-like behaviour depending on how the grains interact with each other. Numerical studies at grain-scale allow a precise understanding of the internal flow structure. However, even in simplified geometries such as those investigated in the laboratory-scale experiments, DEM suffers from a serious short-coming in the number of grains that can be simulated in a reasonable time. This is a critical issue for more complex geometries or when granular processes which occur on a long time-scale are considered. For this reason, most numerical studies are performed in 2D or simple particles shapes and size distributions are considered.

Classical modelling strategies based on the finite element method (FEM) cannot be used for the simulation of very large deformations due to mesh distortion effects. In various application

of FEM, this problem is treated by means of technical tools such as re-meshing. These methods are, however, not robust and lead to round-off errors and are sensitive to the mesh characteristics. Recent works on granular materials suggest that a continuum law may be incapable of revealing in-homogeneities at the grain-scale level, such as orientation of force chains, collapse of local voids and grain rearrangements, which are purely micro-structural effects (Rycroft et al., 2009). Discrete element approaches are capable of simulating the granular material as a discontinuous system allowing one to probe into local variables such as position, velocities, contact forces, etc. The fundamental question is how to model granular materials which exhibit complex phenomena. It is important to understand the mechanics of granular flows and the ability and limitations of continuum methods in modelling the granular flow dynamics.

## 4.2 Granular column collapse

The collapse of a granular column, which mimics the collapse of a cliff, has been extensively studied in the case of dry granular material (Hogg, 2007; Kerswell, 2005; Lajeunesse et al., 2004; Lo et al., 2009; Lube et al., 2005; Staron and Hinch, 2007; Zenit, 2005). The granular column collapse experiment involves filling a rectangular channel of height  $H_0$  and width  $L_0$  with a granular material of mass ‘m’ (see figure 4.1). The granular column is then released *en masse* by quickly removing the gate, thus allowing the granular material to collapse onto the horizontal surface, forming a deposit having a final height  $H_f$  and length  $L_f$ . Despite the complexity of the intermediate flow dynamics, experimental investigations have shown that the flow evolution, the spreading velocity, the final extent of the deposit, and the energy dissipation can be scaled in a quantitative way independent of the substrate properties, grain size, density, the shape of the granular material and the released mass (Lajeunesse et al., 2005; Lube et al., 2005; Staron and Hinch, 2007). The granular collapse has also been studied using discrete element method, which allows precise measurement of the internal flow structure (Lo et al., 2009; Staron and Hinch, 2007; Staron et al., 2005; Utili et al., 2014). Power laws relating the final run-out and height to the initial aspect ratio ( $a = H_0/L_0$ ) of the column were observed. These findings immediately pose a question: are these simple scalings fortuitous, an oversimplification, or in fact indicative of a simple dynamical balance?

Granular flows are conventionally modelled as a frictional dissipation process in continuum mechanics but the lack of influence of inter-particle friction on the energy dissipation and spreading dynamics (Lube et al., 2005) is surprising. However, Kerswell (2005) showed the run-out behaviour has a clear material dependence. Although, the collapse of a granular column on a horizontal surface is a simple case of granular flow, a proper model that describes the flow dynamics is still lacking. Simple mathematical models based on conservation of

## 4.2 Granular column collapse

## 3

horizontal momentum capture the scaling laws of the final deposit, but fail to describe the initial transition regime. From a theoretical point of view, the spreading has been described using depth averaged equations (Kerswell, 2005; Larrieu et al., 2006). The depth-averaged and Saint-Venant equations, however, struggle to recover the precise dynamic behaviour of the system (Warnett et al., 2013) and only succeeds in predicting the scaling observed for an aspect ratio less than one. Describing the behaviour of larger aspect ratio and capturing the initial stage of the collapse, when the grains experience a rapid change of direction from vertical to horizontal, remain an open challenge.

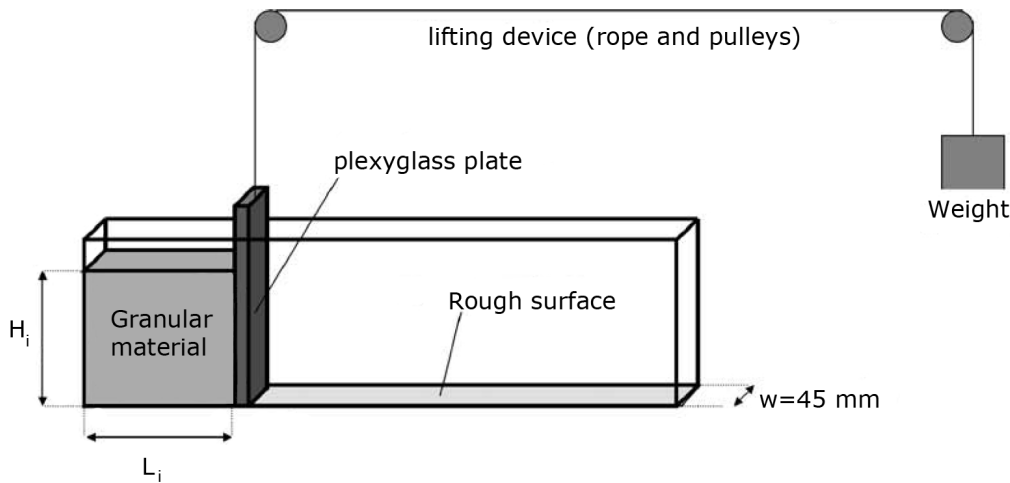


Figure 4.1 Schematic of experimental configuration for 2-D collapse in a rectangular channel, (Lajeunesse et al., 2004)

In the present study, multi-scale numerical modelling, i.e. grain-scale modelling and continuum analyses, of quasi-two-dimensional collapse of granular columns are performed using two-dimensional Discrete Element Method (DEM) and Generalised Interpolation Material Point Method (GIMPM). GIMPM, a hybrid Eulerian–Lagrangian approach, with a Mohr–Coloumb failure criterion is used to describe the continuum behaviour of the granular column collapse. Whereas, the micro-mechanics of the flow is captured using DEM simulations. Comparing the grain-scale behaviour with the continuum simulations highlights the limitations of the continuum approach in modelling dense granular flows and their ability in capturing the complex flow kinematics which are due to micro-scale rheology.

#### 4.2.1 Numerical set-up

In this study, the numerical set-up of granular columns are analogous to the experimental investigation performed by Lajeunesse et al. (2004). The experimental configuration of Lajeunesse et al. (2004) is shown in figure 4.1. Granular material of mass  $m$  is poured into a container to

form a rectangular heap of length  $L_0$ , height  $H_0$  and thickness  $W$ . The internal friction angle and  
 1 the wall friction between the wall and the glass beads measured by [Lajeunesse et al. \(2004\)](#) are  
 2 listed in table 4.1. The gate is then quickly removed to release the granular mass that spreads in  
 3 the horizontal channel until it comes to rest. The final run-out distance  $L_f$  and the collapsed  
 4 height  $H_f$  are measured. The run-out distance and collapse height exhibit a power law relation  
 5 with the initial aspect ratio ‘ $a$ ’ ( $= H_0/L_0$ ) of the column.

Table 4.1 Material properties of glass ballotini ([Lajeunesse et al., 2004](#))

Parameter	Value
Mean grain diameter	1.15 mm
Repose angle	$22 \pm 0.5^\circ$
Avalanche angle	$27.4 \pm 0.5^\circ$
Wall friction angle	$24.8 \pm 0.2^\circ$

6 Granular materials when released suddenly on a horizontal surface exhibit transient flow.  
 7 In this study, the mechanism of flow initiation, spreading dynamics and energy dissipation are  
 8 studied for varying initial aspect ratios of the granular column. The soil grain characteristics  
 9 of the DEM sample match that of the experiment. The particle size distribution (PSD) is  
 10 one of the most important factors controlling landslide initiation and soil permeability ([Utili  
   et al., 2014](#)). Cumulative  $\beta$  distribution (described in ??) is used to generate a graded sample  
 12 with a mean grain diameter of 1.15mm (see figure 4.2b). The DEM sample is composed  
 13 of  $\sim 3000$  disks with a uniform distribution of diameters by volume fractions in the range  
 14  $[d_{min}, d_{max}] = 0.92 - 1.38$  mm with polydispersity  $r = \frac{d_{max}}{d_{min}} = 1.5$ . The granular column is  
 15 prepared by allowing randomly placed grains to undergo ballistic deposition with a constant  
 16 potential head between layers of soil grains. A snapshot of the sample generated is shown  
 17 in figure 4.2a. A DEM sample with soil grains arranged in a regular hexagonal lattice is also  
 18 used to study the influence of crystallisation and jamming on the run-out behaviour.

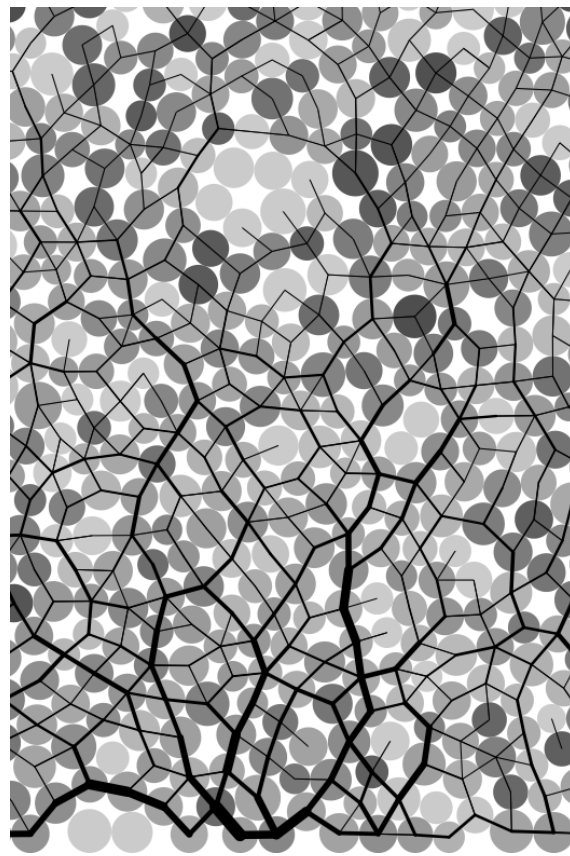
19 The overlap between grains is determined by the stiffness  $k_n$  of the spring in the normal  
 20 direction. Typically, an average overlap in the range 0.1 to 1.0% is desirable ([Zenit, 2005](#)) and  
 21 the spring constant is chosen to produce grain overlaps in this range. The stiffness is determined  
 22 as

$$23 \quad k_n = \frac{2\pi G}{(1-v)[2\ln(\frac{2r}{A}) - 1]} \quad (4.1)$$

$$24 \quad A = \left[ \frac{2r(1-v)f_n}{\pi G} \right]^{\frac{1}{2}}, \quad (4.2)$$

## 4.2 Granular column collapse

5



(a) DEM sample prepared using ballistic deposition

(b) DEM grains generated using the cumulative  $\beta$  distribution

Figure 4.2 DEM sample characteristics

<sup>1</sup> where  $f_n$  is the normal contact force; G is the shear modulus; v is the Poisson's ratio and r is  
<sup>2</sup> the radius of the grain. A simpler form of stiffness for a spherical grain is defined as

<sup>3</sup>  $k_n = 4ER,$  (4.3)

<sup>4</sup> where E is the Young's modulus of the material and R is the radius of the grain. [Cambou et al.](#)  
<sup>5</sup> ([2009](#)) observed that the contact model has negligible influence on the run-out behaviour of  
<sup>6</sup> rapid granular flows. The granular collapse simulations performed using non-linear Hertz-  
<sup>7</sup> Mindlin contact model and the linear-elastic contact model showed no significant difference  
<sup>8</sup> in the granular flow behaviour ([Utili et al., 2014](#)). Linear-elastic contact model is used in the  
<sup>9</sup> present study due to its simplicity and lower computation time requirement. The maximum  
<sup>10</sup> tangential force is limited by the Mohr-Coloumb criterion.

<sup>11</sup> [Staron and Hinch \(2007\)](#) observed that the coefficient of restitution  $\varepsilon$  dramatically changes  
<sup>12</sup> the behaviour of the system for  $\varepsilon \rightarrow 1$ ; in particular, this dramatic change is expected to become  
<sup>13</sup> more important for increasing values of  $a$ . On the contrary, for  $\varepsilon \leq 0.8$ , the influence of the  
<sup>14</sup> coefficient of restitution becomes negligible. In the present study, a value of 0.75 is adopted as  
<sup>15</sup> the coefficient of restitution, similar values of restitution coefficient was adopted by [Girolami](#)  
<sup>16</sup> [et al. \(2012\)](#) and [Zenit \(2005\)](#). The normal damping coefficient  $C_n$  is appropriately chosen to  
<sup>17</sup> achieve the required coefficient of restitution  $\varepsilon$ :

<sup>18</sup>  $C_n = 2\gamma\sqrt{m_{ij}k_n},$  (4.4)

<sup>19</sup> where  $\gamma = -\frac{\ln(\varepsilon)}{\sqrt{\pi^2 + \ln^2(\varepsilon)}},$  and  $m_{ij} = \frac{m_i m_j}{m_i + m_j}.$  (4.5)

<sup>21</sup> The micro-mechanical parameters used in this study are presented in table [4.2](#). Due to the  
<sup>22</sup> unsteady nature of the flow, the grains get dispersed on the horizontal plane as discrete bodies  
<sup>23</sup> start to separate from the main mass, hence the run-out distance is calculated as the position of  
<sup>24</sup> the farthest grain which has at least one contact with the main mass.

GIMPM with a Mohr-Coloumb constitutive model is used to simulate plane strain collapse  
<sup>1</sup> of granular columns. [Crosta et al. \(2009\)](#) observed that the Mohr-Coloumb model with non-  
<sup>2</sup> associate flow rule is able to capture granular collapse dynamics and models the strong vertical  
<sup>3</sup> motion. This method does not suffer the limitations of typical shallow water equation techniques.  
<sup>4</sup> In order to understand the ability and limitations of continuum approaches in capturing the  
<sup>5</sup> local rheology, it is important to scale the grain-scale material properties, such as the inter-  
<sup>6</sup> particle friction and stiffness, to the continuum scale (macroscopic friction and Young's  
<sup>7</sup> modulus). [Crosta et al. \(2009\)](#) observed that the friction angle plays a significant role on the  
<sup>8</sup> run-out behaviour.

Table 4.2 Micro-mechanical parameters used in DEM simulations

Parameter	Value
Young's modulus of glass bead	$70 \times 10^9 \text{ N m}^{-2}$
Poisson's ratio	0.22 - 0.24
Diameter of glass beads	0.92 to 1.38 mm
Normal and shear stiffness of grains	$1.6 \times 10^8 \text{ N m}^{-1}$
Normal and shear stiffness of wall	$4 \times 10^8 \text{ N m}^{-1}$
Inter-particle friction coefficient, $\mu$	0.53
Wall friction coefficient	0.466
Coefficient of restitution, $\epsilon$	0.755

In MPM simulations, the granular flow is assumed to be in critical state and the critical state friction angle is used in the Mohr-Coloumb model. In order to obtain the critical state friction angle of the granular sample, a shear test is performed using 1078 DEM grains. A bi-periodic boundary condition is adopted on the sides of the sample (see figure 4.3a). Two layers of fixed grains (shown in black) are placed at the top and the bottom of the shear sample. A normal pressure  $P$  and a horizontal velocity  $v$  is applied to the fixed grains at the top of the shear sample. As the normal effective stress is varied, the average shear stress in the sample is measured. The sample is sheared until critical state is reached. The slope of shear stress versus normal effective stress gives the critical state friction angle. A critical state friction angle of  $22.2^\circ$  is obtained. The macroscopic friction angle is in the range observed by Estrada et al. (2008) and Mitchell and Soga (2005). The Young's modulus of the granular assembly is obtained as the initial slope of the stress-strain plot of a uni-axial compression of a granular column using DEM.

Guilkey et al. (2003) suggests using at least four material points per cell for large deformation problems. In the present study, 16 material points per cell is adopted. If the mesh is too fine and the number of particles is too large, the particle size  $2l/p$  decreases, and the GIMPM interpolation function tends to approach the original MPM function, as shown by Bardenhagen and Kober (2004). Hence, GIMPM loses the merit that it reduces the numerical noise due to material points crossing the background mesh. In addition, the probability of particles crossing the background mesh increases with decrease in the mesh size, hence, more noise may be produced (Abe et al., 2013). The effect of the number of material points per cell on the run-out behaviour is discussed in section 4.3.5. In the present study, each material point represents one-fourth of a DEM soil grain. The parameters used for the continuum analyses are presented in table 4.3.

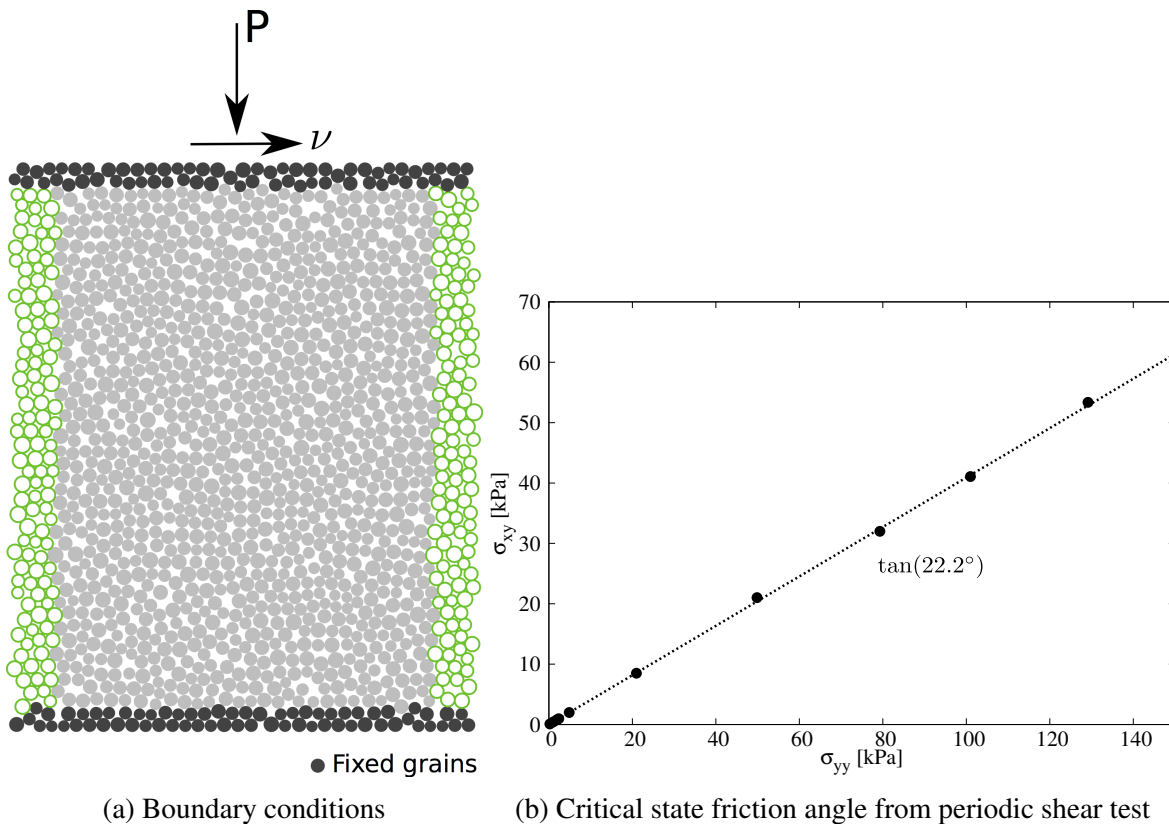


Figure 4.3 Periodic shear test

Table 4.3 Parameters used in continuum simulations

Parameter	Value
Material point spacing	0.575 mm
Number of material points per cell	16
Young's Modulus, E	$1.98 \times 10^6 \text{ N m}^{-2}$
Poisson's ratio, $\nu$	0.22 to 0.24
Friction angle, $\phi$	$23.2 \pm 0.2^\circ$
Dilatancy angle, $\Phi$	$0^\circ$
Density, $\rho$	$1800 \text{ kg m}^{-3}$
Wall friction	0.466
Time step increment	$1.0 \times 10^{-6} \text{ s}$

<sup>18</sup> **4.2.2 Deposit morphology**

<sup>19</sup> Two-dimensional plane-strain MPM and DEM simulations of granular column collapse are  
<sup>20</sup> performed by varying the initial aspect ratio of the column from 0.2 to 10. The normalized final  
<sup>21</sup> run-out distance,  $\Delta L = (L_f - L_0)/L_0$ , as a function of the initial aspect ratio ‘a’ of the column  
<sup>1</sup> is presented in figure 4.4. Similar to the experimental behaviour a power law relation between  
<sup>2</sup> the run-out and the initial aspect ratio of the column is observed. Two distinct flow regimes can  
<sup>3</sup> be seen: (a) for ‘a’ < 2.7 a linear relation between the spread and aspect ratio can be observed,  
<sup>4</sup> and (b) for ‘a’ > 2.7 a power-law relationship exists. In the present study, the following scaling  
<sup>5</sup> law for the run-out (using DEM) is observed:

$$\frac{L_f - L_0}{L_0} \approx \begin{cases} 1.67a, & a \lesssim 2.7 \\ 2.7a^{2/3}, & a \gtrsim 2.7 \end{cases} \quad (4.6)$$

<sup>6</sup> Both, MPM and DEM simulations are able to capture the linear relationship for ‘a’ < 2.7,  
<sup>7</sup> and the simulation results agree with the experimental investigation ([Lajeunesse et al., 2005](#)).  
<sup>8</sup> This shows that a simple frictional dissipation model is able to capture the flow dynamics for  
<sup>9</sup> columns with small aspect ratios. For ‘a’ < 2.7, the normalised run-out distance predicted using  
<sup>10</sup> DEM simulations are very close to those observed in the experiment. DEM simulations with  
<sup>11</sup> hexagonal packing shows shorter run-out distances in comparison to randomly packed sample.  
<sup>12</sup> This difference in the run-out behaviour might be due to the crystallisation and jamming effects  
<sup>13</sup> in hexagonal packing. The small difference in the final run-out between the DEM and the  
<sup>14</sup> experimental results can be attributed to the variation in the packing of grains. Also, the  
<sup>15</sup> experimental data corresponds to granular column collapse in a rectangular channel, where the  
<sup>16</sup> collapse is not a pure two-dimensional collapse as in the case of numerical simulations.  
<sup>17</sup>

<sup>18</sup> Significant difference in the final run-out between MPM, which is based on a simple  
<sup>19</sup> frictional model for dissipation of potential energy, and DEM simulations indicates a change in  
<sup>20</sup> the mechanism of energy dissipation for columns with large aspect ratios (‘a’ > 2.7). [Staron and](#)  
<sup>21</sup> [Hinch \(2005\)](#) observed that a constant frictional dissipation model cannot describe a power-law  
<sup>22</sup> relation observed at large aspect ratios. A transition in the run-out behaviour at an aspect ratio  
<sup>23</sup> of 2.7 indicates a change in the flow kinematics. Similar behaviour in the run-out distance was  
<sup>24</sup> observed by [Bandara \(2013\)](#) for columns with large aspect ratios ( $a \geq 2$ ).  
<sup>25</sup>

<sup>26</sup> The longer run-out distance in MPM simulations at large aspect ratios might be influenced  
<sup>27</sup> by the amount of material mobilised during the collapse. In tall columns, the entire column  
<sup>28</sup> participates in the flow, in contrast to short columns where the collapse is due to avalanching of  
<sup>29</sup> flanks ([Lajeunesse et al., 2004](#)). It is possible that MPM simulations collapse more resulting  
<sup>30</sup> in longer run-out distances. Figure 4.5 shows the normalized final height as a function of the

initial aspect ratio of the column. Similar to the run-out behaviour, the normalised-height also shows two distinct regimes. The scaling of final height of the column with the initial aspect ratio of the column can be written as

$$\frac{H_f}{L_i} \propto \begin{cases} a, & a \lesssim 0.7 \\ a^{2/3}, & a \gtrsim 0.7 \end{cases} \quad (4.7)$$

31  
32  
33

34  
35

1 The final height predicted by both DEM and MPM simulations match the experimental data  
 2 for columns with smaller aspect ratio ( $a \leq 0.7$ ). Linear relationship between the final height and  
 3 the aspect ratio indicates that only a part of the granular column is mobilised during the collapse.  
 4 For tall columns, both approaches predict similar normalised height. However, the normalised  
 5 height observed in MPM is higher than in DEM simulations, which is in contrast to the idea of  
 6 increase in the amount of material mobilised during the collapse in MPM simulations resulting  
 7 in longer run-out distance. Hence, the longer run-out observed in MPM simulations is due a  
 8 change in the flow dynamics at higher aspect ratios, which is not captured in MPM simulations.  
 9 The final height of a column is controlled by the amount of static region in the granular column  
 10 collapse, while the run-out distance is essentially a function of the flowing mass. Hence, it is  
 11 important to compare the evolution of flow and the internal flow structure in DEM and MPM  
 12 simulations.

### 13 4.2.3 Flow evolution and internal flow structure

14 The normalised run-out and height as a function of the aspect ratio indicates that, for a given  
 1 granular material and substrate properties, the flow dynamics and the final deposit morphology  
 2 are independent of the volume of granular material released, but depend only on the geometry  
 3 of the column. A power law relationship is observed between the run-out distance and the  
 4 initial aspect ratio of the column. A transition in the run-out behaviour at an aspect ratio of 2.7  
 5 indicates a change in the flow dynamics.

For short columns ('a' < 2.7), the flow is initiated by a failure at the edge of the pile along a  
 well-defined fracture surface. The granular mass fails through avalanching of flanks producing  
 a truncated cone-like deposit ('a' < 0.7) or conical deposit ('a' > 0.7). The grains located above  
 the failure surface move "*en masse*" leaving a static region underneath the failure surface.

Dimensional analysis of granular column collapse reveals an intrinsic time defined as  
 $\sqrt{H_0/g}$ . This intrinsic time is a transient time of order  $\tau_c$ , at which the flow is fully developed,  
i.e., the potential energy available at the initial stage of collapse is now fully converted to  
kinetic energy. Numerical simulation of the velocity profile of a granular column ('a'=0.4) at  
critical time  $\tau_c$  is presented in figure 4.6. At critical time, the velocity field depends only on the

1  
2  
3  
4  
5

6  
7  
8  
9

10  
11  
12  
13  
14

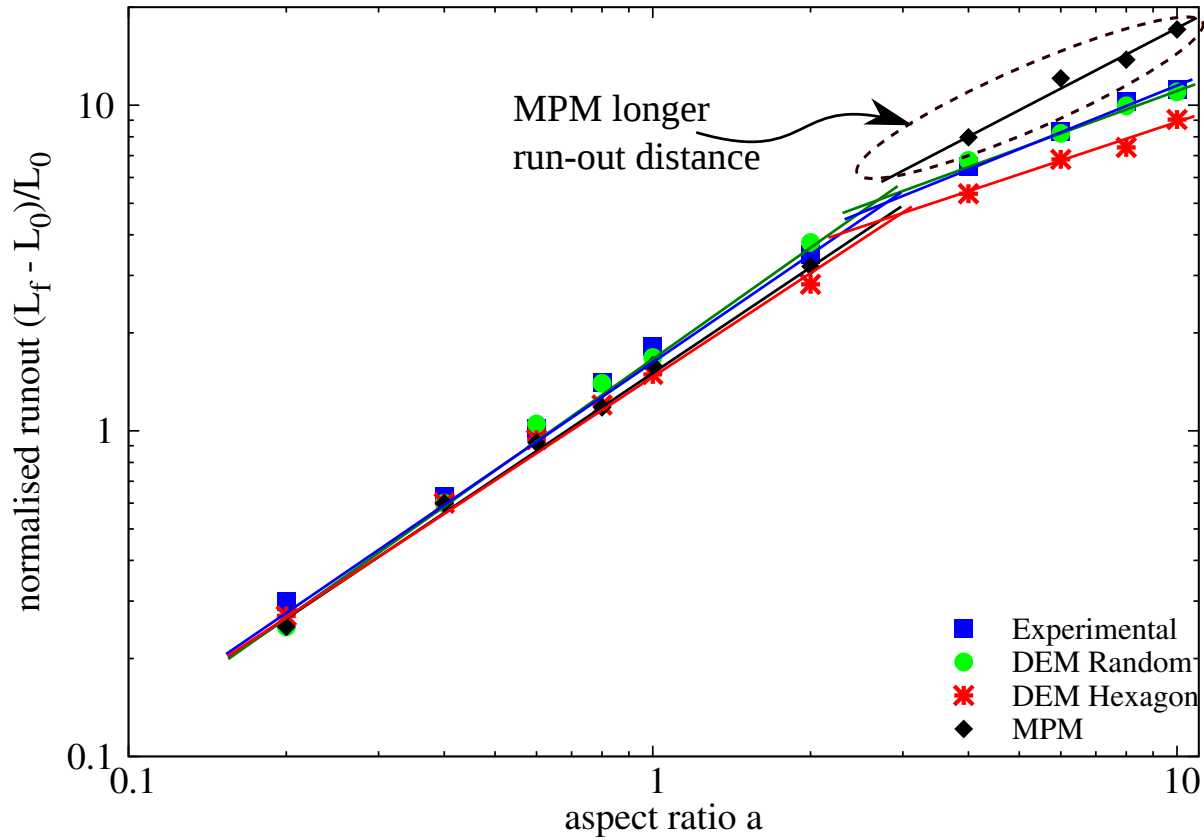


Figure 4.4 Normalised final run-out distance for columns with different initial aspect ratios

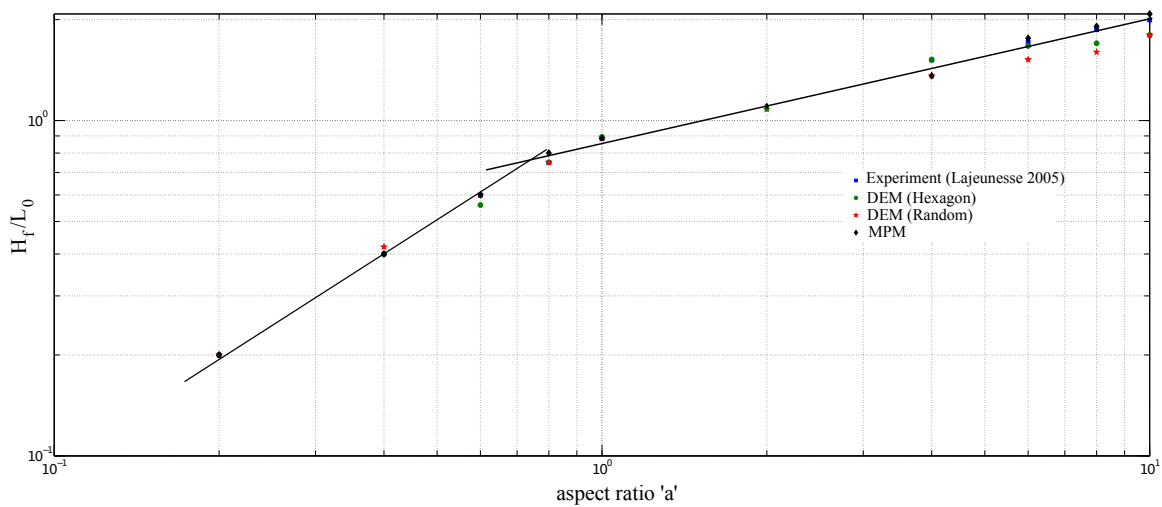


Figure 4.5 Normalised final collapse height for columns with different initial aspect ratios

position of the grain along the sliding mass. The maximum velocity is observed at the front of the flowing mass corresponding to that of a plug flow in horizontal direction. Particulate and continuum simulations show similar run-out distance at the critical time. Both approaches show similar quantity of material destabilised above the failure surface. However, the crystalline arrangement of soil grains in a hexagonal packing results in a different flow mechanics, which also shows the effect of jamming at the flow front. The continuum nature of MPM results in a slightly different geometry of the material destabilised above the failure surface in comparison to DEM simulations. The velocity profile is similar to a steady granular surface flow observed by Lajeunesse et al. (2004).

For columns with lower initial aspect ratios, the run-out distance is proportional to the mass flowing above the failure surface. The spreading results from a Coulomb-like failure of the edges and implies no free fall of the column. Daerr and Douady (1999) also observed active Coulomb yielding in transient granular surface flows. In this case, the effective friction properties of the flow can be simply predicted from the shape of the final deposit. The amount of mass mobilized during the collapse is significantly affected by the angle of the failure surface. Figure 4.6 shows that both numerical techniques predict a distinct failure surface when the flow is fully developed at critical time  $\tau_c$ . The angle of the failure surface is found to be about 55°. The failure surface begins from the toe of the column and propagates inwards at an angle of 50 to 55°. The formation of the “truncated conical deposit” or “conical deposit” depends only on the initial length of the column, as the angle of the failure surface is found to be independent of the aspect ratio. The failure angle is consistent with the interpretation in terms of *active Coulomb failure* (Lajeunesse et al., 2004), which leads to a predicted failure angle  $\theta_y = 45^\circ + \delta/2$ , where  $\delta$  is the friction angle of the granular material. In the present study, the macroscopic friction angle is 22°, which leads to  $\theta_y = 45^\circ + 22^\circ/2 = 56^\circ$ , which is in good agreement with the numerical simulations and experimental observations by Lajeunesse et al. (2004). The fracture angle has a direct effect on the transition between the truncated cone and the conical deposit occurring at an aspect ratio of 0.7. Schaefer (1990) observed the onset of instabilities in a narrow wedges of 56 to 65° for Cambridge-type constitutive models that describes granular flows, which is in-line with the failure angle observed in the present study.

The final profile of the granular column with an initial aspect ratio of 0.4 is shown in figure 4.7. Both MPM and DEM show similar run-out behaviour. The continuum approach is able to capture the flow dynamics of short columns, where the failure mechanism is active Coulomb failure. In dense hexagonal packing, the failure surface is steep due to crystallisation effect. The variation in the angle of the failure surface causes a difference in the amount of material destabilised, and in turn the run-out distance. This crystallisation phenomenon is found to have a significant influence on the final deposit of the granular column. Lacaze and

## 4.2 Granular column collapse

## 13

<sup>29</sup> Kerswell (2009) observed that poly-disperse grains are less susceptible to crystallize especially  
<sup>30</sup> in the case of tall columns.

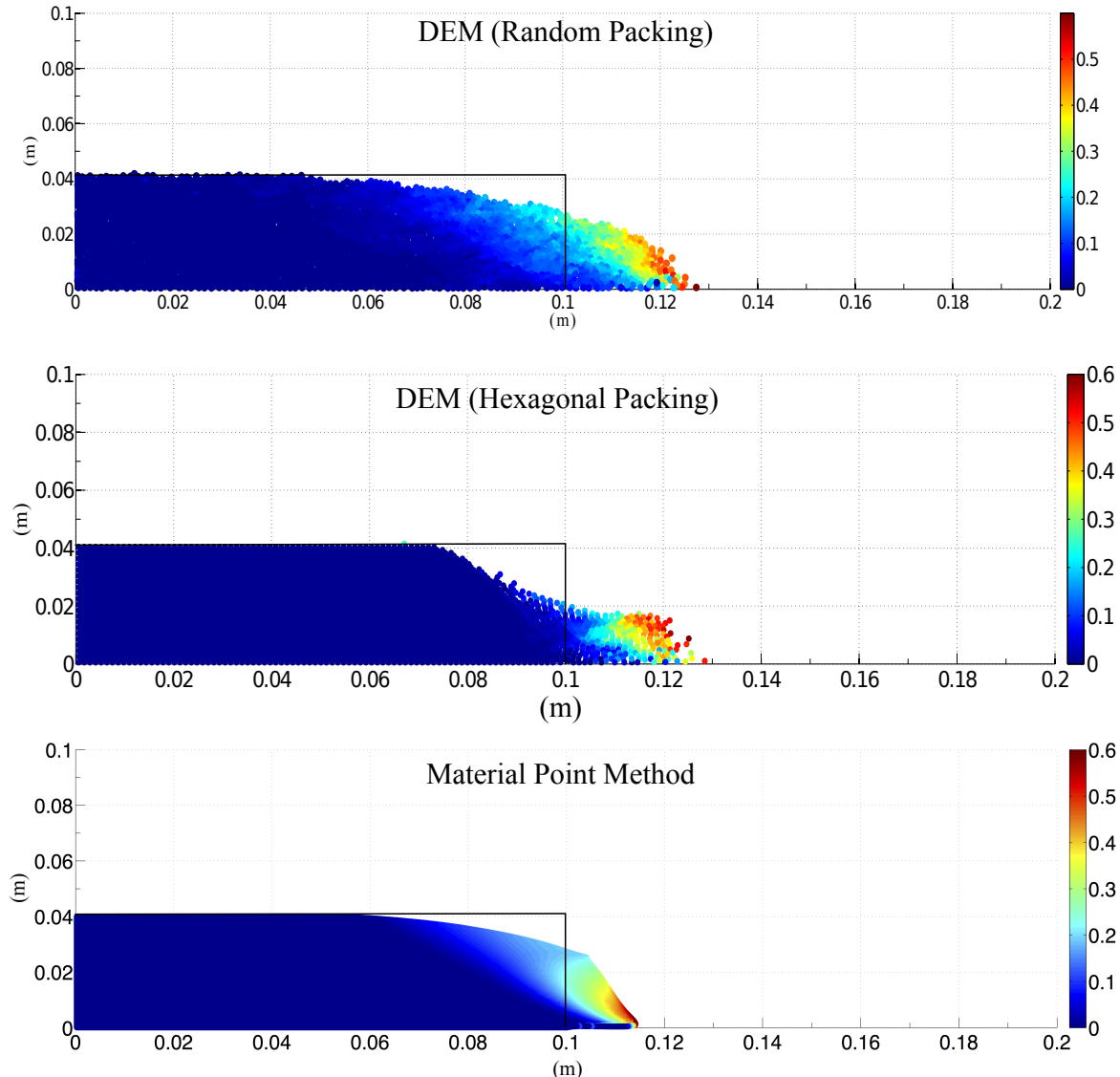


Figure 4.6 Velocity profile of a granular column collapse ( $a = 0.4$  &  $t = \tau_c$ )

<sup>31</sup> For tall columns ('a' > 2.7), the flow is still initiated by a well defined failure surface as  
<sup>32</sup> can be seen in figure 4.8. However, in this case the initial granular column is much higher  
<sup>33</sup> than the top of the failure surface. Due to gravity most of the grains in the column experience  
<sup>34</sup> free-fall consuming the column along their way. When they reach the vicinity of the failure  
<sup>35</sup> surface, the flow gets deviated along the horizontal direction releasing a huge amount of kinetic  
<sup>36</sup> energy gained during the free fall. For larger aspect ratio ( $a > 0.7$ ), the resulting static region is

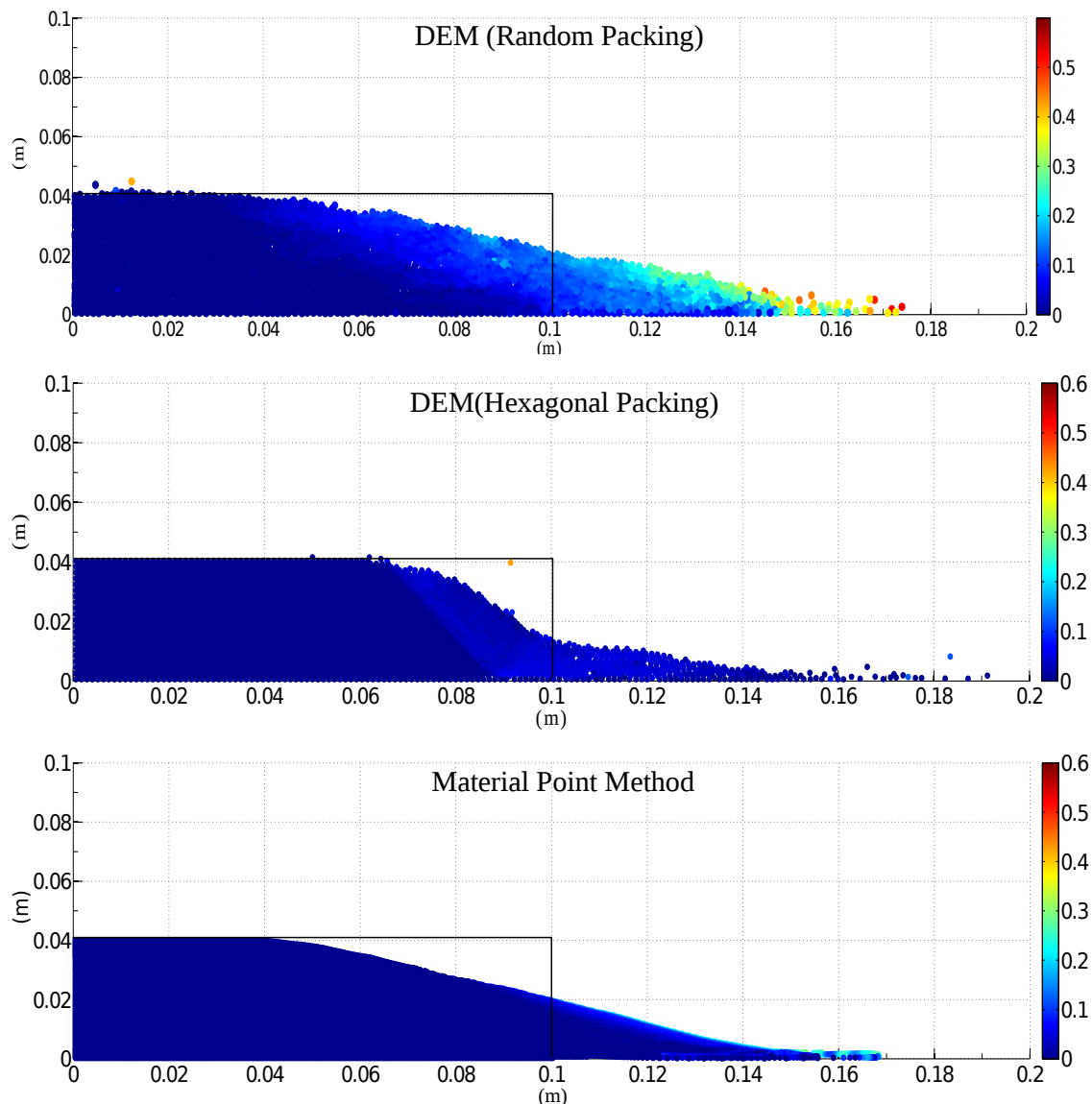


Figure 4.7 Velocity profile of a granular column collapse ( $a = 0.4$  &  $t = 3 \times \tau_c$ )

a cone, the final height of the cone, i.e.,  $H_f$  lies above the summit of the failure surface. Hence, a different evolution is observed from that of the axis-symmetric geometry (Lube et al., 2005), where the final height coincides with the summit of the failure surface forming a truncated conical deposit. Lajeunesse et al. (2004) observed that the variation in the deposit morphology between the axis-symmetric case and the rectangular collapse to be a geometrical effect rather than as an experimental artefact.

An initial failure surface starting from the toe end of the column at an angle of about 55° can be observed at the critical time  $\tau_c$ . As the collapse of the granular collapse progresses, successive failure planes parallel to the initial failure surface are formed and shear failure occurs along these planes. The presence of several shear bands in the final profile of the collapsed granular column confirms this behaviour. Crystallisation in hexagonal packing has a significant effect on the run-out distance by forming series of parallel shear bands, resulting in unnatural flow kinematics. This observation throws light on the mechanics of propagation of shear bands in massive landslides such as the Storegga submarine landslide. The flow behaviour becomes similar to that of columns with lower aspect ratio as the flow starts descending along the failure plane. The final profile of the collapsed granular column with an initial aspect ratio of 6 is presented in figure 4.9. For tall columns, the dissipation process is more complex due to the free-fall dynamics. The vertical acceleration of the grains induces a non-trivial mass distribution in the flow during spreading. This mass distribution plays a dominant role in the power-law scaling observed in the run-out (Staron and Hinch, 2007).

Regardless of the experimental configuration and the initial aspect ratio of the columns, the flow is initiated by a well-defined rupture surface, above which the material slides down leaving a static region underneath the failure plane. Depending on the aspect ratio of the column, two asymptotic behaviours are observed. For smaller aspect ratios, the flow is dominated by friction where as the large aspect ratio columns are influenced by the pressure gradient.

To study the influence of aspect ratio on the flow dynamics of granular columns, the flow front  $L(t)$  and the maximum height of column  $H(t)$  are tracked. The evolution of scaled height ( $H_f/L_0$ ) and the run-out distance ( $L_f - L_0$ )/ $L_0$  with time for granular columns with an initial aspect ratio of 0.4 and 6 are presented in figure 4.10. Three distinct regions can be observed in the flow evolution of a granular column collapse regardless of the initial aspect ratio of the column. An initial transient acceleration phase is observed for a time  $0.8\tau_c$ . This phase is followed by a heap movement of granular materials at the foot with a constant spreading velocity  $V$  for about  $2\tau_c$ . When time ‘ $t$ ’ >  $\tau_c$ , the velocity varies linearly with depth in the flowing layer and decreases exponentially with depth near the static layer. This velocity profile is similar to those observed in steady granular surface flows (Lajeunesse et al., 2004). Most of the run-out happens during this phase. The final phase involves deceleration of the flow

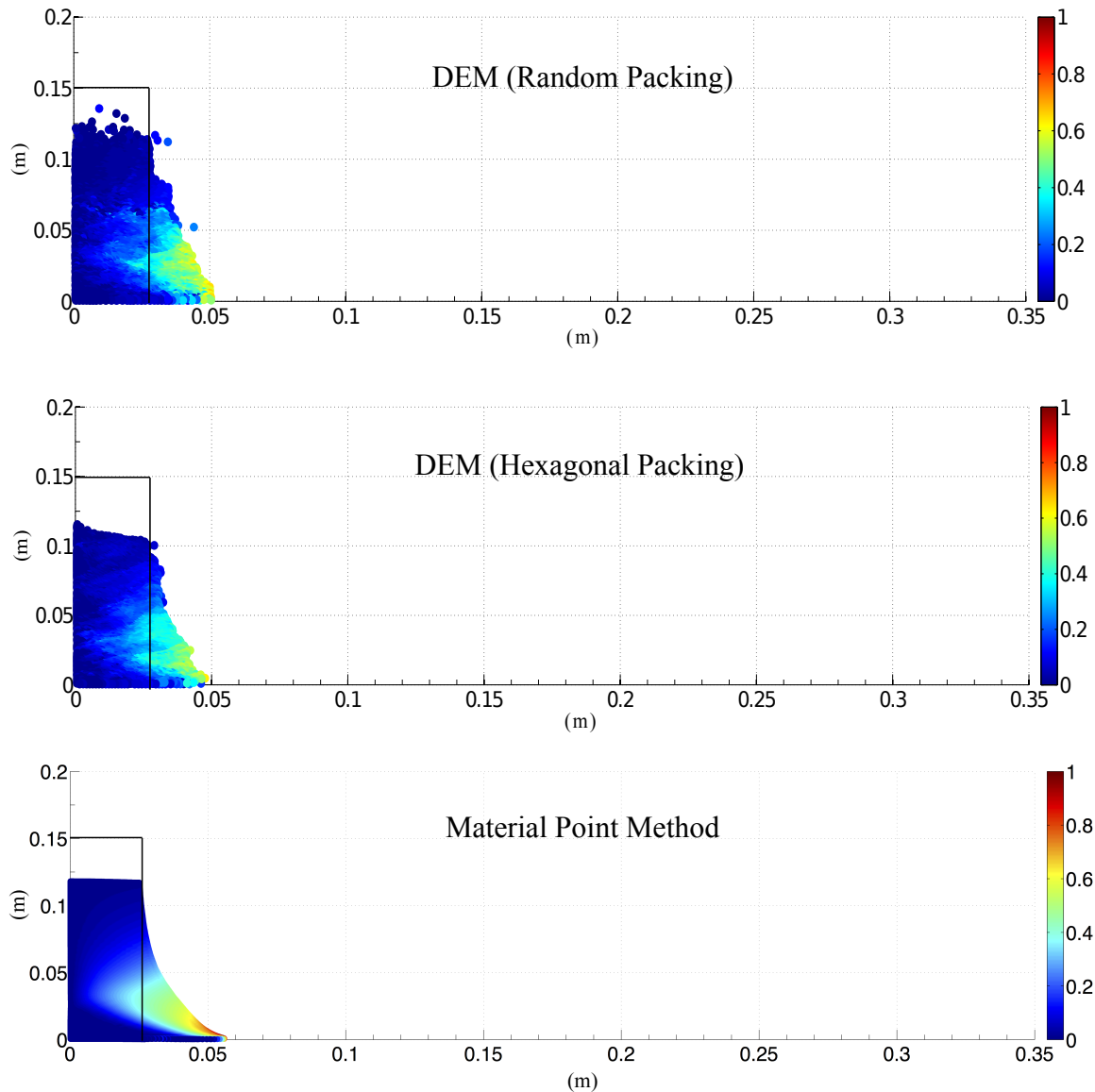


Figure 4.8 Velocity profile of a granular column collapse ( $a = 6$  &  $t = \tau_c$ )

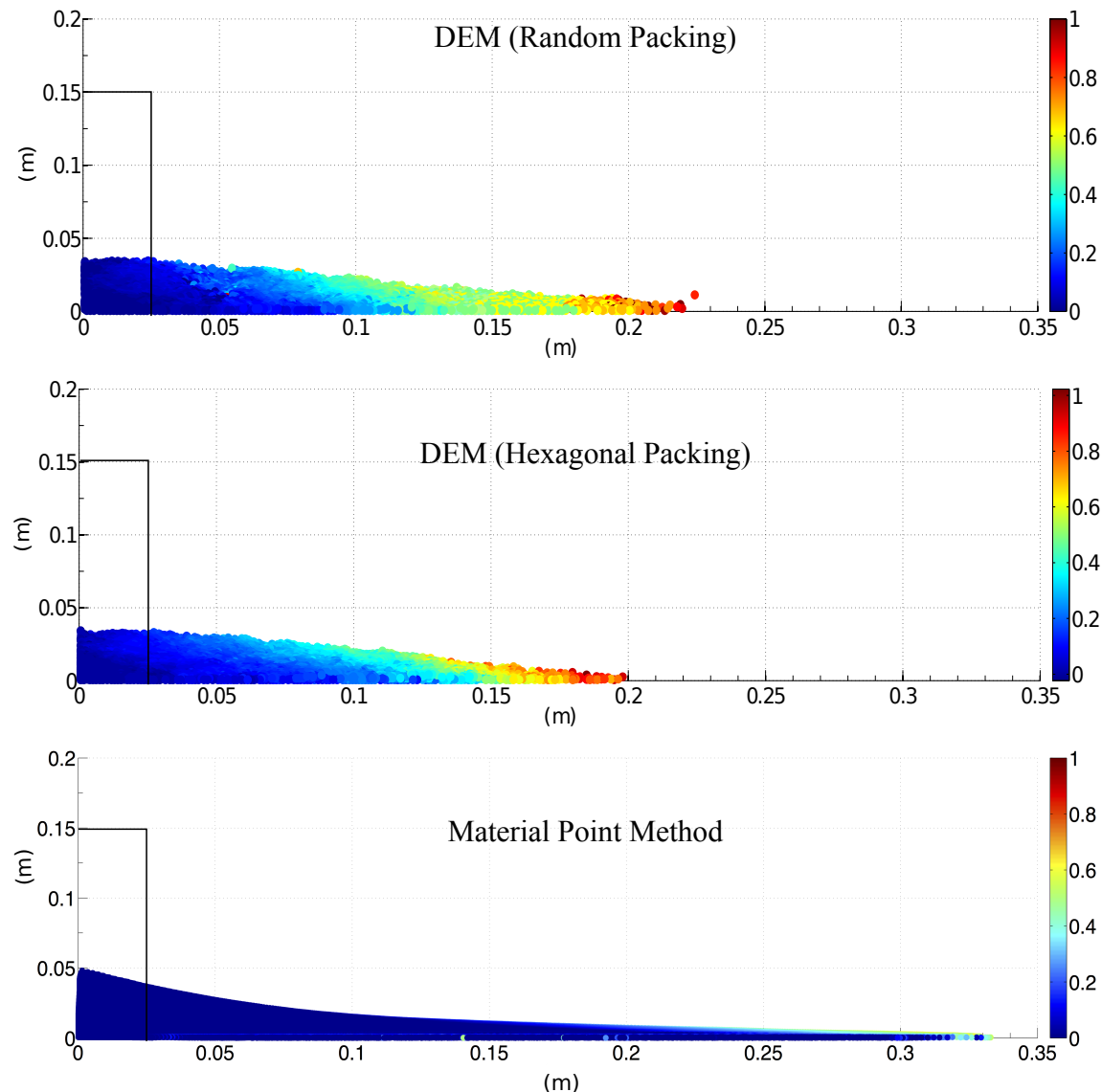


Figure 4.9 Velocity profile of a granular column collapse ( $a = 6$  &  $t = 3 \times \tau_c$ )

1 front and the flow comes to rest after about  $0.6\tau_c$ . The spreading of the granular column ceases  
2 after a time in the order of about  $3\tau_c$ , however some motion still persists along the free surface  
3 behind the flow front for a much longer time due to internal rearrangement, the duration of  
4 which can last up to  $t \approx 6\tau_c$ .

5 The critical time is evaluated as the time at which the potential energy available for the flow  
6 has been converted to the kinetic energy. In short columns, the critical time observed in both  
7 hexagonal and random packing of grains matches the experimental observations. However, the  
8 material point method overestimates the critical time by a factor of 0.75, which means that it  
9 takes longer for the flow to be fully mobilized. However, the actual run-out duration of the flow  
10 is short and the granular mass comes to rest at about  $t = 3\tau_c$ .

11 For columns with larger aspect ratios, the continuum and particulate approaches simulate  
12 similar flow evolution up to  $3\tau_c$ , beyond which particulate simulation decelerates and comes  
13 to rest, while the flow continues to evolve in MPM simulation resulting in longer run-out  
14 distance. The flow comes to rest at time  $t = 6\tau_c$ . The three phases in a granular flow can be  
15 distinctly observed in the flow evolution plot for a column with an initial aspect ratio of 6 (see  
16 figure 4.10b). The flow evolution behaviour observed in the case of DEM simulation matches  
17 the experimental observation by [Lajeunesse et al. \(2004\)](#). Hexagonal packing predicts longer  
18 time for the flow to evolve, which can be attributed to jamming of grains. In MPM simulations,  
19 the failure starts at the toe of the column and slowly propagates up to form the failure surface.  
20 This results in slower initiation of the flow. Whereas in DEM, the initial stage of collapse is  
21 characterised by free-fall under gravity. It can be observed that MPM overestimates the critical  
22 time by 50%. Although, MPM and DEM simulations show the same run-out at time  $t = 3\tau_c$ ,  
23 the flow evolution between both the approaches is different. MPM simulations continue to  
24 accelerate beyond  $3\tau_c$  and ceases to flow at  $6\tau_c$ . In order to understand the difference in the  
25 flow dynamics in the case of material point method, it is important to study the mechanism of  
26 energy dissipation.

#### 27 4.2.4 Energy dissipation mechanism

28 The energy dissipation mechanism during the collapse provides useful insights into the flow  
29 dynamics. In the case of small aspect ratios, the columns undergo no free fall. The spreading  
30 mainly results from the failure of the edges, while the top of the column remains essentially  
31 undisturbed in the central area. [Staron and Hinch \(2007\)](#) showed that the amount of energy  
32 dissipated during the spreading  $\delta E$  can be easily recovered using the simple shape of the final

## 4.2 Granular column collapse

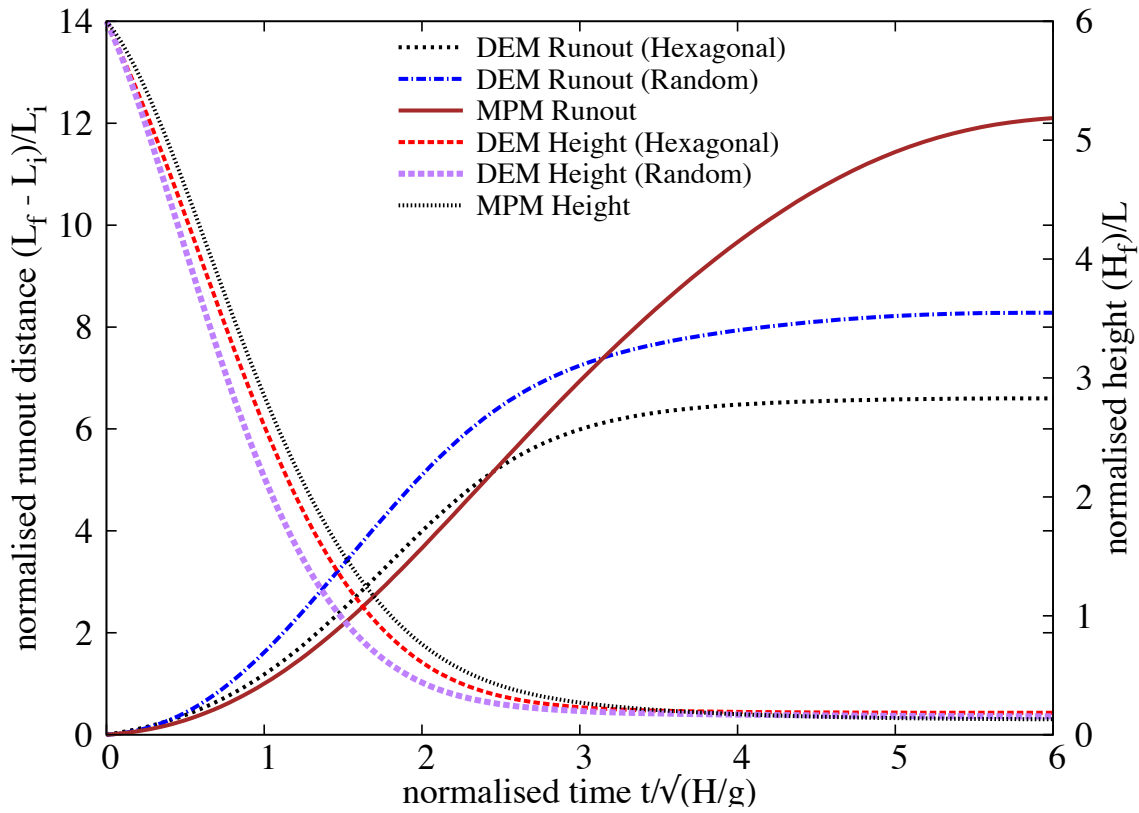
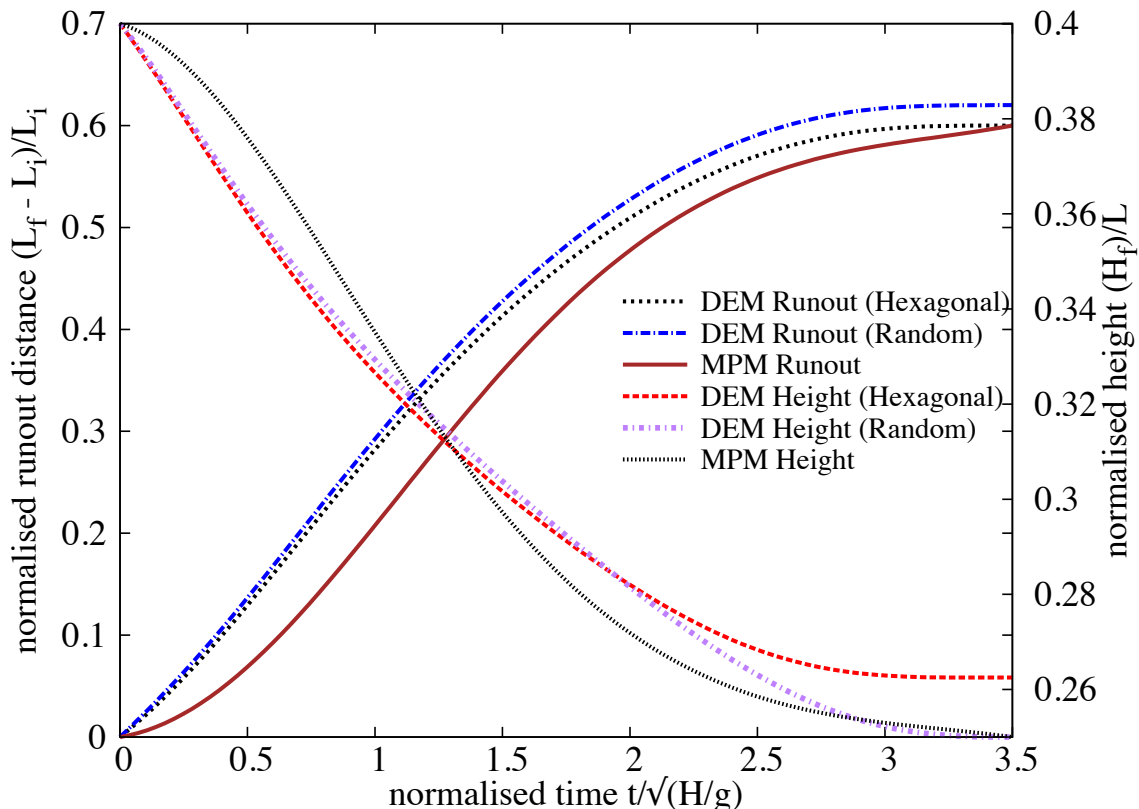


Figure 4.10 Flow evolution of granular column collapse

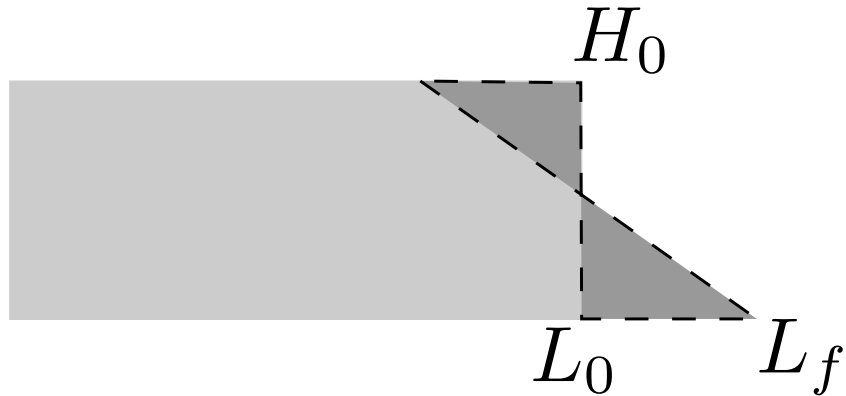


Figure 4.11 Scheme of collapse for small aspect ratio columns. The amount of energy  $\delta E$  lost in the process can be evaluated from the run-out distance  $L_f - L_0$  (after [Staron and Hinch \(2007\)](#)).

<sup>1</sup> deposit and volume conservation (see figure 4.11). The difference of potential energy between  
<sup>2</sup> the initial and the final states gives

$$\delta E = \frac{1}{6} g \rho (L_f - L_0) H_0^2, \quad (4.8)$$

<sup>4</sup> where  $\rho$  is the density of the packing. It is assumed that this energy is dissipated by the  
<sup>5</sup> work of frictional forces  $W_\mu$  over the total run-out distance by the center of mass G of the  
<sup>6</sup> spreading material. [Staron et al. \(2006\)](#) considers two regions of dissipation: the amount of mass  
<sup>7</sup> destabilised  $\frac{1}{4}(L_f - L_0)H_0$  over two thirds of the runout distance  $2(L_f - L_0)/3$  (considering the  
<sup>8</sup> triangular shape of the final deposit and the initial and the final positions of the center of mass).  
<sup>9</sup> The effective coefficient of friction  $\mu_e$  characterizes the mean dissipation in the flow. The work  
<sup>10</sup> of friction forces is

$$W_\mu = \frac{1}{6} \mu_e g \rho (L_f - L_0) H_0^2, \quad (4.9)$$

<sup>12</sup> Equating  $\delta E$  and  $W_\mu$  gives  $\mu_e(L_f - L_0) = H_0$ . The scaling of the runout leads directly  
<sup>13</sup> to the relation  $\mu_e = \lambda^{-1}$ , which is the numerical constant, which depends on the material  
<sup>14</sup> properties ([Balmforth and Kerswell, 2005](#)), in the power-law relation between the run-out and  
<sup>15</sup> the initial aspect ratio. The amount of energy  $\delta E$  dissipated during the spreading is compared  
<sup>16</sup> with  $W = N_p g m_p r_p$ , where  $N_p$  is the total number of grains,  $m_p$  is their mass, and  $r_p$  is the  
<sup>17</sup> total horizontal distance run by each of them. We observe that the dissipation energy  $\delta E$  is  
<sup>18</sup> proportional to  $W$ . [Staron and Hinch \(2007\)](#) observed that the coefficient of proportionality  
<sup>19</sup> gives a measure of the effective friction and observed a power law dependence between  $\mu_e$   
<sup>20</sup> and internal friction angle  $\mu$ :  $\mu_e = 0.425\mu^{0.2}$ . In this study, an effective friction angle  $\mu_e$  of  
<sup>1</sup> 21° is observed, which is very close to the critical state friction angle of 22° used in MPM  
<sup>2</sup> simulations. This proves that the energy dissipation mechanism modelled in a continuum

sense as a frictional dissipation process captures the flow kinematics observed in DEM and experiments, for short columns.

Figure 4.12a shows the time evolution of the normalised potential energy ( $E_p/E_0$ ) and kinetic energy ( $E_k/E_0$ ) for granular columns with an initial aspect ratio ‘a’ = 0.4. The normalised potential and kinetic energy are computed as

$$E_p = \sum_{p=1}^{N_p} m_p g h_p, \quad (4.10)$$

$$E_{ki} = \frac{1}{2} \sum_{p=1}^{N_p} m_p v_p^2, \quad (4.11)$$

where  $N_p$  is the total number of grains,  $m_p$  is the mass of a grain ‘p’,  $h_p$  is the height and  $v_p$  is the velocity of the grain ‘p’. The cumulative dissipation energy is computed as

$$\frac{E_d}{E_0} = 1 - \frac{E_k}{E_0} - \frac{E_p}{E_0}. \quad (4.12)$$

It can be observed that both MPM and DEM show similar energy dissipation mechanism. The DEM simulation shows 3% more potential energy dissipation in comparison with MPM simulations. This small difference in the potential energy is due to grain rearrangements. This shows the ability of continuum approach in capturing the flow kinematics of columns with small aspect ratios ( $a \leq 2.7$ ).

The evolution of normalised kinetic and potential energy of a tall column collapse (‘a’ of 6) is shown in figure 4.12b. It can be observed that the initial potential energy stored in the grains is converted to kinetic energy which is dissipated as the granular material flows down. Three successive stages can be identified in the granular column collapse. In first stage, similar to short columns, the flow is initiated by a well defined failure surface. However, the centre of gravity of the granular column is much higher than the top of the failure surface, which results in free fall of grains under gravity consuming the column along their way. In this stage which lasts for ( $t < 0.8\tau_c$ ), the initial potential energy stored in the grains is converted into vertical motion. In the second stage, when the grains reach the vicinity of the failure surface, they undergo collisions with the bottom plane and the neighbouring grains, thus causing the flow to deviate along the horizontal direction releasing a large amount of kinetic energy gained during the free fall (see figure 4.9). In the third stage, the grains eventually leave the base area of the column and flow sideways (Lajeunesse et al., 2004). As the process involves collective dynamics of all the grains, it is difficult to predict the exact trajectory of a grain, however, the overall dynamics can be explained.

DEM simulations model both collisional and frictional dissipation process during the collapse of tall columns. However, MPM simulations assume that the total initial potential energy stored in the system is completely dissipated through friction over the entire run-out distance, this results in longer run-out distance. Figure 4.12b shows the evolution of energy with time. At the initial stage of collapse, characterised by free fall of grains under gravity, DEM simulation due its particulate nature shows a rapid reduction in the potential energy in comparison with MPM, where the failure begins from the toe of the column. The continuum nature of MPM simulations results in slower initiation of collapse (see figure 4.10b). It can be also observed from figure 4.12b that dissipation energy in MPM is 25% less than DEM simulations. In order to understand the mechanism of energy dissipation, it is important to separate the contribution from the cumulative frictional and collisional parts. The frictional dissipation (basal and internal friction) observed in DEM is almost identical to the frictional dissipation observed in MPM (figure 4.12b). The difference in the dissipation energy is due to the collisional regime, which occurs at  $0.8\tau_c$ . The total dissipation and the frictional dissipation curves diverge around  $0.8\tau_c$  where the grains near the vicinity of the failure surface undergo collisions with the bottom plane and the neighbouring grains resulting in collisional dissipation of the stored potential energy. DEM simulation show drop in the peak kinetic energy at  $\approx 0.8\tau_c$ , which is at the beginning collisional dissipation stage. MPM lacks this collision dissipation mechanism, which results in longer run-out distances for columns with large aspect ratios.

$\mu(I)$  rheology, discussed in ??, describes the granular behaviour using a dimensionless number, called the *inertial number I*, which is the ratio of inertia to the pressure forces. Small values of I corresponds to critical state of soil mechanics and large values of I corresponds to the fully collisional regime of kinetic theory.  $\mu(I)$  rheology is adopted in MPM simulations to understand the characteristics of the flow regime. Mohr-Coulomb model was used along with  $\mu(I)$  rheology. The friction angle is changed according to a friction law (Da Cruz et al., 2005) that is dependent on the inertial number I as  $\mu = \mu_{min} + bI$  where  $\mu_{min} = 0.22$  and  $b = 1$ . Figure 4.13 shows the flow evolution of granular column collapse for aspect ratio ‘a’ of 0.4 and 6 using  $\mu(I)$  rheology. For short columns, the evolution of flow based on  $\mu(I)$  rheology is identical to the MPM simulation using Mohr-Coloumb model. However, for tall columns,  $\mu(I)$  rheology evolves at the same rate as the DEM simulations up to  $t = 0.8\tau_c$ , after which MPM simulation continues to accelerate due to lack of collisional dissipation, while the DEM simulation decelerates with time.

Figure 4.23b shows that the short column attains a maximum inertial number of 0.012, which is in the dense granular flow regime, inertial number  $I \approx 10^{-3}$  to 0.1 (Da Cruz et al., 2005). However, the maximum inertial number  $I \approx 0.04$ , for tall is still within the dense granular flow regime. DEM simulations, however, showed a collisional regime that has inertial

## 4.2 Granular column collapse

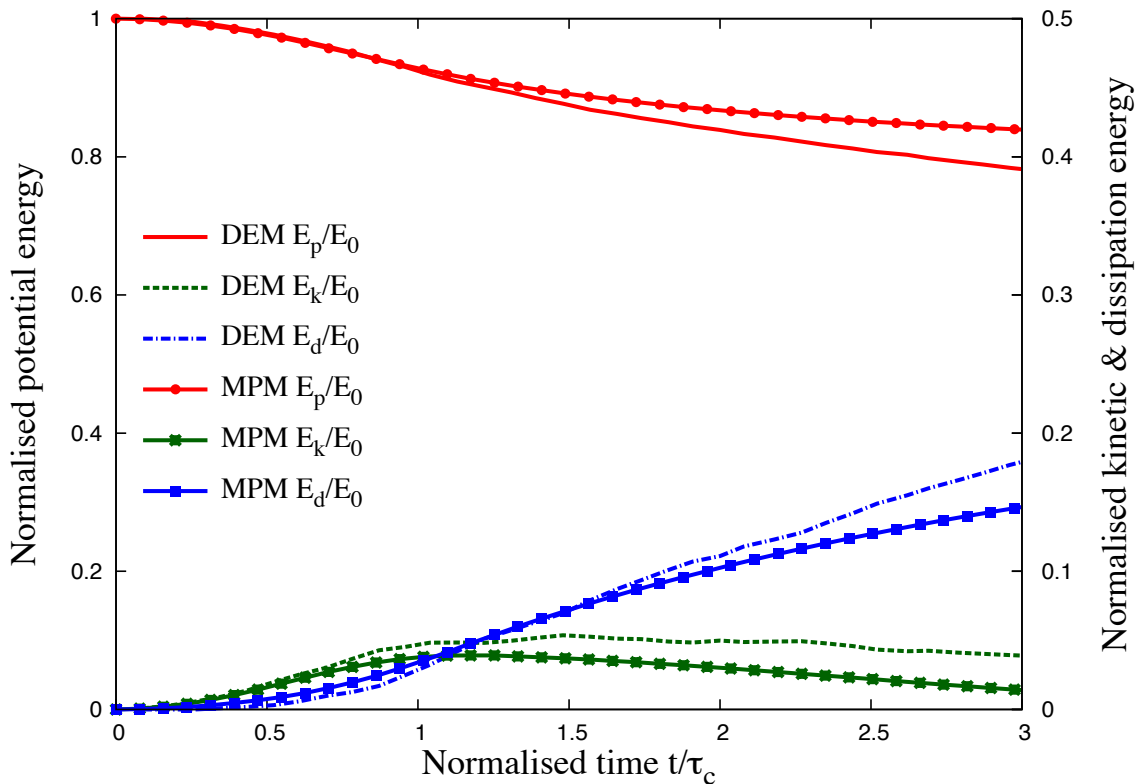
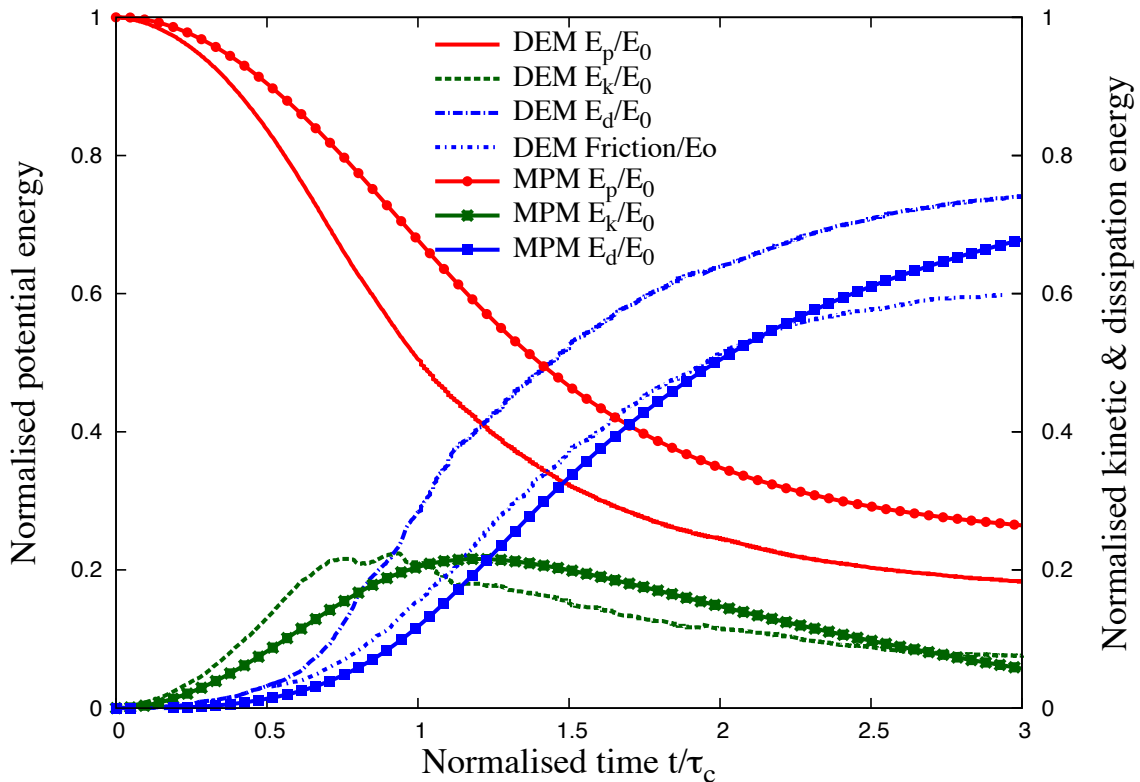
(a) Energy evolution of a column with  $a = 0.4$ (b) Energy evolution of a column with  $a = 6$ 

Figure 4.12 Energy evolution of granular column collapse

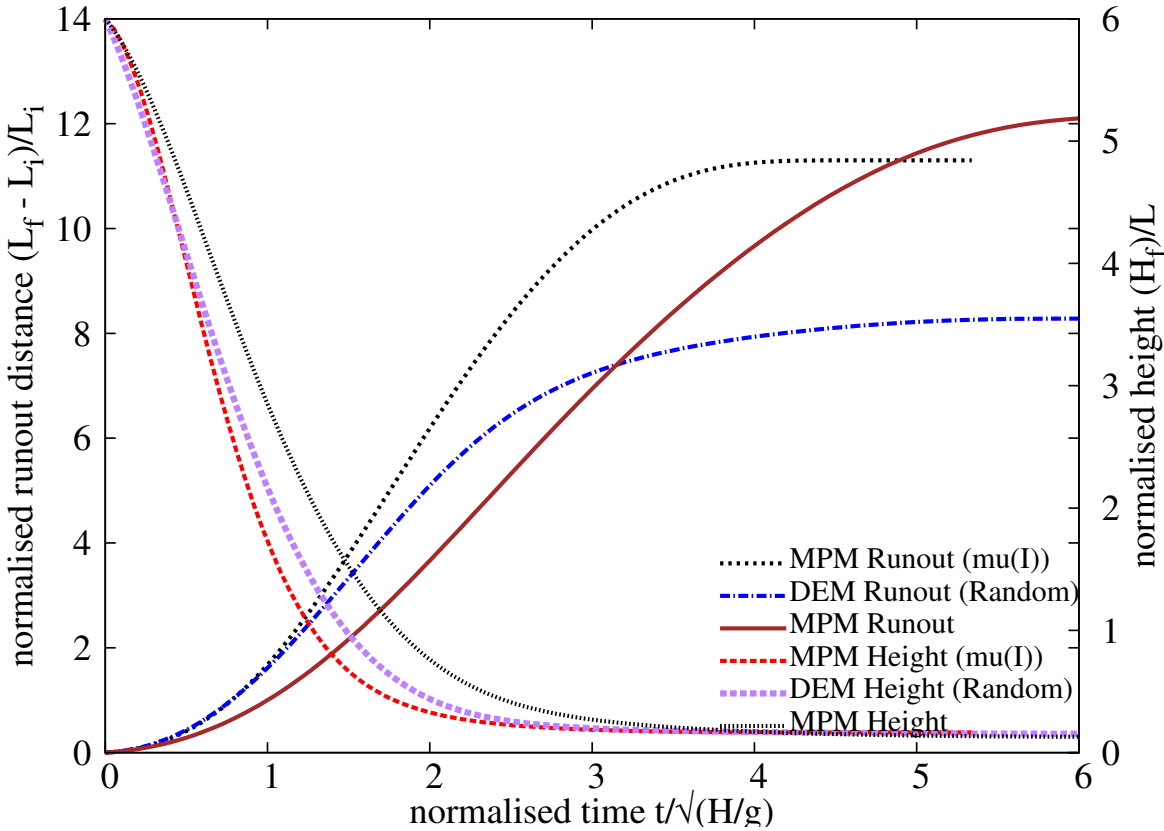
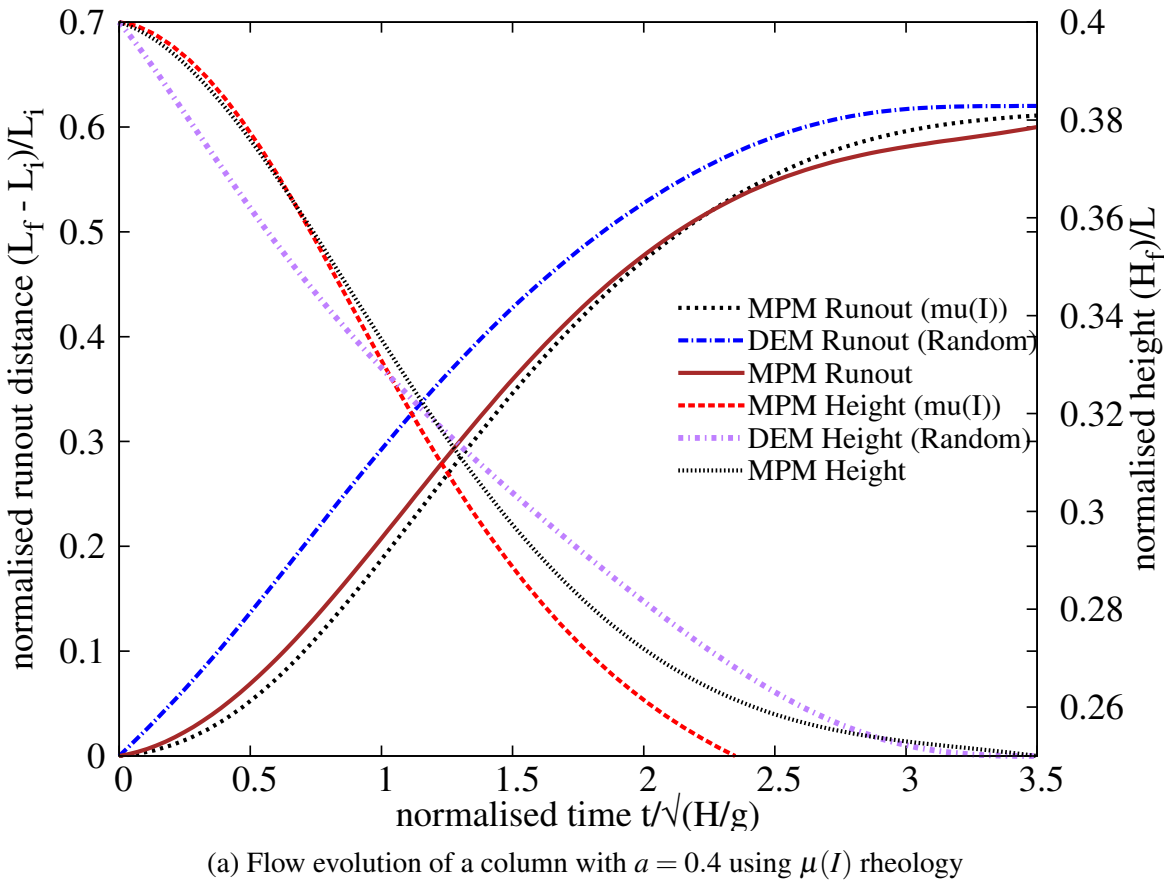


Figure 4.13 Flow evolution of granular column collapse using  $\mu(I)$  rheology

<sup>35</sup> number higher than 0.1. This shows that continuum approach using frictional laws are able to  
<sup>1</sup> capture the flow kinematics at small aspect ratios, however are unable to precisely describe the  
<sup>2</sup> flow dynamics of tall columns, which is characterised by an initial collisional regime.

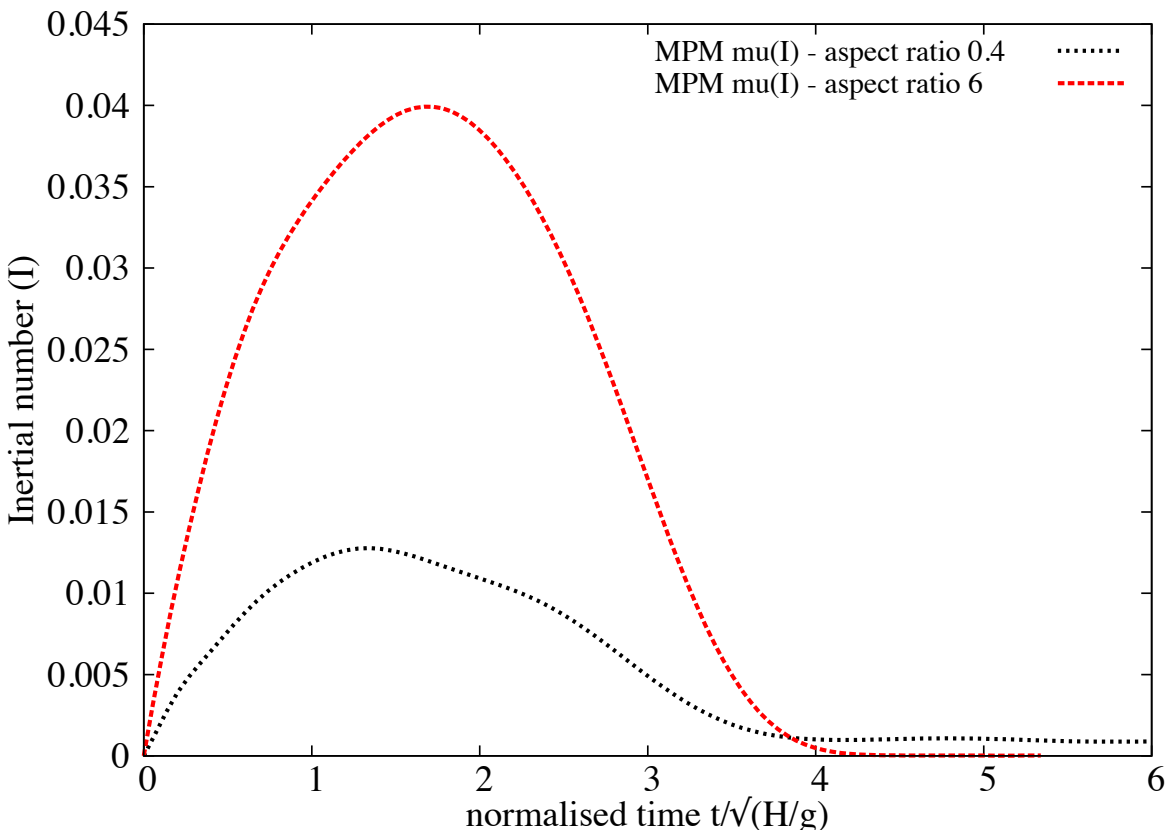


Figure 4.14 Evolution of inertial number with time for columns with  $a = 0.4$  and  $a = 6$

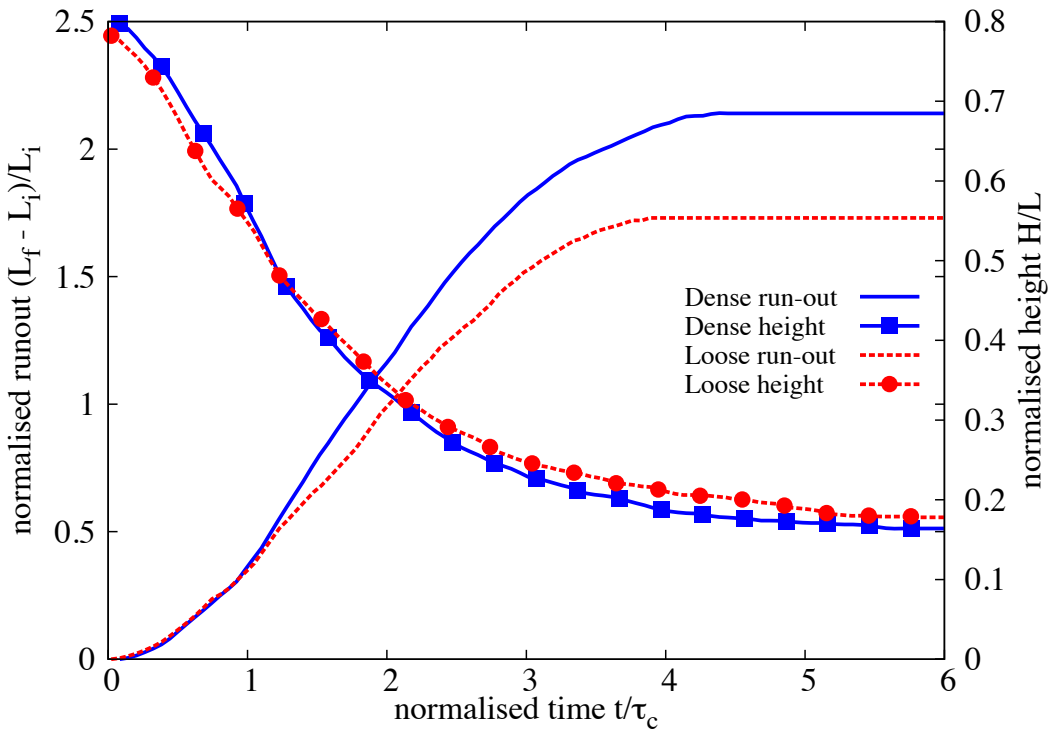
### <sup>3</sup> 4.2.5 Role of initial grain properties

<sup>4</sup> Lube et al. (2005) observed that the run-out distance scales with the initial aspect ratio of the  
<sup>5</sup> column, independent of the material properties. The run-out evolution after the initial transition  
<sup>6</sup> regime is a frictional dissipation process, and the lack of influence of material properties on the  
<sup>7</sup> run-out behaviour is inconsistent with frictional dissipation in continuum modelling of granular  
<sup>8</sup> flow behaviour. Balmforth and Kerswell (2005) observed that the material properties have  
<sup>9</sup> almost no influence on the exponent of the normalised run-out as a function of the initial aspect  
<sup>10</sup> ratio. The numerical constant of proportionality, however, showed clear material dependence.  
<sup>11</sup> This corroborates the conclusions of Lajeunesse et al. (2004) and softens that of Lube et al.  
<sup>12</sup> (2005). Daerr and Douady (1999) also observed strong influence of initial packing density and  
<sup>13</sup> the internal structure on the behaviour of granular flows.

14 It should be noted that the collapse experiment is highly transient and no clear stationary  
15 regime is observed. On the contrary, the acceleration and the deceleration phases cover nearly  
16 the whole duration of the spreading. This makes it difficult to analyse the flow structure and  
17 its relation with other characteristic of the system. The knowledge of the final run-out is not a  
1 sufficient characterization of the deposit: one also needs to know how the mass is distributed  
2 during the flow to understand the dynamics and the dissipation process. This is expected to be  
3 true in natural contexts as well as in experiments. While the inter-grain friction does not affect  
4 the early vertical dynamics, nor the power-law dependence, it controls the effective frictional  
5 properties of the flow, and its internal structure ([Staron and Hinch, 2007](#)). It is interesting to  
6 note that the details of the structure of the flow do not influence the final run-out dependence,  
7 and thus seem to play a marginal role in the overall behaviour of the spreading. This could  
8 explain why simple continuum model with a frictional dissipation could reproduce the run-out  
9 scaling for columns with small aspect ratios.

10 The run-out behaviour of a loose (79% packing density) and a dense (83% packing density)  
11 granular column ( $a = 0.8$ ) are studied to understand the influence of material properties.  
12 The evolution of normalised run-out with time for two different initial packing densities are  
13 presented in figure [4.15](#). At the initial stage of collapse  $t = \tau_c$ , the flow evolution is identical  
14 in both dense and loose conditions. However, the dense column flows 30% longer than the  
15 loose condition. Both the columns come to rest at around  $t = 4\tau_c$ . The columns, however,  
16 show similar evolution of the normalised height. This shows that only a part of the column is  
destabilised during the collapse.

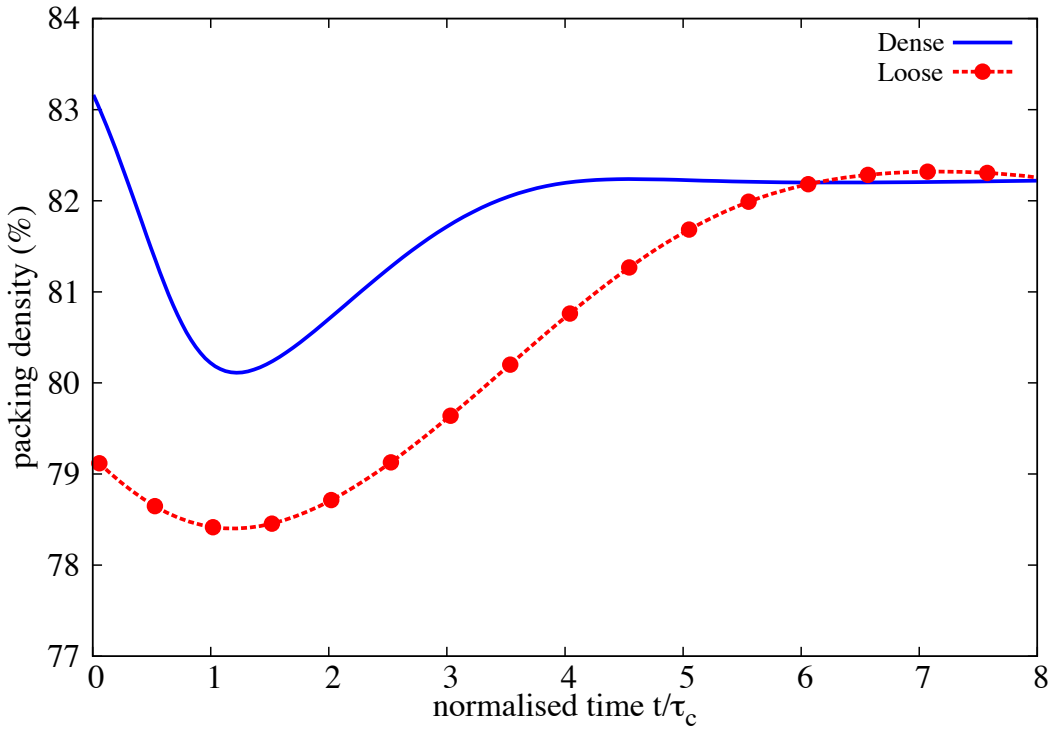
2 Figure [4.17](#) show the evolution of potential and kinetic energy with time. Similar potential  
3 energy evolution in both dense and loose conditions reveals that there is no change in the  
4 overall mechanism of collapse. The dense condition has slightly higher peak kinetic energy  
5 than the loose column. In the free-fall phase, the dense column shows a steeper increase in  
6 the horizontal kinetic energy in comparison to the loose column. This indicates that dense  
7 granular mass is pushed farther away more quickly than the loose column. Loose column  
8 exhibits higher vertical kinetic energy which may be due to particle rearrangement resulting in  
9 densification of the granular mass. Figure [4.16](#) shows that the loose sample densifies as the flow  
10 evolves. Both dense and loose granular columns dilate during the initial stage of collapse, this  
11 is due to grains experiencing shear along the fracture surface. In both cases, the granular mass  
12 attains similar packing density at the end of the flow. Dense granular column dilates, while the  
13 loose column compacts to achieve the same critical density. The dense condition has higher  
14 mobilised potential energy during the initial stage of collapse, which yields higher horizontal  
15 kinetic energy for the flow. However in loose condition, a higher proportion of the available  
16 energy is lost during compaction. This behaviour in addition to higher mobilised potential

Figure 4.15 Effect of density on run-out evolution  $a = 0.8$ 

17 energy results in longer run-out distance in dense granular column. [Lajeunesse et al. \(2004\)](#)  
 18 observed that the flow comes to rest at around  $3\tau_c$ , but the grains continue to re-arrange until  
 19  $6\tau_c$ , similar behaviour is observed in DEM simulations.

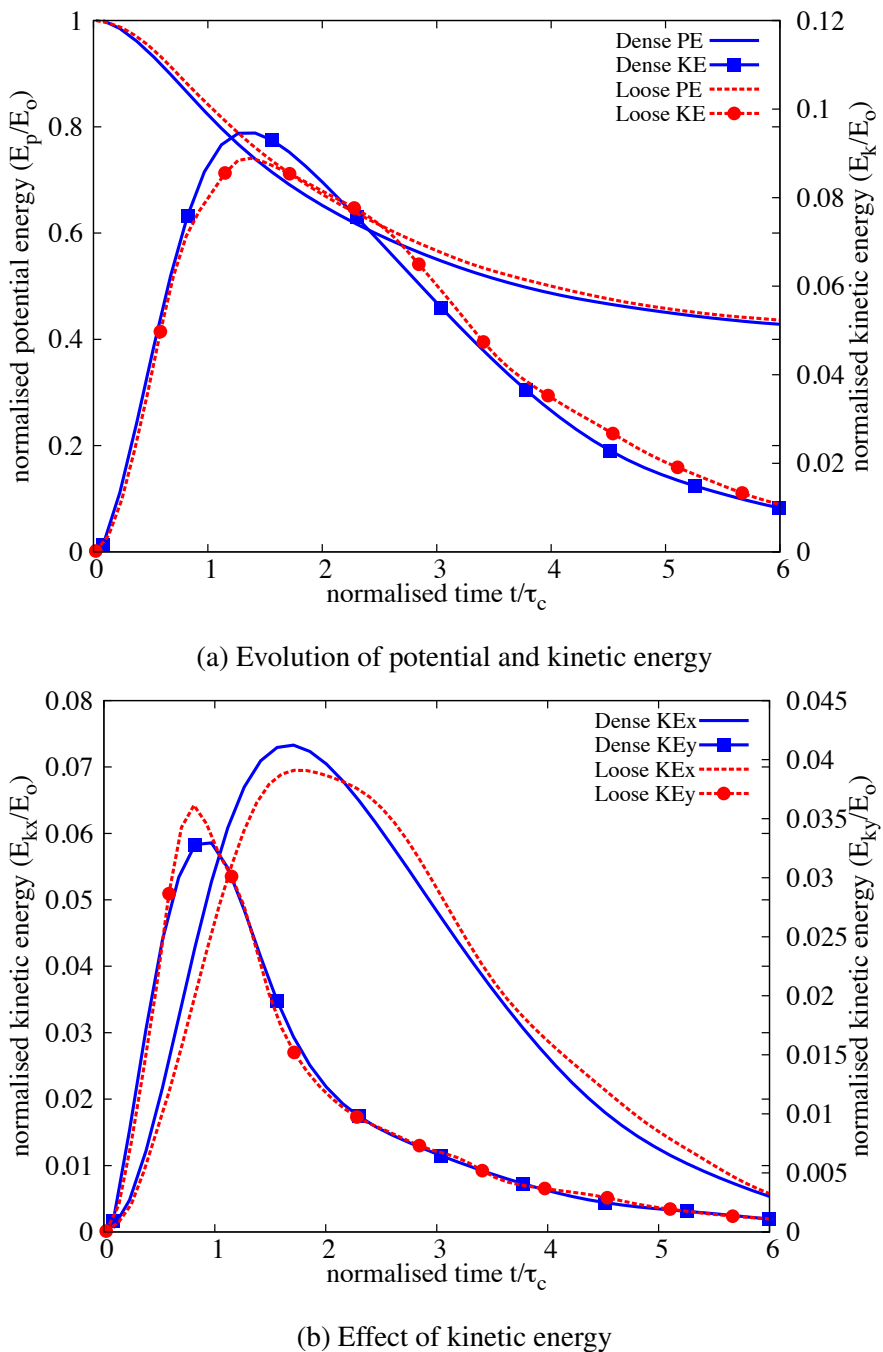
20 In order to remove the effect of crystallisation on the run-out behaviour, a highly poly-  
 21 disperse sample ( $r = d_{max}/d_{min} = 6$ ) is used. The flow kinematics of a dense (relative density  
 22  $D_r = 74\%$ ) and a loose ( $D_r = 22\%$ ) granular column with aspect ratio of 0.8 is studied. Similar  
 23 to the previous case, the dense granular column exhibits longer run-out distance (see figure 4.18).  
 24 Due to compaction of grains in loose condition, almost 20% of the initial potential energy  
 25 available for collapse is lost in densification due to grain rearrangements in comparison to the  
 26 dense condition (see figure 4.20). The compaction of grains in loose column and the dilation  
 27 in dense column results in significantly different flow structure, especially at the flow front  
 28 (figure 4.19). As the loose column densifies, more granular mass is pushed to the flow front  
 29 resulting in higher vertical effective stress. The loose column exhibits a more parabolic final  
 30 deposit profile in comparison to the dense column, which shows a triangular deposit at the  
 31 front.

32 In short column, only a part of the granular column above the failure surface participates in  
 the flow. However, it appears that the collapse for large aspect ratios mixes two very different  
 dynamics: the first stage shows a large vertical acceleration, while the second stage consists

Figure 4.16 Evolution of local packing density  $a = 0.8$ 

of a “conventional” horizontal granular flows. The effect of density on the run-out behaviour of tall columns is investigated. Similar to short columns, the dense granular column with an aspect ratio of 6 shows higher run-out distance in comparison to the loose condition. The dense granular column flows almost twice as much as that of the loose column. Unlike short columns, the evolution of run-out is different even at the initial stage of the collapse. The dense granular column, which has higher initial potential energy show a rapid increase in the run-out due to free-fall and higher mobilised potential energy. During this stage of collapse, the dense granular column has 15 % higher normalised kinetic energy available for the horizontal push. This results in longer run-out distance for dense granular column in comparison to initially loose granular column.

The initial packing fraction and the distribution of kinetic energy in the system has a significant influence on the flow kinematics and the run-out behaviour, this suggests that triggering mechanisms play a crucial role in the case of natural flows. This stresses the necessity of accounting for initiation mechanisms while modelling the run-out behaviour using continuum approaches to predict realistic granular flow behaviour.

Figure 4.17 Effect of density on energy evolution  $a = 0.8$

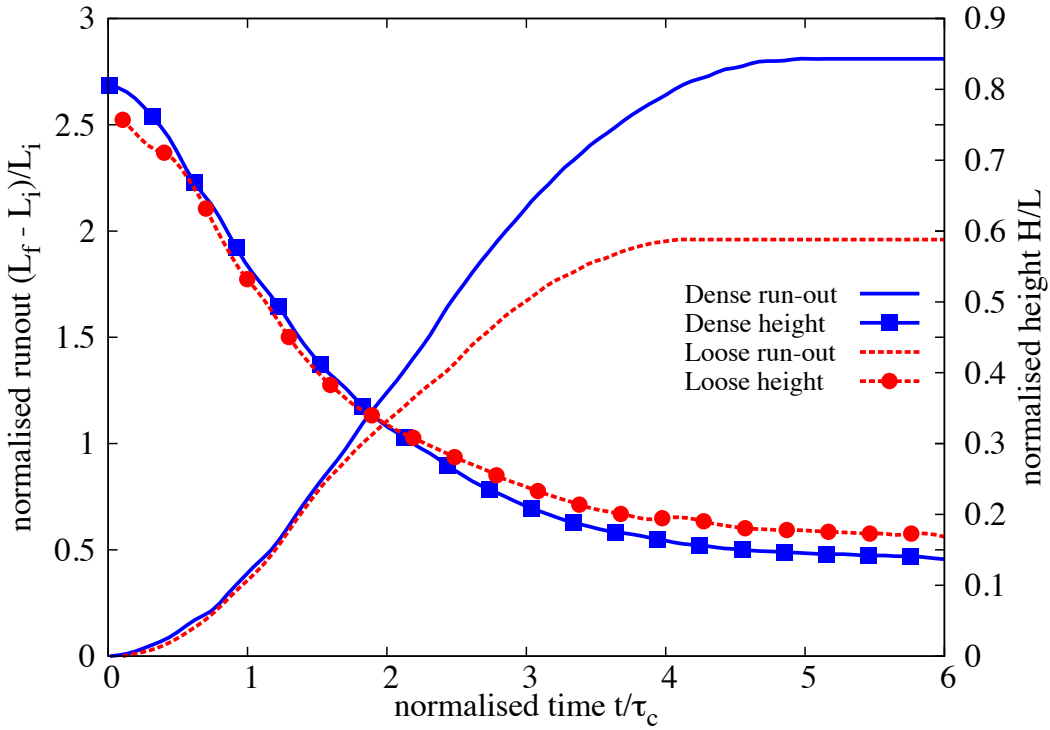
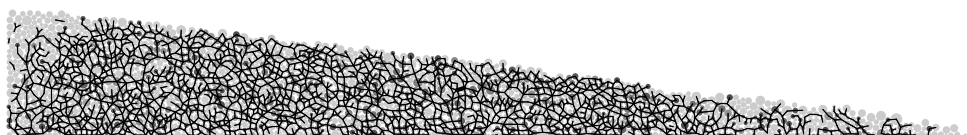
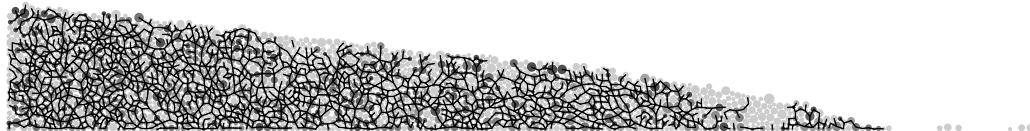


Figure 4.18 Effect of density on run-out evolution  $a = 0.8$  (poly-dispersity ‘r’ = 6)

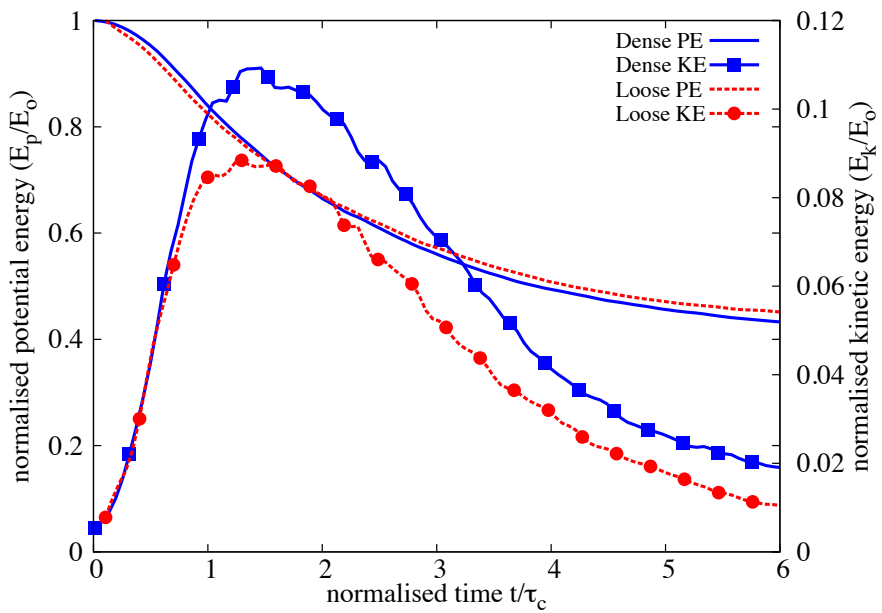


(a) Dense initial packing

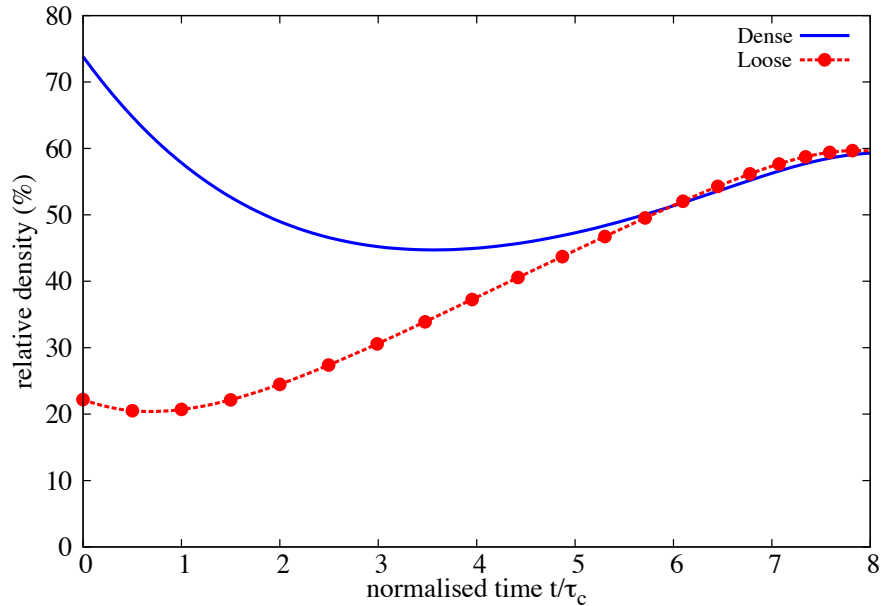


(b) Loose initial packing

Figure 4.19 Snapshots of granular column collapse  $t = 6\tau_c$

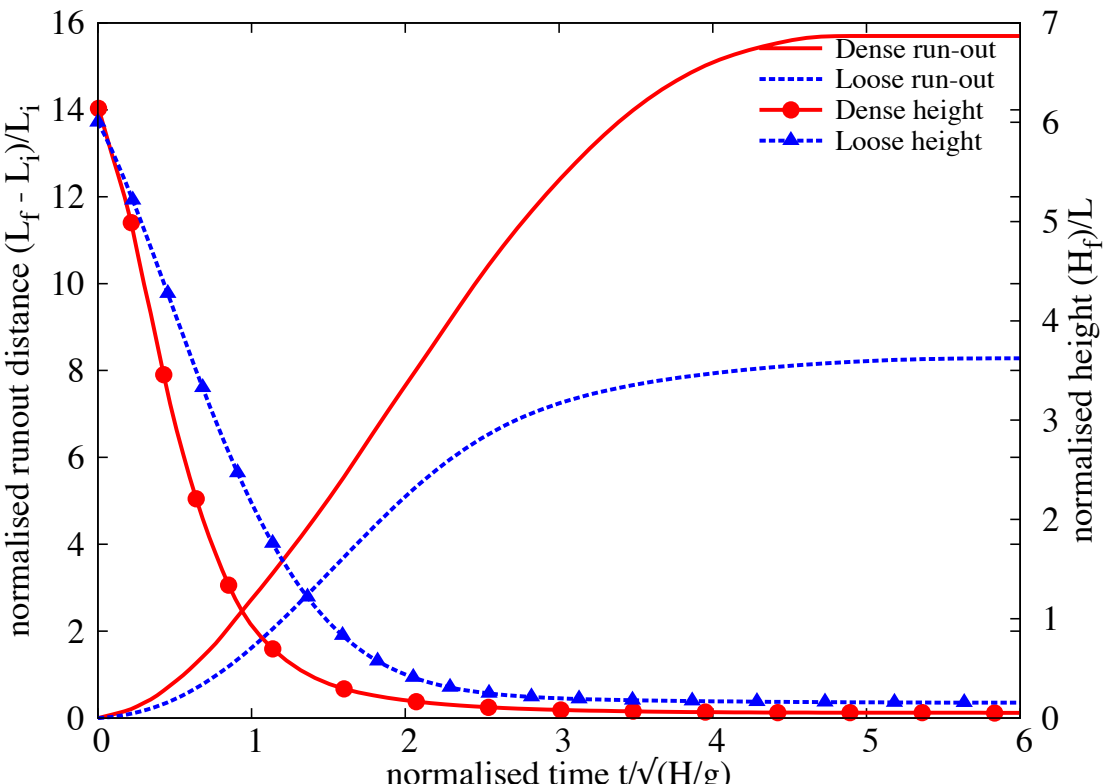


(a) Evolution of potential and kinetic energy

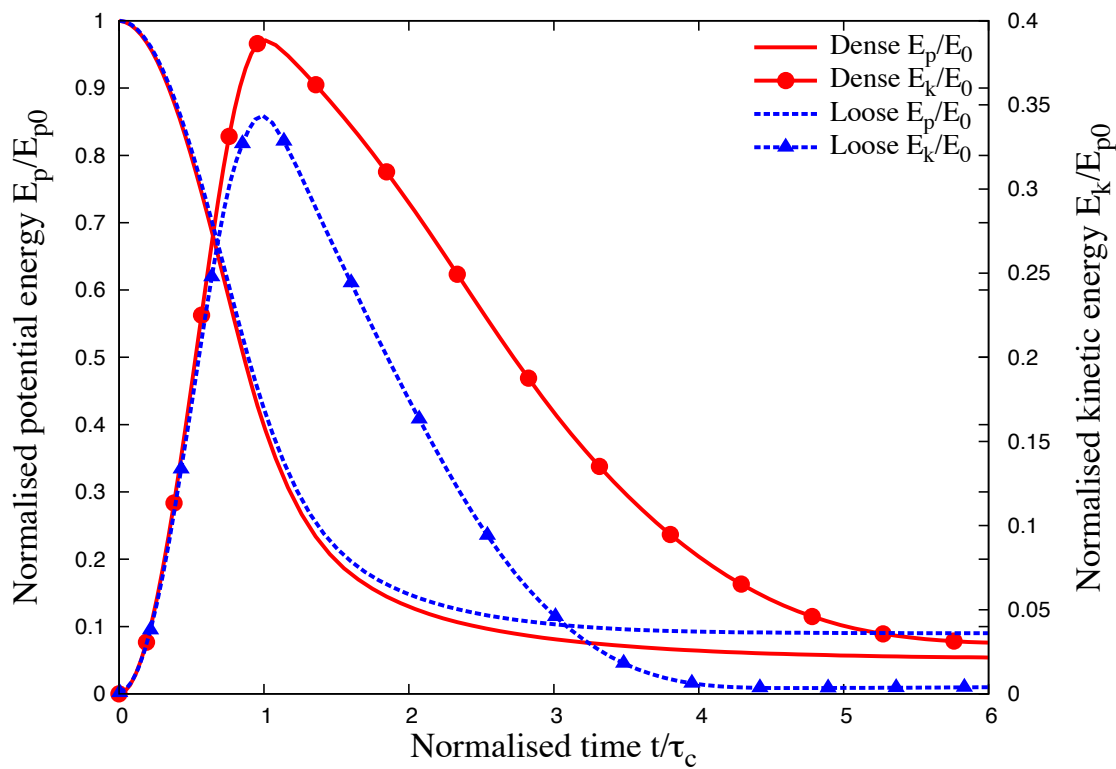


(b) Evolution of packing density

Figure 4.20 Effect of density on energy and packing fraction evolution  $a = 0.8$  (poly-dispersity ‘r’ = 6)



(a) Effect of density on run-out evolution



(b) Effect of density on energy evolution

Figure 4.21 Effect of density on run-out behaviour and energy evolution  $a = 0.6$

## 4.3 Slopes subjected to impact loading

Transient granular flows occur very often in nature. Well-known examples are rockfalls, debris flows, and aerial and submarine avalanches. In the geotechnical context, transient movements of large granular slopes is a substantial factor of risk due to their destructive force and the transformations they may produce in the landscape. Natural granular flows may be triggered as a result of different processes such as gradual degradation, induced by weathering or chemical reactions, liquefaction and external forces such as earthquakes. Most contemporary research on granular materials deals with the steady-state flow. Transients and inhomogeneous boundary conditions are much less amenable to observation and analysis, and have thus been less extensively studied despite their primary importance in engineering practice. In most cases of granular flow, an initially static pile of grains is disturbed by external forces, it then undergoes an abrupt accelerated motion and spreads over long distances before relaxing to a new equilibrium state. The kinetic energy acquired during destabilisation is dissipated by friction and inelastic collisions.

This section investigates the ability of MPM, a continuum approach, to reproduce the evolution of a granular pile destabilised by an external energy source. In particular, a central issue is whether power-law dependence of the run-out distance and time observed with respect to the initial geometry or energy can be reproduced by a simple Mohr-Coulomb plastic behaviour for granular slopes subjected an impact energy. Effect of different input parameters, such as the distribution of energy and base friction, on the run-out kinematics are studied by comparing the data obtained from DEM and MPM simulations.

### 4.3.1 Numerical set-up

The DEM sample is composed of  $\sim 13000$  disks with a uniform distribution of diameters by volume fractions ( $d_{max} = 1.5d_{min}$ ). The mean grain diameter and mass are  $d \simeq 2.455$  mm and  $m \simeq 0.0123$  kg, respectively. The grains are first poured uniformly into a rectangular box of given width and then the right-hand side wall is shifted further to the right to allow the grain to spread. A stable granular slope is obtained when all grains come to rest; see figure 4.22. This procedure leads to a mean packing fraction  $\simeq 0.82$ . Soil grains with mean density of  $2600$   $\text{kg m}^{-3}$  and internal friction coefficient of 0.4 between grains is adopted.

The initial static pile is set into motion by applying a constant horizontal gradient  $v_{0x}(y) = k(y_{max} - y)$  with  $k > 0$ . Such a configuration mimics the energy transfer mechanism of a horizontal quake along the bottom of the pile. The evolution of pile geometry and the total kinetic energy as a function of the initial input energy  $E_0$  is studied. The run-out distance  $L_f$  is the distance of the rightmost grain, which is still in contact with the main mass when the

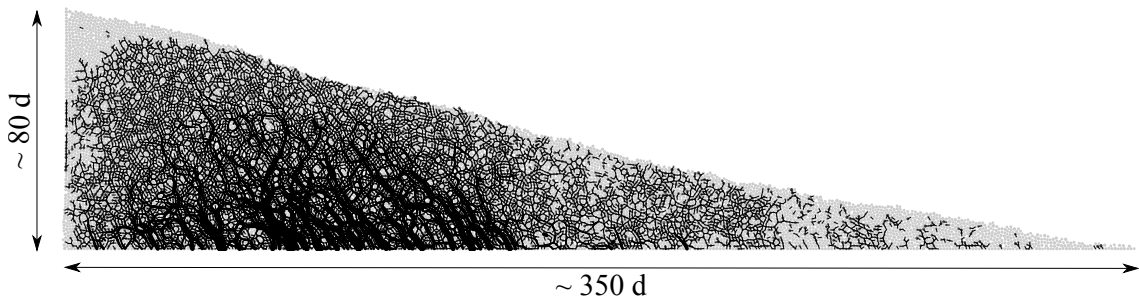


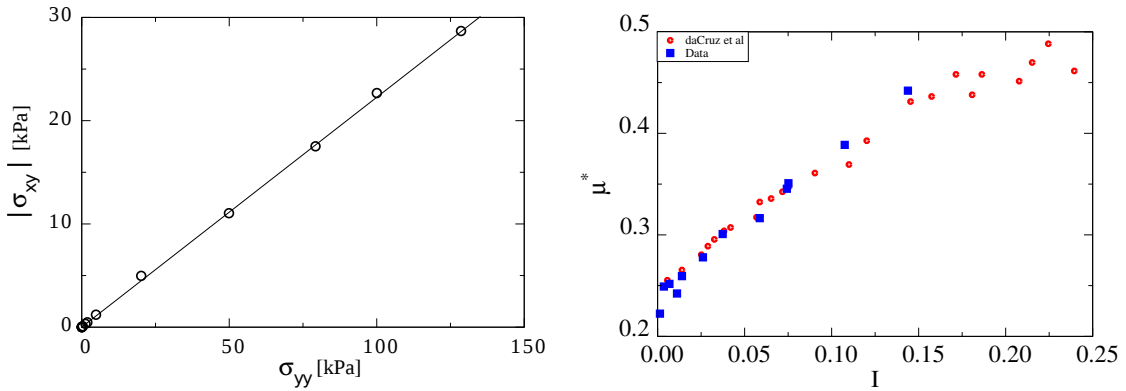
Figure 4.22 Initial geometry and dimensions of the pile

18 pile comes to rest. The run-out will be normalized by the initial length  $L_0$  of the pile, as in the  
 19 experiments of collapsing columns. The total run-out duration  $t_f$  is the time taken by the pile  
 20 to reach its final run-out distance  $L_f$ .

21 For grain-scale simulations, classical DEM and Contact Dynamics approach are used. This  
 22 research is done in collaboration with Patrick Mutabaruka, University of Montpellier, who  
 23 performed Contact Dynamics (CD) simulations that are presented in this section. A detailed  
 24 description of the Contact Dynamics method can be found in Jean (1999); Moreau (1993);  
 25 Radjai and Dubois (2011); Radjai and Richefeu (2009). The CD method is based on implicit  
 26 time integration of the equations of motion and a nonsmooth formulation of mutual exclusion  
 1 and dry friction between particles. The CD method requires no elastic repulsive potential and  
 2 no smoothing of the Coulomb friction law for the determination of forces. For this reason, the  
 3 simulations can be performed with large time steps compared to discrete element simulations.  
 4 The unknown variables are particle velocities and contact forces, which are calculated at each  
 5 time step by taking into account the conservation of momenta and the constraints due to mutual  
 6 exclusion between particles and the Coulomb friction. An iterative research algorithm based on  
 7 a non-linear Gauss-Seidel scheme is used. The only contact parameters within the CD method  
 8 are the friction coefficient  $\mu$ , the normal restitution coefficient  $\epsilon_n$  and the tangential restitution  
 9 coefficient  $\epsilon_t$  between grains.

10 In MPM simulations the material point spacing is same as the mean grain diameter in DEM.  
 11 A mesh size of 0.0125m is adopted with 25 material points per cell. The effect of mesh size and  
 12 the number of material points per cell is investigated in section 4.3.5. A Mohr-Coulomb model  
 13 with no dilation is used to simulate the continuum behaviour of the granular pile. Periodic  
 14 shear tests using CD, see figure 4.23a, reveals a macroscopic friction coefficient of 0.22. The  
 15 evolution of inertial number with friction is presented in figure 4.23b. The natural units of the  
 16 system are the mean grain diameter  $d$ , the mean grain mass  $m$  and gravity  $g$ . For this reason,  
 17 the length scales are normalised by  $d$ , time by  $(d/g)^{1/2}$ , velocities by  $(gd)^{1/2}$  and energies by  
 $mgd$ .

## 4.3 Slopes subjected to impact loading



(a) Evaluating the critical state friction angle from periodic shear test.  
(b) Evolution of Inertial number with friction  $\mu$

Figure 4.23 Periodic shear test using CD ([Mutabaruka, 2013](#)).

### 4.3.2 Evolution of pile geometry and run-out

19

Figure 4.24 shows the initial evolution of granular slope subjected to an initial impact energy  $E_0 = 61$  (in dimensionless units) using MPM. As the granular slope is sheared along the bottom, the shear propagates to the top leaving a cavity in the vicinity of the left wall. This cavity gets partially filled as the granular mass at the top collapse behind the flowing mass due to inertia.

20

21

22

23

- <sup>1</sup> Similar behaviour is observed during the initial stages of the flow evolution using DEM and
- <sup>2</sup> CD techniques (see figure 4.25). Due to inertia, the grains at the top of the granular heap roll
- <sup>3</sup> down to fill the cavity, while the pile continues to spread.

<sup>4</sup> The flow involves a transient phase with a change in the geometry of the pile followed  
<sup>5</sup> by continuous spreading. The gradient input energy applied to the granular slope mimics a  
<sup>6</sup> horizontal quake. Despite the creation of a cavity behind the flowing mass, the granular heap  
<sup>7</sup> remains in contact with the left wall irrespective of the input energy. Figure 4.26a shows the  
<sup>8</sup> normalized run-out distance  $(L_f - L_0)/L_0$  and total run-out time  $t_f$  as a function of the input  
<sup>9</sup> energy  $E_0$ . Two regimes characterized by a power-law relation between the run-out distance  
<sup>10</sup> and time as a function of  $E_0$  can be observed. In the first regime, corresponding to the range  
<sup>11</sup> of low input energies  $E_0 < 40 \text{ mgd}$ , the run-out distance observed varies as  $L_f \propto (E_0)^\alpha$  with  
<sup>12</sup>  $\alpha \simeq 0.206 \pm 0.012$  over nearly one decade. Overall, the run-out distance predicted by the  
<sup>13</sup> continuum approach matches the DEM simulations. At very low energies, DEM simulations  
<sup>14</sup> show longer run-out distance due to local fluidisation. The difference in the run-out between  
<sup>15</sup> DEM and CD arise mainly from the scales of description and the inelastic nature of Contact  
<sup>16</sup> Dynamics. Similar behaviour between DEM and CD approaches was observed by [Radjai et al.](#)  
<sup>17</sup> (1997).

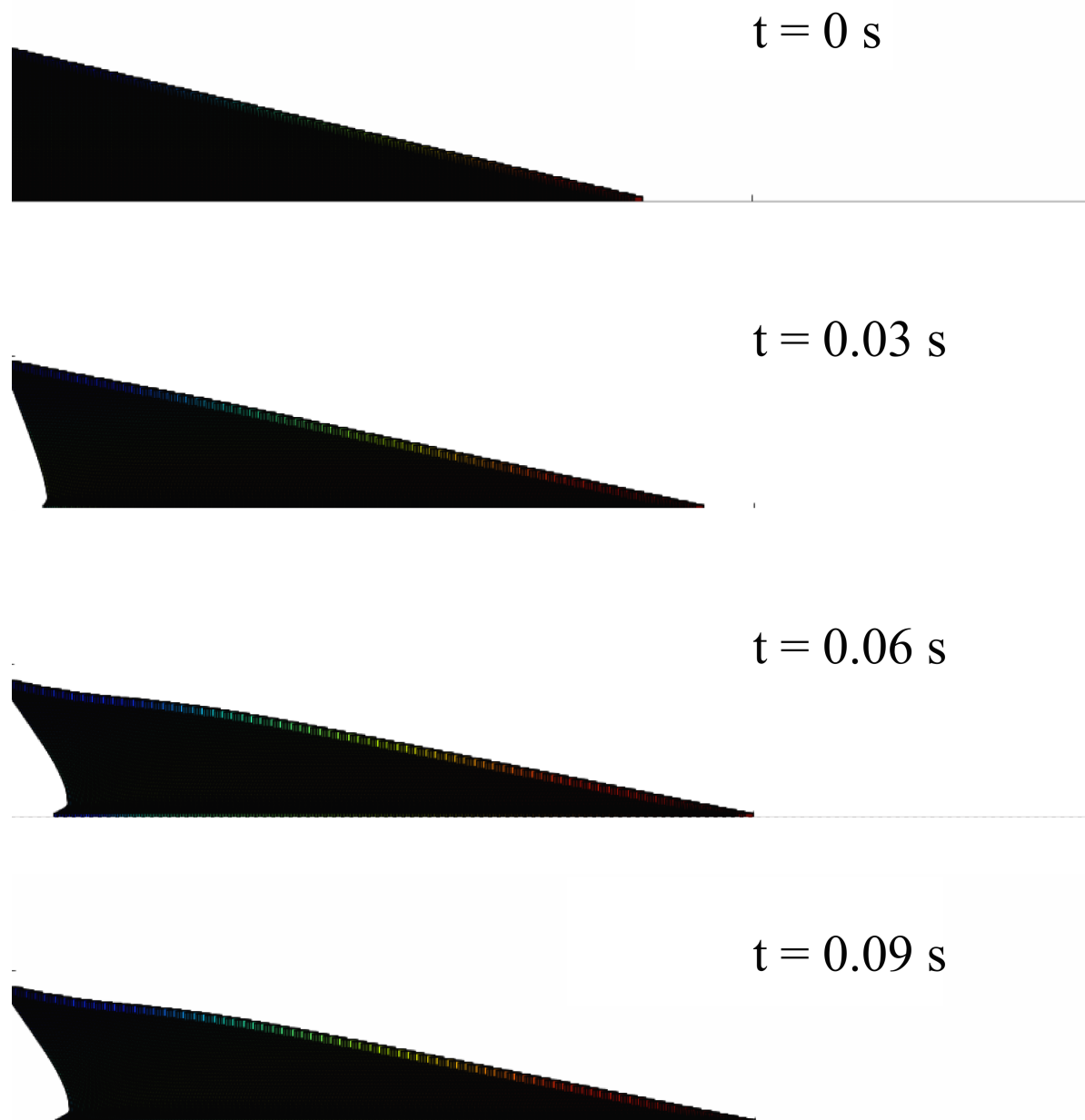


Figure 4.24 MPM simulation of the initial stages of granular pile subjected to a gradient impact energy.

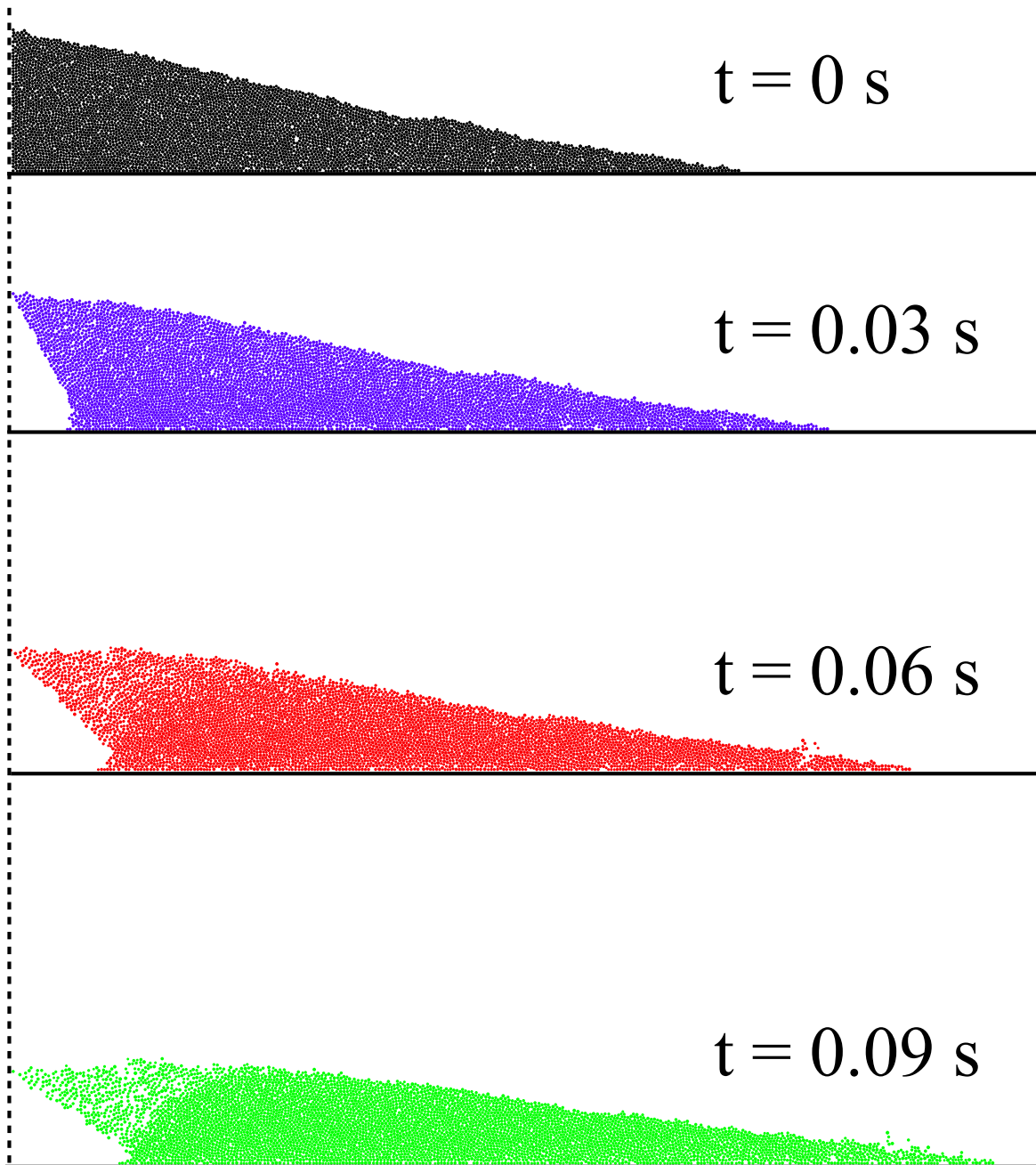


Figure 4.25 CD simulation of the initial stages of granular pile subjected to a gradient impact energy. ([Mutabaruka, 2013](#)).

While the run-out exhibits a power-law relation with the initial input energy, DEM simulations show that the flow duration remains constant at a value  $t_f \simeq 60 (d/g)^{0.5}$  irrespective of the value of  $E_0$ . The constant run-out time, in grain-scale simulations, indicates the collapse of grain into the cavity left behind the pile. An average run-out speed can be defined as  $v_s = (L_f - L_0)/t_f$ . According to the data,  $v_s \propto (E_0)^{0.52 \pm 0.012}$ . The error on the exponent represents the confidence interval of linear fits on the logarithmic scale. Since the initial average velocity varies as  $v_0 \propto (E_0)^{0.5}$ , this difference between the values of the exponents suggests that the mobilized mass during run-out declines when the input energy is increased.

In the second regime, corresponding to the range of high input energies  $E_0 > 40 \text{ mgd}$ , the run-out distance varies as  $L_f \propto (E_0)^{\alpha'}$  over one decade with  $\alpha' \simeq 0.56 \pm 0.04$  while the duration increases as  $t_f \propto (E_0)^{\beta'}$  with  $\beta' \simeq 0.33 \pm 0.02$ . Hence, in this regime the average run-out speed varies as  $v_s \propto (E_0)^{0.498 \pm 0.01}$ . This exponent is close to the value 0.5 in  $v_0 \propto (E_0)^{0.5}$ , and hence, within the confidence interval of the exponents. In the second regime, both DEM and MPM predict almost the same run-out behaviour. However, MPM predicts longer duration with increase in the input energy.

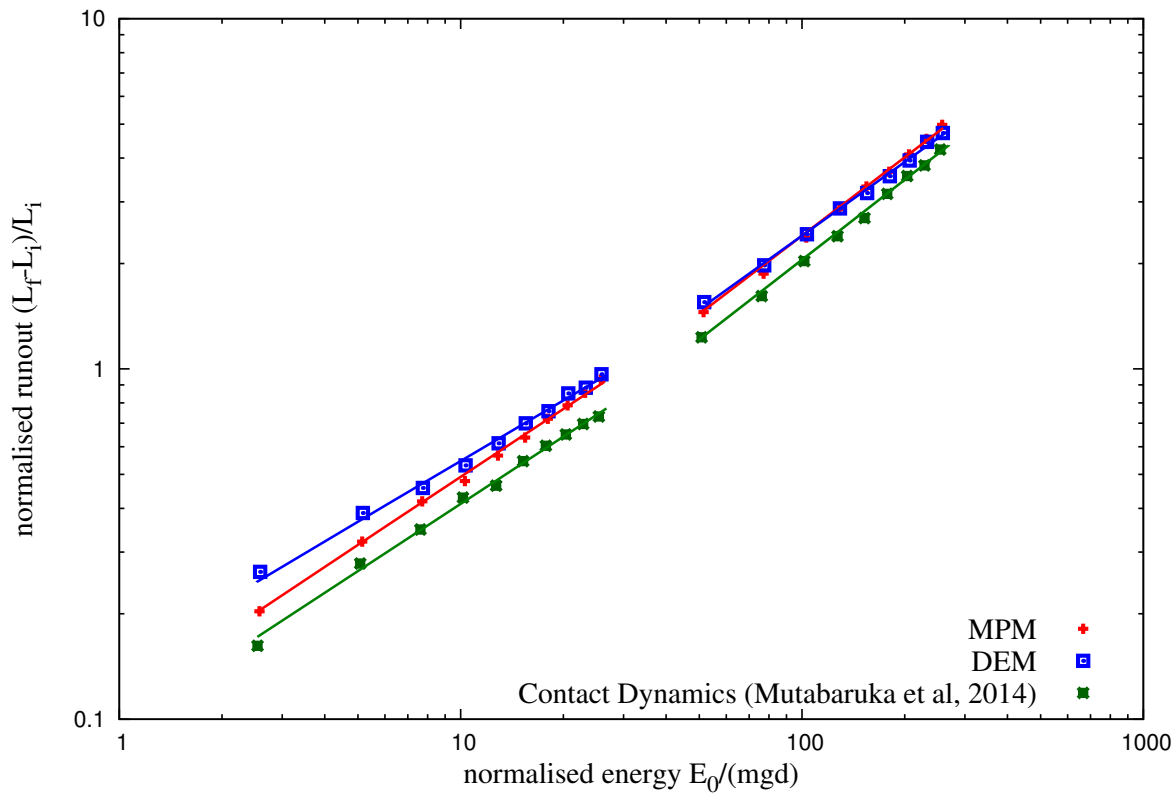
It is worth noting that a similar power-law dependence of the run-out distance and time were found in the case of granular column collapse with respect to the initial aspect ratio. In the column geometry, the grains spread away owing to the kinetic energy acquired during gravitational collapse of the column. [Topin et al. \(2012\)](#) found that the run-out distance varies as a power-law of the available peak kinetic energy at the end of the free-fall stage with an exponent  $\simeq 0.5$ . This value of exponent is lower than the run-out evolution observed in the second regime. This is, however, physically plausible since the distribution of kinetic energies at the end of the collapse is more chaotic than in this case where the energy is supplied from the very beginning in a well-defined shear mode. As pointed out by [Staron et al. \(2005\)](#), the distribution of kinetic energies is an essential factor for the run-out distance.

### 4.3.3 Decay of kinetic energy

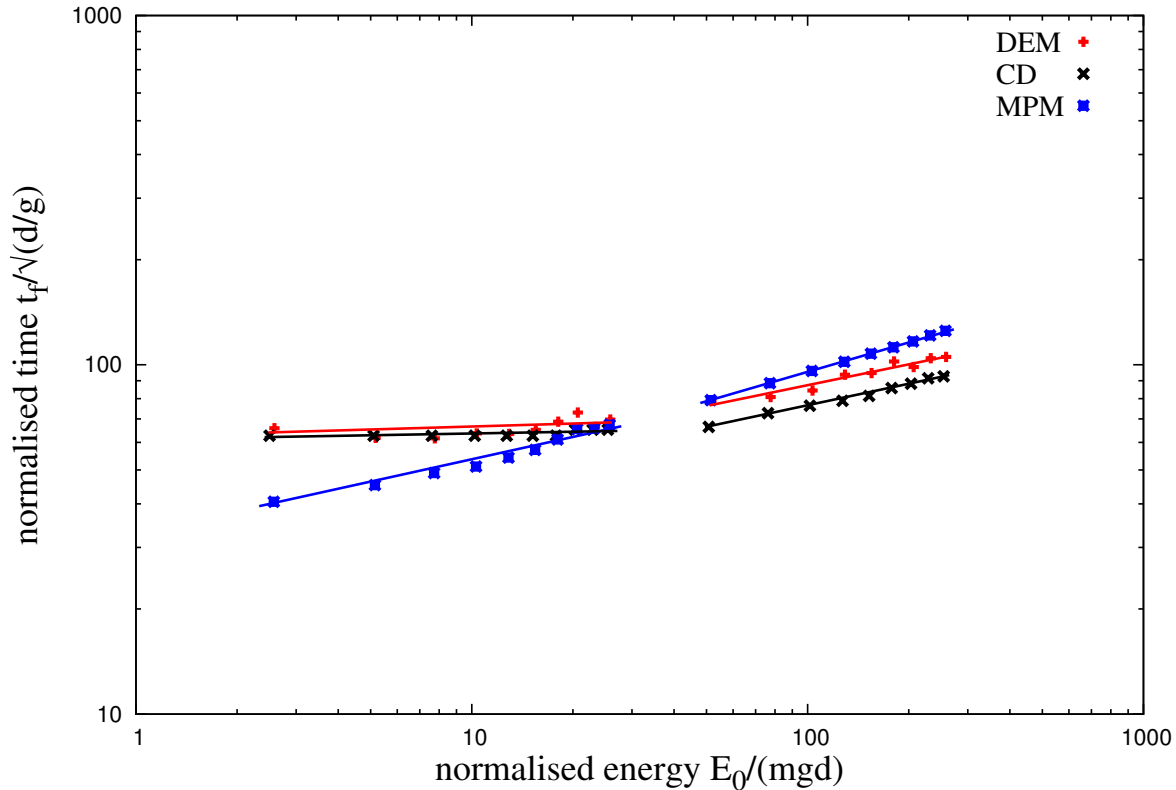
The non-trivial evolution of the pile geometry in two regimes suggests that the energy supplied to the pile is not simply dissipated by shear and friction along the bottom plane. It is important to split the kinetic energy into vertical and horizontal components ( $K_{Ex}$  and  $K_{Ey}$ ) of the velocity field. Although, the input energy is in the  $x$  component, a fraction of energy is transferred to the vertical component of the velocity field and dissipated during the transient phase. The evolution of kinetic energy is studied to understand the behaviour of granular flow that is consistent with the evolution of the pile shape.

The evolution of total kinetic energies  $E_k$  with time for different values of the input energy  $E_{ki}$  based on MPM simulations are shown in figure 4.27. MPM simulations shows two distinct

## 4.3 Slopes subjected to impact loading



(a) Run-out distance as a function of normalised input kinetic energy



(b) Duration of run-out as a function of normalised input kinetic energy

Figure 4.26 Run-out behaviour of a pile subjected a gradient impact energy

regimes in the normalised kinetic energy plot as a function of normalised time in figure 4.27b. However, DEM simulations (see figure 4.28) show that the energy evolution corresponding to low energy regime nearly collapse on to a single time evolution. This is consistent with the observation of run-out time  $t_f$  independent of the input energy. In contrast, MPM simulations predict a power law relation between the run-out duration and input energy. However, the plots corresponding to the high energy regime (figure 4.27), collapse only at the beginning of the run-out i.e. for  $t < t_1 \simeq 7.5 (d/g)^{0.5}$ . Although MPM simulations show longer duration of run-out (figure 4.27), the total kinetic energy is completely dissipated at  $t = 60\sqrt{d/g}$ . DEM simulations predict  $t = 80\sqrt{d/g}$  for the kinetic energy to be completely dissipated. This is due to particle rearrangement at the free surface (figure 4.29). The granular mass densifies as the flow progresses, after the initial dilation phase for  $t = 20\sqrt{d/g}$ .

Figure 4.30 displays the evolution of kinetic energy in the translational ( $E_x$  and  $E_y$ ) degrees of freedom.  $E_x$  decays similar to the total energy dissipation, but  $E_y$  increases and passes through a peak before decaying rapidly to a negligible level. The transient is best observed for  $E_y$ , which has significant values only for  $t < t_1$ . This energy represents the proportion of kinetic energy transferred to the y component of the velocity field due to the destabilisation of the pile and collapse of grains in the cavity behind the pile. Higher proportion of vertical acceleration  $E_{ky}/E_0$  is observed for lower values of input energy  $E_0$ . This means that, at lower input energies a larger fraction of the energy is consumed in the destabilisation process. Whereas at a higher input energies, most of the energy is dissipated in the spreading phase. For this reason, the total duration  $t_1$  of this destabilisation phase is nearly the same in both regimes and its value is controlled by the gravity rather than the input energy. The height of the pile being of the order of  $80 d$ , the total free-fall time for a particle located at this height is  $\simeq 12 (d/g)^{0.5}$ , which is of the same order as  $t_1$ . DEM simulations show that the contribution of the rotational energy during the transient stage and the spreading stage is negligible.

To analyse the second phase for higher input energies, the kinetic energy  $E'_{kx0}$  available at the end of the transient phase is considered. This energy is responsible for most of the run-out and hence it is expected to control the run-out distance and time. Figure 4.31 shows the evolution of  $E_{kx}$  normalized by  $E'_{kx0}$  as a function of time. The plots have seemingly the same aspect but they show different decay times. A decay time  $\tau$  can be defined as the time required for  $E_{kx}$  to decline by a factor 1/2. Figure 4.32 shows the same data in which the time  $t'$  elapsed since  $t_1$ , normalized by  $\tau$ . Interestingly, now all the data nicely collapse on to a single curve. However, this curve can not be fitted by simple functional forms such as variants of exponential decay. This means that the spreading of the pile is not a self-similar process in agreement with the fact that the energy fades away in a finite time  $t'_f$ .

## 4.3 Slopes subjected to impact loading

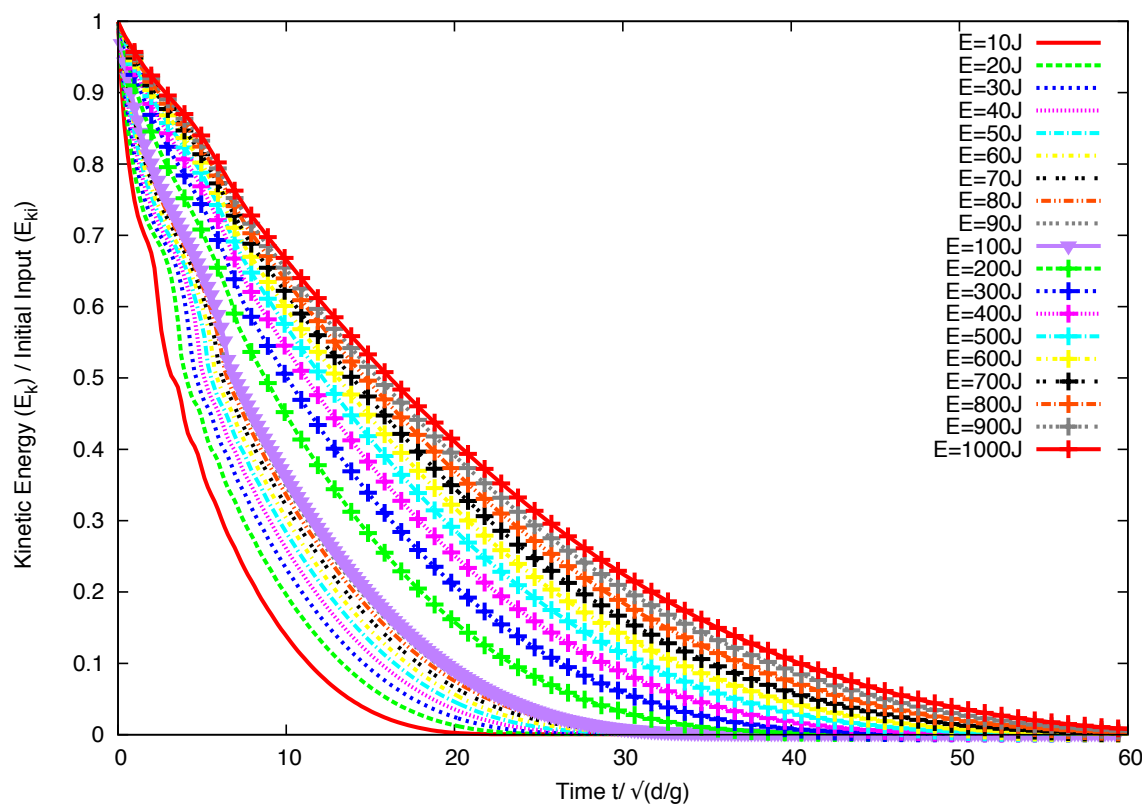
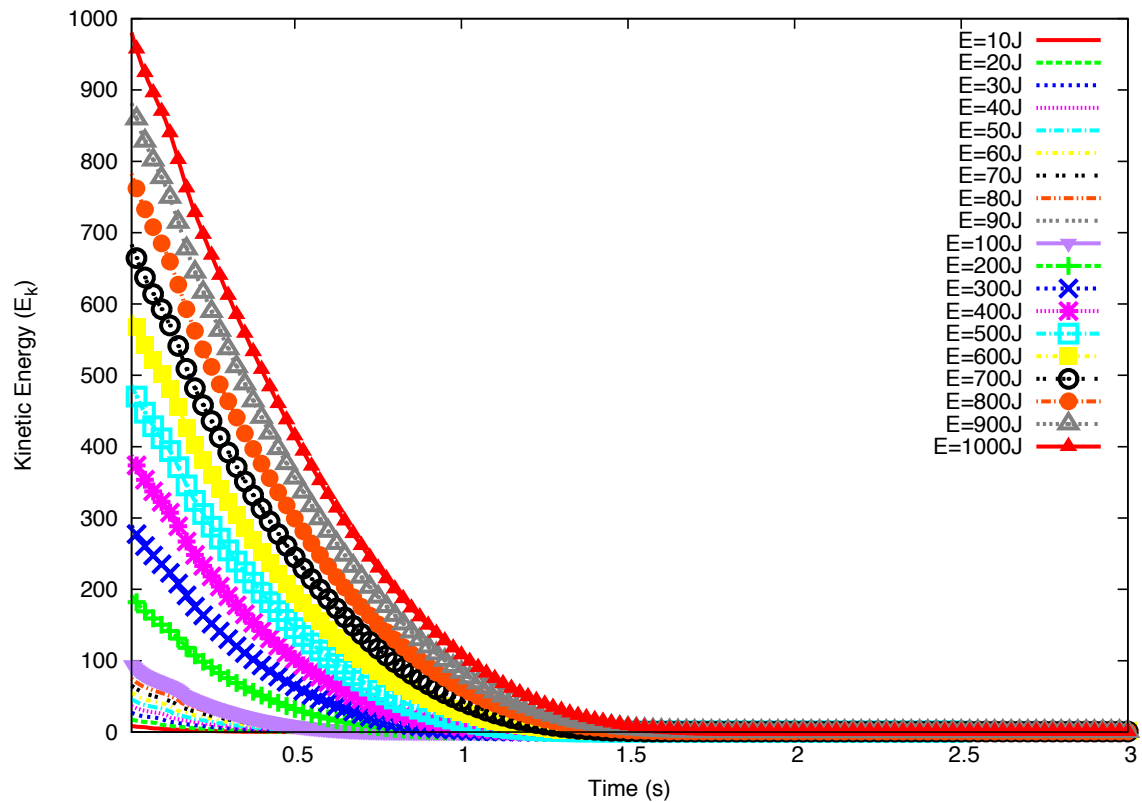


Figure 4.27 Evolution of kinetic energy with time (MPM)

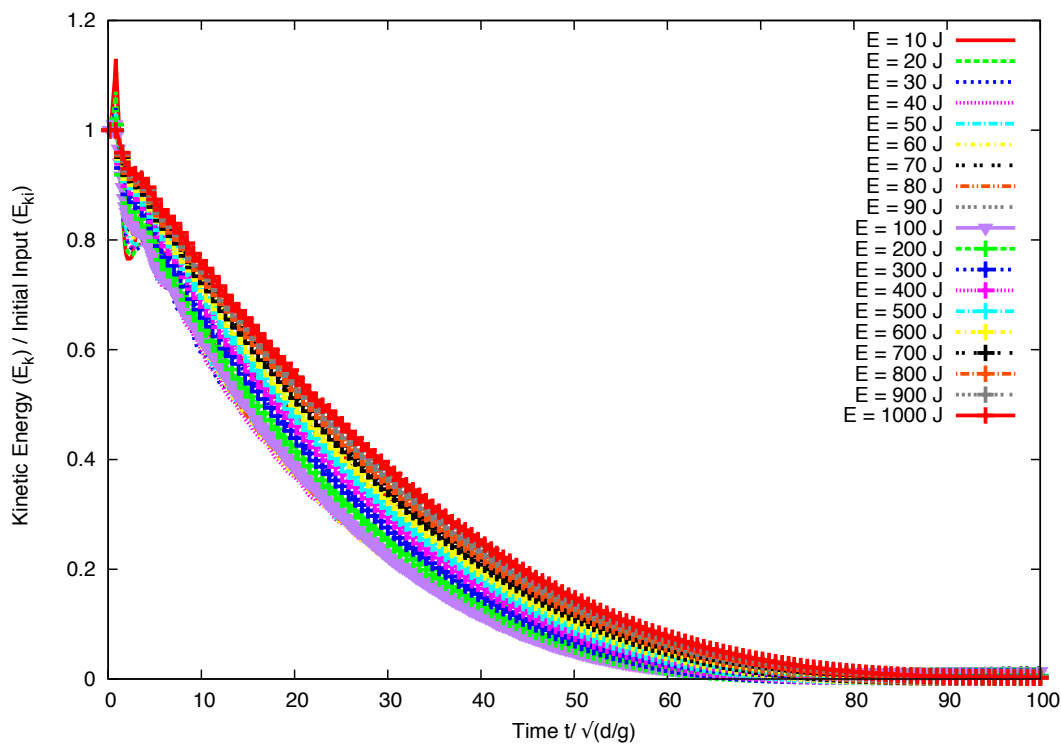


Figure 4.28 Evolution of normalised kinetic energy with normalised time

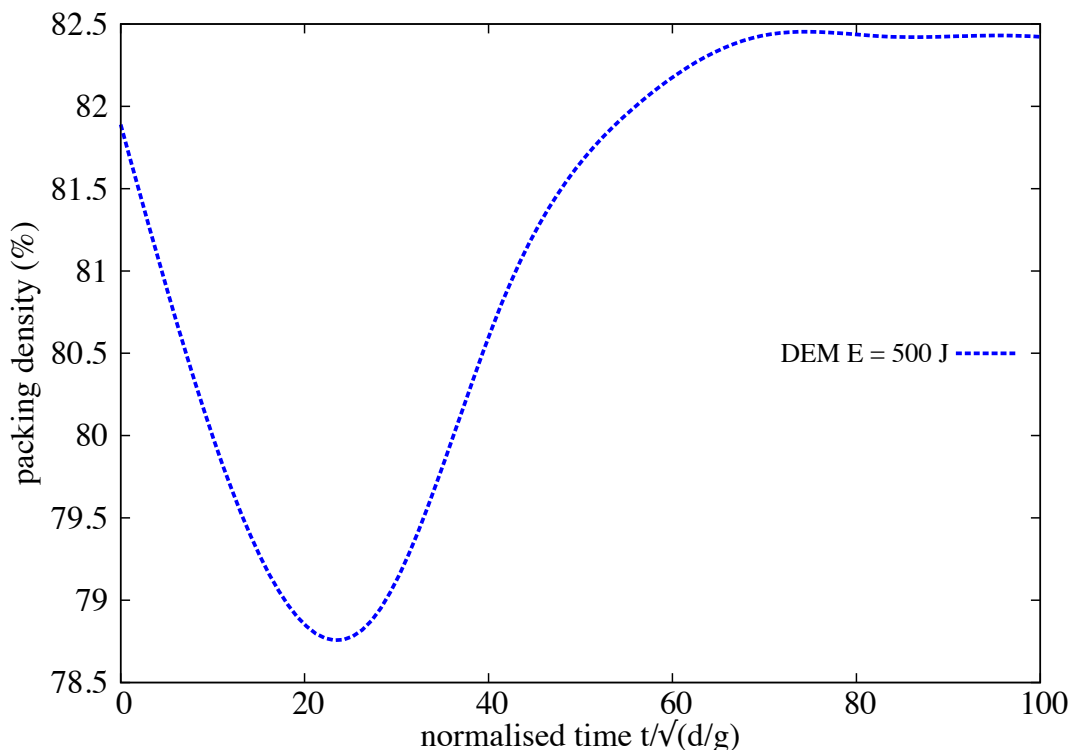
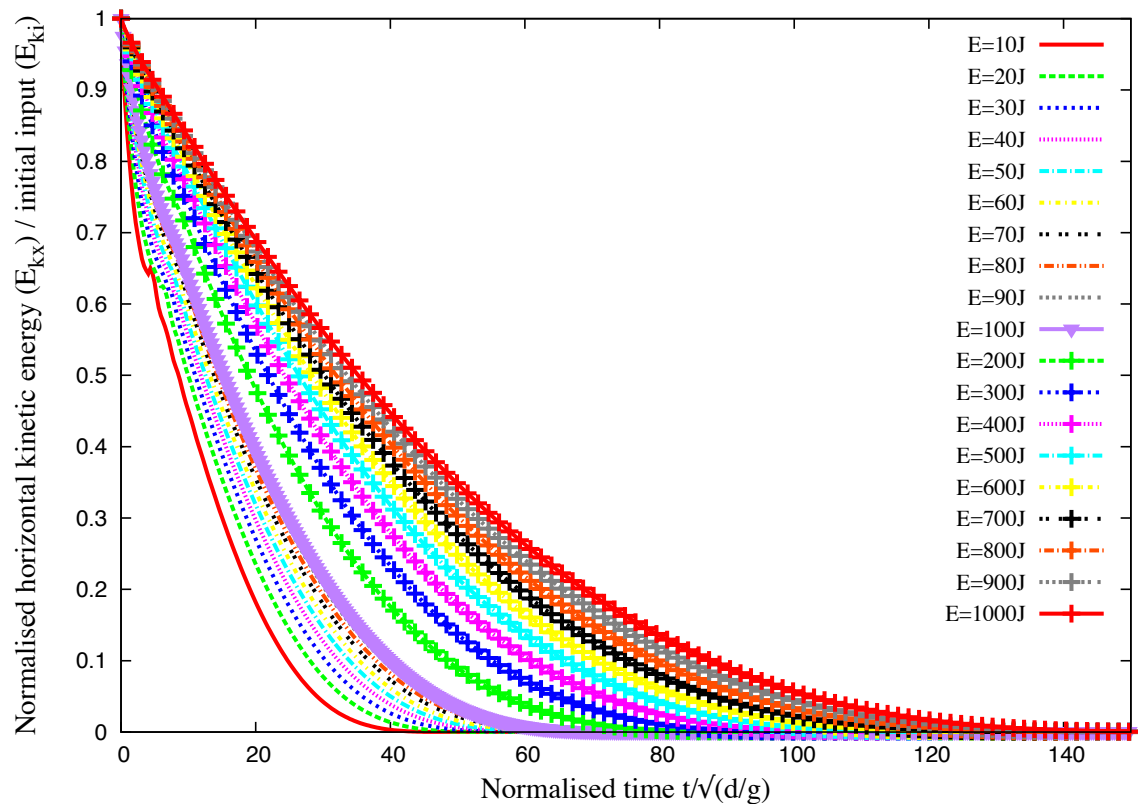
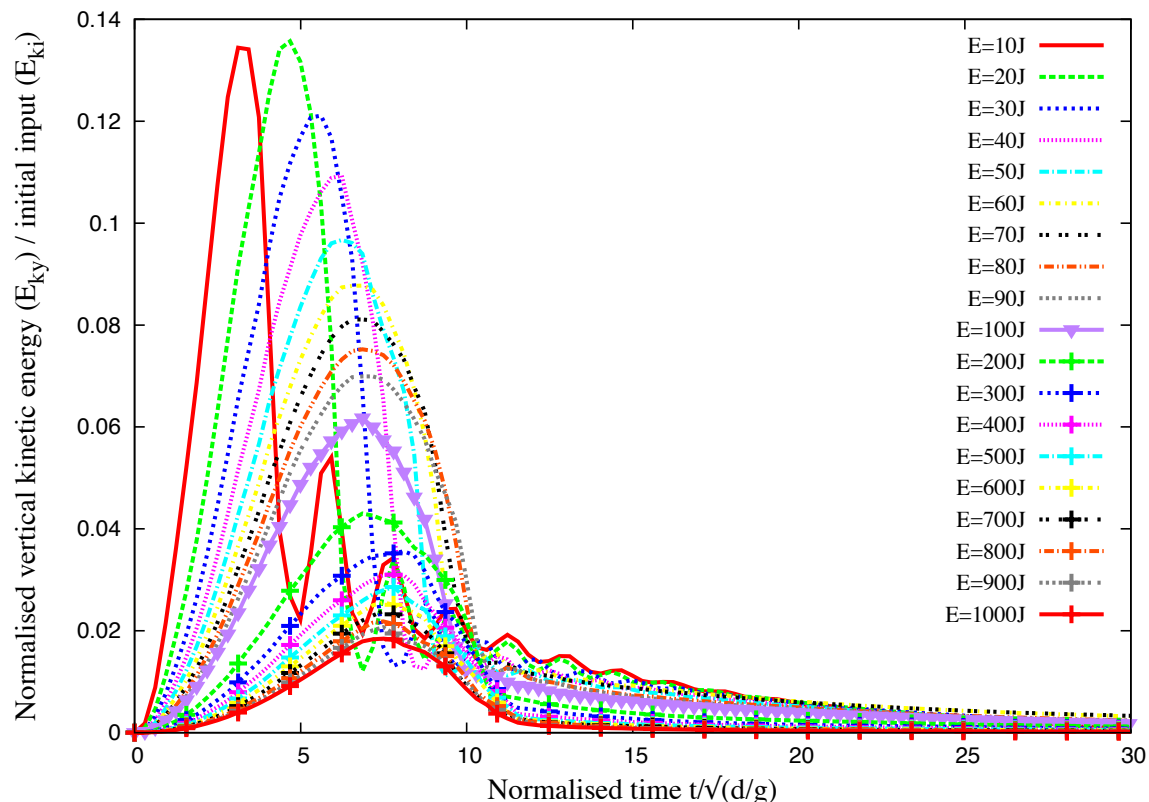


Figure 4.29 Evolution of packing density with time  $E_0 = 152mgd$  (DEM)

## 4.3 Slopes subjected to impact loading



(a) Evolution of normalised horizontal kinetic energy with time



(b) Evolution of normalised vertical kinetic energy with time

Figure 4.30 Evolution of vertical and horizontal kinetic energy with time (MPM)

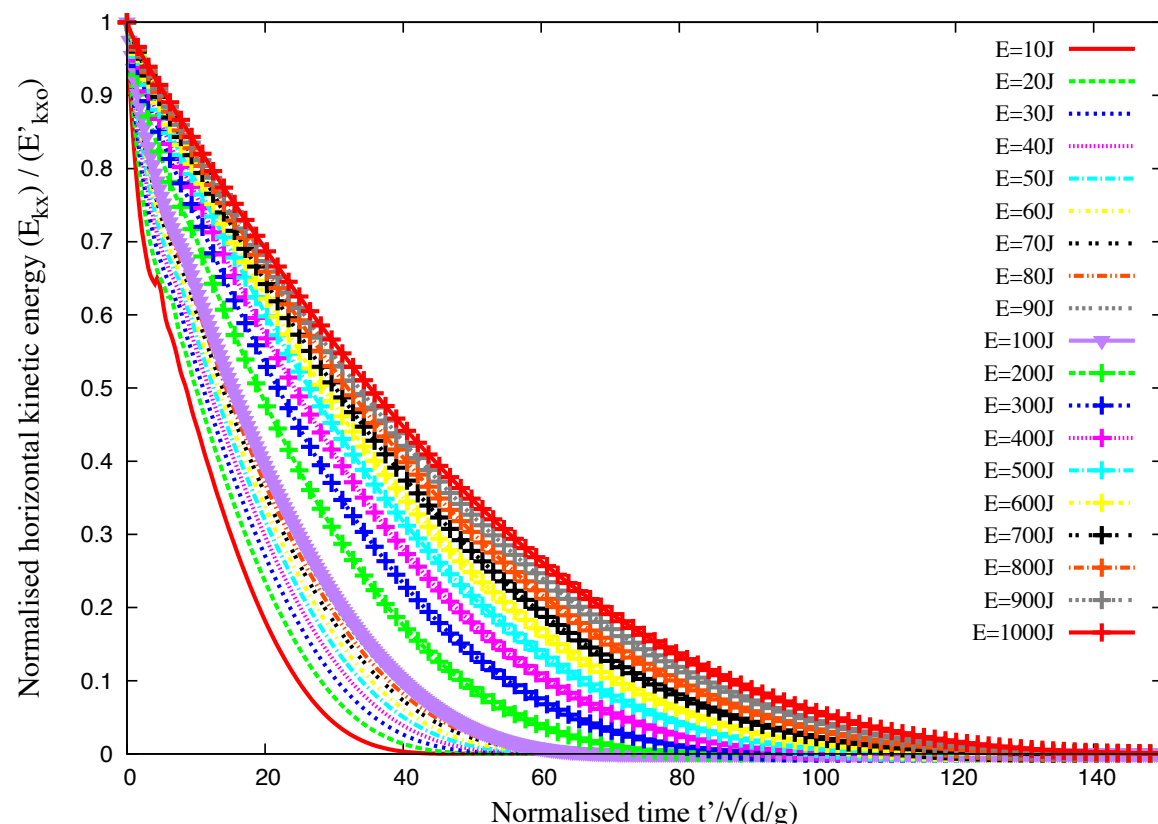


Figure 4.31 Evolution of kinetic energy in the  $x$  component of the velocity field normalized by the available kinetic energy at the end of the transient as a function of time elapsed since the same instant (MPM).

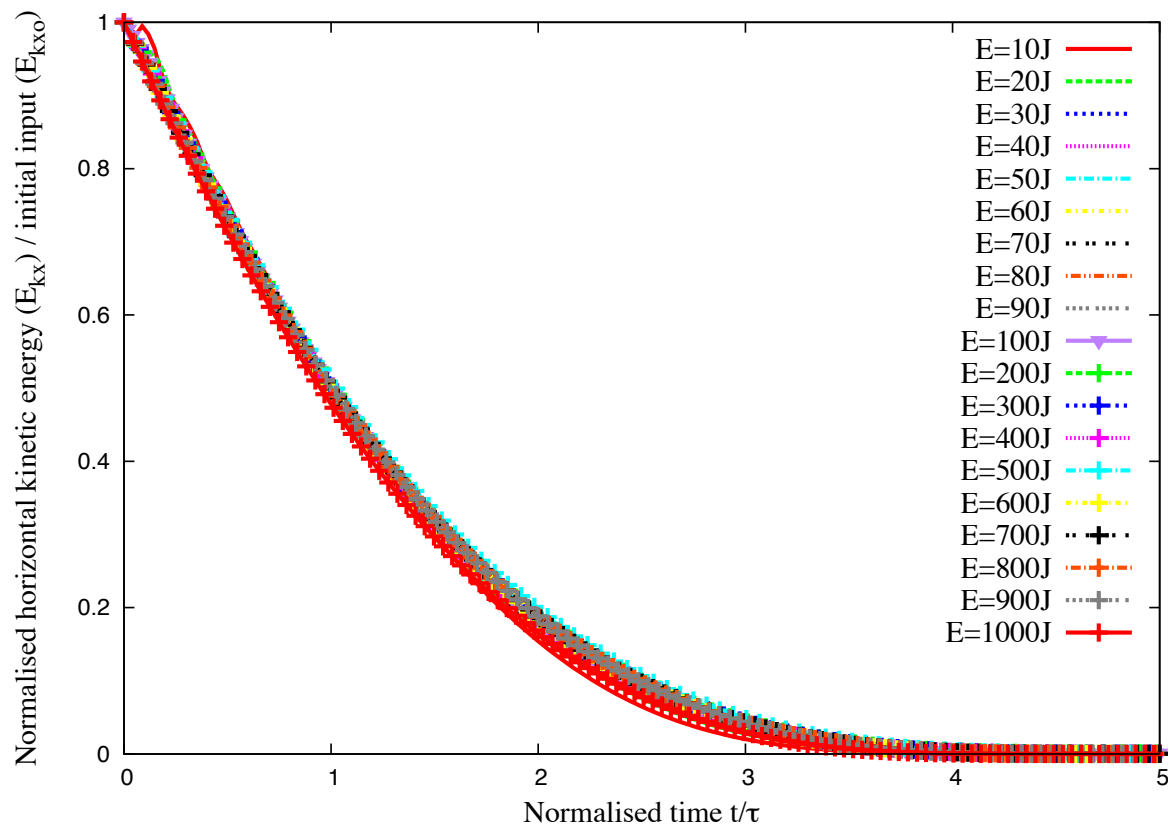


Figure 4.32 Evolution of kinetic energy in the  $x$  component of the velocity field normalized by the available kinetic energy at the end of the transient as a function of normalized time (MPM).

The scaling of the data with the decay time  $\tau$  suggests that the run-out time  $t'_f$ , since the beginning of the second phase, might be a simple function of  $\tau$ . Figure 4.33a shows both  $t'_f$  and  $\tau$  as a function of  $E'_{x0}$ , where a power-law relation can be observed for both time scales. The run-out time  $t'_f \propto (E'_{x0})^{\beta'}$  has the same exponent  $\beta' \simeq 0.33 \pm 0.02$  as  $t_f$  as a function of  $E_0$ . For the decay time we have  $\tau \propto (E'_{x0})^{\beta''}$  with  $\beta'' \simeq 0.38 \pm 0.03$ . The relation between the two times can thus be expressed as (see figure 4.33b)

$$t'_f = k \tau (E'_{x0})^{\beta'' - \beta'}, \quad (4.13)$$

where  $k \simeq 5 \pm 0.4$  and  $\beta'' - \beta' \simeq -0.06 \pm 0.05$ . This value is small enough to be neglected within the confidence interval of the data. It is therefore plausible to assume that the run-out time is a multiple of the decay time and the spreading process is controlled by a single time. A weak dependence on the energy  $E'_{kx0}$  is consistent with the fact that the energy available at the beginning of the second phase is not dissipated in the spreading process (calculated from the position of the tip of the pile) since the pile keeps deforming by the movements of the grains at the free surface even when the tip comes to rest. This can explain the small difference between the two exponents as observed here.

### 4.3.4 Effect of friction

The run-out distance, duration of flow, and the dissipation of kinetic energy are controlled by the input energy and collective dynamics of the whole pile. However, the run-out behaviour is expected to depend also on the base friction. A series of simulations with different values of base friction was performed using MPM to analyse the influence of friction on the run-out behaviour. The influence of friction on the run-out behaviour is shown in figure 4.34a. The exponent of the power-law relation between the run-out and input energy has a weak dependence on the base friction, however, the proportionality constant is affected by the change in the base friction. This behaviour is similar to that observed in granular column collapse with varying initial properties (Balmforth and Kerswell, 2005; Lajeunesse et al., 2005).

CD simulations using different values of coefficient of restitution show no difference in the run-out behaviour. At large input energies, the pile remains in a dense state so that multiple collisions inside the pile occur at small time scales compared to the deformation time. When the restitution coefficients are increased, more collisions occur during a longer time interval but the overall energy dissipation rate by collisions remains the same. This effect is a seminal example of collective effects which erase the influence of local parameters at the macroscopic scale.

## 4.3 Slopes subjected to impact loading

47

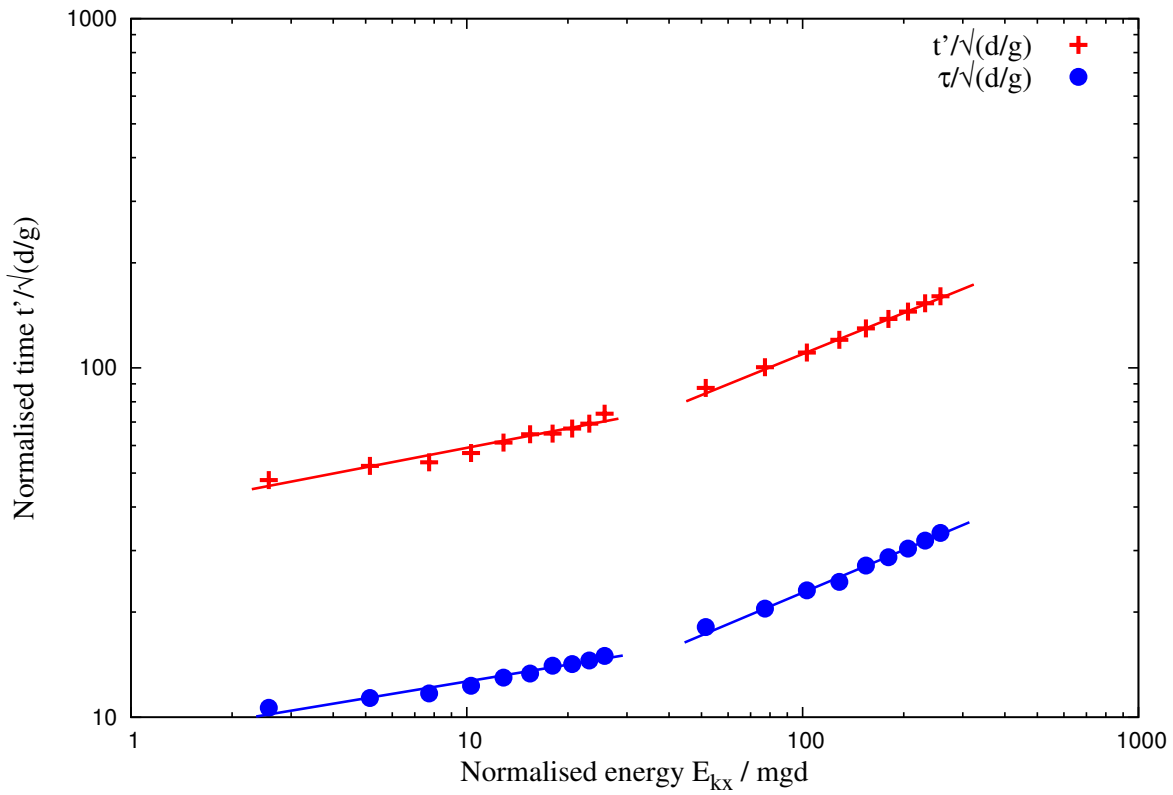
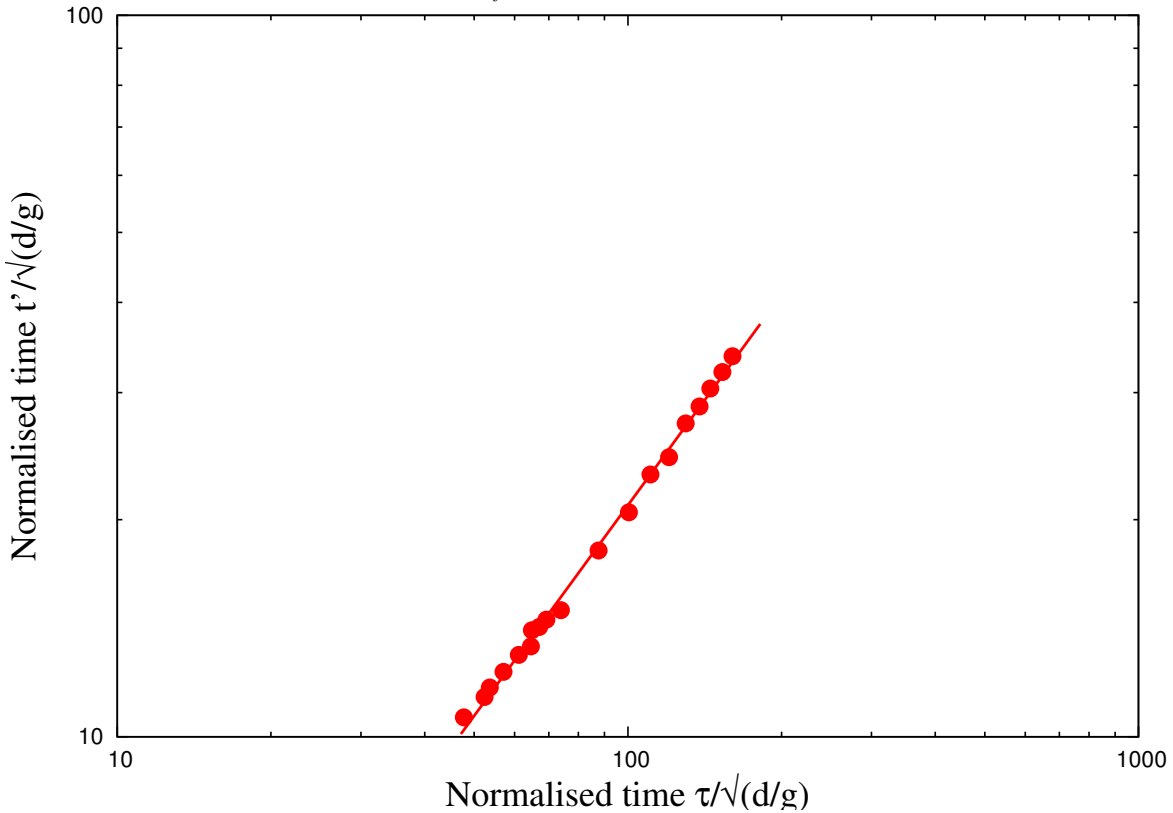
(a) Power law evolution of  $t'_f$  and  $\tau$  as a function of kinetic energy  $E'_{kx0}$ .(b) Linear relationship between decay time and run-out time after the transient as a function of the normalised kinetic energy  $E_{kx0}$ .

Figure 4.33 Decay time and run-out time as a function of the normalised kinetic energy  $E_{kx0}$ .

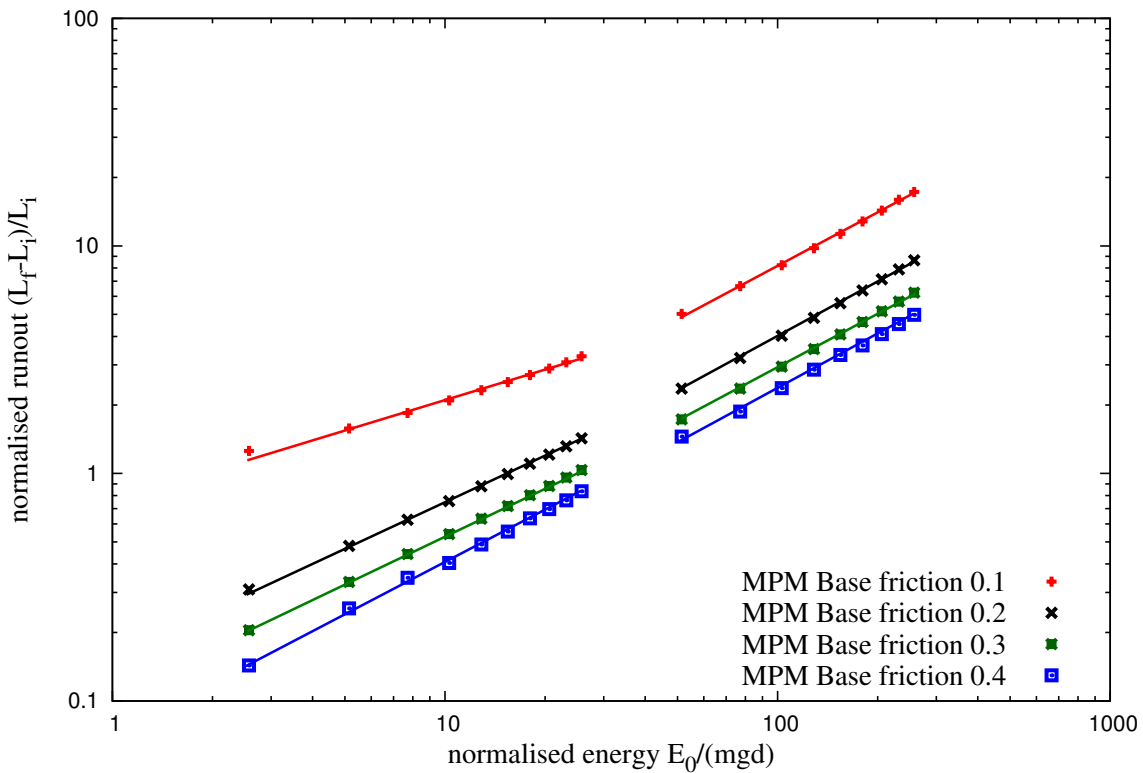
In contrast with the restitution coefficients, the effect of friction coefficient, however, is quite important for the run-out. MPM simulations with varying friction coefficient shows that, both the run-out distance and the decay time decrease as the friction coefficient is increased. This effect is much more pronounced at low values of the friction coefficient. The run-out time, for example, is reduced by a factor of  $\approx 4$  as  $\mu_s$  is increased from 0.1 to 0.2 while the change in the run-out and duration is less effected with increase in friction coefficient. This “saturation effect” can be observed in a systematic way in simple shear tests. The dissipation rate may reach a saturation point where the dilation of granular materials and rolling of the grains change in response to increase in friction coefficient (Estrada et al., 2008).

## Effect kinetic energy distribution

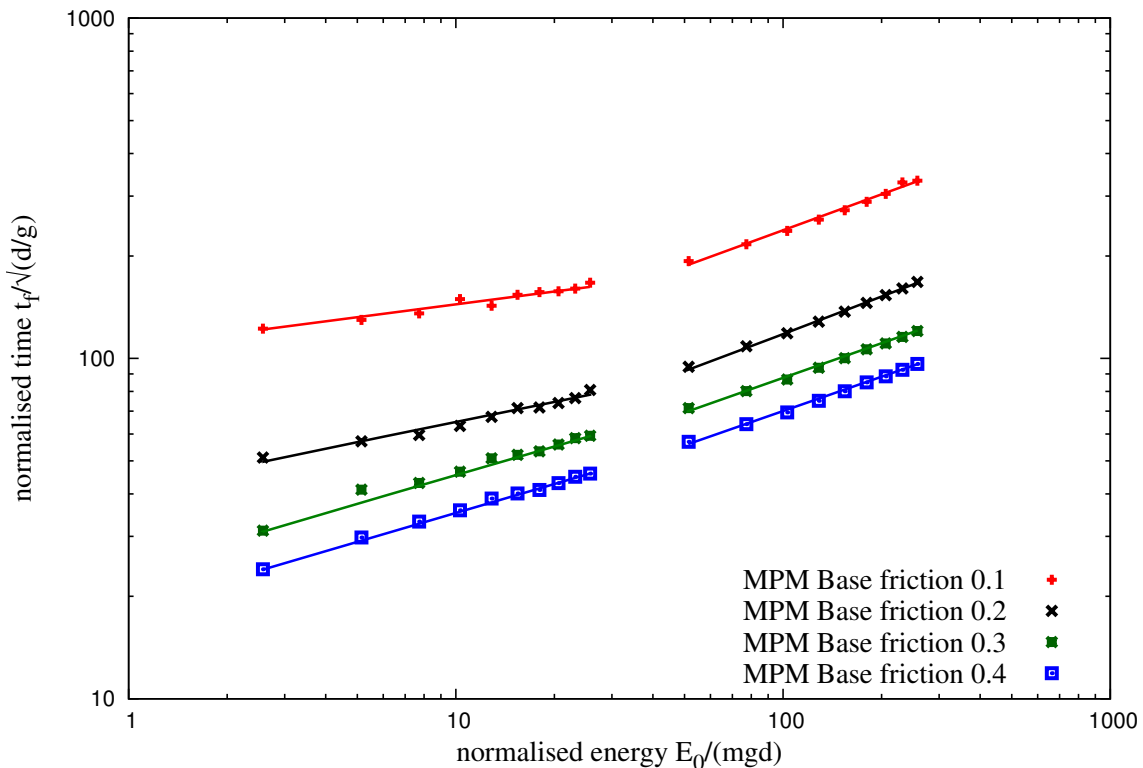
Staron et al. (2005) observed that the distribution of kinetic energy in the granular system is an essential factor for the run-out distance. In order to understand the influence of energy distribution on the run-out behaviour, granular pile subjected to two different velocity fields were studied. A uniform velocity  $V_{xo}(y) = V_0$  is applied to the entire pile, in contrast to the gradient impact velocity. Snapshots of flow kinematics at initial stages are shown in figure 4.35 (MPM simulations) and figure 4.36 (DEM). It can be observed from the figures that the continuum behaviour is identical to that of grain-scale simulations. As each grain experiences the same velocity, grains located at the top of the slope are pushed farther away and unlike the gradient input velocity, the cavity left behind the granular mass is not filled by the soil grains at the top.

Figure 4.37a shows the influence of velocity distribution on the run-out behaviour. At low input energy, the gradient velocity distribution shows significantly longer run-out in comparison to uniform velocity distribution. Section 4.3.3 shows that at low input energies a larger fraction of the energy is consumed in the destabilisation process. Which means that the amount energy available for flow is less, in uniform velocity distribution, this energy is even smaller as the initial velocity is distributed uniformly throughout the granular mass. However at higher input energy, where most of the energy is dissipated during the spreading phase, the run-out distance has a weak dependence on the distribution of velocity in the granular mass. The duration of the flow shows similar behaviour to the run-out, however, a slope subjected to a gradient velocity flows quicker than a slope subjected to a uniform impact velocity. Gradient velocity distribution provides more input energy at the initial stage to overcome the frictional resistance at the base. This shows that the material property and the distribution of kinetic energy in the system has a non-trivial influence on the flow kinematics and the internal flow structure.

## 4.3 Slopes subjected to impact loading



(a) Effect of friction on the run-out distance



(b) Effect of friction on the duration of run-out.

Figure 4.34 Effect of friction on the run-out behaviour

$t = 0 \text{ s}$



$t = 0.03 \text{ s}$



$t = 0.06 \text{ s}$



$t = 0.09 \text{ s}$



Figure 4.35 Snapshots of MPM simulations of the evolution of granular pile subjected to a gradient impact energy  $E_0 = 61 \text{ mgd}$ .

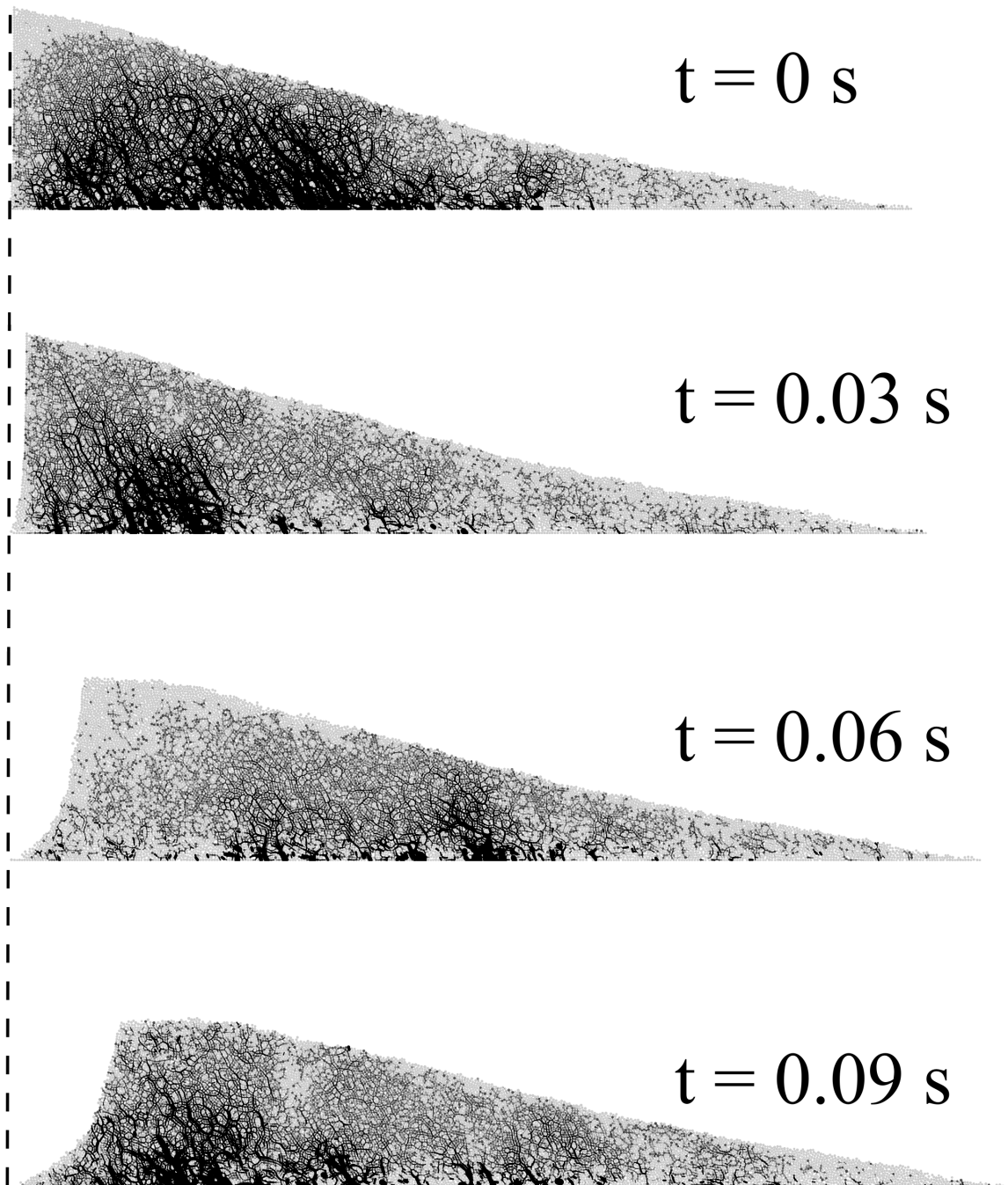
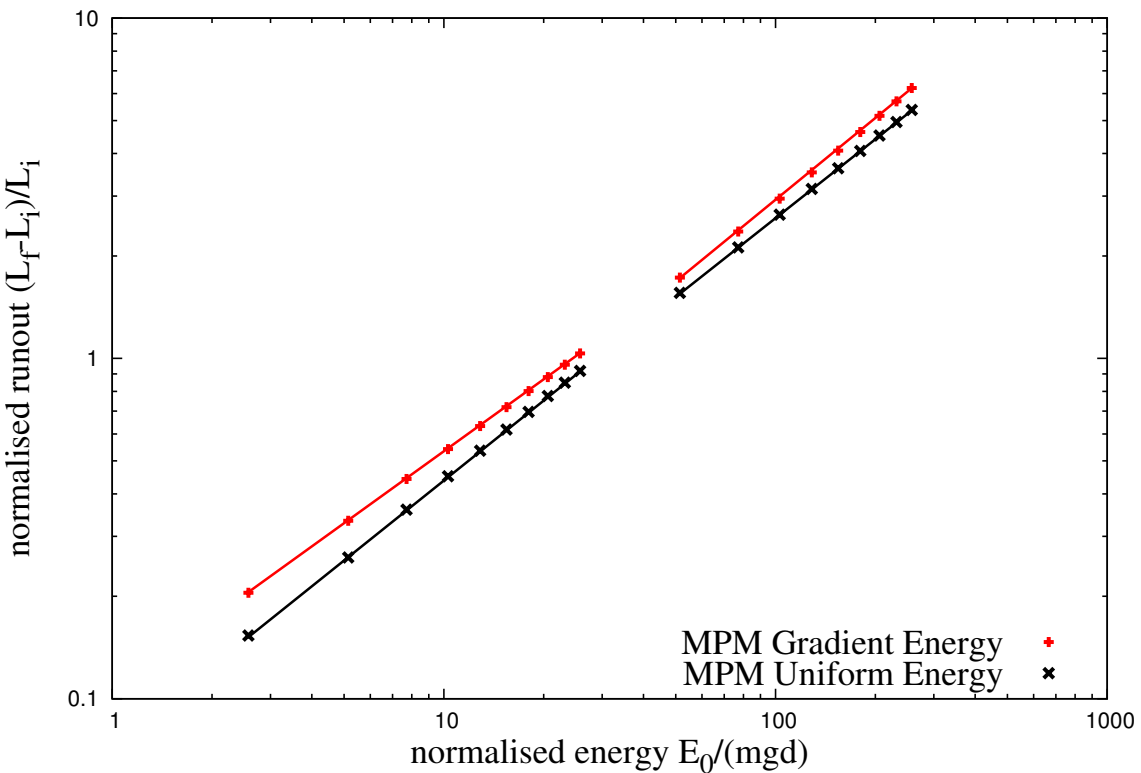
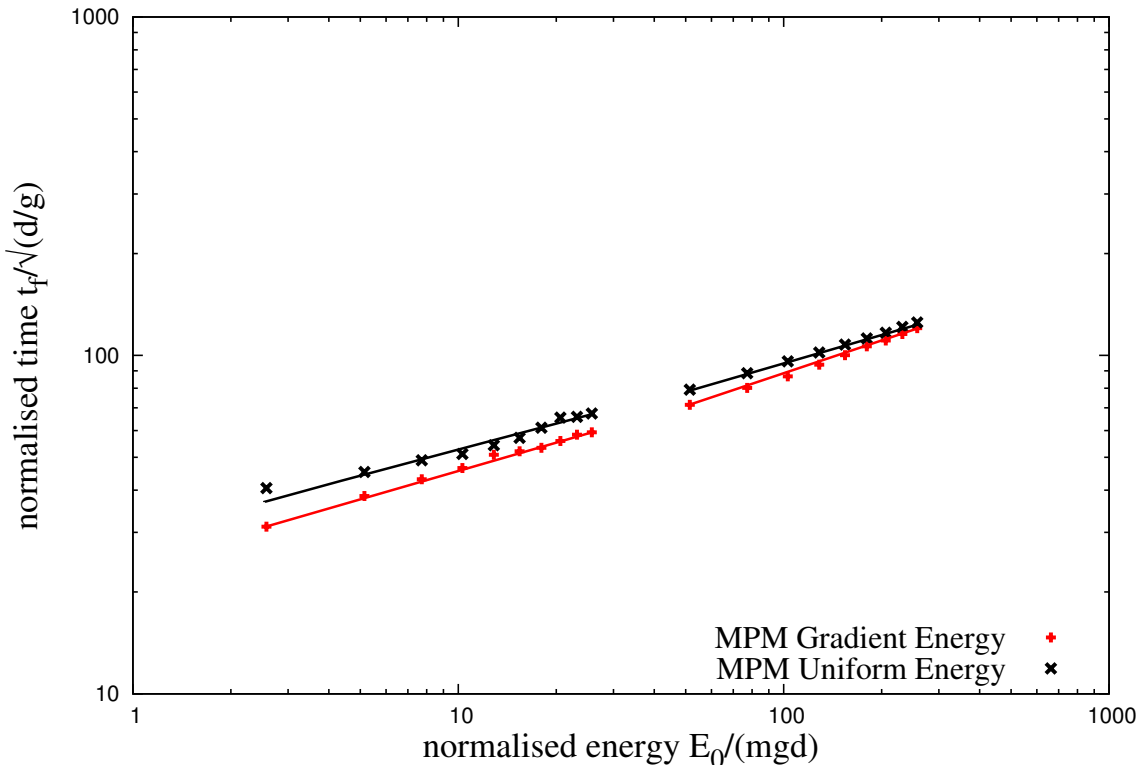


Figure 4.36 Snapshots of DEM simulations of the evolution of granular pile subjected to a gradient impact energy  $E_0 = 61 \text{ mgd}$ .



(a) Run-out distance as a function of normalised input kinetic energy



(b) Duration of run-out as a function of normalised input kinetic energy

Figure 4.37 Effect of input velocity distribution on the run-out behaviour

### 4.3.5 Effect of mesh size and number of material points per cell

Abe et al. (2013) observed that for a coarse mesh, the numerical error decreases with increase in the number of material points per cell. In contrast, they observed an opposite trend for the fine meshes (0.01 m). The influence of numerical noise due to particles crossing the background mesh was not observed when the mesh size is greater than 0.05 m. Coetzee et al. (2005) also found that the numerical error decreases with increase in mesh refinement.

In the present study, the effect of mesh size and the number of material points per cell on the run-out behaviour is investigated. For a mesh size of 0.0125 m, the number of material points per cell (PPC) is varied as 4, 16, 25, 36, 64, 81 and 100. The effect of number of material points on the run-out behaviour is presented in figure 4.38. At a low input energy of 50 J, 4 and 16 material points per cell result in longer run-out distance, where as the run-out distance converges when the number of PPC is more than 25. While at a high input energy of 500 J, both 4 and 16 PPC predict almost the same run-out distance, but is higher than the run-out predicted with more than 25 material points per cell.

The evolution of the granular pile during the initial stage of flow is show in figure 4.39 for different number of material points per cell. At low input energy, fewer material points per cell results in larger separation of the spreading mass from the left wall. Distinct shear bands can be observed for more than 16 PPC. The flow structure remains unchanged with increase in PPC of more than 25. At a higher input energy (see figure 4.40), almost all cases predict similar flow structure, except in the case of 4 PPC.

Figure 4.41 shows the evolution of kinetic energy with time for varying number of material points per cell. At low input energy, the horizontal kinetic energy evolution is identical for all cases. A slightly quicker run-out evolution during the spreading phase can be observed for the case of 4 PPC. However, increase in the number of material points per cell significantly affects the evolution of the vertical kinetic energy  $E_{ky}$ . At low energy, a large proportion of the input energy is dissipated in the destabilisation process. This results in material points falling behind the spreading mass to the fill the cavity. Fewer number of material points per cell results in cell crossing noise as the material points filling the cavity experience free-fall due to gravity. The effect of cell-crossing noise can be seen in the osciallation of vertical kinetic energy for fewer material points per cell. However, at high input energy, most of the input velocity is dissipated during the spreading process. This means that only a small fraction of energy is available in the vertical component resulting in almost similar behaviour for all cases. Four material points per cell predicts a higher peak vertical kinetic energy in comparison with other cases, unlike the low energy case, no oscillations were observed for the high input energy.

The effect of mesh size on the flow kinematics is studied by comparing two mesh sizes: 0.01 m and 0.0125 m (see figure 4.42). It can be observed that the run-out distance converges

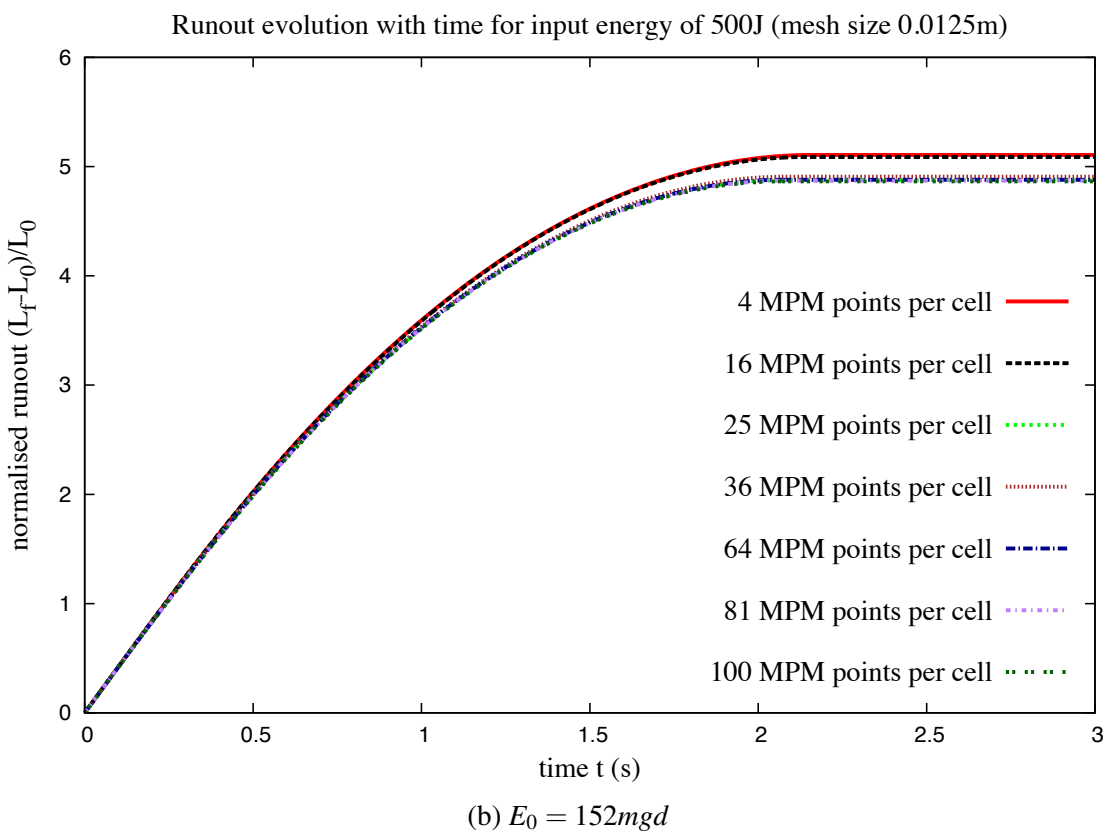
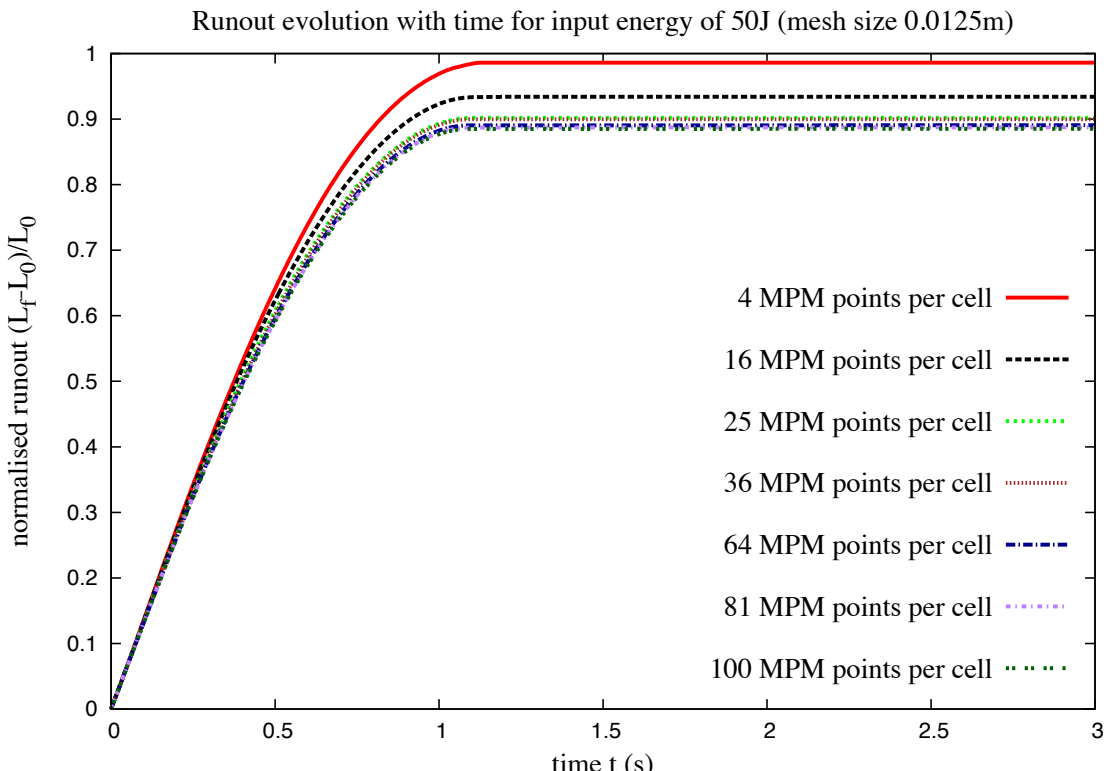


Figure 4.38 Evolution of run-out with time for varying material points per cell.

## 4.3 Slopes subjected to impact loading

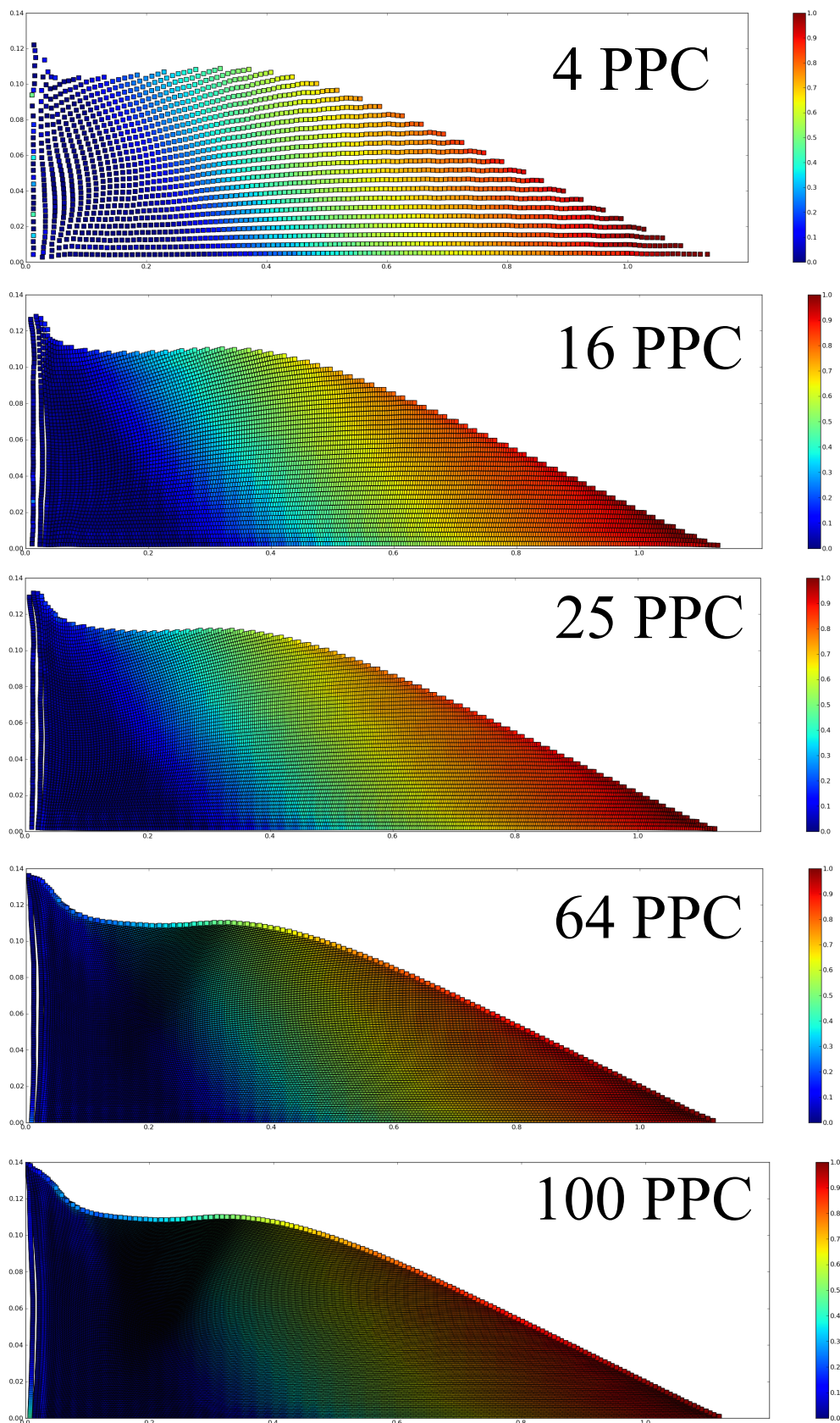


Figure 4.39 Effect of number of material points on cell on the run-out behaviour  $E_0 = 12.7mgd$ . Velocity profile (m/s) of granular pile subjected to gradient impact loading.

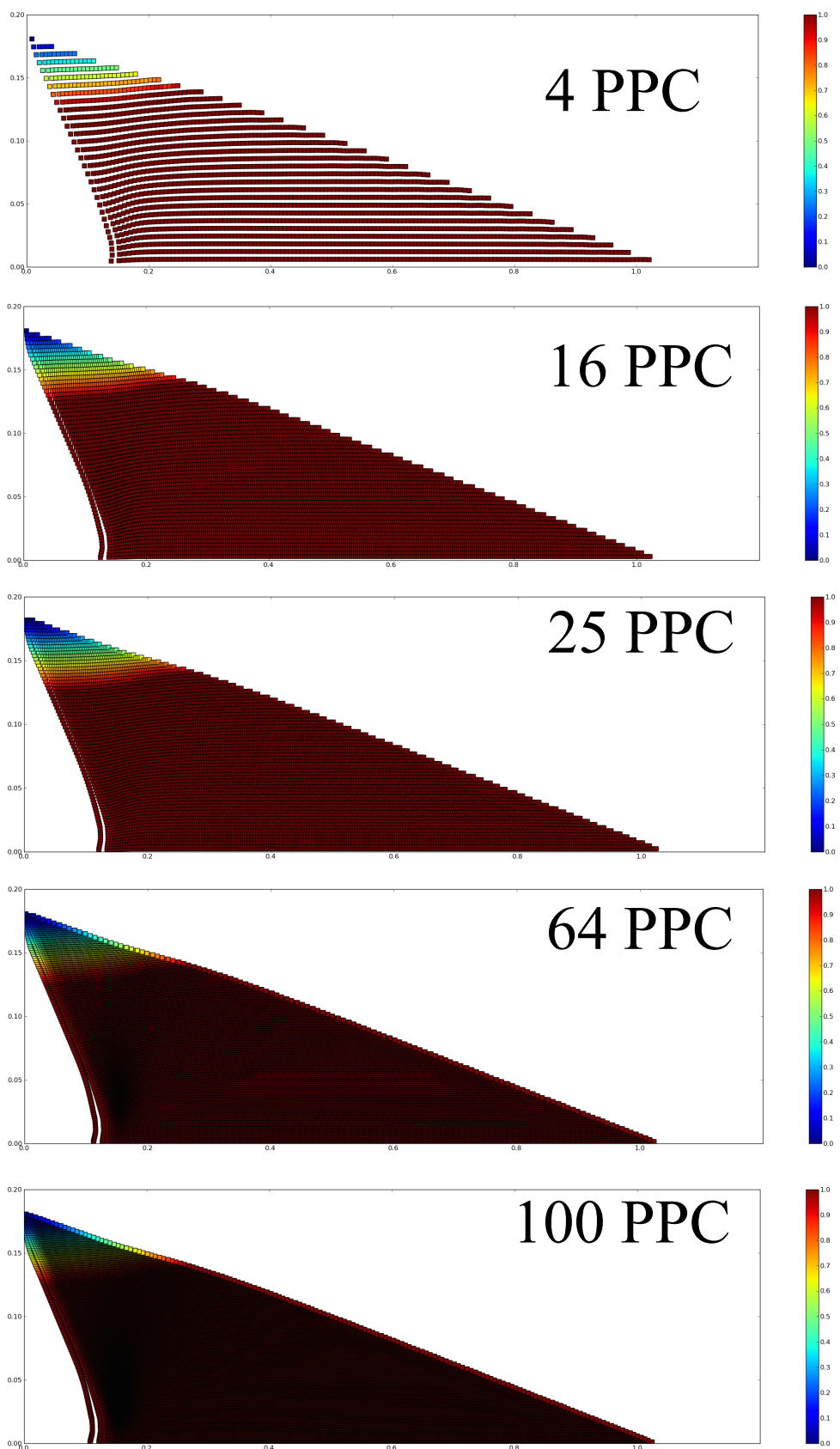


Figure 4.40 Effect of number of material points on cell on the run-out behaviour  $E_0 = 152mgd$ . Velocity profile (m/s) of granular pile subjected to gradient impact loading.

## 4.3 Slopes subjected to impact loading

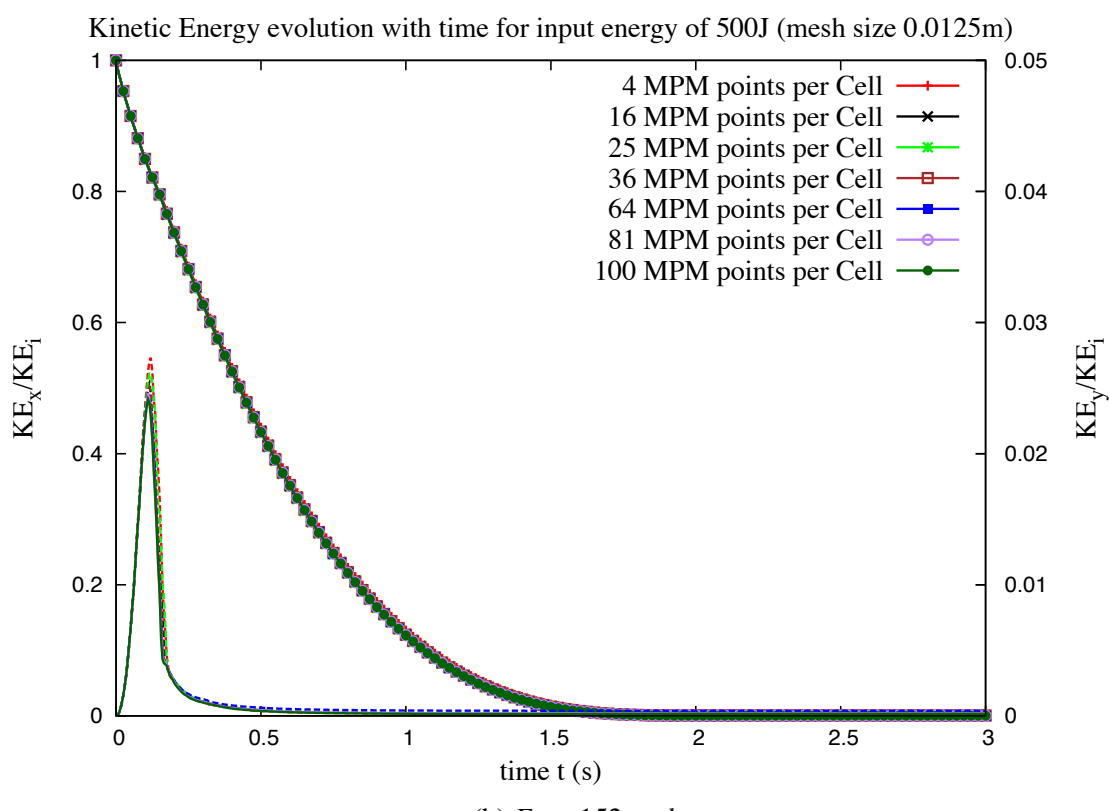
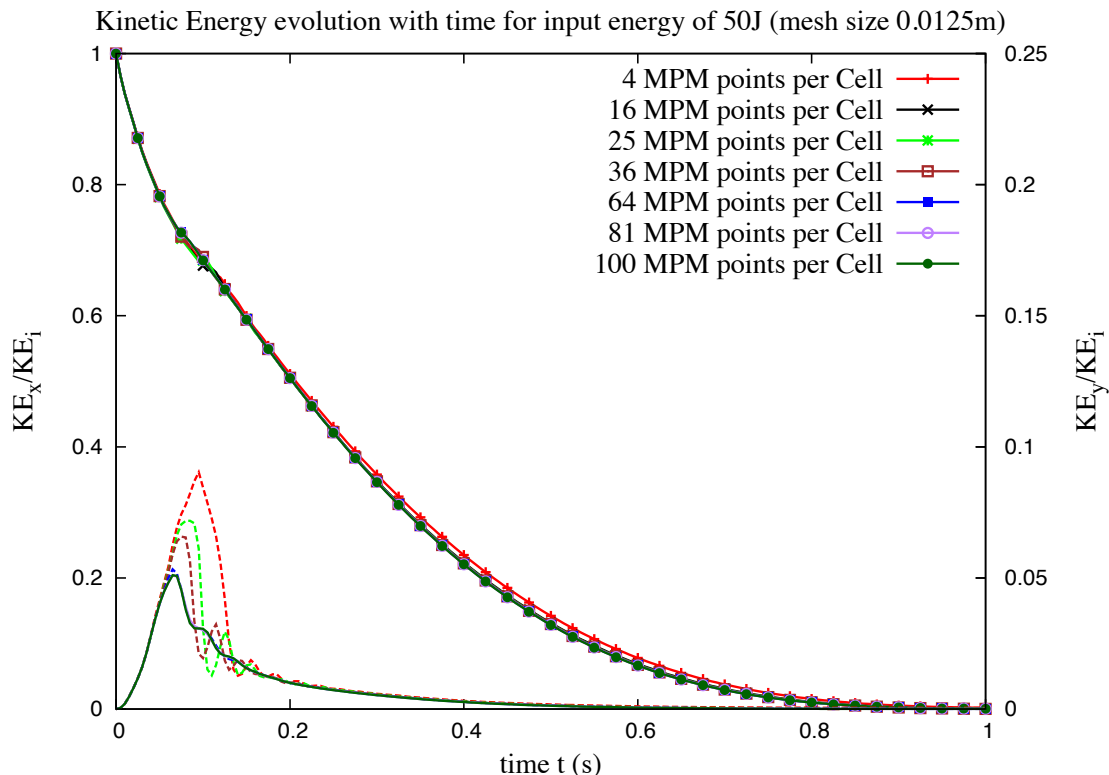


Figure 4.41 Evolution of kinetic with time for varying material points per cell

with increase in the number of material points per cell in both cases. Less than 1% difference in the run-out distance was observed between a mesh size of 0.0125 m and 0.01 m. The final run-out duration is almost unaffected by the increase in the number of material points per cell.

This shows that the run-out distance is affected by the number of material points per cell. However, the duration of the run-out is independent of the number of material points per cell. The computation time increases with increase in the number of material points per cell and decrease in the mesh size. However, the run-out distance converges with increase in number of material points per cell. Hence, an optimum number of 25 material points per cell was adopted in this case. In summary, for conducting a successful MPM analysis, a careful selection of the mesh size and the number of particles is necessary.

#### 4.3.6 Comparison with granular column collapse

Figure 4.43 shows the run-out behaviour of granular column collapse and the slope subjected to impact velocities as a function of normalised kinetic energy. In the case of column collapse, the peak energy at  $\tau_c$  is used as the energy available for the flow. It can be observed that MPM and DEM predict similar run-out behaviour for low energy regime (short columns), which undergo frictional failure along the flanks. However MPM predicts longer run-out for high energy regime (corresponding to a  $> 2.7$ ), where the granular column experiences significant collisional dissipation. The lack of a collisional energy dissipation mechanism in MPM results in over prediction of run-out distances. In the case of granular column subjected to impact velocity, the dissipation is friction and MPM is able to predict the run-out response in good agreement with DEM simulations. At very low energy, DEM simulations show longer run-out in the case of slope subjected to impact due to local destabilisation at the flow front. Both granular flows, column collapse and slope subjected to impact, show power-law relation with the energy. This shows that the power-law behaviour is a granular flow characteristic.

### 4.4 Summary

Multi-scale simulation of dry granular flows were performed to capture the local rheology, and to understand the capability and limitations of continuum models in realistic simulation of granular flow dynamics. MPM with a simple frictional dissipation model is able to capture the flow kinematics of dry granular flows. However, the lack of collisional dissipation in MPM is a limitation in modelling the collapse of tall columns. Both DEM and MPM simulations show a power-law dependence of the run-out and time with the initial aspect ratio of the column.

## 4.4 Summary

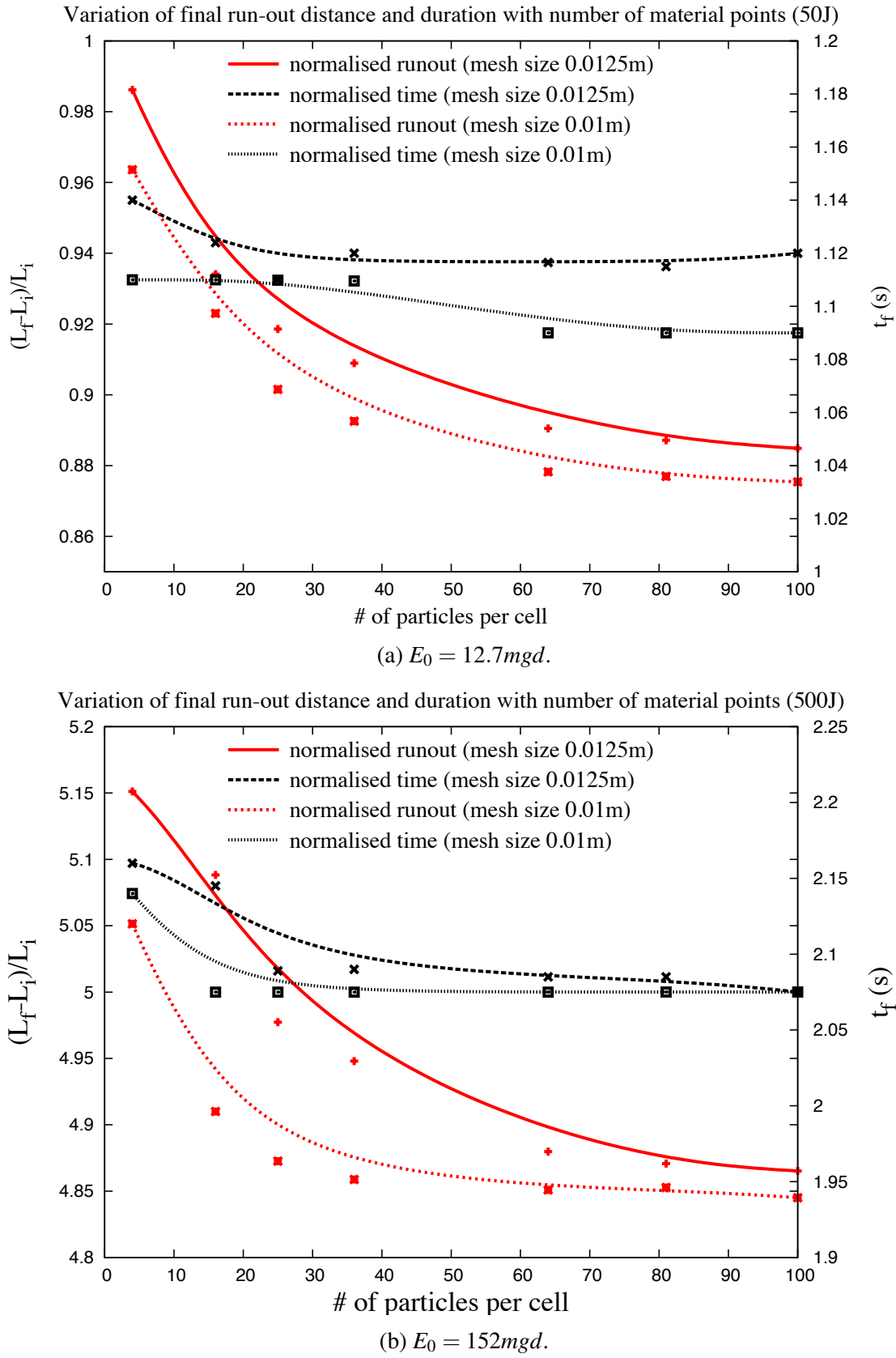


Figure 4.42 Evolution of run-out and duration of flow for varying material points per cell.

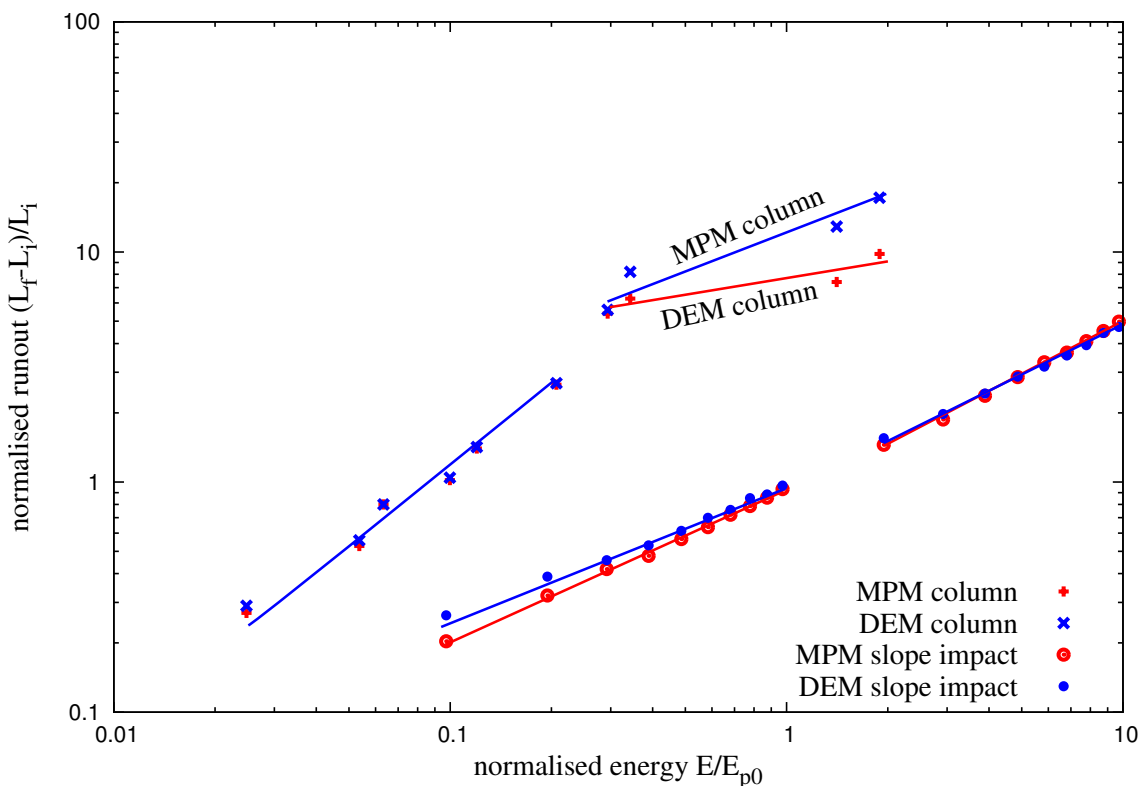


Figure 4.43 Comparison of column collapse with slope subjected to impact loading.

The initial configuration and the material properties have a significant influence on the run-out behaviour.

Natural granular flows are triggered by different mechanisms. The distribution of kinetic energy in the granular mass is found to have an effect on the flow kinematics. A multi-scale analyses of granular slope subjected to impact velocity reveals a power-law dependence of the run-out distance and time as a function of the input energy with non-trivial exponents. This reveals that the power-law behaviour is a generic feature of granular dynamics. The values of the exponents are not simple functions of the geometry.

We also observe two regimes with different values of the exponents: a low-energy regime and a high-energy regime. The low energy regime reflects mainly the destabilisation of the pile, with a run-out time independent of the input energy. Whereas, the second regime is governed by the spreading dynamics induced by higher input energy. The evolution of granular slope in the high-energy regime can be described by a characteristic decay time and the energy available at the end of the first stage, where the pile is destabilised. MPM is successfully able to simulate the transient evolution with a single input parameter, the macroscopic friction angle. This study exemplifies the ability of MPM, a continuum approach, in modelling complex granular flow dynamics and opens the possibility of realistic simulation of geological-scale flows on complex topographies.



# Chapter 5

21

## Underwater granular flows

22

### 5.1 Introduction

23

Avalanches, landslides, and debris flows are geophysical hazards, which involve rapid mass movement of granular solids, water, and air as a single phase system. Globally, landslides cause billions of pounds in damage, and thousands of deaths and injuries each year. Hence, it

24

1 is important to understand the triggering mechanism and the flow evolution. The momentum  
2 transfer between the discrete and continuous phases significantly affects the dynamics of the  
3 flow as a whole (Topin et al., 2012). Although certain macroscopic models are able to capture  
4 simple mechanical behaviours (Peker and Helvacı, 2007), the complex physical mechanisms  
5 occurring at the grain scale, such as hydrodynamic instabilities, formation of clusters, collapse,  
6 and transport, (Topin et al., 2011) have largely been ignored. In particular, when the solid phase  
7 reaches a high volume fraction, the strong heterogeneity arising from the contact forces between  
8 the grains, and the hydrodynamic forces, are difficult to integrate into the homogenization  
9 process involving global averages.

25

26

10 In order to describe the mechanism of immersed granular flows, it is important to consider  
11 both the dynamics of the solid phase and the role of the ambient fluid (Denlinger and Iverson,  
12 2001). The dynamics of the solid phase alone is insufficient to describe the mechanism of  
13 granular flow in a fluid. It is important to consider the effect of hydrodynamic forces that  
14 reduce the weight of the solids inducing a transition from dense-compacted to dense-suspended  
15 flows, and the drag interactions which counteract the movement of the solids (Meruane et al.,  
16 2010). Transient regimes characterized by change in the solid fraction, dilation at the onset of  
17 flow and development of excess pore pressure, result in altering the balance between the stress  
18 carried by the fluid and that carried by the grains, thereby changing the overall behaviour of the  
19 flow.

20 The presence of a fluid phase in a granular medium has profound effects on its mechanical behaviour. In dry granular media the rheology is governed by grain inertia and static stresses  
 1 sustained by the contact network depending on the shear-rate and confining pressure, respectively  
 2 ([Midi, 2004](#)). As the fluid inertia and viscosity come into play, complications arise  
 3 as a result of contradictory effects. On one hand, the fluid may delay the onset of granular  
 4 flow or prevent the dispersion of the grains by developing negative pore pressures ([Pailha et al., 2008; Topin et al., 2011](#)). On the other hand, the fluid lubricates the contacts between  
 5 grains, enhancing in this way the granular flow, and it has a retarding effect at the same time  
 6 by inducing drag forces on the grains. The objective of the present study is to understand the  
 7 differences in the mechanism of flow initiation and kinematics between dry and submerged  
 8 granular flow. In the present study, 2D Lattice-Boltzmann and Discrete Element Method is  
 9 used to model the fluid-soil interactions in underwater granular flows. The choice of a 2D  
 10 geometry has the advantage of cheaper computational effort than a 3D case, making it feasible  
 11 to simulate very large systems.  
 12

## 5.2 LBM-DEM Permeability

In a 3D granular assembly, the pore spaces between grains are interconnected, whereas in a 2-D assembly, a non-interconnected pore-fluid space is formed as the grains are in contact with each other. Which means that the pore-fluid enclosed between the grains cannot flow to neighbouring pore-spaces. This results in an unnatural no flow condition in a 2-D case (see figure 5.1). In order to overcome this difficulty, a reduction in radius is assumed only during LBM computations  
 15 (fluid and fluid – solid interaction). The reduced radius of the soil grain, i.e., the *hydrodynamic*  
 16 *radius* ‘r’, allows for interconnected pore space through which the pore-fluid can flow similar  
 17 to 3D behaviour. The reduction in radius is assumed only during LBM computations, hence  
 18 this technique has no effect on the grain – grain interactions computed using DEM.  
 19

5 Realistically, the hydrodynamic radius can be varied from  $r = 0.7R$  to  $0.95R$ , where ‘R’  
 6 is the grain radius. Different permeability can be obtained, for any given initial packing, by  
 7 varying the hydrodynamic radius of the grains, without changing the actual granular packing.  
 8 Hence, the hydrodynamic radius represents the permeability of the granular assembly. In  
 9 another sense, the hydrodynamic radius can be assumed to represent the irregularities on the  
 10 granular surface. Reducing the hydrodynamic radius represents wider channel and more flow  
 11 between the grains.

12 In order to understand the relation between the hydrodynamic radius and the permeability  
 13 of the granular assembly, horizontal permeability tests are performed by varying the hydro-  
 14 dynamic radius as  $0.7R$ ,  $0.75R$ ,  $0.8R$ ,  $0.85R$ ,  $0.9$  and  $0.95R$ . The transverse permeability of

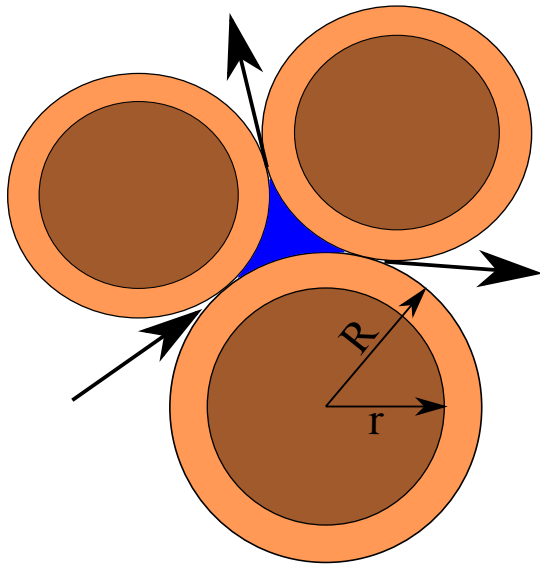


Figure 5.1 Schematic representation of the hydrodynamic radius in LBM-DEM computation

15 a square sample of 50 mm × 50 mm filled with poly-disperse ( $d_{max}/d_{min} = 1.8$ ) grains with  
 16 a mean diameter of 1.7mm is determined. Dirichlet boundary condition (discussed in ??),  
 17 i.e., pressure/density constrain is applied along the left and the right boundaries. The density  
     on the left boundary is increased in small increments ( $10^{-4}\Delta P$ ), which a constant density is  
     maintained on the right boundary. This results in a pressure gradient causing the fluid to flow  
     (see figure 5.2).

The mean velocity of flow ( $v$ ) is determined and the permeability of the sample ( $k$ ) is  
 computed as:

$$k = v \cdot \mu \cdot \frac{\Delta x}{\Delta P}, \quad (5.1)$$

where  $\mu$  is the dynamic viscosity of the fluid (Pa s),  $\Delta x$  is the thickness of the bed of porous  
 medium m, and  $\Delta P$  is the applied pressure difference Pa. For a given hydrodynamic radius, the  
 pressure gradient  $\Delta P$  is varied to obtain different flow rates. Probing the fluid space showed  
 a Poiseuille flow behaviour between grains. The flow is still within the Darcy's laminar flow  
 regime, which is verified by the linear slope between the pressure gradient and mean flow  
 velocity (see figure 5.3). It can be observed that with increase in the hydrodynamic radius  
 the permeability decreases, i.e., the slope of the mean flow velocity to the pressure gradient  
 decreases. At very low pressure gradient ( $\Delta P \leq 0.1$ ), both  $0.9R$  and  $0.95r$  has a no flow  
 condition. A hydrodynamic radius of  $r = 0.95R$  shows almost no flow behaviour, even at higher  
 pressure gradients. A high value of hydrodynamic radius  $r > 0.95R$  results in unnatural flow  
 behaviour. Hence, hydrodynamic radii in the range of 0.7 to 0.95R are adopted in the present  
 study.

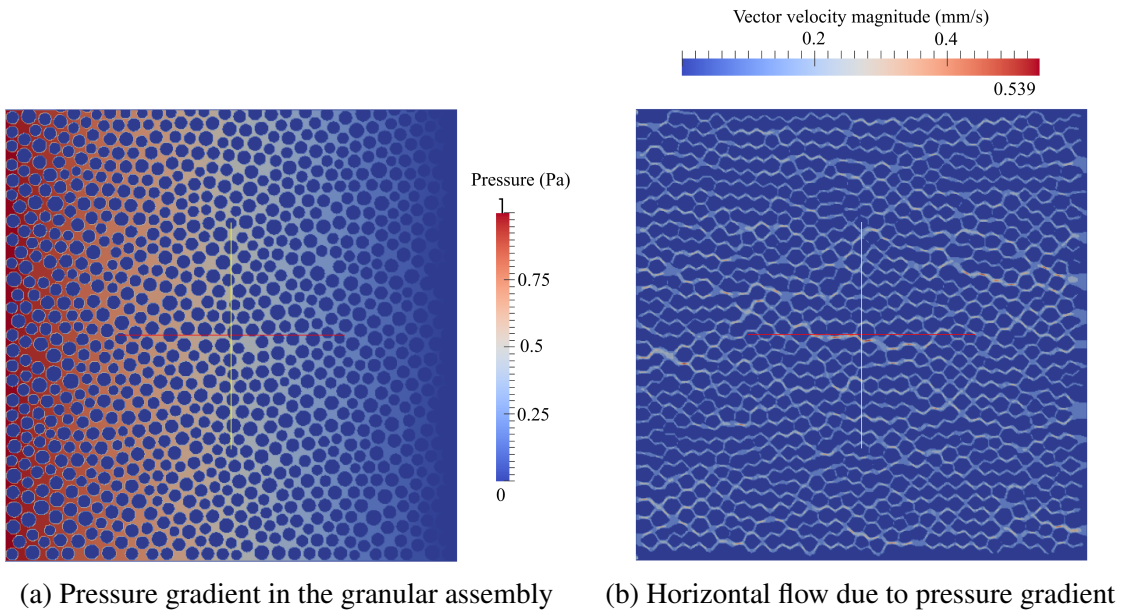


Figure 5.2 Evaluation of the horizontal permeability for a hydrodynamic radius of 0.7R.

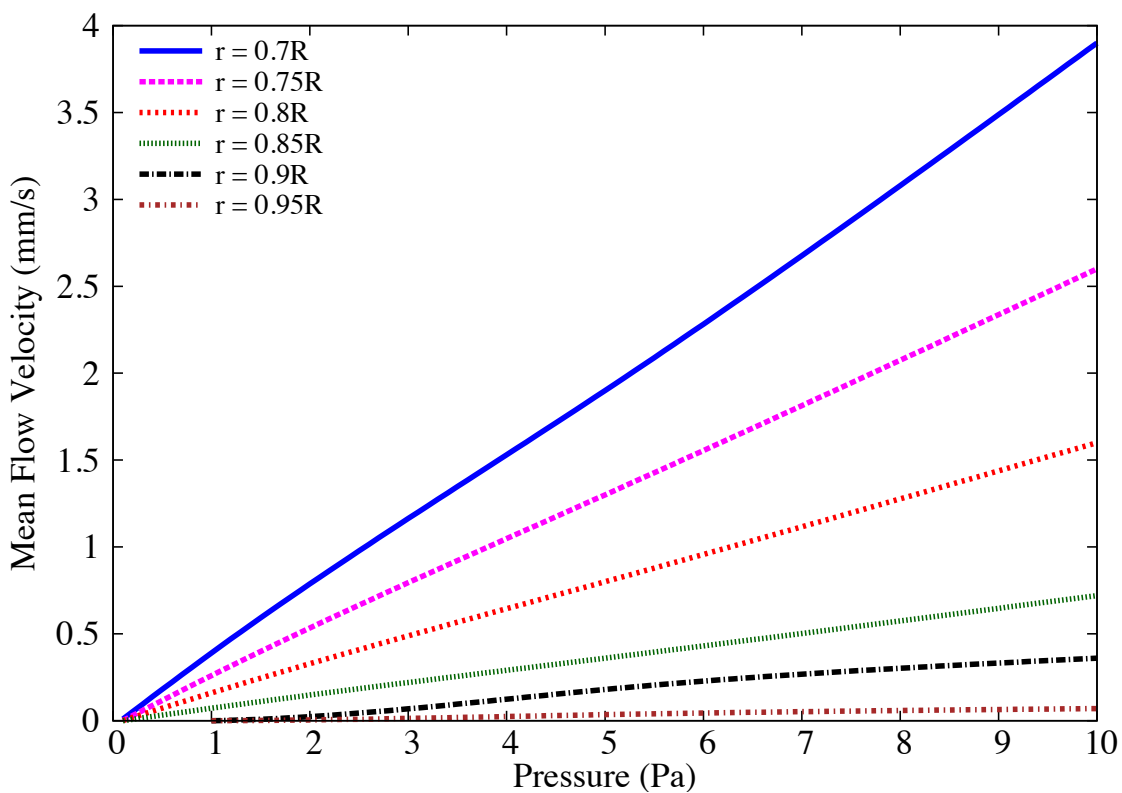


Figure 5.3 Variation of the mean flow velocity with pressure gradient for different hydrodynamic radius.

Increase in the hydrodynamic radius from 0.7 to 0.95 reduces the porosity from 0.60 to 0.27. The permeability computed from LB – DEM method is verified by comparing it with the analytical solution. One of the widely used analytical solution for permeability is the Carman – Kozeny equation (CK Model), which is based on the Poiseuille flow through a pipe and is mainly used for 3D, homogeneous, isotropic, granular porous media at moderate porosities. In the present study, a modified Carman – Kozeny equation that takes into account the micro-structure of the fibres and that is valid in a wide range of porosities is adopted ([Yazdchi et al., 2011](#)). The normalized permeability is defined as

$$\frac{k}{d^2} = \frac{\varepsilon}{\psi_{CK}(1-\varepsilon)^2}. \quad (5.2) \quad 27$$

In the CK model, the hydraulic diameter  $D_h$ , is expressed as a function of measurable quantities: porosity and specific surface area

$$D_h = \frac{4\varepsilon V}{S_v} = \frac{\varepsilon d}{(1-\varepsilon)}, \quad (5.3) \quad 30$$

$$a_v = \frac{\text{grain surface}}{\text{grain volume}} = \frac{S_v}{(1-\varepsilon V)} = \frac{4}{d}, \quad (5.4) \quad 1 \\ 2$$

where  $S_v$  is the total wetted surface, and  $a_v$  is the specific surface area. The above value of  $a_v$  is for circles (cylinders) - for spheres  $a_v = 6/d$ .  $\psi_{CK}$  is the empirically measured CK factor, which represents both the shape factor and the deviation of flow direction from that in a duct. It is approximated for randomly packed beds of spherical grains. The normalized permeability for different porosity obtained by varying the radius from 0.7 to 0.95 is presented in figure 5.4. The normalized permeability is found to match the qualitative trend of the Carman-Kozeny equations. The LB – DEM permeability curve lies between the permeability curves for spherical and cylindrical grain arrangements implying a better approximation of three-dimensional permeability using a 2D granular assembly with a reduced grain radius during LBM computations. Thus using hydrodynamic radius, realistic fluid - grain interactions can be obtained in a 2D geometry.

### 5.3 Granular collapse in fluid

The collapse of a granular column, which mimics the collapse of a cliff, has been extensively studied in the case of dry granular material, when the interstitial fluid plays no role (see section 4.2). The problem of the granular collapse in a liquid, which is of importance for submarine landslides, has to our knowledge attracted less attention ([Rondon et al., 2011](#)). [Thompson and](#)

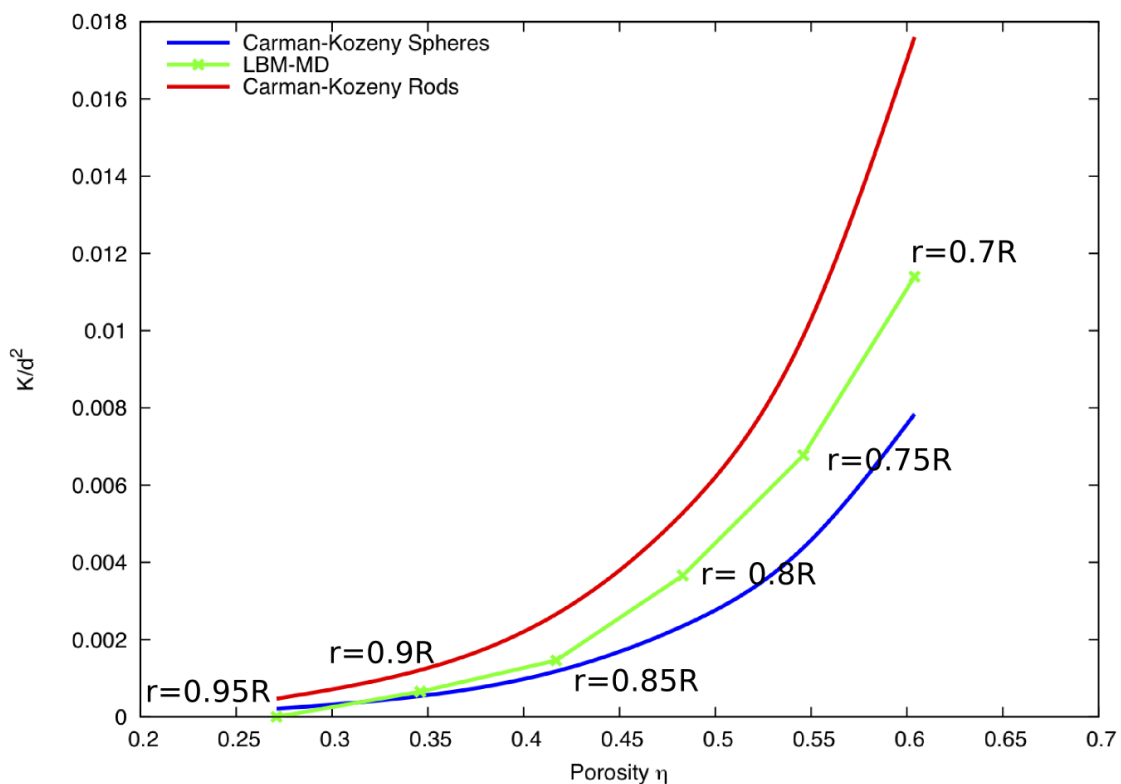


Figure 5.4 Relation between permeability and porosity for different hydrodynamic radius and comparison with the analytical solution.

Hupper (2007) observed that the presence of liquid dramatically changes the way a granular column collapses compared to the dry case. The destabilization of a granular pile strongly depends on the initial volume fraction of the packing. For dense packings the granular flow is localized at the free surface of the pile, whereas for loose packings the destabilization occurs in the bulk of the material and has a parabolic profile (Bonnet et al., 2010; Iverson, 2000; Topin et al., 2011).

### 5.3.1 LBM-DEM set-up

In the present study, the collapse of a granular column in fluid is studied using 2D LBM - DEM. The effect of initial aspect on the run-out behaviour is investigated. The flow kinematics are compared with the dry and buoyant granular collapse to understand the influence of hydrodynamic forces and lubrication on the run-out. Unlike dry column, the role of permeability and the initial volume fraction is expected to have a significant influence on the flow dynamics. Hence the effect of permeability and the initial packing density on the run-out behaviour is investigated.

The granular collapse set-up in fluid is very similar to the dry granular column collapse. A rectangular channel of length  $L_0$  and height  $H_0$  is filled with poly-dispersed discs having ( $d_{max}/d_{min} = 1.8$ ) (see Figure 5.5). The granular column is then placed in a fluid with a density of  $1000 \text{ kg m}^{-3}$  and a kinematic viscosity of  $1 \times 10^{-6} \text{ m}^2 \text{ s}^{-1}$ . The gate supporting the right-hand side boundary of the granular column is opened allowing the column to collapse and flow in fluid. The final run-out distance is measured as  $L_f$  and final collapse height as  $H_f$ . The collapse takes place on a horizontal surface. The initial aspect ratio of the column is varied as 0.2, 0.4, 0.6, 0.8, 1, 2, 4 and 6.

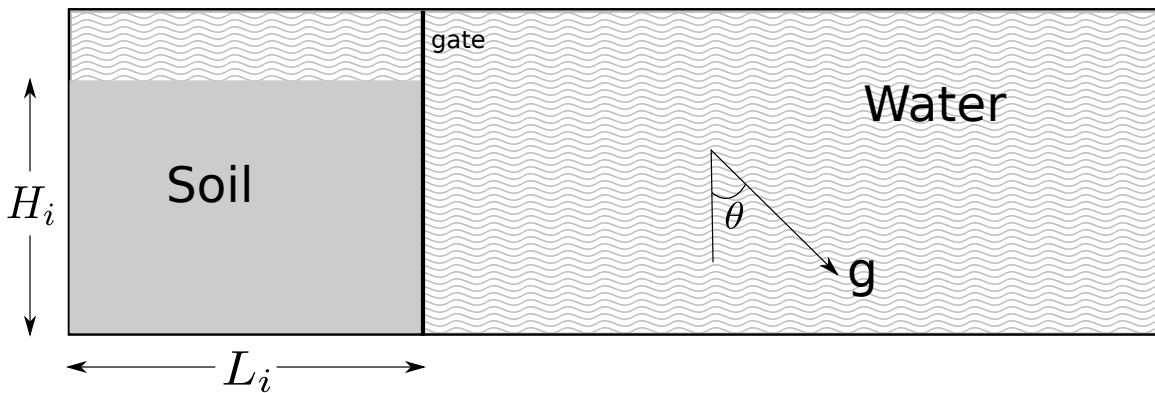


Figure 5.5 Underwater granular collapse set-up.

The cumulative  $\beta$  distribution is adopted to generate grains with  $d_{max}$  and  $d_{min}$  as 1.25 mm and 2.2 mm, respectively. The soil column is modelled using  $\approx 2000$  discs of density

- <sup>18</sup>  $2650 \text{ kg m}^{-3}$  and a contact friction angle of  $26^\circ$ . A linear-elastic contact model is used in the DEM simulations. The granular assemble has a packing fraction of 83%. The critical time step for DEM is computed based on the local contact natural frequency and damping ratio. A sub-cycling time integration is adopted in DEM (see ??). A fluid flow (LBM) time step,  $\Delta t = 2.0E^{-5}\text{s}$  is determined based on the viscosity and relaxation parameter  $\tau = 0.506$ . An integer ratio  $n_s$ , between the fluid flow time step  $\Delta t$  and DEM time step  $\Delta t_D$  is determined as 15, i.e., every LBM iteration involves a sub-cycle of 15 DEM iterations.

In order to capture realistic physical behaviour of the fluid – grain system, it is essential to model the boundary condition between the fluid and the grain as a non-slip boundary condition, i.e. the fluid near the grain should have similar velocity as the grain boundary. The solid grains inside the fluid are represented by lattice nodes. The discrete nature of lattice, results in a stepwise representation of the surfaces (see figure 5.6), which are otherwise circular, hence sufficiently small lattice spacing  $h$  is required. The smallest DEM grain in the system controls the size of the lattice. In the present study, a very fine discretisation of  $d_{min}/h = 10$  is adopted, i.e., the smallest grain with a diameter  $d_{min}$  in the system is discretised into 100 lattice nodes ( $10h \times 10h$ ). This provides a very accurate representation of the interaction between the solid and the fluid nodes. A hydrodynamic radius of  $0.7R$  is adopted during LBM computations.

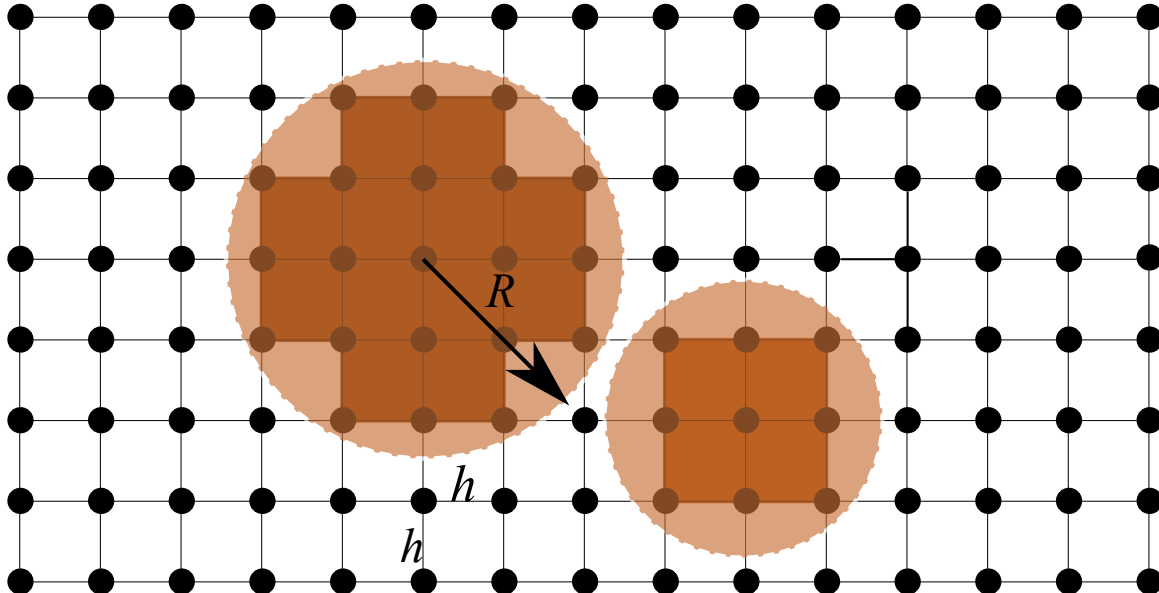


Figure 5.6 Discretisation of solid grains in LBM grid. Shows the step-wise representation of circular disks in the lattice.

### 5.3.2 Collapse in fluid: Flow evolution

Two-dimensional plane-strain LBM-DEM simulations of granular column collapse are performed by varying the initial aspect ratio of the column from 0.2 to 6. The normalized final run-out distance is computed as  $\Delta L = (L_f - L_0)/L_0$ . Similar to dry granular collapse, the duration of collapse is normalised with a critical time  $\tau_c = \sqrt{H/g}$ . Where,  $H$  is the initial height of the granular column and  $g$  is the acceleration due to gravity. Dry and buoyant analyses of granular column collapse are also performed to understand the effect of hydrodynamic forces on the run-out distance.

Snapshots of flow evolution of a granular column collapse with an initial aspect ratio of 0.4 is shown in figure 5.7. The failure begins at the toe end of the column, and the fracture surface propagates into the column at an angle of about  $50^\circ$ , similar to dry column. For the short column, the failure is due to collapse of the flanks. Once the material is destabilised, the granular mass interacts with the surrounding fluid resulting in formation of turbulent vortices. These vortices interact with the grains at the surface, resulting in irregularities on the free surface. Force chains can be observed in the static region of collapse, which indicates the flow can be described using a continuum theory. As the granular material ceases to flow, force chains develop at the flow front, revealing consolidation of the granular mass resulting in increase in strength.

The evolution of run-out with time for a short column ( $a = 0.4$ ) is presented in figure 5.8a. The dry column exhibits longer run-out distance in comparison to the submerged column. The collapse of a dry column using DEM represents a collapse in vacuum, without any influence of drag forces or viscosity of air. A LBM-DEM simulation of a granular column collapse using the kinematic viscosity of air is performed to compare the dry column with the collapse in air. It can be observed that both the “dry” condition and the collapse in air show almost the same run-out behaviour. However, the collapse in fluid (water) results in a much shorter run-out distance. The granular mass in fluid has the buoyant mass, in contrast to the dry density. A dry granular collapse with the buoyant unit weight is performed to understand the effect of buoyancy on the run-out behaviour. The dry column with buoyant unit weight also exhibits longer run-out behaviour than the collapse in fluid. However, due to decrease in the initial potential energy, the run-out observed in the buoyant condition is shorter than the dry condition. The column collapse in fluid takes longer to evolve when submerged in water, which might be due to the development of large negative porewater pressure that is generated during the shear failure along the fracture surface. The large negative pore pressure has to be dissipated before the granular mass above the fracture surface can collapse and flow. The shorter run-out distance in the fluid case, in comparison with the dry and buoyant conditions, shows that the collapse in fluid is significantly affected by the hydrodynamic drag force acting on the soil

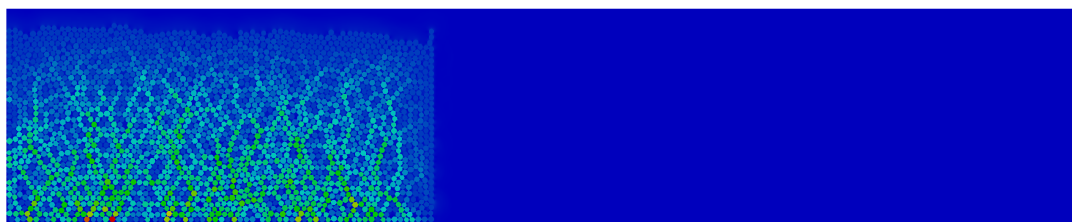
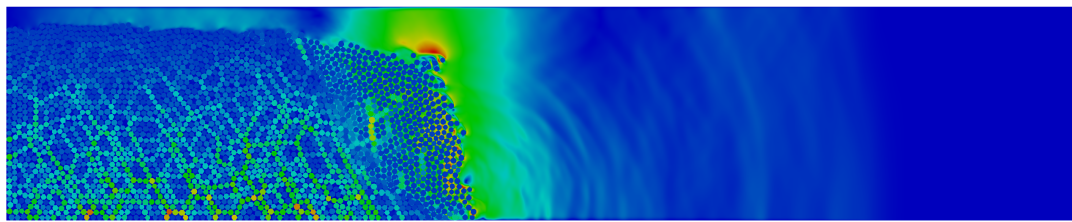
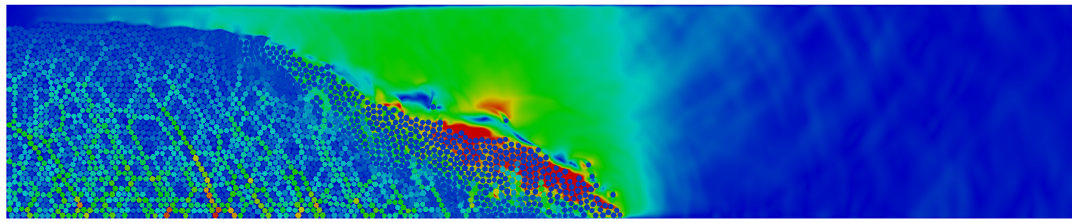
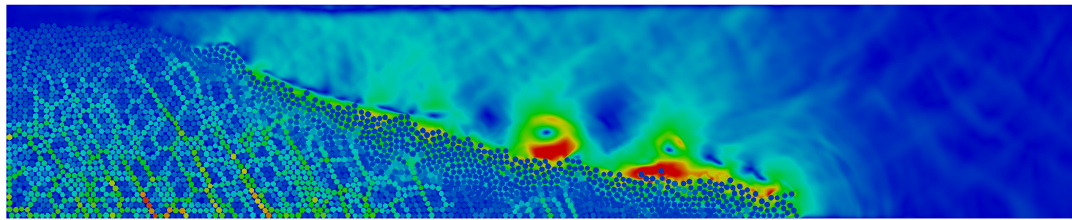
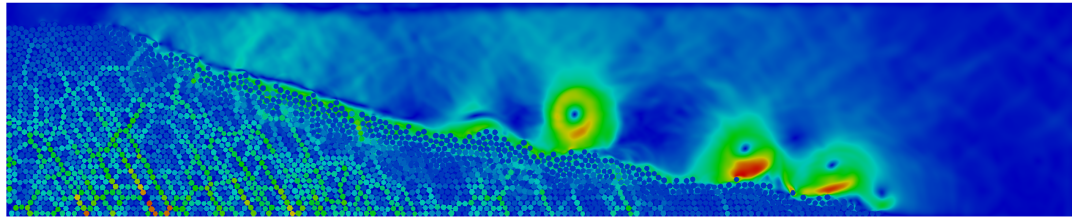
(a)  $t = 0\tau_c$ (b)  $t = 1\tau_c$ (c)  $t = 3\tau_c$ (d)  $t = 6\tau_c$ (e)  $t = 8\tau_c$ 

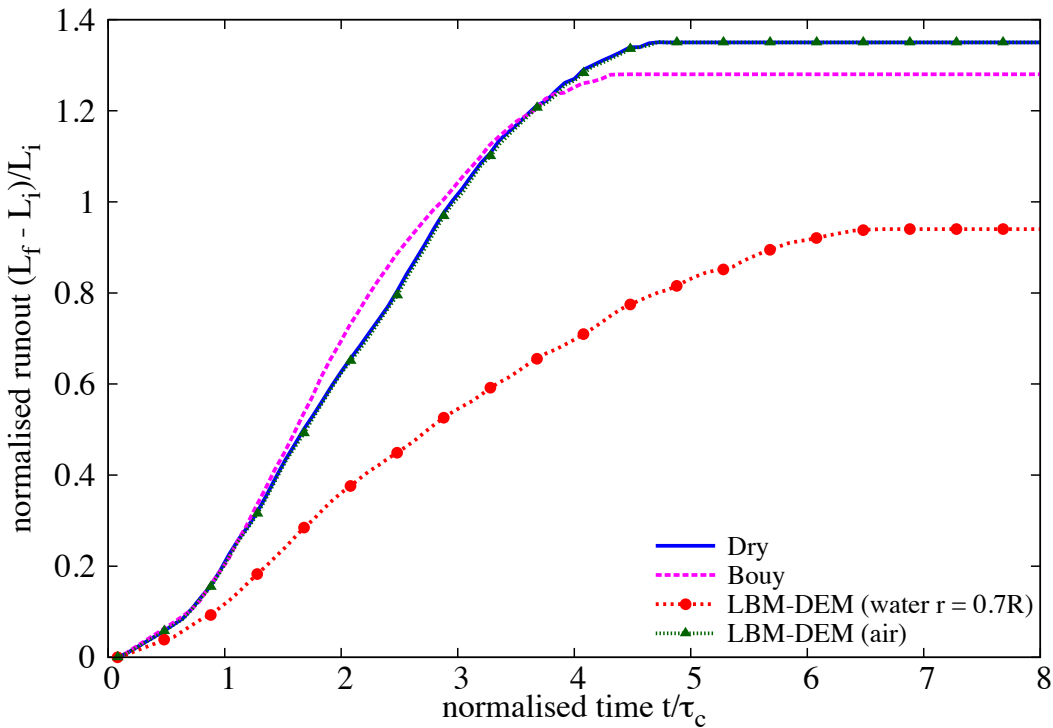
Figure 5.7 Flow evolution of a granular column collapse in fluid ( $a = 0.4$ ). Shows the velocity profile of fluid due to interaction with the grains (red - higher velocity).

<sup>17</sup> grains. The evolution of height  $H/L$  is presented in [??](#). Since the failure of the column is only  
<sup>18</sup> at the flank, the central static region remains unaffected. Hence, the final height of the column  
<sup>19</sup> is the same in dry and submerged conditions.

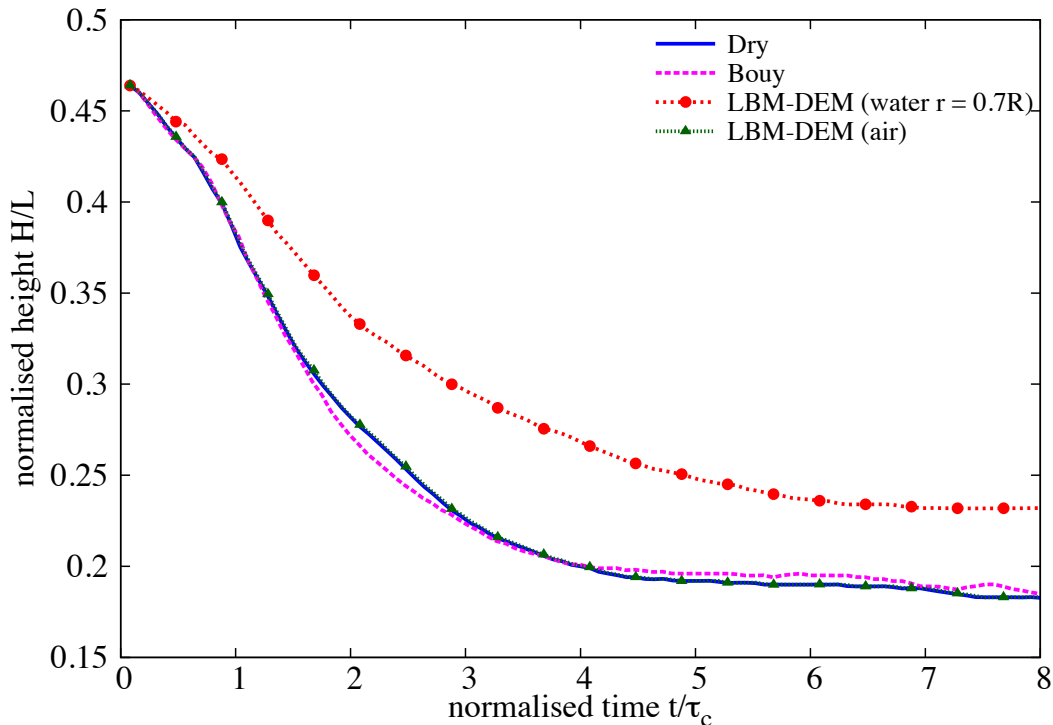
<sup>20</sup> The evolution of normalised kinetic energy with time for a column with an initial aspect  
<sup>21</sup> ratio of 0.4 is shown in figure [5.9](#). It can be observed that the peak kinetic energy is attained later  
<sup>22</sup> in the submerged condition than the dry collapse. This can be attributed to the time required  
<sup>23</sup> to overcome the negative pore pressure generated during the shear along the fracture surface.  
<sup>24</sup> For short columns the critical time  $\tau_c$  is controlled by the vertical kinetic energy. The amount  
<sup>25</sup> of kinetic energy in submerged case is significantly lower than the dry condition. Also, the  
<sup>26</sup> potential energy evolution (see figure [5.10](#)) shows a significant influence of the hydrodynamic  
<sup>27</sup> forces on the amount of material destabilised during the collapse. The drag forces reduces and  
<sup>28</sup> slows down the amount of material that undergo collapse resulting in shorter run-out distance  
<sup>29</sup> for short columns.

<sup>30</sup> Snapshots of the flow evolution of a granular column collapse with an initial aspect ratio  
<sup>31</sup> of 4 is shown in figure [5.11](#). For a tall column, the collapse mechanism changes. The entire  
<sup>32</sup> column is involved in the collapse. The height of the static region, which is below the fracture  
<sup>33</sup> surface, is shorter than the total height of the column. This results in a free-fall of grains  
<sup>34</sup> above the fracture surface. As the grains experience free-fall they interact with the surrounding  
<sup>35</sup> fluid. However, no vortices are observed during the initial stage of collapse. In the second  
<sup>36</sup> phase, when the grains reach the base, the vertical acceleration gained during the free-fall is  
<sup>1</sup> converted to horizontal kinetic energy. As the grains are ejected horizontally, the free surface  
<sup>2</sup> of the granular mass interacts with the fluid resulting in formation of the turbulent vortices.  
<sup>3</sup> Unlike short columns, these vortices have significant influence on the mass distribution along  
<sup>4</sup> the run-out. Heaps of granular material can be observed in front of each vortices. The number  
<sup>5</sup> of vortices formed during a collapse is found to be proportional to the amount of material  
<sup>6</sup> destabilised, i.e., the length of free-surface interacting with the fluid influences the number  
<sup>7</sup> of vortices generated during the collapse. The reappearance of force chains at  $t = 6\tau_c$  &  $8\tau_c$   
<sup>8</sup> indicates the granular mass is consolidating resulting in an increase in the shear strength.

<sup>9</sup> The time evolution of the run-out and height of a tall column ( $a=4$ ) is presented in figure  
<sup>1</sup> [5.12a](#) and figure [5.12b](#), respectively. Similar to the short column, the run-out observed in  
<sup>2</sup> the dry condition is much longer than that observed in submerged condition. Also, the evolution  
<sup>3</sup> of run-out is slower in case of submerged condition, which indicates the influence drag force on  
<sup>4</sup> the run-out evolution. The height of the column is significantly affected by the hydrodynamic  
<sup>5</sup> forces (see figures [5.12b](#) and [5.13](#)), which reduces the amount of material destabilised during  
<sup>6</sup> collapse.



(a) Evolution of run-out with time



(b) Evolution of height with time

Figure 5.8 Evolution of height and run-out with time for a column collapse in fluid ( $a = 0.4$ )

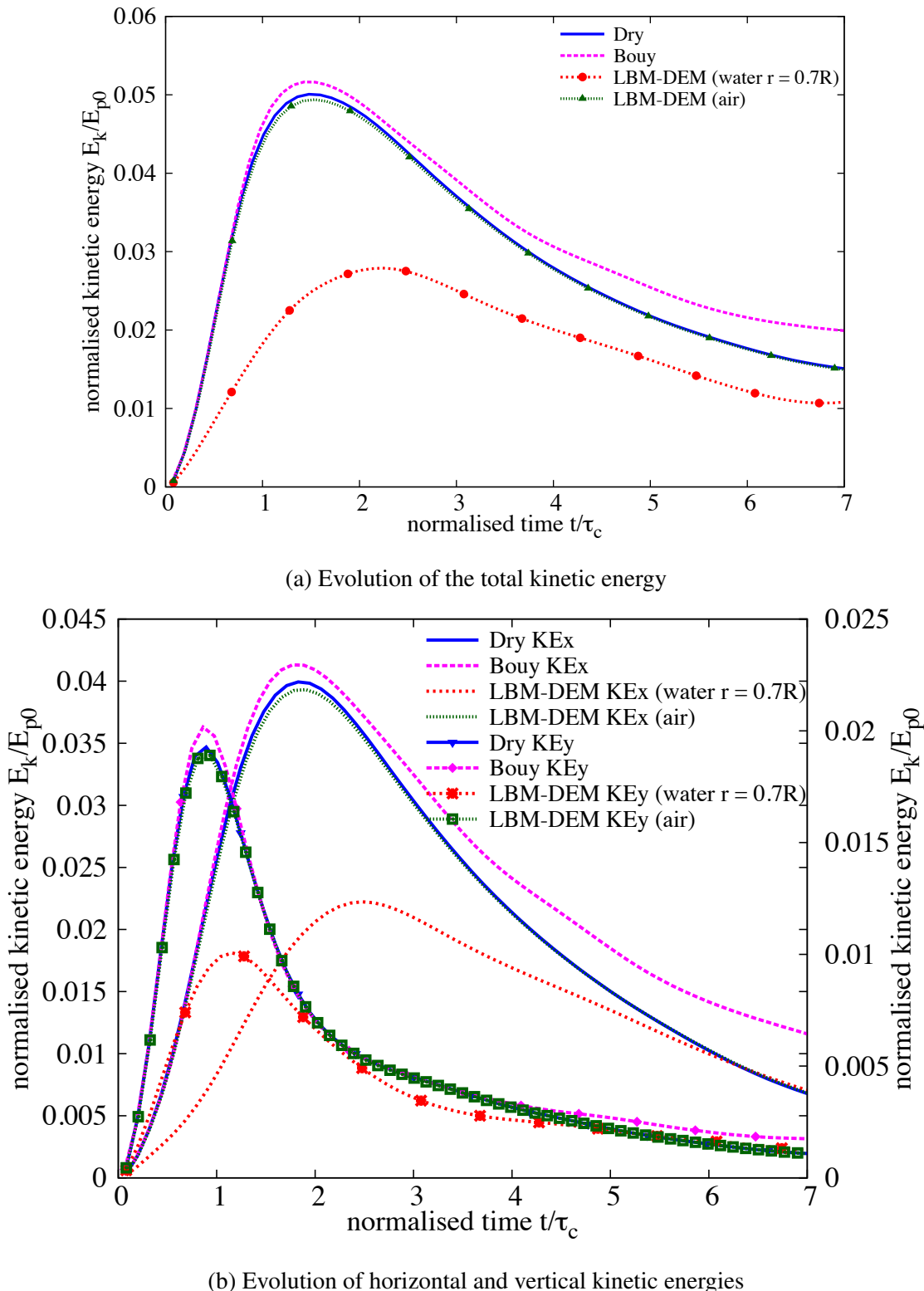


Figure 5.9 Evolution of kinetic energies with time for a granular column collapse in fluid ( $a = 0.4$ )

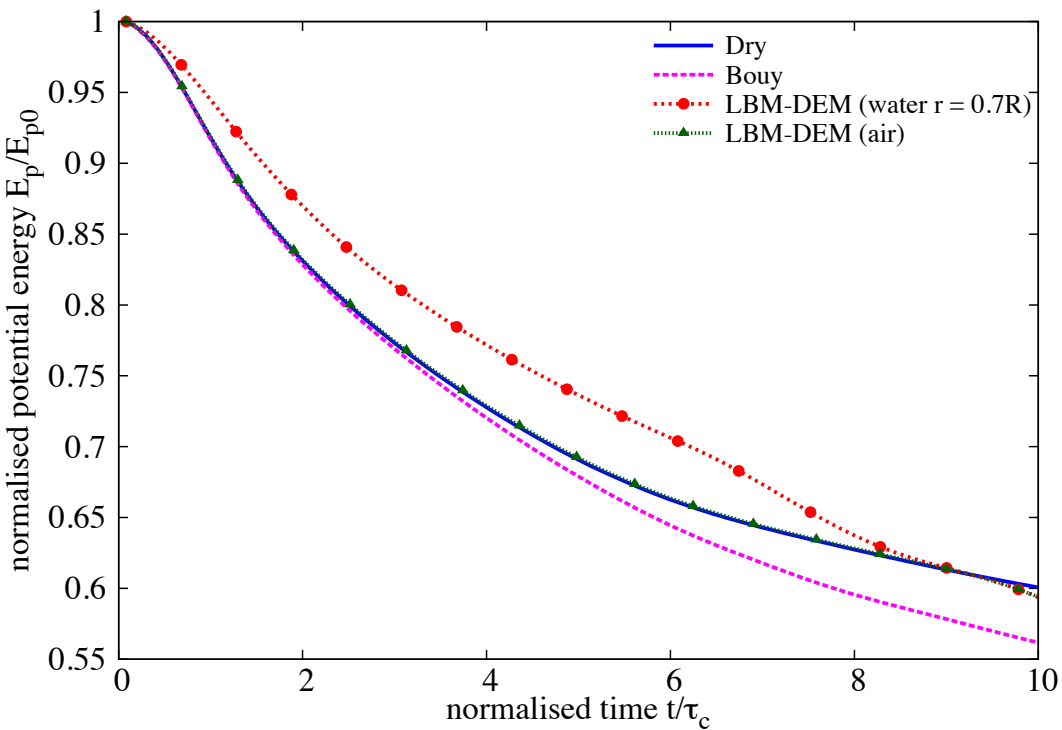
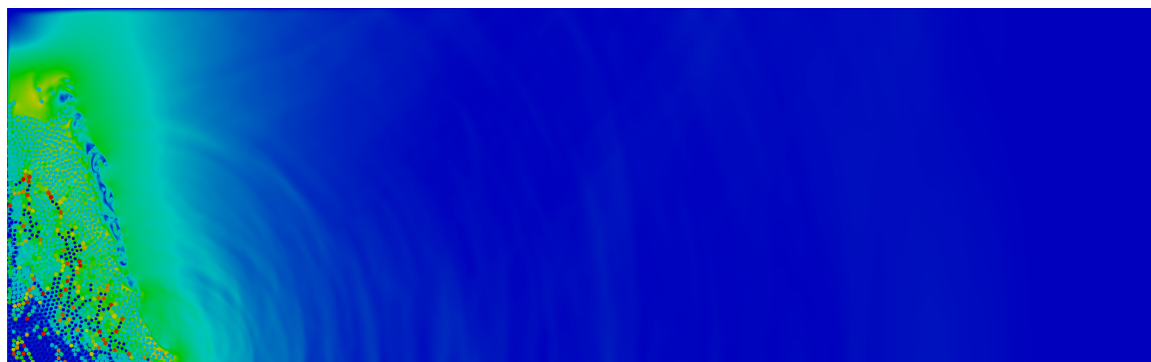
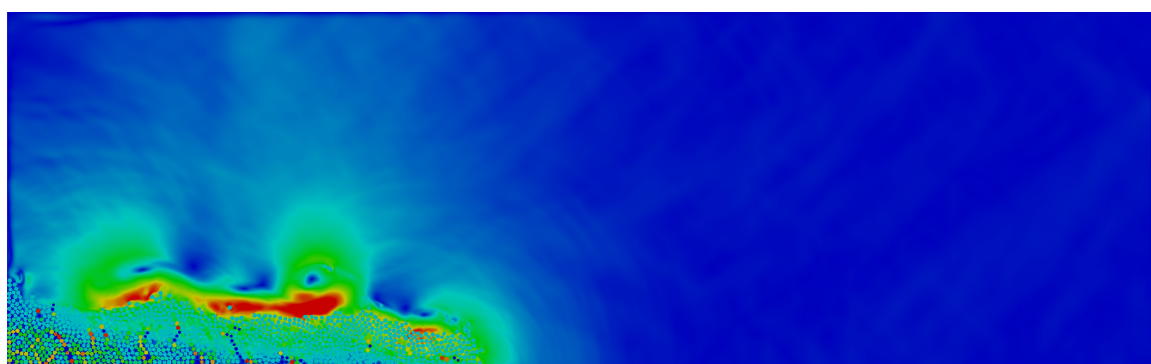


Figure 5.10 Evolution of the potential energy with time for a granular column collapse in fluid ( $a = 0.4$ )

The evolution of kinetic energies with time for aspect ratio 4 is presented in figure 5.14. Even during the free-fall stage, the peak vertical energy is delayed in the case of fluid, which shows the influence of the viscosity on the flow evolution. Almost half of the kinetic energy that is available in the case of dry granular collapse is dissipated due to the drag force experienced by the grains. This shows that the influence of viscous drag on the run-out evolution is significantly higher than the effect of lubrication.

The initial aspect ratio of the column is varied from 0.2 to 6. The final run-out distance as a function of the initial aspect ratio of the column is presented in figure 5.15a. For all aspect ratios, the run-out observed in the dry case is significantly higher than the submerged condition. For short columns, the run-out distance is found to have a linear relationship with the initial aspect ratio of the column. A power law relation is observed between the run-out and the initial aspect ratio of the column. The normalized final height as a function of the initial aspect ratio of the column is presented in figure 5.15b. It can be observed that the final collapse height is much higher in fluid than the dry condition. The drag force on the granular column reduces the amount of collapse, resulting in a shorter run-out distance. The drag force seems to have a predominant influence on the run-out behaviour than the lubrication effect in fluid.

 $t = 0\tau_c$  $t = 1\tau_c$  $t = 3\tau_c$

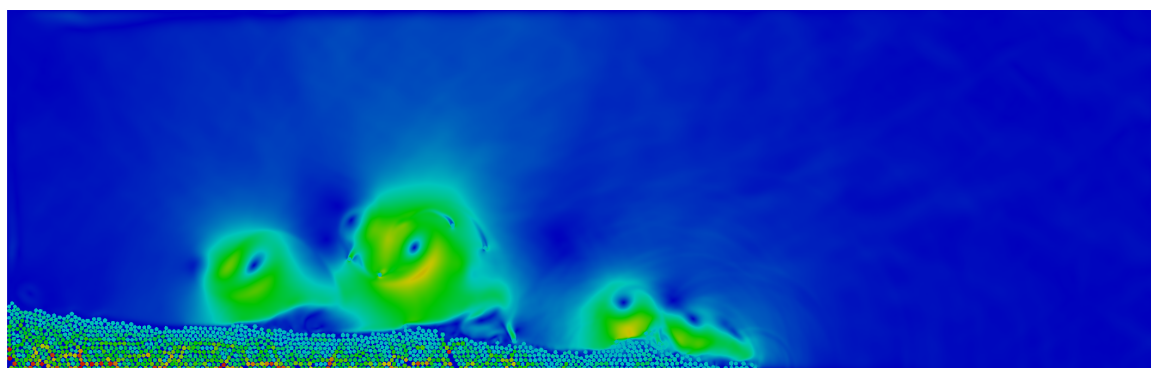
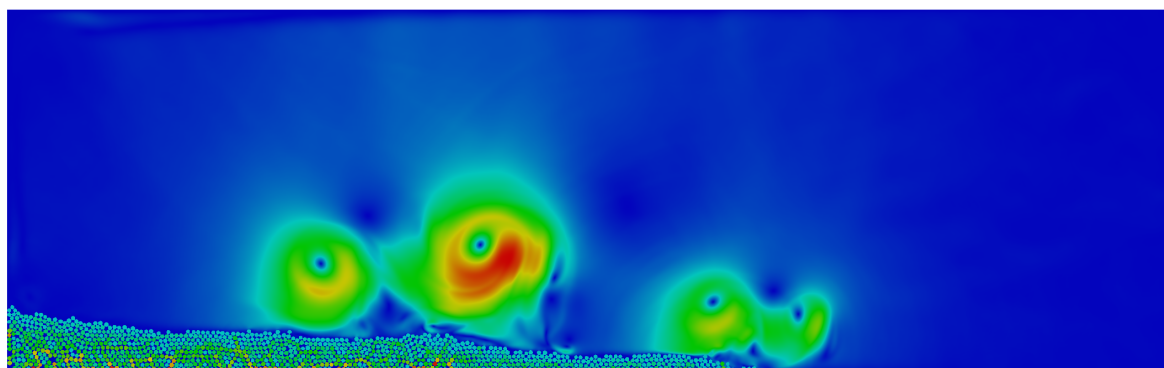
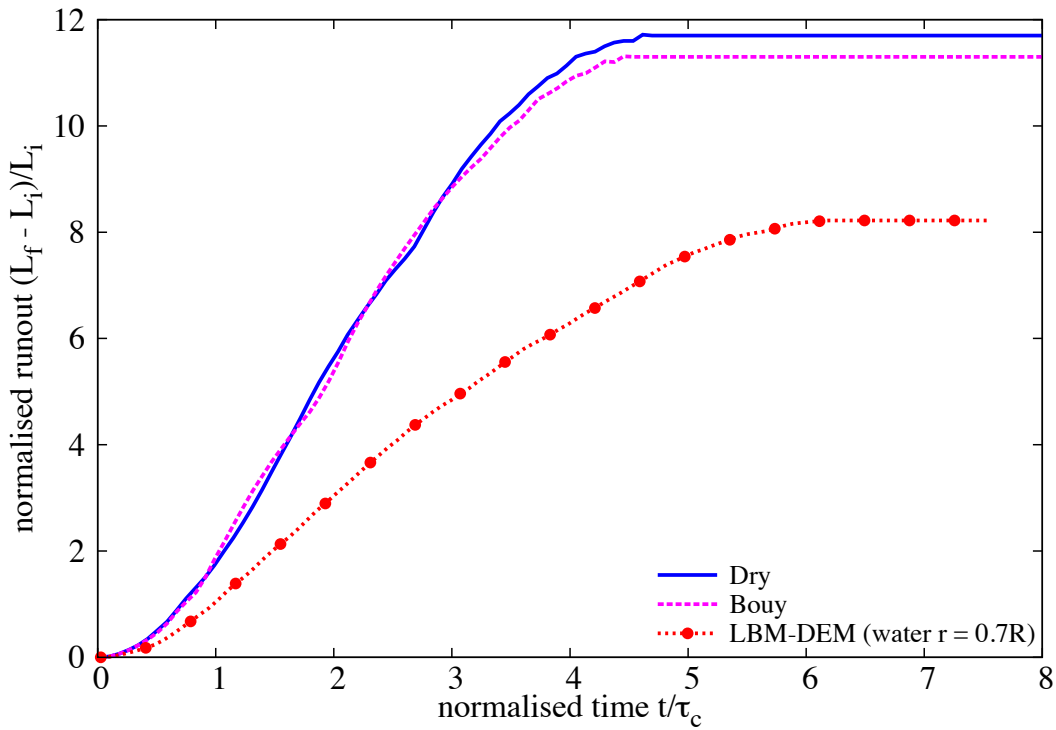
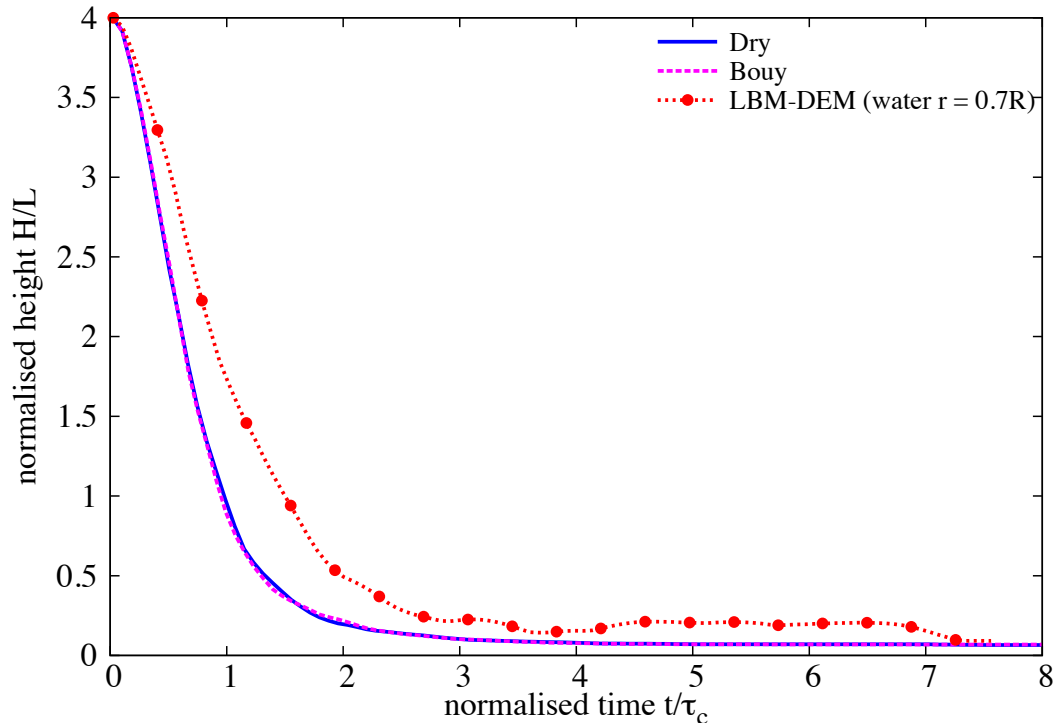
 $t = 6\tau_c$  $t = 8\tau_c$ 

Figure 5.11 Flow evolution of a granular column collapse in fluid ( $a = 4$ ). Shows the velocity profile of fluid due to interaction with the grains (red - higher velocity).



(a) Evolution of run-out with time



(b) Evolution of height with time

Figure 5.12 Evolution of run-out and height with time for a column collapse in fluid ( $a = 4$ )

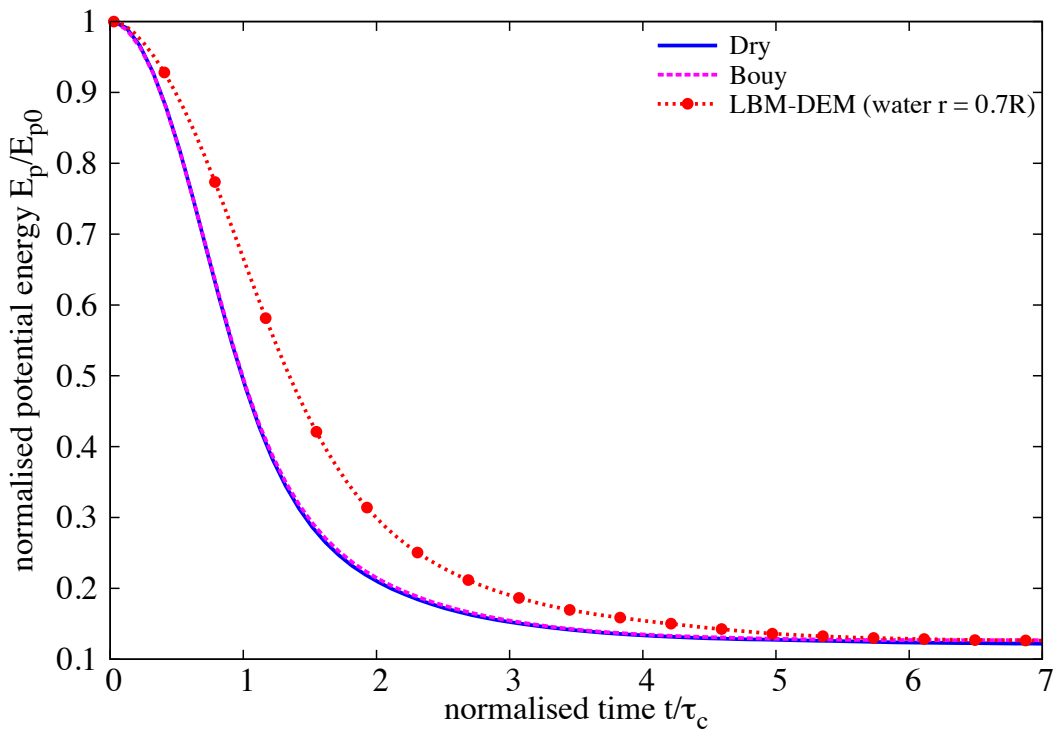
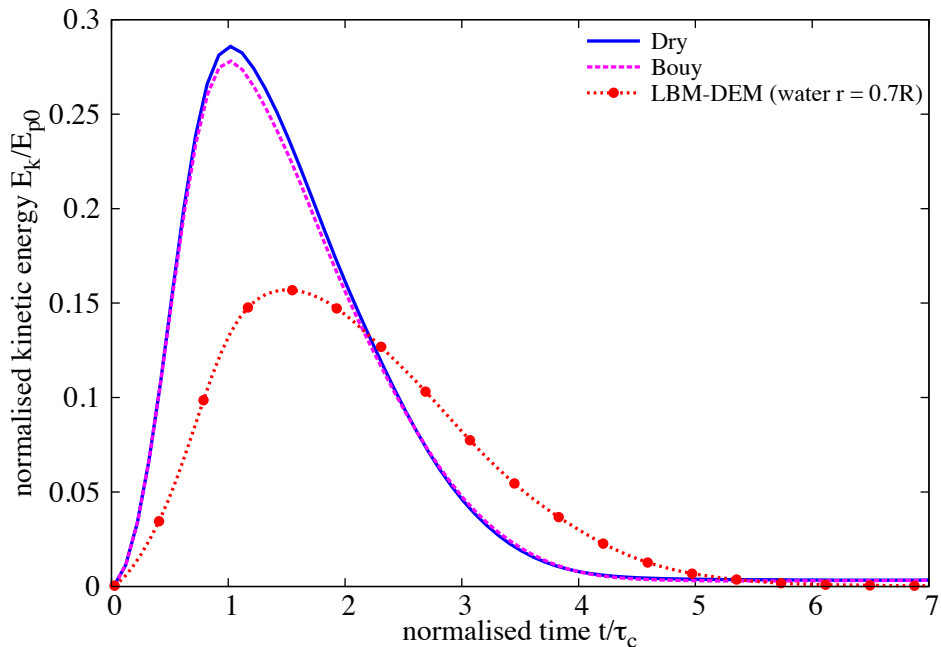
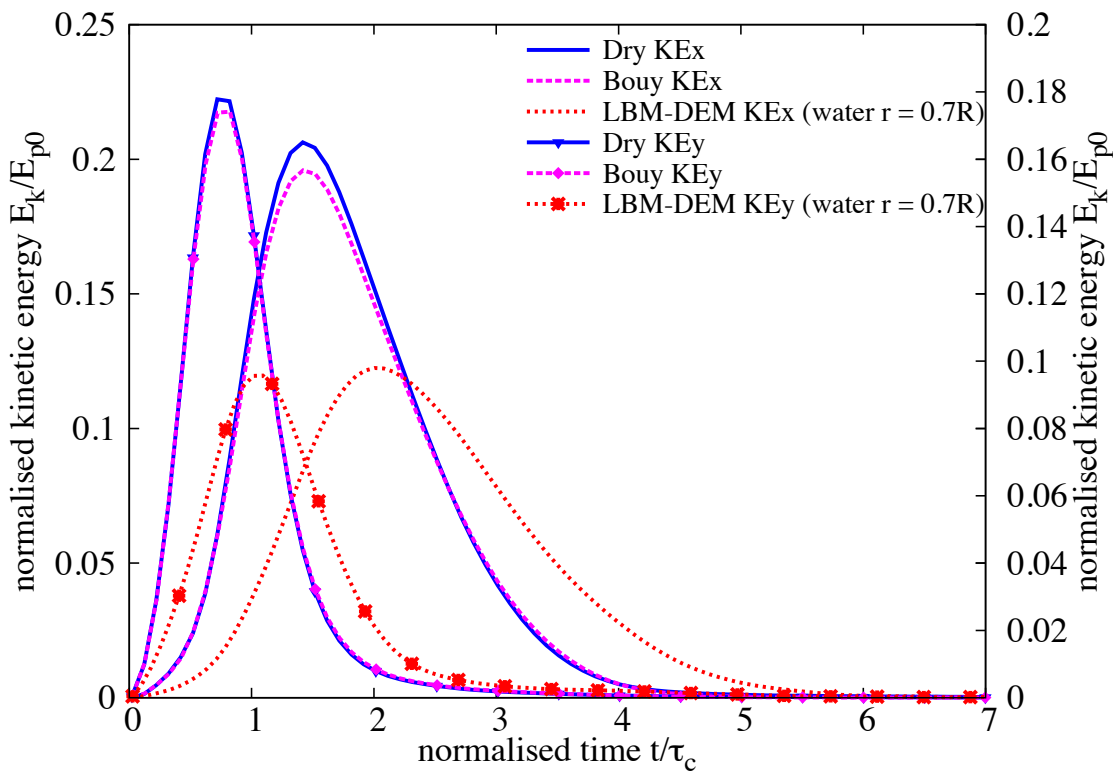


Figure 5.13 Evolution of the potential energy with time for a granular column collapse in fluid ( $a = 4$ )

$$\frac{L_f - L_0}{L_0} \propto \begin{cases} a, & a \lesssim 2.7 \\ a^{2/3}, & a \gtrsim 2.7 \end{cases} \quad (5.5)$$

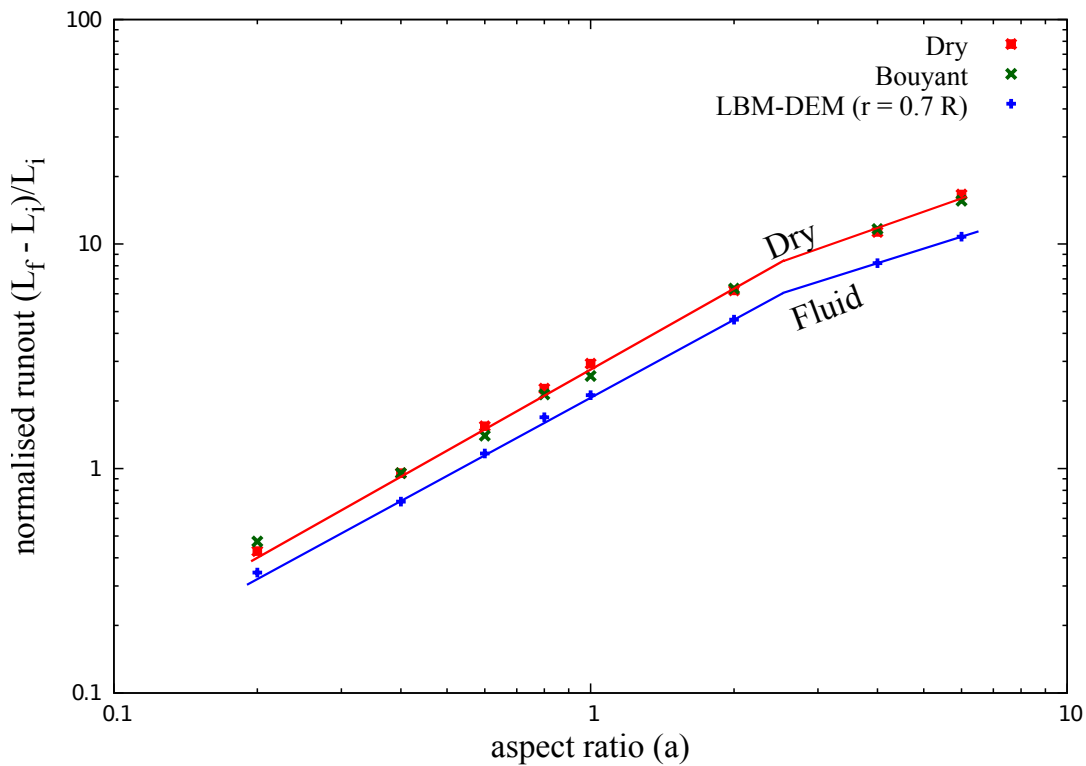


(a) Evolution of the total kinetic energy

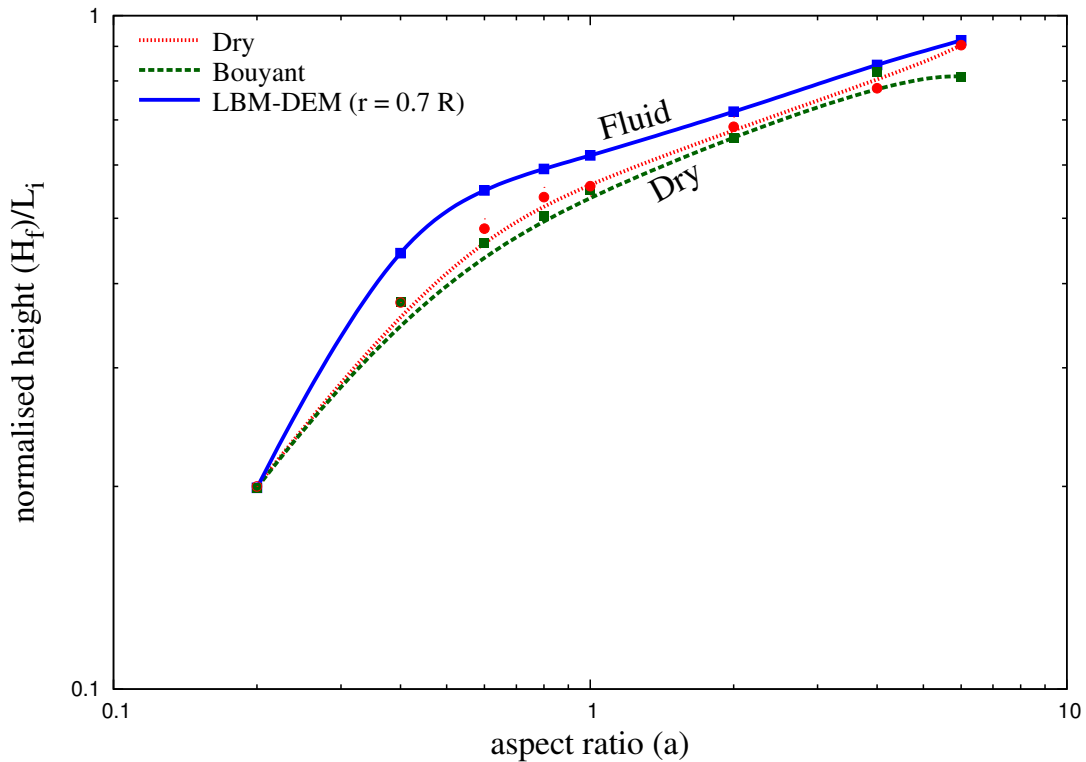


(b) Evolution of horizontal and vertical kinetic energies

Figure 5.14 Evolution of kinetic energies with time for a granular column collapse in fluid ( $a = 4$ )



(a) Normalised final run-out distance for columns with different initial aspect ratios. Comparison of dry and submerged granular column collapse.



(b) Normalised final collapse height for columns with different initial aspect ratios. Comparison of dry and submerged granular column collapse.

Figure 5.15 Normalised final collapse run-out and height for columns with different initial aspect ratios.

### <sup>8</sup> 5.3.3 Effect of permeability

<sup>9</sup> Topin et al. (2011) observed development of large negative pore pressure during dispersion  
<sup>10</sup> of grains. The rate of dissipation of the negative pore pressure is directly proportional to  
<sup>11</sup> the permeability of the granular assembly. In the previous section, the evolution of run-out  
<sup>12</sup> with the initial aspect ratio is studied using a constant hydrodynamic radius  $r = 0.7 R$ . In  
<sup>13</sup> order to understand the effect of permeability on the run-out behaviour, the hydrodynamic  
<sup>14</sup> radius  $r$  is varied from  $0.7 R$  through  $0.95 R$ . Increase in hydrodynamic radius decreases the  
<sup>15</sup> permeability of the granular assembly resulting in longer duration for the dissipation of negative  
<sup>16</sup> pore pressure.

<sup>17</sup> The normalise run-out for different hydrodynamic radius for a granular column collapse  
<sup>18</sup> with an initial aspect ratio of 0.8 is presented in figure 5.16. The run-out increases with decrease  
<sup>19</sup> in the permeability, which is equivalent to increase in the hydrodynamic radius. An increase  
<sup>20</sup> in the hydrodynamic radius from  $0.7$  to  $0.95 R$ , increases the normalised run-out by 25%.  
<sup>21</sup> However, even under very low permeable condition ( $r = 0.95 R$ ), the run-out observed in fluid  
<sup>22</sup> is shorter than the dry and the buoyant conditions.

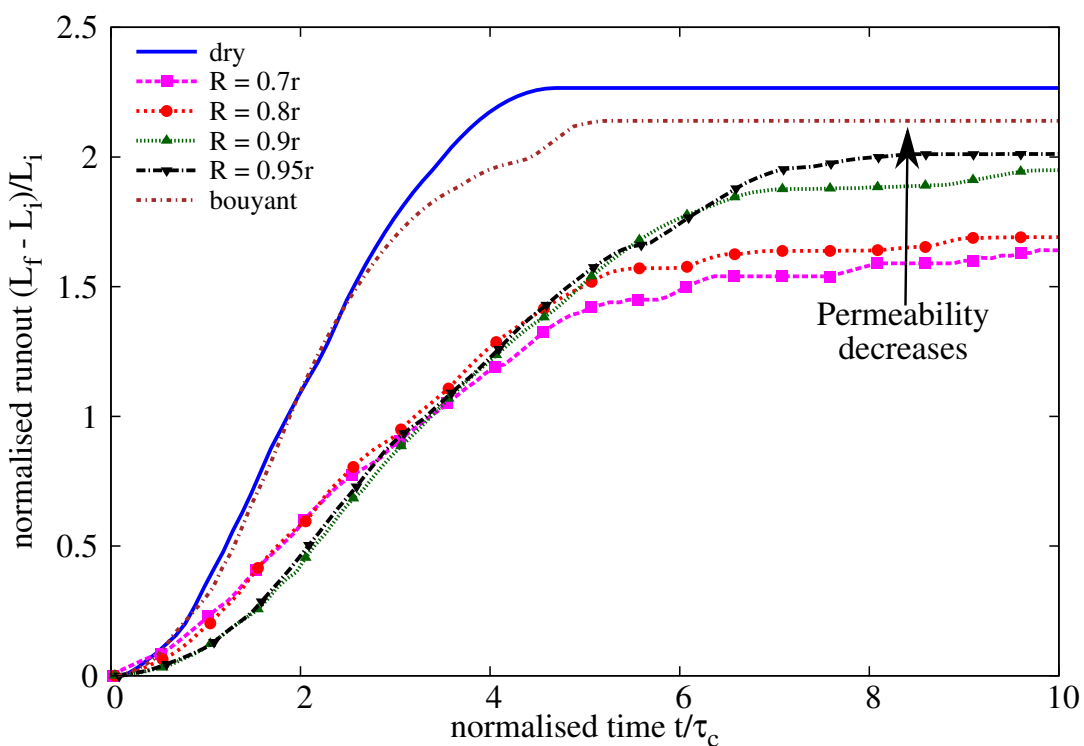


Figure 5.16 Effect of permeability on the evolution of run-out for a column collapse in fluid ( $a = 0.8$ )

<sup>23</sup> At high permeability ( $r = 0.7 R$ ), the evolution of run-out at the initial stage is quicker,  
<sup>24</sup> which means that the negative pore-pressure that is developed during the shearing along the

fracture surface is dissipated faster. Even though the negative pore-pressure is dissipate, due to the development of negative pore-pressure the evolution of run-out in fluid is slower than its dry counterpart. The rate of dissipation decreases with decrease in the permeability. This can be observed by a flatter slope in the run-out evolution with decrease in permeability. figure 5.17 shows the distribution of pore-pressure in high and low permeable granular media. At the same time  $t = \tau_c$ , the high permeable ( $r = 0.7 R$ ) shows smaller negative pore-pressure in comparison to large negative pore-pressures observed in the shearing zone for low permeable column ( $r = 0.9 R$ ). This shows that not only does it take longer time for the pore-pressure to dissipate with decrease in permeability, the negative pore-pressure developed in the low permeable condition is almost twice that of high permeable case (see figure 5.17b).

Although low permeable granular columns take longer duration for the run-out to evolve, the final run-out distance is found to be much longer than high permeable condition. figure 5.18 shows that the potential energy available for the flow for low permeable column is 20% smaller than the collapse of high permeable granular column. The kinetic energy evolution (see figure 5.19) shows that the low permeable column has a wider peak kinetic energy distribution in comparison to a sharp peak observed in high permeable condition. This indicates the influence of lubrication, i.e., hydroplaning of the granular flow in low permeable conditions. The evolution of horizontal kinetic energy reveals that the peak kinetic energy is sustained longer as the permeability of the granular material decreases (see figure 5.19b). Although, the peak kinetic energy is smaller in the low permeability case, the hydroplaning of the flowing granular mass results in longer run-out distance. A high positive pore-pressure is observed at the base of the granular flow in low permeability condition (figure 5.20b) indicating the occurrence of hydroplaning. The evolution of local packing density shows a drop in the packing density at low permeability (see figure 5.21). The drop in the value of packing density between  $t = 2\tau_c$  and  $t = 3\tau_c$  corroborates with the duration of hydroplaning during which large amount of water is entrained at the flow front.

High permeable column shows lower water entrainment, which indicates that at highly permeable flows the drag force acting on the soil grains predominates over the lubrication effect. In both low permeable and high permeable granular flows, the granular material consolidates at the final stage of the flow. This can be observed as the packing density increases at the final stage due to grains settling and expulsion of entrained water. The final deposit profile for both low and high permeability condition is shown in figure 5.22. High permeable collapse show a more parabolic (convex) deposit profile in contrast to the more concave profile observed in low permeability condition. The observation of hydroplaning in low permeable condition may be due to the distribution of the granular mass at the flow front. Instigation of hydroplaning is controlled by the balance of gravity and inertia forces at the debris front and is suitably

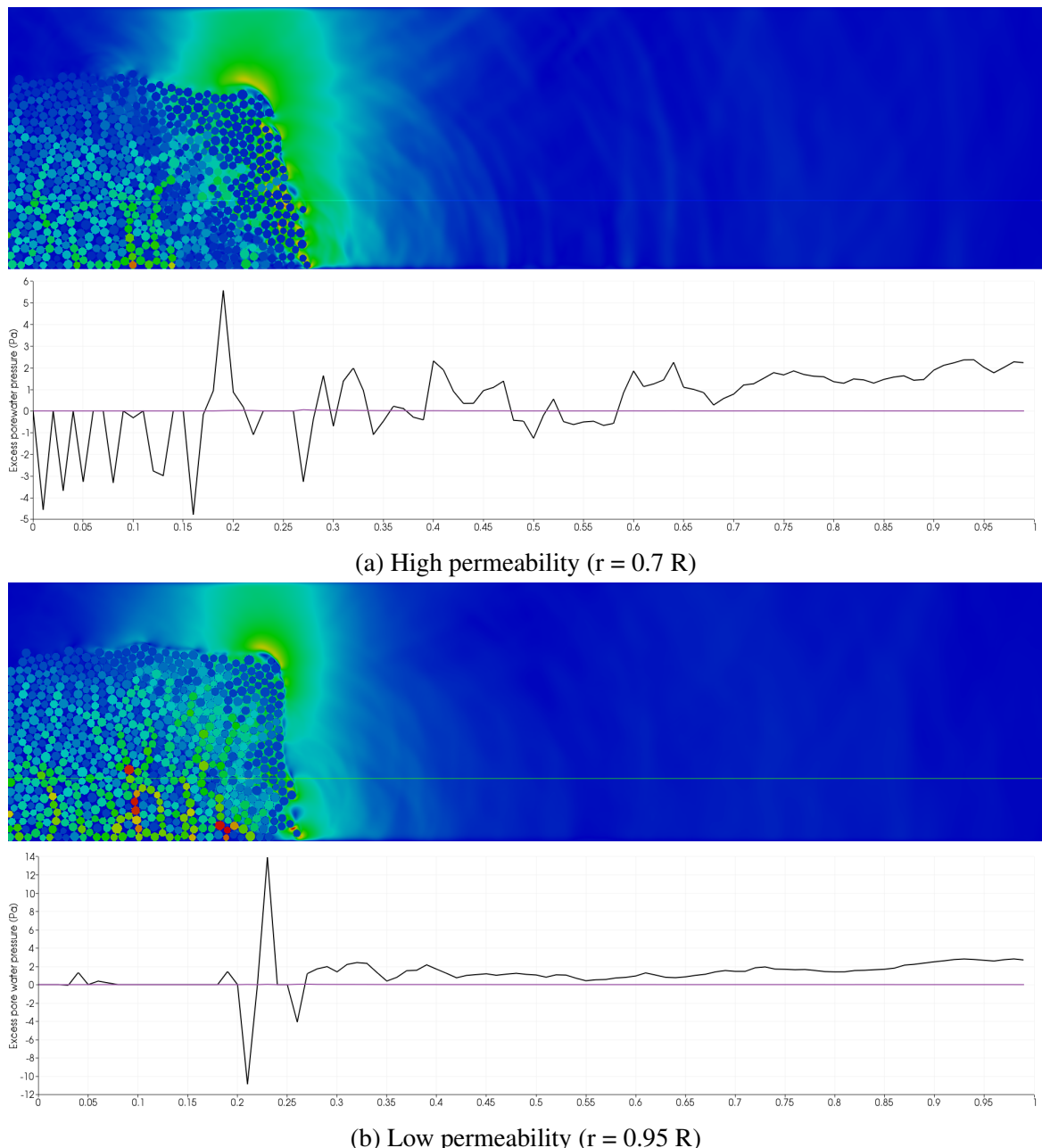


Figure 5.17 Effect of permeability on the excess pore water pressure distribution for a granular column collapse in fluid ( $a = 0.8$  & dense packing) at  $t = \tau_c$

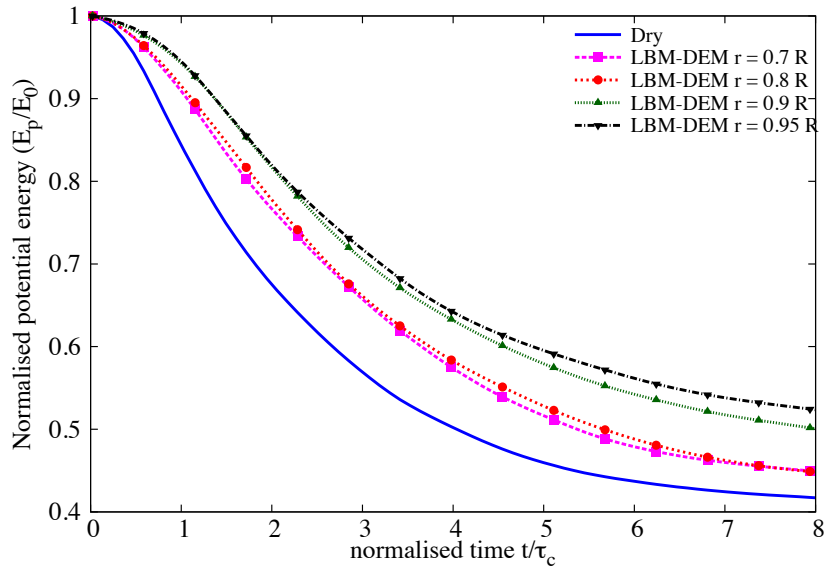


Figure 5.18 Effect of permeability on the evolution of the potential energy with time for a granular column collapse in fluid ( $a = 0.8$ )

<sup>8</sup> characterized by the densimetric Froude's number:

$$\text{Fr}_d = \frac{U}{\sqrt{(\frac{\rho_d}{\rho_w} - 1)gH \cos \theta}} \quad (5.6)$$

<sup>10</sup> where  $U$  is the average velocity of sliding mass,  $\rho_p$  and  $\rho_w$  are the densities of soil and water,  
<sup>11</sup> respectively,  $H$  is the thickness of the sliding mass,  $g$  is acceleration due to gravity and  $\theta$   
<sup>12</sup> represents the slope angle. Harbitz (2003); Mohrig and Ellis (1998) observed hydroplaning  
<sup>13</sup> above a critical value of densimetric Froude's number of 0.4. A  $\text{Fr}_d$  value of 0.427 is observed  
<sup>1</sup> for low permeable flow ( $r = 0.95 R$ ), which indicates the occurrence of hydroplaning. Where as  
<sup>2</sup> a  $\text{Fr}_d = 0.273$  is observed for high permeable granular flow indicating absence of hydroplaning,  
<sup>3</sup> the low permeable collapse is predominated by the viscous drag force resulting in a parabolic  
<sup>4</sup> profile and shorter run-out distance.

<sup>5</sup> The normalised final run-out distance as a function of the initial aspect ratio of the column  
<sup>6</sup> is presented in figure 5.23. For all aspect ratios, the dry condition yields the longest run-out  
<sup>7</sup> distance. For a given aspect ratio, the dry collapse acquires the highest kinetic energy due to  
<sup>8</sup> the lack of fluid dissipation during vertical collapse. This extra kinetic energy is high enough  
<sup>9</sup> to propel the heap, in-spite of a high frictional dissipation, over a distance that is longer than  
<sup>10</sup> the run-out distance in the fluid regime. In submerged condition, for the same aspect ratio, the  
<sup>11</sup> kinetic energy available for spreading is lower and the dissipation due to viscous drag is higher,  
<sup>12</sup> thus leading to a much shorter run-out distance.

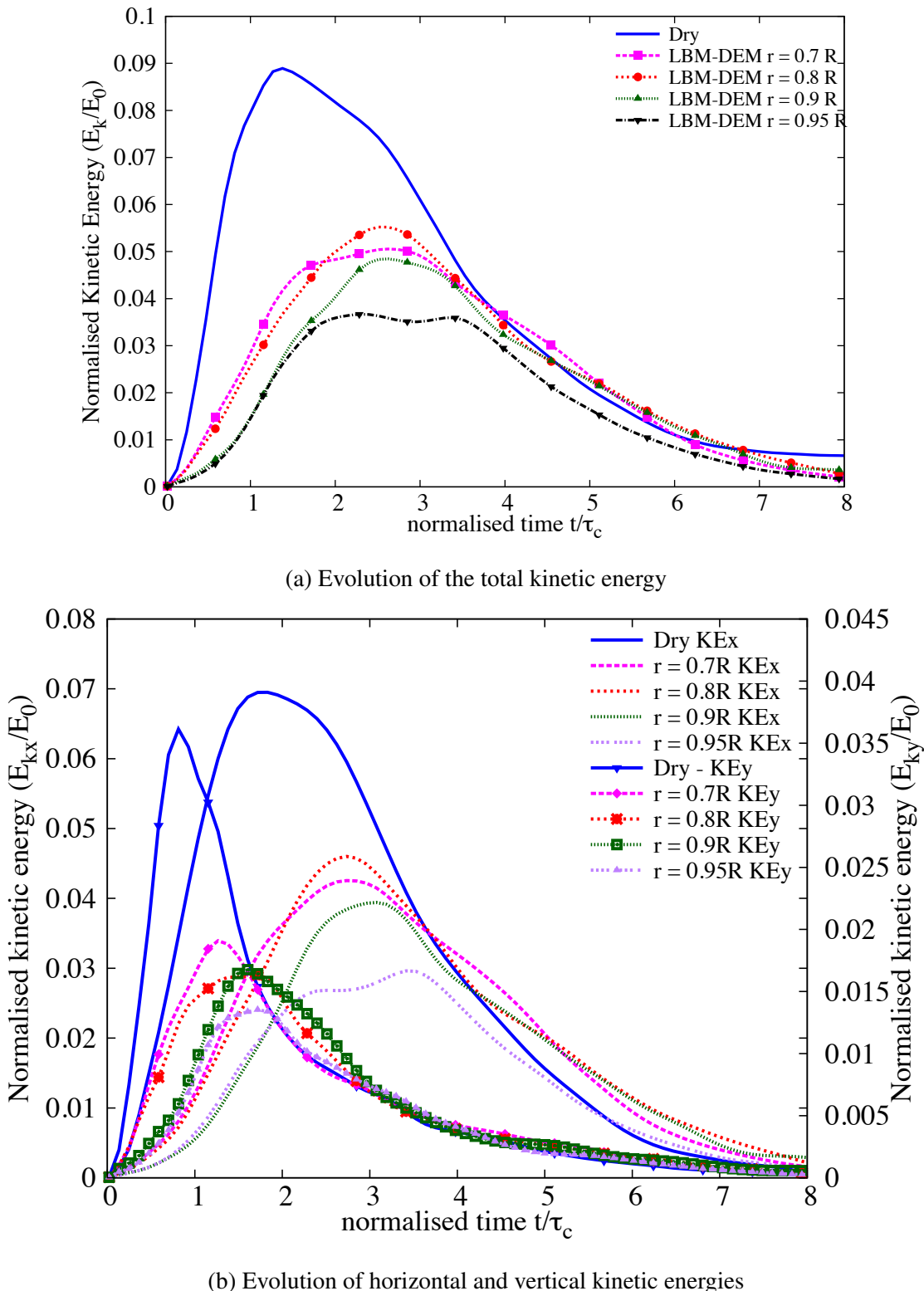


Figure 5.19 Effect of permeability on the evolution of kinetic energies with time for a granular column collapse in fluid ( $a = 0.8$ )

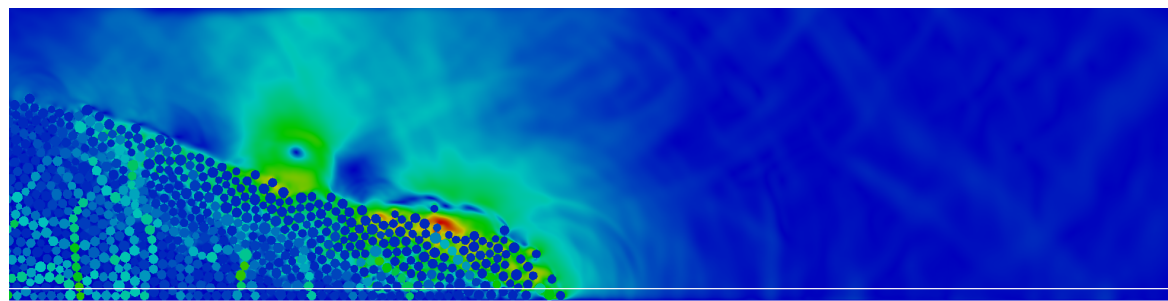
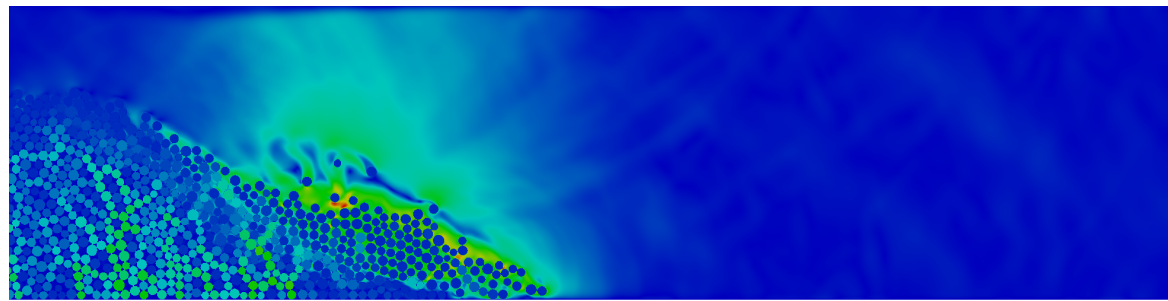
(a) High permeability ( $r = 0.7 R$ )(b) Low permeability ( $r = 0.95 R$ )

Figure 5.20 Effect of permeability on the excess pore water pressure distribution for a granular column collapse in fluid ( $a = 0.8$  & dense packing) at  $t = 2\tau_c$

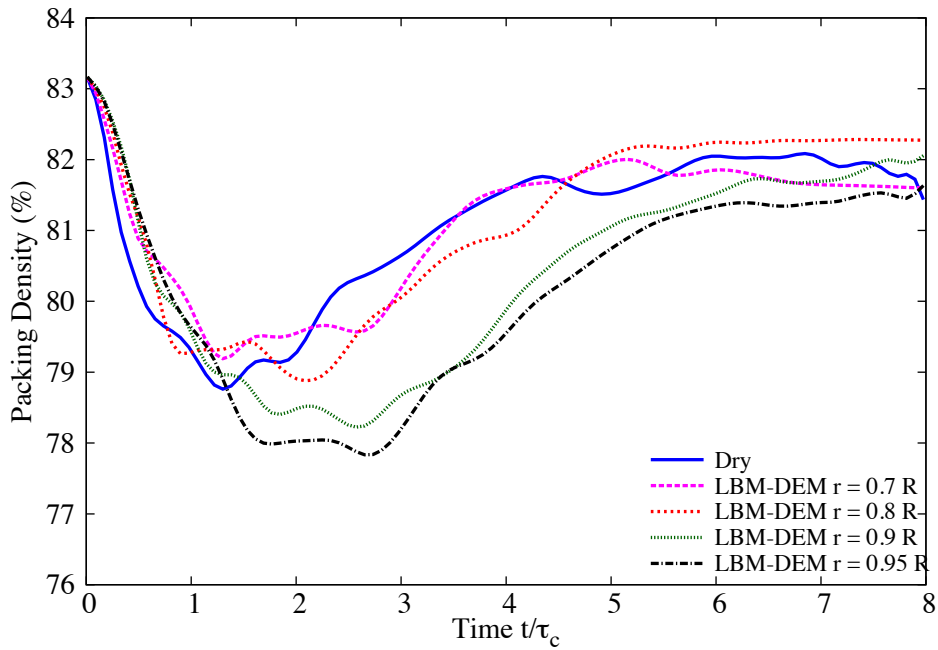
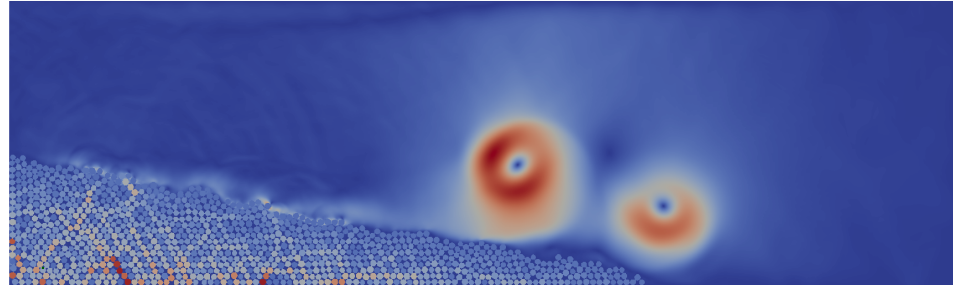
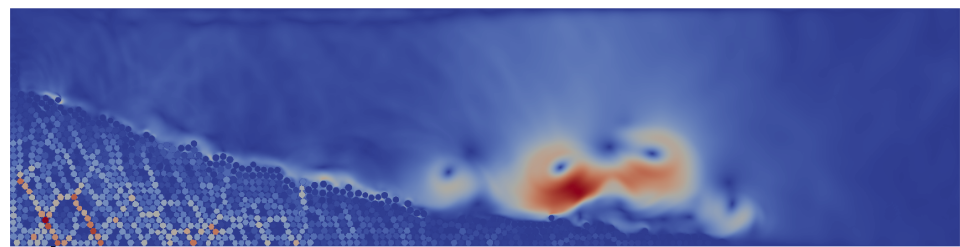


Figure 5.21 Effect of permeability on the evolution of packing density for a granular column collapse in fluid ( $a = 0.8$  & dense initial packing)



(a) High permeability ( $r = 0.7 R$ )



(b) Low permeability ( $r = 0.95 R$ )

Figure 5.22 Effect of permeability on the deposit morphology of a granular column collapse in fluid ( $a = 0.8$ )

For short columns, with decrease in permeability the run-out distance increases, however, the run-out distance is not higher than the dry condition. At higher aspect ratios, decrease in permeability from  $r = 0.8 R$  to  $r = 0.9 R$  does not have a significant influence on the run-out behaviour. This can be attributed to the turbulent nature of the granular flows for tall columns. The run-out behaviour is a result of transformation of (part of) the initial potential energy to the peak kinetic energy, which in turn controls the subsequent run-out along the plane. The run-out distance is plotted as a function of the normalised peak kinetic energy in figure 5.24. For the same aspect ratio, the peak kinetic energy is higher in the case of dry column. This represents grain inertial regime in dry granular collapse, which indicates that a part of the potential energy, in the presence of the fluid, is dissipated during the vertical collapse due to viscous friction. In all regimes, the run-out distance increases as a power law  $L_f \propto KE_{max}^\gamma$ . For the same value of peak kinetic energy, the run-out distance in fluid is longer than the dry column collapse. Also, with decrease in permeability the run-out distance increases for the same peak kinetic energy.

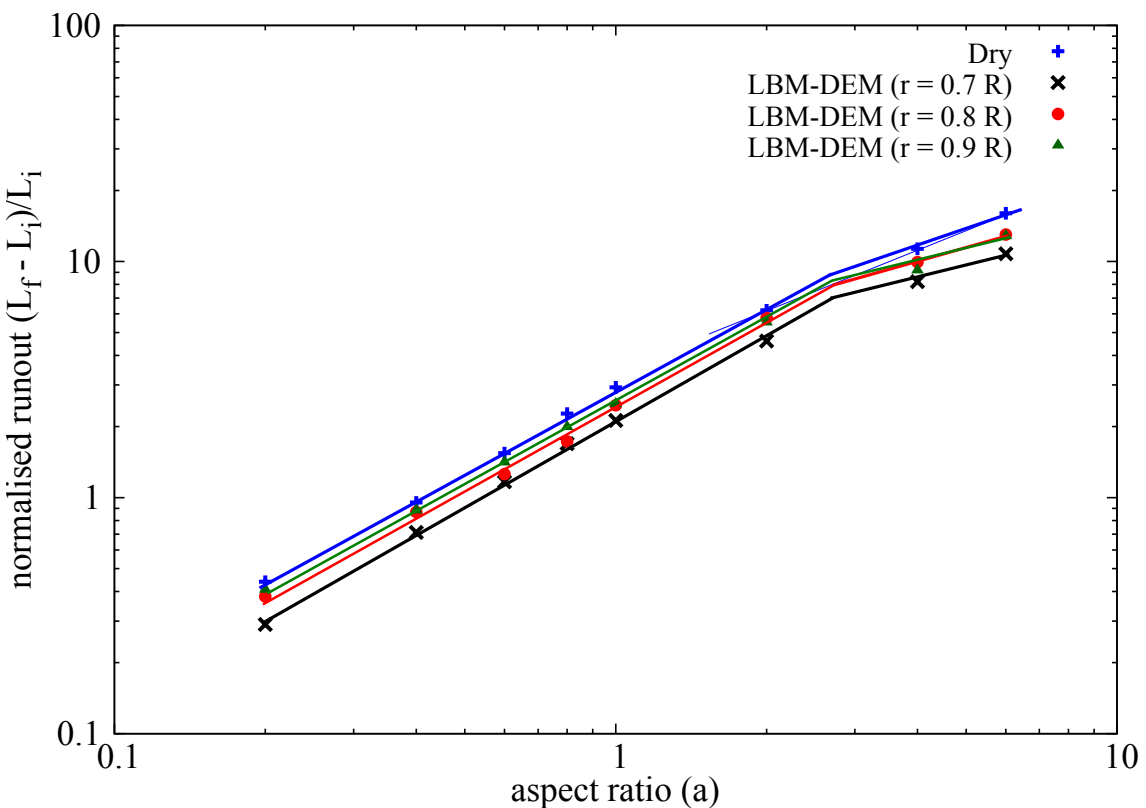


Figure 5.23 Normalised final run-out distance for columns with different initial aspect ratios. Comparison of dry and submerged granular column collapse for different hydrodynamic radius (0.7R, 0.8R and 0.9R).

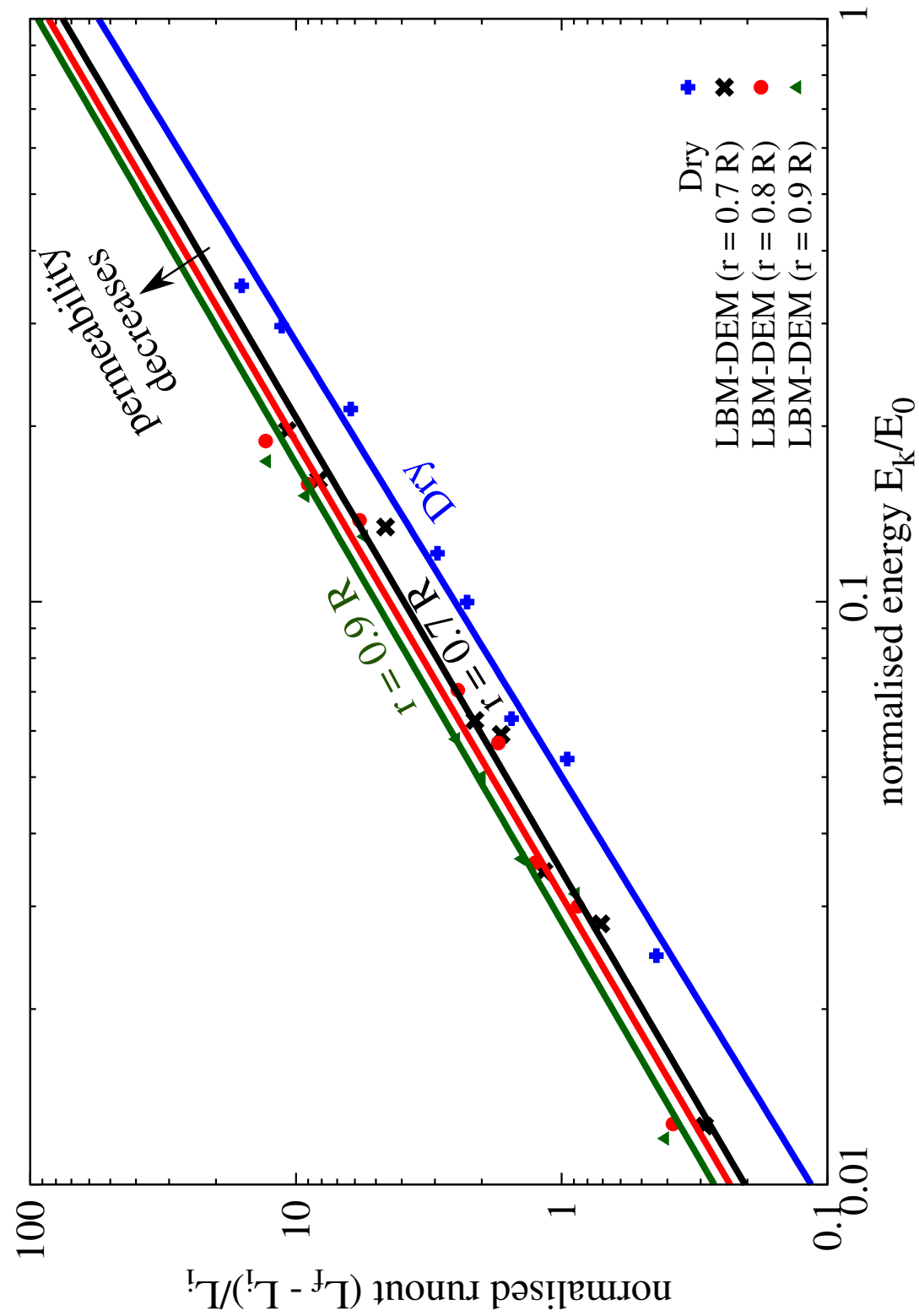


Figure 5.24 Normalised final run-out distance for columns as a function of peak kinetic energy. Comparison of dry and submerged granular column collapse for different hydrodynamic radius (0.7R, 0.8R and 0.9R).

### 26 5.3.4 Effect of initial packing density

27 Rondon et al. (2011) observed that the loose packings flow rapidly on a time scale proportional  
28 to the initial height and results in longer run-out distance in comparison to the dense packing.  
29 Hydroplaning occurs above a critical Froude's number of 0.4. The Froude's number is inversely  
30 related to the thickness of the flow and its density. Hence, for the same thickness of flow, a  
31 loose granular column will experience more hydroplaning than a dense granular flow. This  
32 effect might result in longer run-out behaviour in fluid than the dry condition for the same  
33 initial aspect ratio. The initial density and the permeability of a 2D granular column with an  
34 initial aspect ratio of 0.8 is varied to understand their influence on the run-out behaviour. The  
35 run-out behaviour of the dense case (83% packing density), discussed in the previous section,  
36 is compared with a loose granular column (79% packing fraction). The permeability is varied by  
changing the hydrodynamic radius from 0.7 R to 0.95 R.

1 The normalised run-out evolution with time for a loose initial packing (79% packing  
2 fraction) with different hydrodynamic radius 0.7 R, 0.8 R, 0.9 and 0.95 R. The run-out evolution  
3 of dry and a column with grains in suspension with an initial aspect ratio of 0.8 is also presented  
4 to understand the influence of hydrodynamic forces on the flow kinematics. Similar to dense  
5 granular column, the run-out distance increases with increase in the hydrodynamic radius  
6 (i.e., decrease in permeability). At low permeability ( $r = 0.9$  and  $0.95R$ ), the run-out distance  
7 is longer than the dry condition. This shows that the lubrication effect in low permeability  
8 condition overcomes the influence of the drag force and the development of large negative pore  
9 pressure resulting in longer run-out distance. Although suspended granular mass experience  
10 high drag force and turbulent effects, the run-out evolves almost at the same rate in comparison  
11 with granular columns with high permeability. This shows the effect of permeability on the  
12 dissipation rate of negative pore pressure developed during the initial stage of collapse.  
13

Figure 5.26 shows the development of negative pore pressure in low permeability ( $r = 0.95$   
14 R) and dissipation of negative pore pressure in high permeability ( $r = 0.7$  R) at the same time  
15  $t = \tau_c$ . This difference in the quantity and the rate of dissipation of negative pore pressure  
16 results in difference in the rate of flow evolution. Low permeable column takes longer duration  
17 for the flow to evolve. As the flow progresses, low permeability of the granular column  
2 causes hydroplaning to occur at the base of the column resulting in longer run-out distance  
3 (see figure 5.27).

4 The evolution of potential energy with time reveals that at very low permeability ( $r = 0.95$   
5 R), the initial potential energy mobilised is smaller than at  $r = 0.9R$ . Also with decrease in  
6 permeability, the time required to dissipate the negative pore pressure increases. This results in  
7 a shorter run-out distance in the case of  $r = 0.95$  R than  $r = 0.9$  R. As the amount of material  
8 destabilised is small, which results in a thinner flow having a high Froude's number. However,

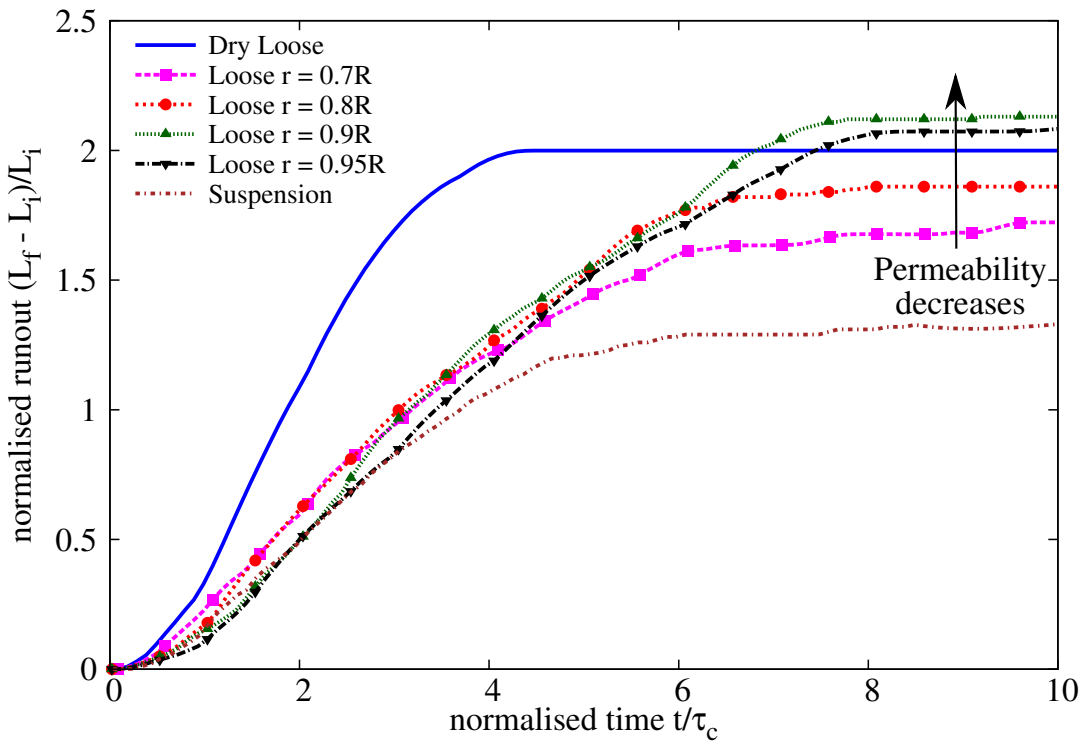


Figure 5.25 Effect of permeability on the evolution of run-out for a column collapse in fluid ( $a = 0.8$  & loose packing)

the peak horizontal kinetic velocity observed in the case of  $r = 0.9$  R is higher than  $r = 0.95$  R (see figure 5.30b). A Froude's number of 0.59 for  $r = 0.9$  R is observed in contrast to 0.46 for  $r = 0.94$  R. Both values of hydrodynamic radius result in a Froude's number that indicates occurrence of hydroplaning. The difference in the amount of material destabilised for  $r = 0.95$  R and the decreased effect of hydroplaning results in shorter run-out distance for  $r = 0.95$  R in comparison to  $r = 0.9$  R.

As the column collapses, water is entrained at the flow front. This can be observed by decrease in the packing fraction during  $t = 1\tau_c$  to  $t = 3\tau_c$ . As the flow progresses, the entrained water is expelled and the soil grains consolidate to reach a critical packing density at the end of the flow (see figure 5.29). The permeability (hydrodynamic radius) plays a crucial role in the rate of dissipation of the entrained water. As the permeability decreases, the water entrained at the flow front takes longer time to be dissipated resulting in lubrication of the flow at low permeability. This lubrication effect results in increased run-out for columns with low permeability.

The evolution grain trajectories with time is presented in figure 5.31 for low permeability ( $r = 0.95$  R) and ( $r = 0.9$  R). It can be observed that the column with high permeability shows a more parabolic (convex) final profile in contrast to the more concave profile observed in low permeability condition. This difference in the flow thickness results in higher value of

(a) High permeability ( $r = 0.7 R$ )(b) Low permeability ( $r = 0.95 R$ )

Figure 5.26 Effect of permeability on the excess pore water pressure distribution for a granular column collapse in fluid ( $a = 0.8$  & loose packing) at  $t = \tau_c$

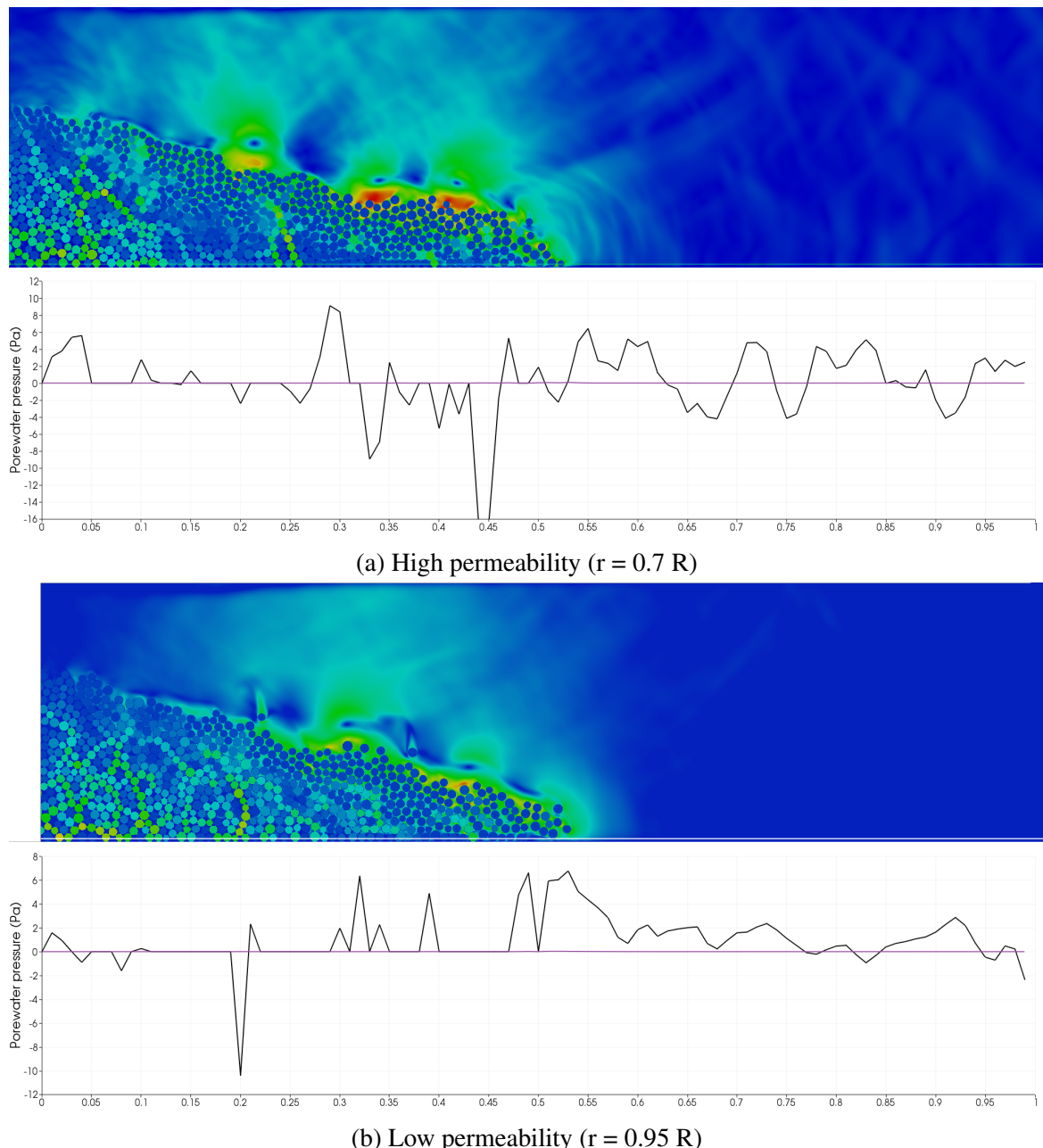


Figure 5.27 Effect of permeability on the excess pore water pressure distribution for a granular column collapse in fluid ( $a = 0.8$  & loose packing) at  $t = 2\tau_c$

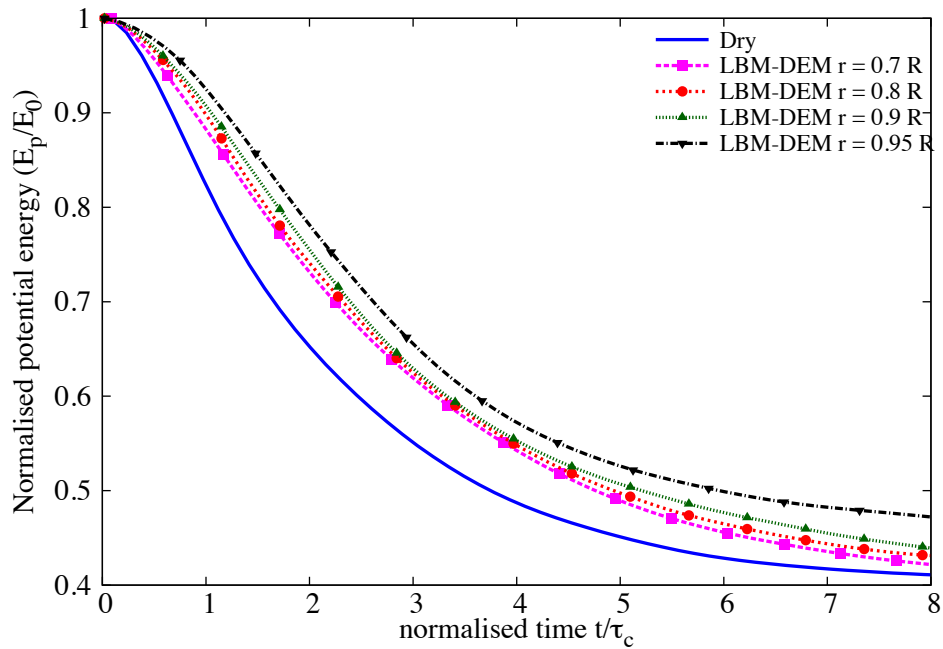


Figure 5.28 Effect of permeability on the evolution of the potential energy with time for a granular column collapse in fluid ( $a = 0.8$  & loose packing)

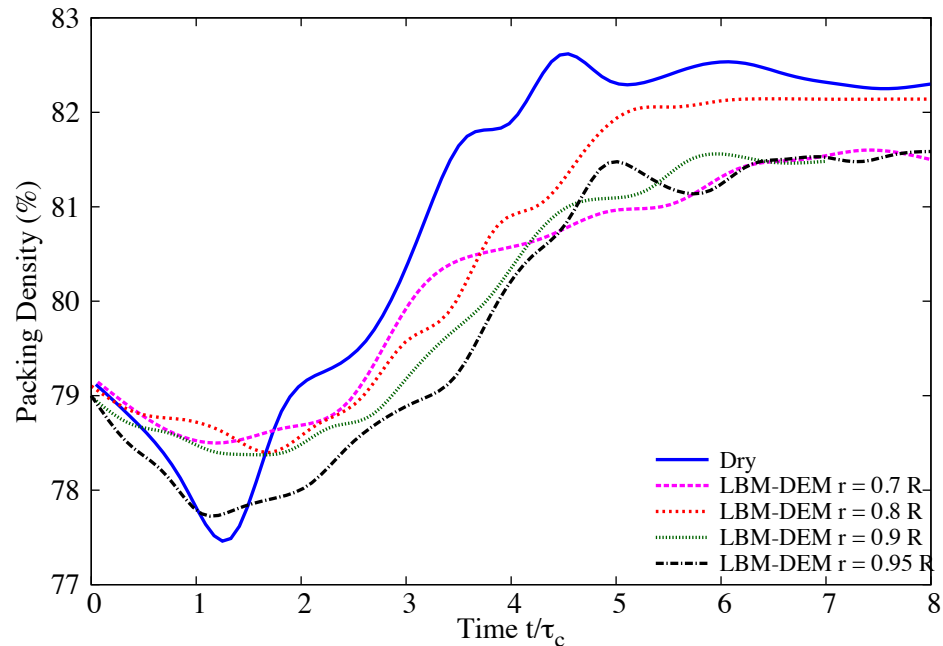
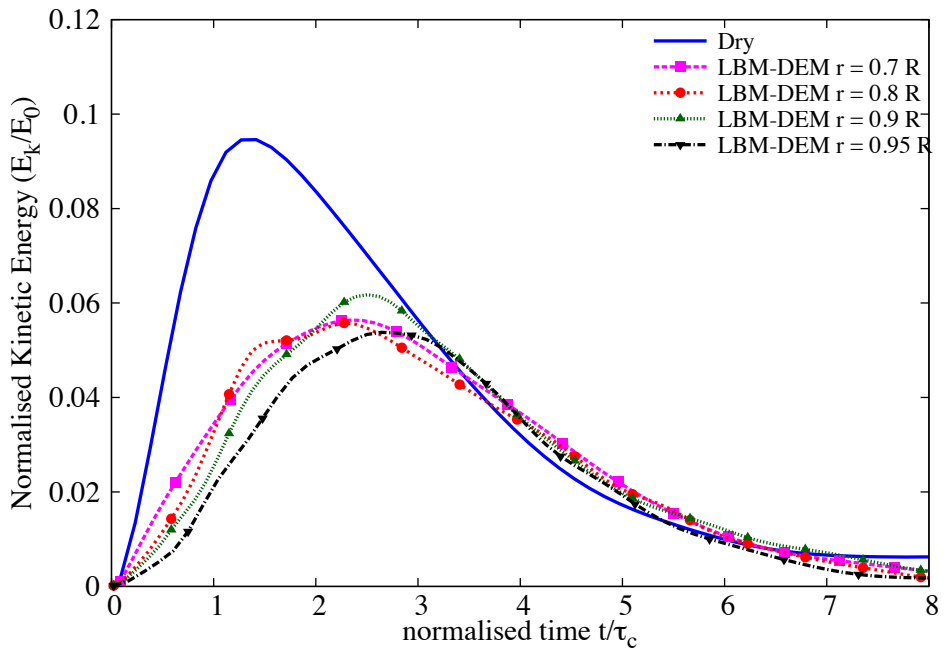
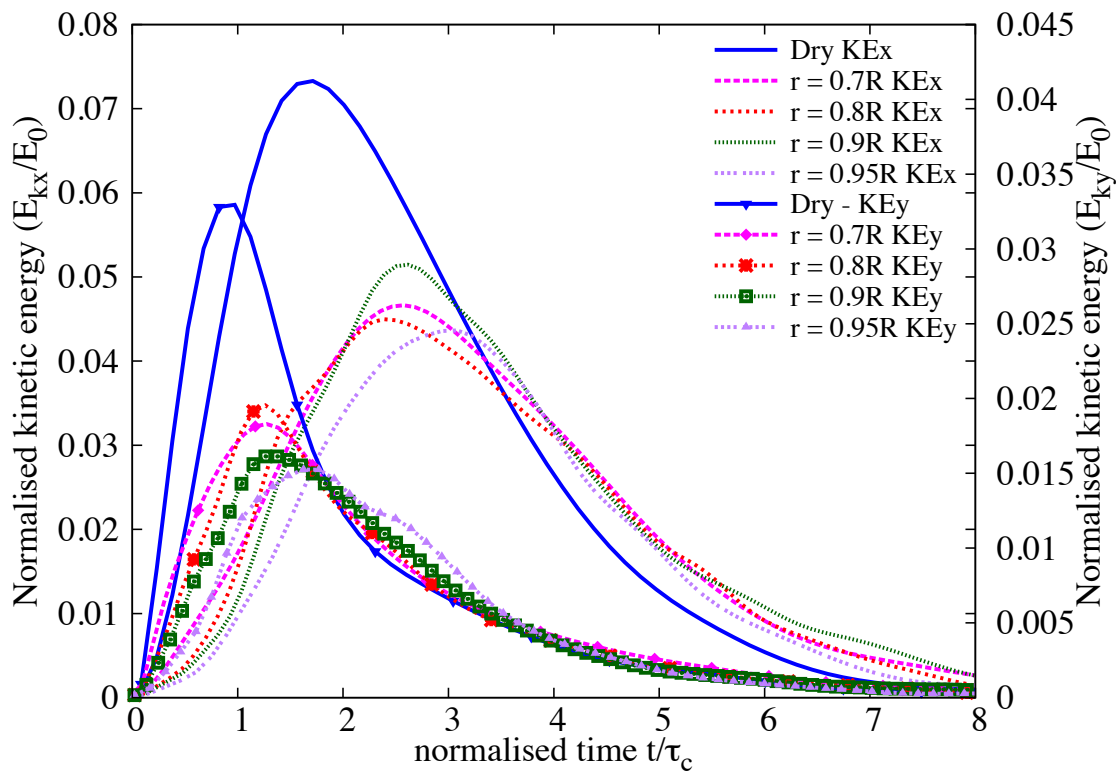


Figure 5.29 Effect of permeability on the evolution of packing density for a granular column collapse in fluid ( $a = 0.8$  & loose initial packing)



(a) Evolution of the total kinetic energy



(b) Evolution of horizontal and vertical kinetic energies

Figure 5.30 Effect of permeability on the evolution of kinetic energies with time for a granular column collapse in fluid ( $a = 0.8$  & loose packing)

26 Froude's number and the occurrence of hydroplaning in low permeability condition. Due  
27 to high permeability, the water entrained at the flow front is dissipated quicker and thus no  
28 lubrication effect is observed. A Froude's number of 0.272 (no hydroplaning) is observed  
29 for high permeability condition ( $r = 0.7 R$ ). This shows that the drag force predominates at  
1 high permeability, while the low permeability condition is characterised by hydroplaning and  
2 lubrication.

3 Figure 5.32 shows the normalised pressure at the base for low and high permeability  
4 flows at  $t = 2\tau_c$ . The normalised effective stress plotted is obtained as the average over 5  
5 time steps at  $2\tau_c$ . The effective stress at the base is normalised to the effective stress of a  
6 static granular column before collapse. A value of 1 indicates that the effective stress hasn't  
7 changed, which is observed in the static region of the granular column. It can be observed that  
8 the normalised effective stress is significantly high for low permeability condition at the flow  
9 front in comparison to almost non-existence of effective stress in low permeability condition.  
10 The observation of trivial effective stress at the flow front corroborates the lubrication effect  
11 observed at low permeability conditions.

12 Figure 5.33 shows the grain trajectories of a dense and a loose initial packing for a hydro-  
13 dynamic radius ( $r = 0.95R$ ). It can be observed that the dense initial packing results in a lot of  
14 turbulent behaviour at the flow surface in contrast to the more plug like flow observed in the  
15 loose condition. The thickness of the deposit in both dense and loose condition is almost the  
16 same, however the density of the flow results in a Froude's number of 0.46 and 0.429 for loose  
17 and dense conditions, respectively. The low initial density results in more hydroplaning in the  
18 loose condition. The effect of water entrainment at the flow front between dense and loose  
19 condition can be seen in figure 5.34. Comparing the packing density (see figures 5.21 and 5.29)  
20 reveals almost the same amount of water entrainment in both dense and loose conditions.  
21 Hence, it is the density of the flowing granular mass that controls the influence of hydroplaning  
22 for a given hydrodynamic radius and initial aspect ratio. A loosely packed granular column  
23 with low permeability entrains more water at the flow front, resulting in a hydroplaning effect  
24 that overcomes the influence of viscous drag forces and thereby yields a higher run-out distance  
25 than the dry condition.

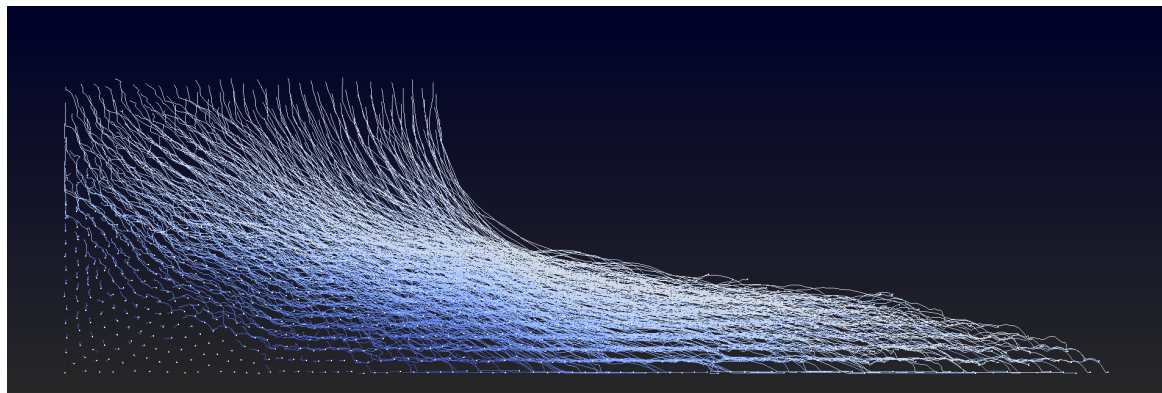
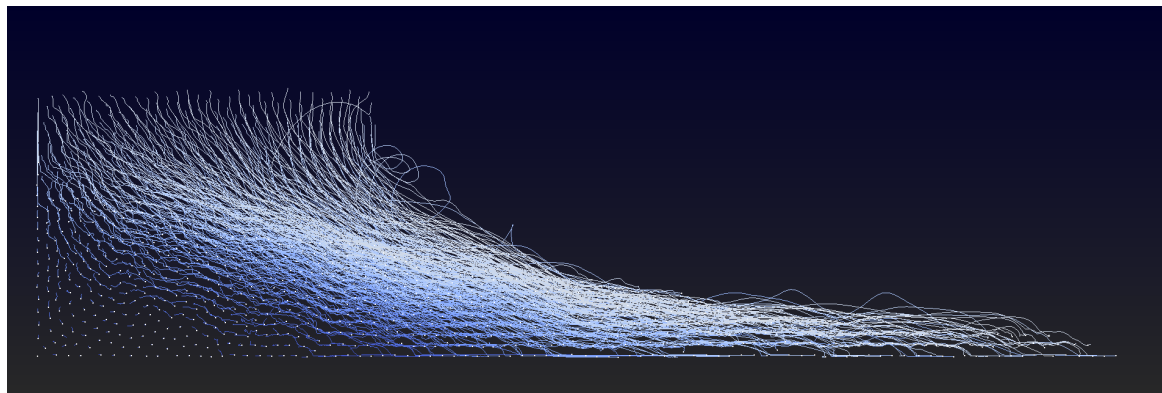
(a) High permeability ( $r = 0.7 R$ )(b) Low permeability ( $r = 0.95 R$ )

Figure 5.31 Particle tracking of the deposit morphology for a granular column collapse in fluid ( $a = 0.8$  & loose packing), influence of permeability

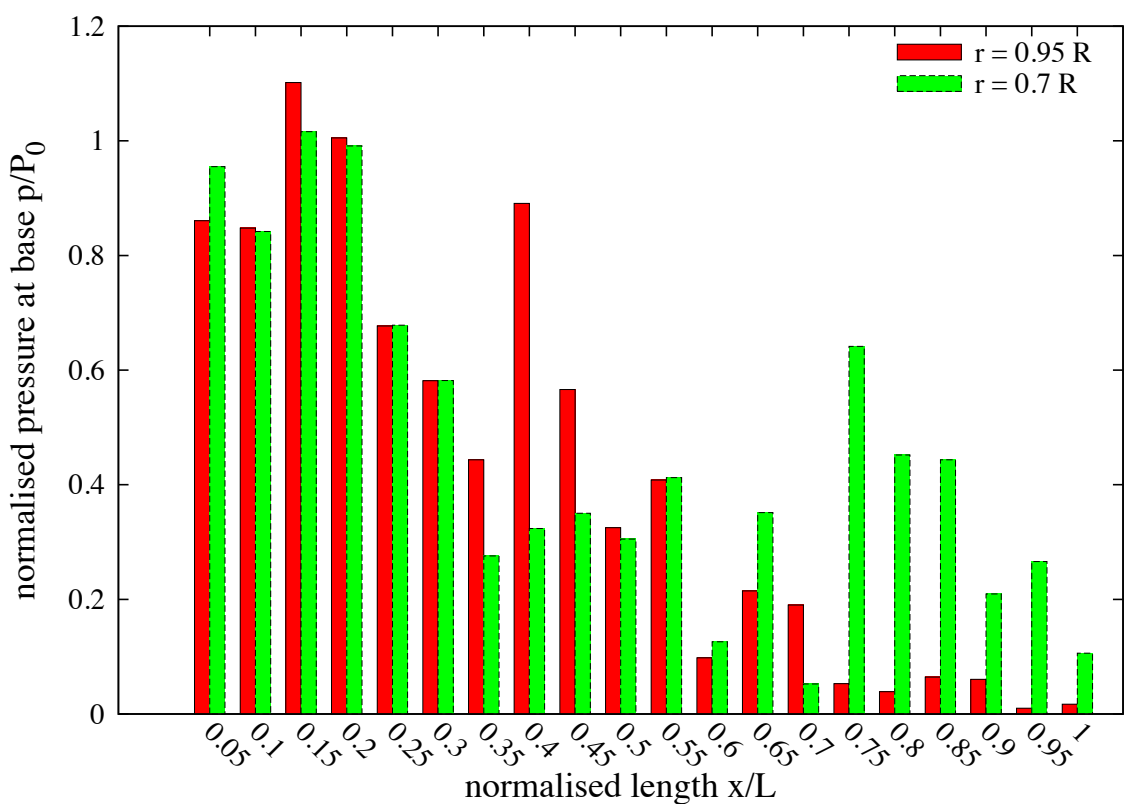
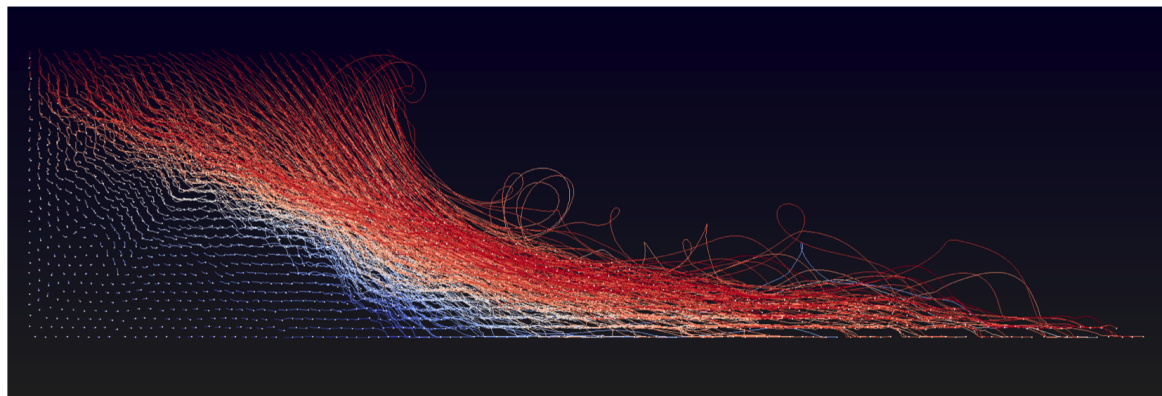
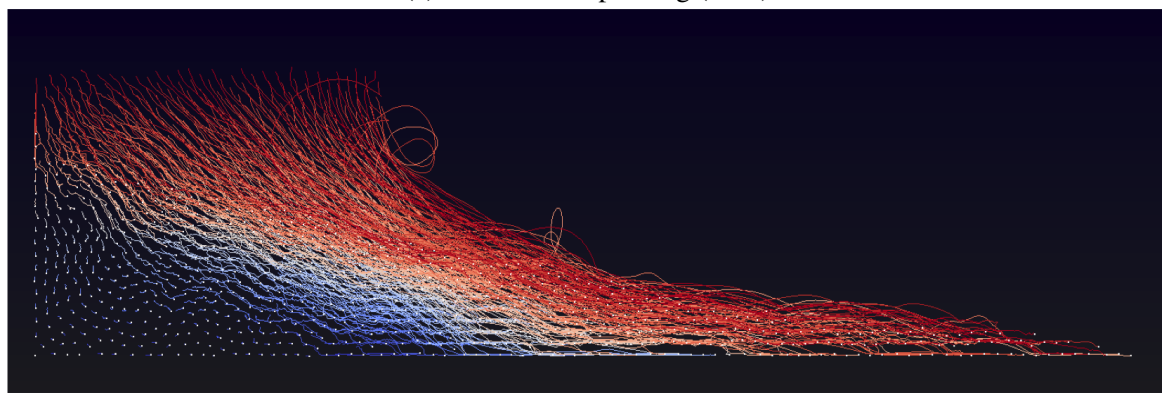


Figure 5.32 Effect of permeability on the normalised effective stress for loose initial packing at  $t = 2\tau_c$



(a) Dense initial packing (83%)

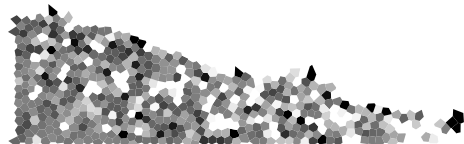


(b) Loose initial packing (79%)

Figure 5.33 Effect of initial density on the deposit morphology for a granular column collapse in fluid ( $\alpha = 0.8$ ). Dense vs loose initial packing fraction ( $r = 0.95R$ ). Darker means dense packing, white indicates loose packing density.



(a) Dense initial packing (83%)



(b) Loose initial packing (79%)

Figure 5.34 Evolution of packing fraction at  $t = \tau_c$  for dense and loose initial packing fraction.

## 26 5.4 Submarine granular flows down incline plane

27 Slope failure is a problem of high practical importance for both civil engineering structures and  
 28 natural hazards management. Catastrophic events as landslides, debris flows, rock avalanches  
 29 or reservoir embankment failures exemplify the potential consequences of a soil gravitational  
 30 instability. One of the most critical situation concerns a submerged sandy slope since pore pres-  
 31 sure changes, related to groundwater seepage flow or soil dilation/contraction, can significantly  
 32 affect the stability of many earth structures or natural soils.

33 In this study, a 2D poly-disperse system ( $d_{max}/d_{min} = 1.8$ ) of circular discs in fluid was  
 34 used to understand the behaviour of granular flows on inclined planes (see ??). The soil column  
 1 was modelled using 1000 discs of density  $2650 \text{ kg m}^{-3}$  and a contact friction angle of  $26^\circ$ .  
 2 The collapse of the column was simulated inside a fluid with a density of  $1000 \text{ kg m}^{-3}$  and a  
 3 kinematic viscosity of  $1 \times 10^{-6} \text{ m}^2 \text{ s}^{-1}$ . The choice of a 2D geometry has the advantage of  
 4 cheaper computational effort than a 3D case, making it feasible to simulate very large systems.  
 5 A granular column of aspect ratio ‘a’ of 0.8 was used. A hydrodynamic radius  $r = 0.9R$  was  
 6 adopted during the LBM computations. Dry analyses were also performed to study the effect  
 7 of hydrodynamic forces on the run-out distance.

### 8 5.4.1 Effect of initial density

9 The morphology of the granular deposits in fluid is shown to be mainly controlled by the initial  
 10 volume fraction of the granular mass and not by the aspect ratio of the column (Pailha et al.,  
 11 2008; Rondon et al., 2011). In order to understand the influence of the initial packing density  
 12 on the run-out behaviour, a dense sand column (initial packing density,  $\Phi = 83\%$ ) and a loose  
 13 sand column ( $\Phi = 79\%$ ) were used. The granular columns collapse and flow down slopes of  
 14 varying inclinations ( $2.5^\circ$ ,  $5^\circ$  and  $7.5^\circ$ ).

15 The evolution of run-out distances for a dense sand column with time in dry and submerged  
 conditions for varying slope inclinations are presented in figure 5.35. The run-out distance  
 1 is longer in submerged condition than the dry condition for a flow on a horizontal surface.  
 2 However, with increase in the slope angle the run-out in the fluid decreases.  
 3

4 Dense granular columns in fluid take a longer time to collapse and flow, due to the develop-  
 5 ment of large negative pore-pressure, as the dense granular material dilates during the initial  
 6 phase of the flow. The morphology of dense granular flows down slopes of varying inclinations  
 7 at the critical time ( $t = \tau_c = \sqrt{H/g}$ , when the flow is fully mobilised) are shown in figure 5.37.

8 It can be seen that the viscous drag on the dense column tend to predominate over the  
 9 influence of hydroplaning on the run-out behaviour. This influence can be observed in the  
 10 smaller peak kinetic energy for granular column in fluid compared to its dry counterpart

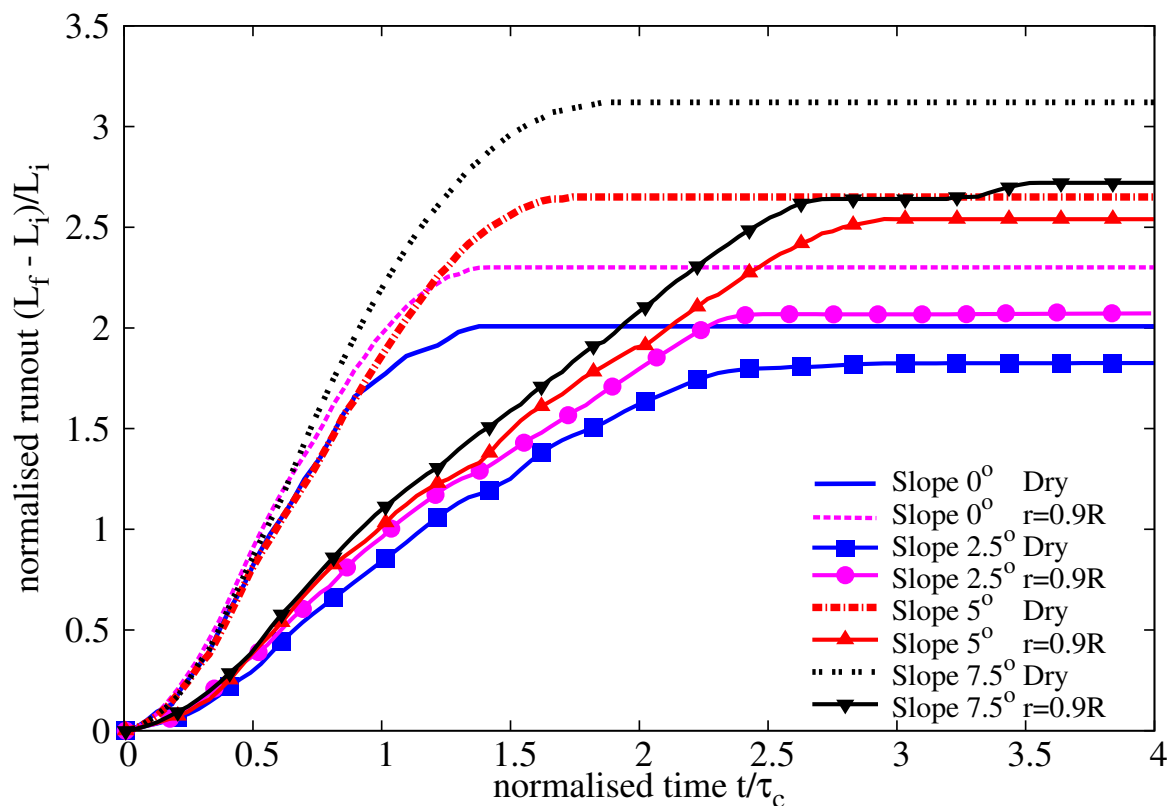


Figure 5.35 Evolution of run-out with time (dense)

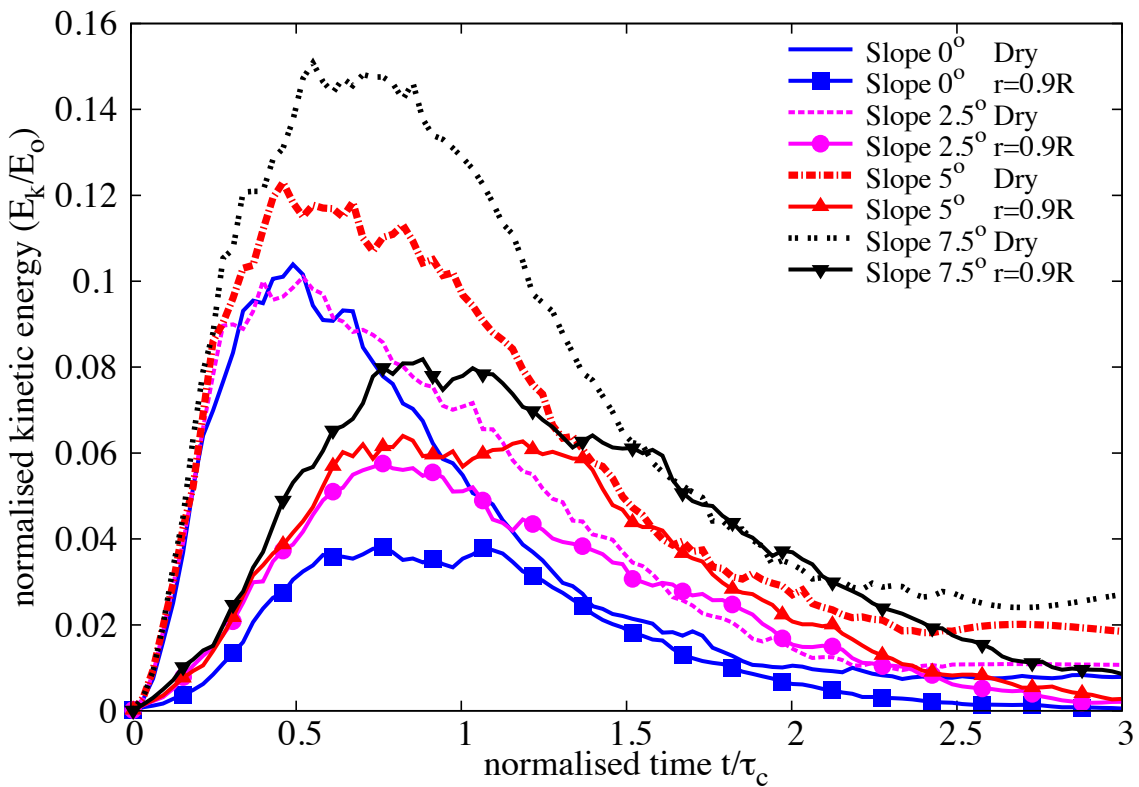
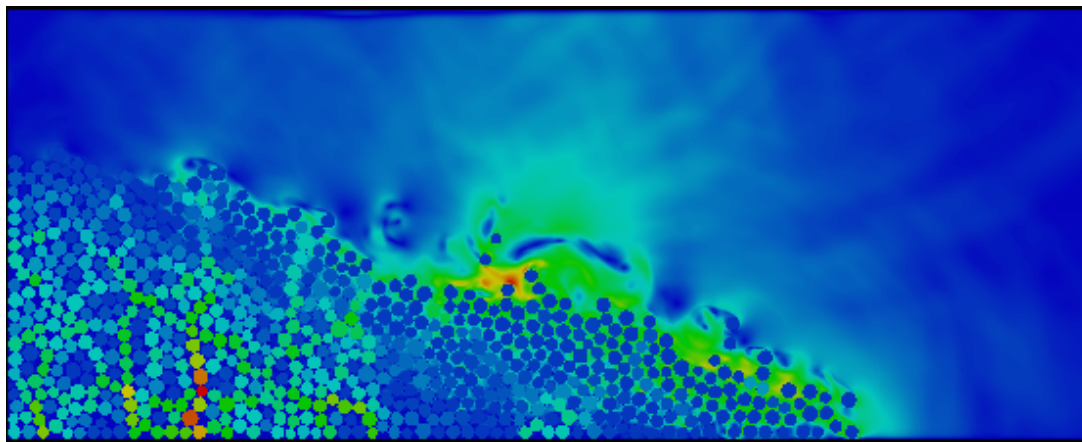


Figure 5.36 Evolution of Kinetic Energy with time (dense case)

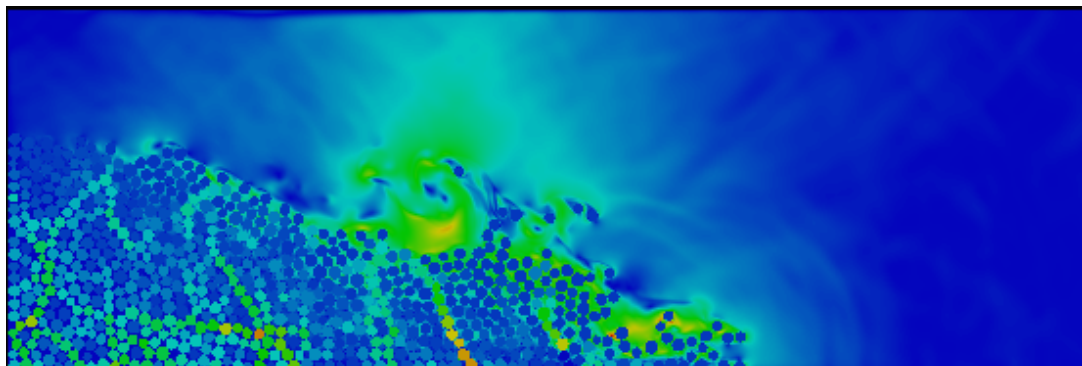
(see Figure 5.36). With increase in slope angle, the volume of material that dilates increases. This results in large negative pore pressures and more viscous drag on the granular material. Hence, the difference in the run-out between the dry and the submerged condition, for a dense granular assembly, increases with increase in the slope angle.

In contrast to the dense granular columns, the loose granular columns (relative density  $I_D = 30\%$ ) show longer run-out distance in immersed conditions (see Figure 5.38). The run-out distance in fluid increases with increase in the slope angle compared to the dry cases. Loose granular material tends to entrain more water at the base of the flow front, creating a lubricating surface, which causes longer run-out distance (see Figure 5.39). The hydroplaning effect causes an increase in the velocity the loose condition in comparison with the dense condition (see Figure 5.40).

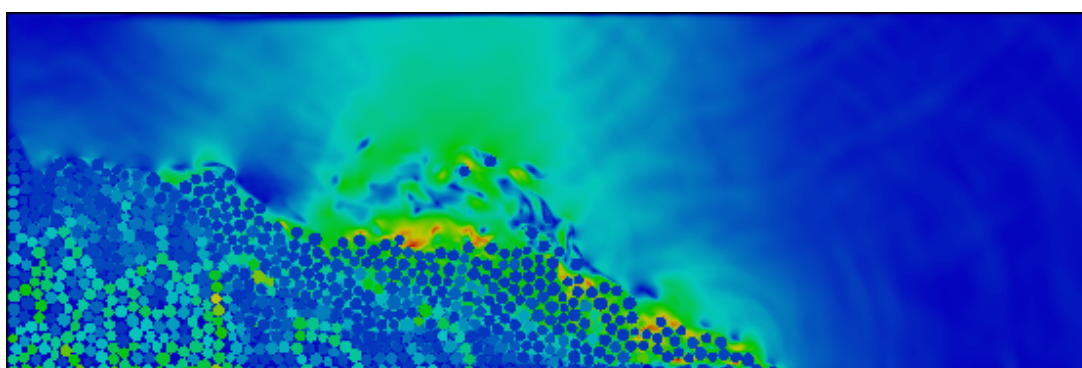
The evolution of packing density (see Figure 5.41) shows that dense and the loose conditions reach similar packing density. This indicates that the dense granular column dilates more and is susceptible to higher viscous drag forces. Where as in the loose condition, a positive pore-pressure is observed at the base of the flow, indicating entrainment of water at the base, i.e. hydroplaning resulting in longer run-out distance.



(a) Slope 2.5



(b) Slope 5.0



(c) Slope 7.5

Figure 5.37 Flow morphology at critical time for different slope angles (dense)

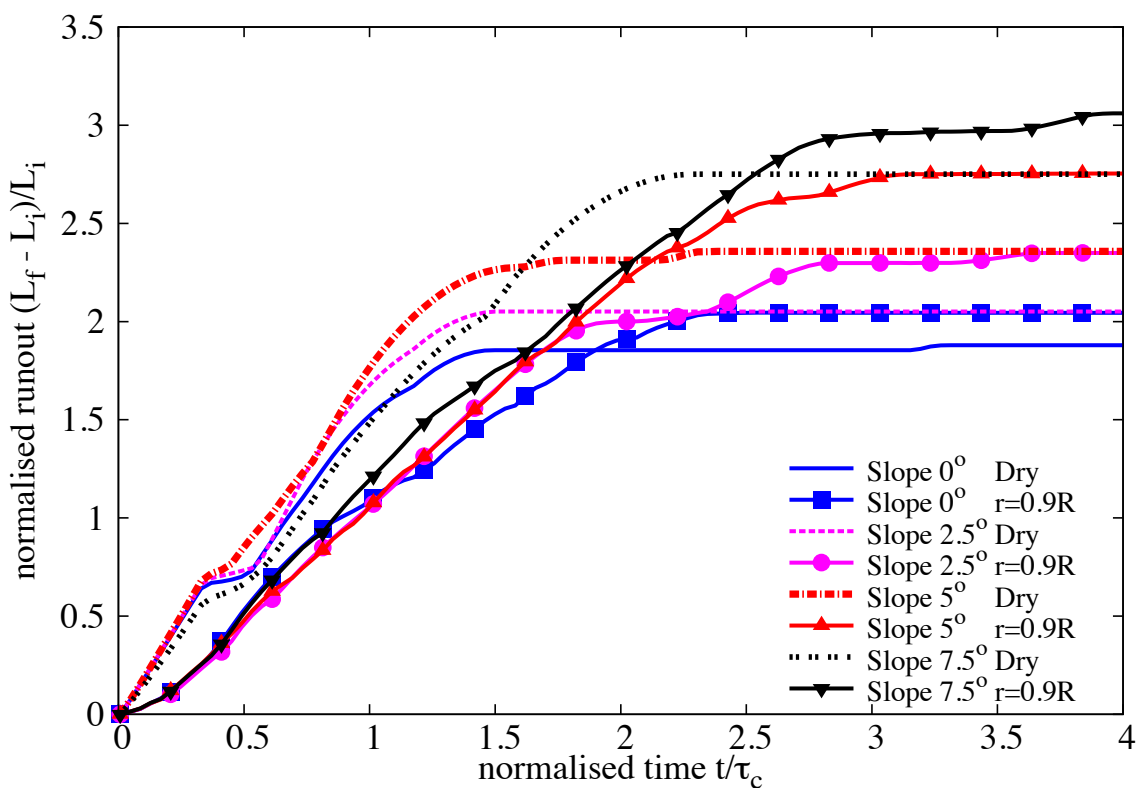
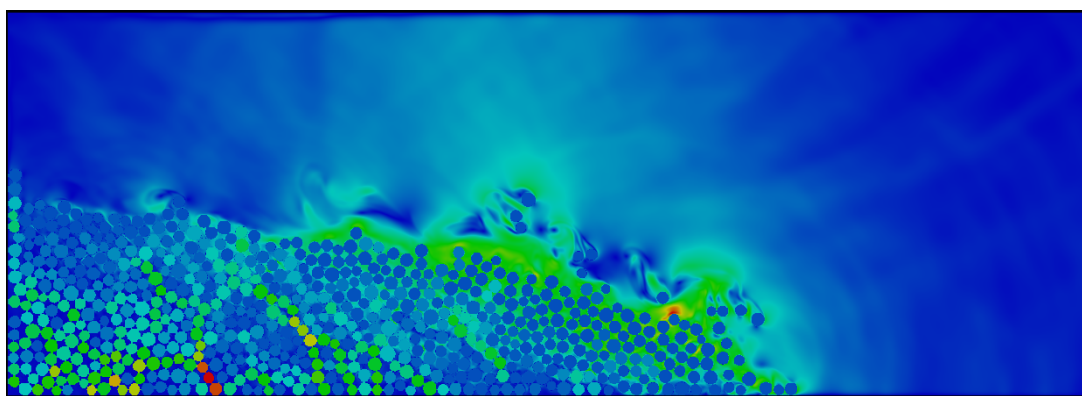
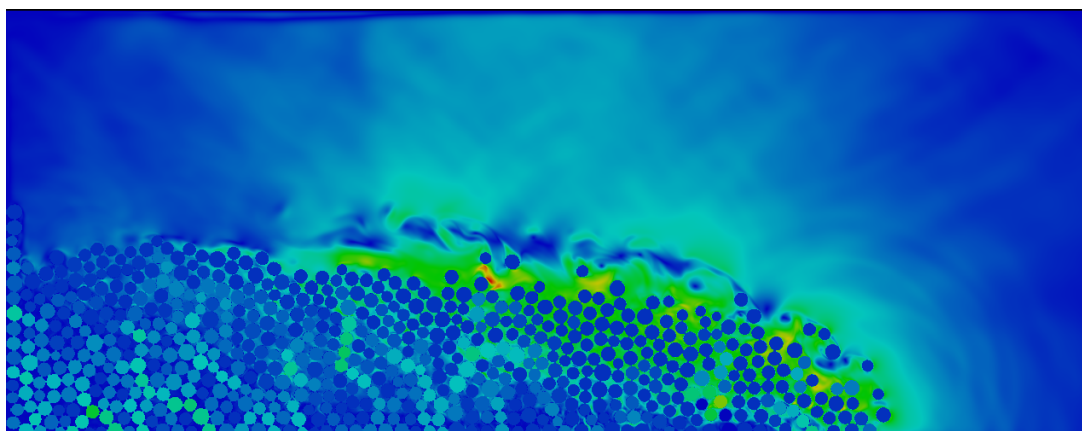


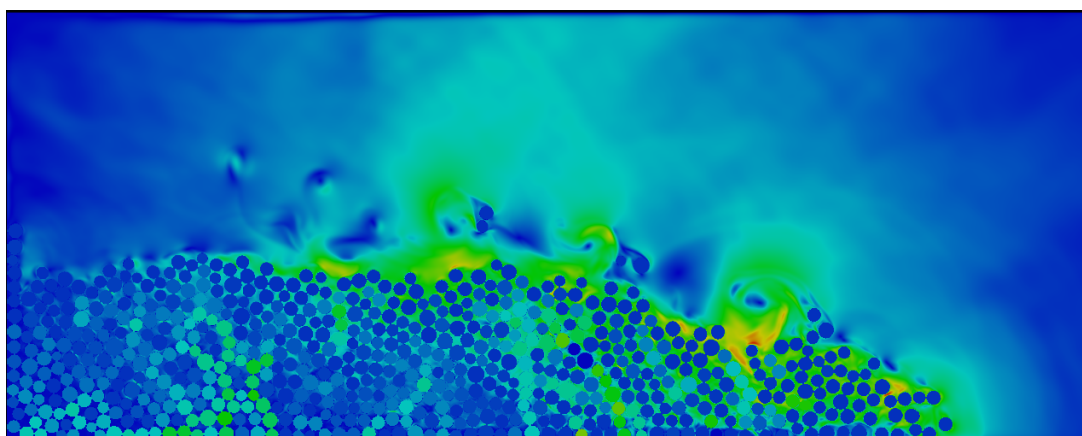
Figure 5.38 Evolution of run-out with time (loose)



(a) Slope 2.5



(b) Slope 5.0



(c) Slope 7.5

Figure 5.39 Flow morphology at critical time for different slope angles (loose)

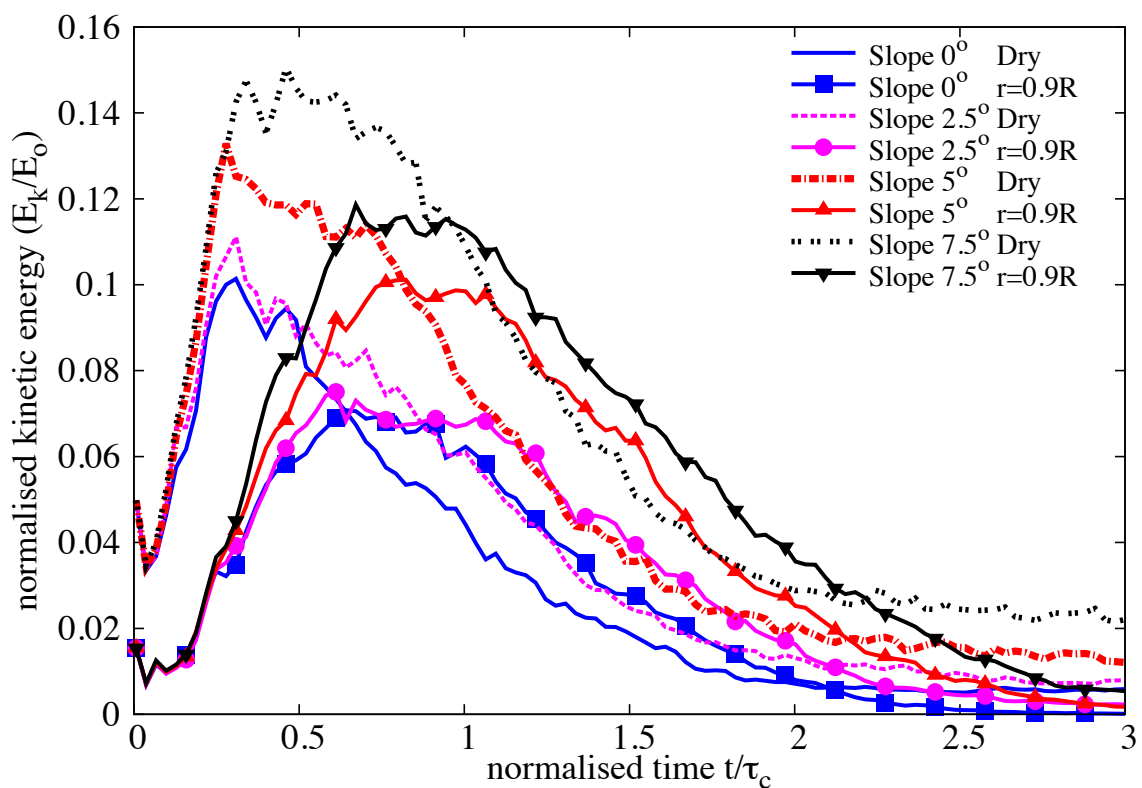


Figure 5.40 Evolution of Kinetic Energy with time (loose)

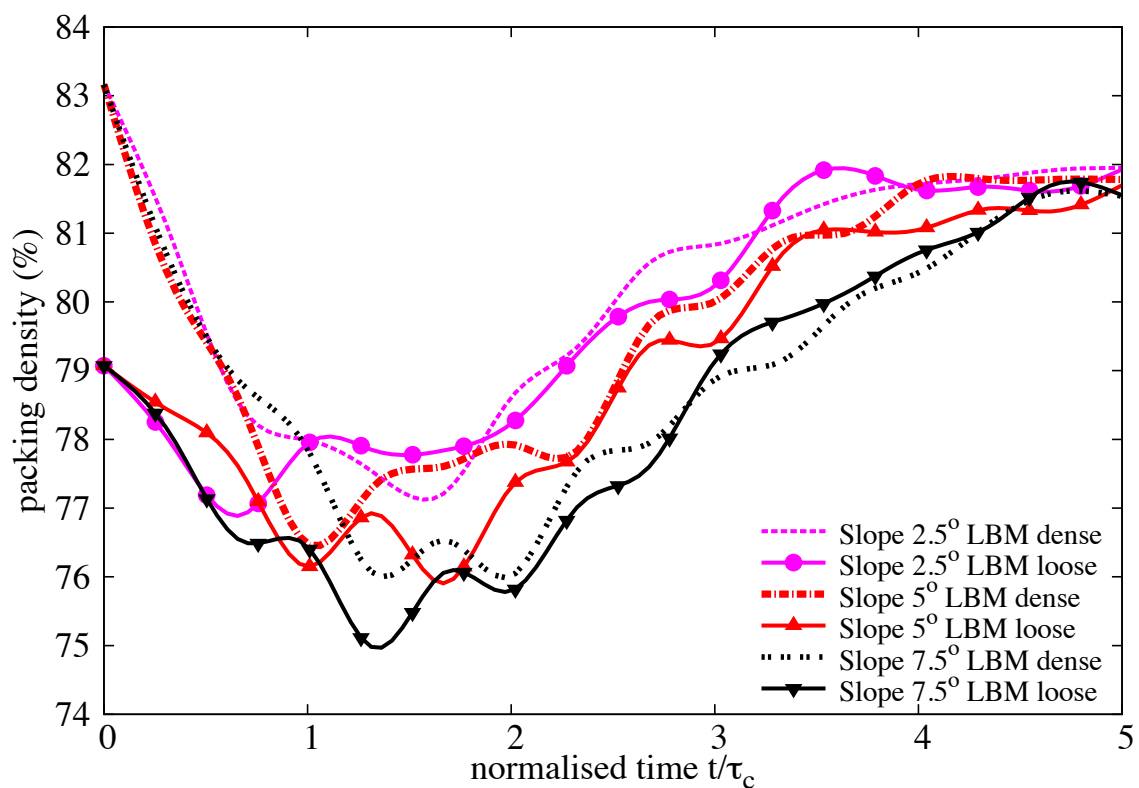
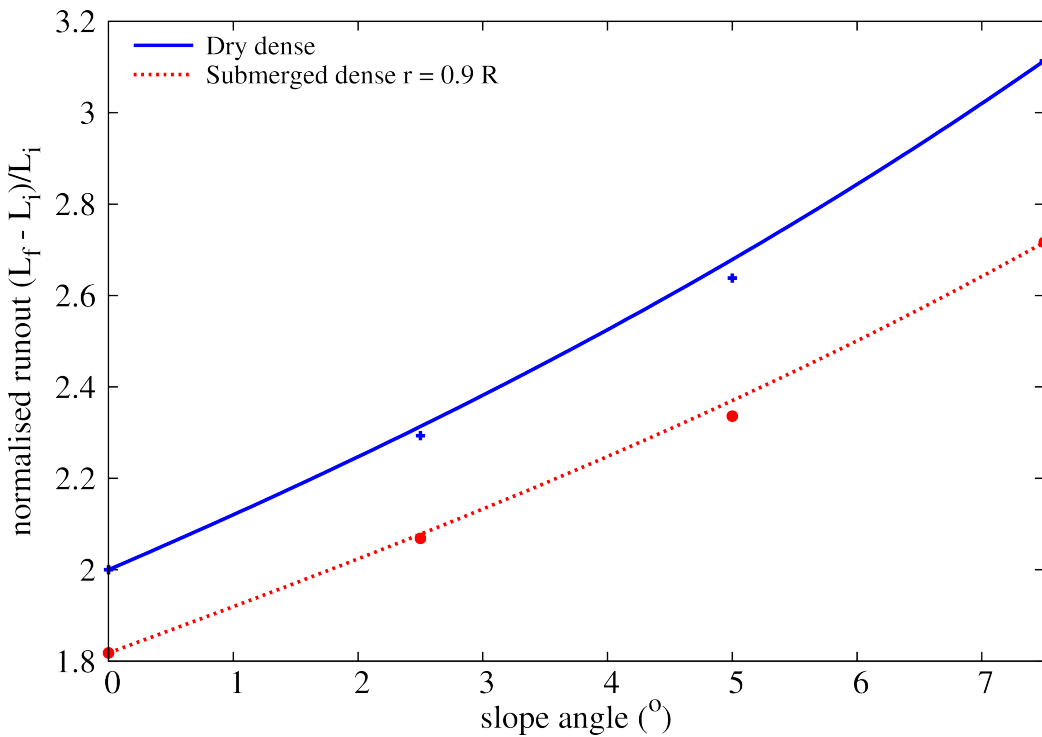
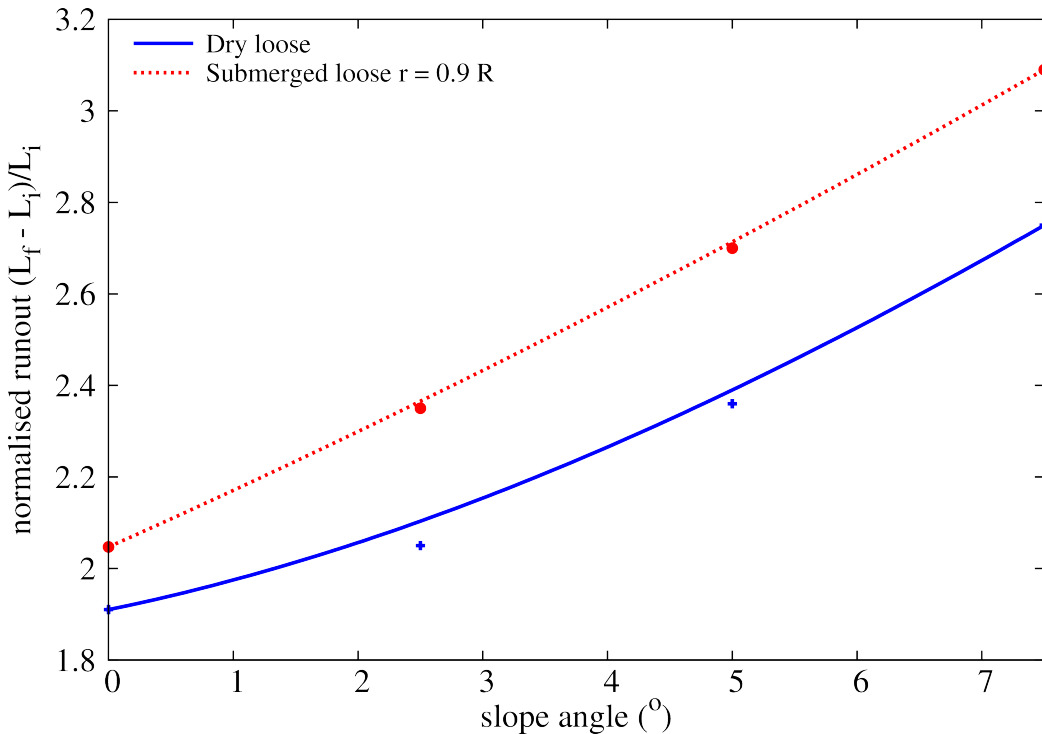


Figure 5.41 Evolution of packing density with time



(a) Effect of slope angle on the run-out distance (Dense). Comparison between dry and submerged granular column.



(b) Effect of slope angle on the run-out distance (Loose). Comparison between dry and submerged granular column.

Figure 5.42 Effect of slope angle on the run-out distance (Dense and Loose). Comparison between dry and submerged granular column.

### 5.4.2 Effect of permeability

For a slope angle of 5°, the hydrodynamic radius of the loosely packed grains was varied from  $r = 0.7R$  (high permeability), 0.75R, 0.8R, 0.85R to 0.9R (low permeability). The run-out distance is found to increase with decrease in the permeability of the granular assembly (see Figure 5.43). The run-out distance for high permeable conditions ( $r = 0.7R – 0.8R$ ) were lower than their dry counterparts. Although, decrease in permeability resulted in an increase in the run-out distance, no significant change in the run-out behaviour was observed for a hydrodynamic radius of up to 0.8R.

With further decrease in permeability ( $r = 0.85R$  and 0.9R), the run-out distance in the fluid was greater than the run-out observed in the dry condition. At very low permeability ( $r = 0.9R$ ), granular material started to entrain more water at the base, which causes a reduction in the effective stress accompanied by a lubrication effect on the flowing granular media. This can be seen as a significant increase in the peak kinetic energy and the duration of the peak energy, in comparison with dry and high permeable conditions (see Figure 5.45).

The permeability of the granular column did not have an influence on the evolution of height during the flow. However, dry granular column tends to collapse more than the immersed granular column (see Figure 5.44).

Positive pore-pressure generation at the base of the flow was observed for low permeable conditions. Inspection of the local packing density showed entrainment of water at the base of the flow, which can also be observed by the steep decrease in the packing density (see Figure 5.46) for the very low permeability condition ( $r = 0.9R$ ). At the end of the flow ( $t \geq 3 \times \tau_c$ ), the excess pore-pressure dissipates and the granular material, irrespective of their permeability, reaches almost the same packing density.

## 5.5 Tall columns

### 5.6 Summary

Two-dimensional LB-DEM simulations were performed to understand the behaviour of submarine granular flows. Unlike dry granular collapse, the run-out behaviour in fluid is dictated by the initial volume fraction. Granular columns with loose packing tend to flow longer in comparison to dense columns, due to entrainment of water at the base resulting in lubrication. The loose column when it starts flowing expands and ejects liquid, leading to a partial fluidization of the material. However, with increase in the slope angle, the run-out in fluid is influenced by the viscous drag on the granular materials. The run-out distance in fluid increases with decrease

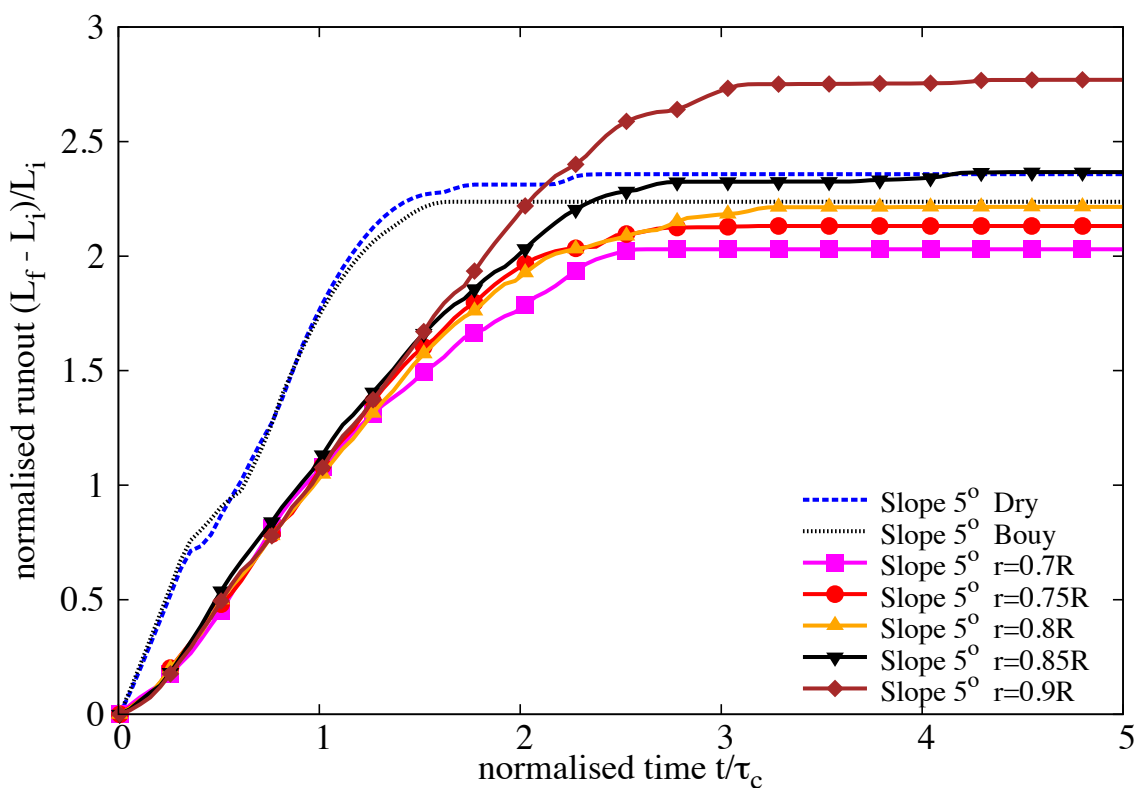


Figure 5.43 Evolution of run-out with time for different permeability (loose slope  $5^\circ$ )

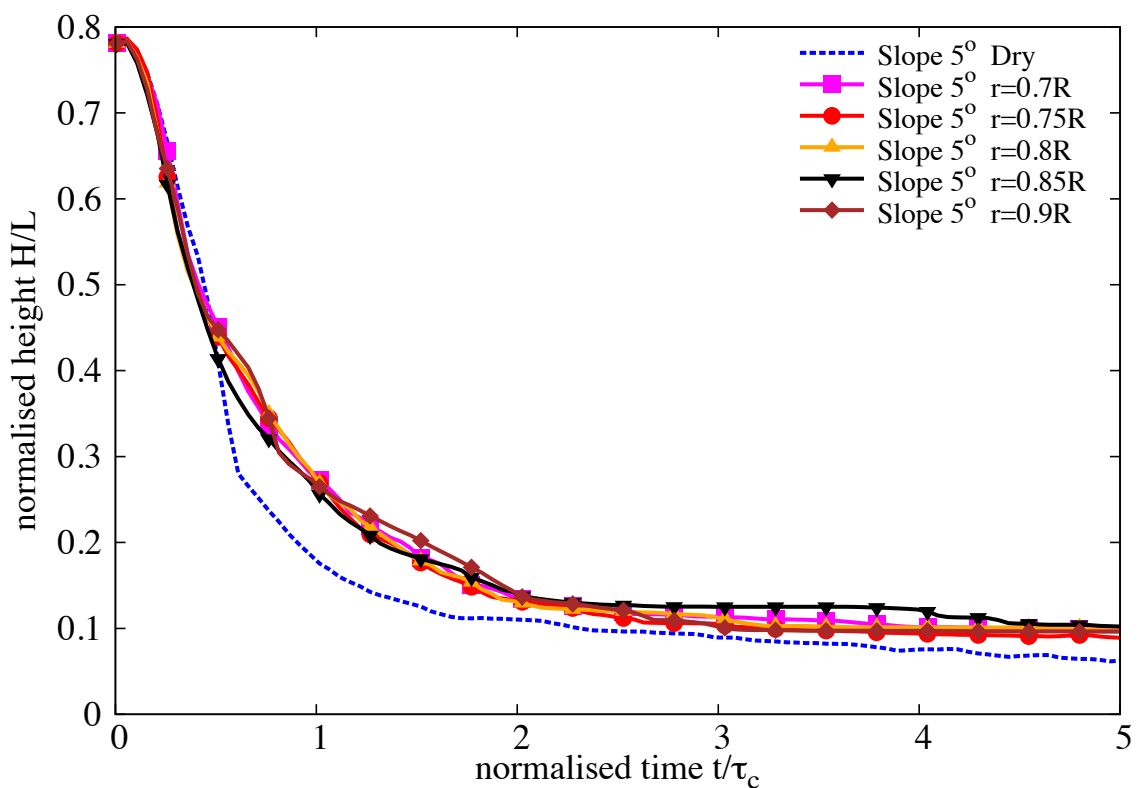


Figure 5.44 Evolution of height with time for different permeability (loose slope 5°)

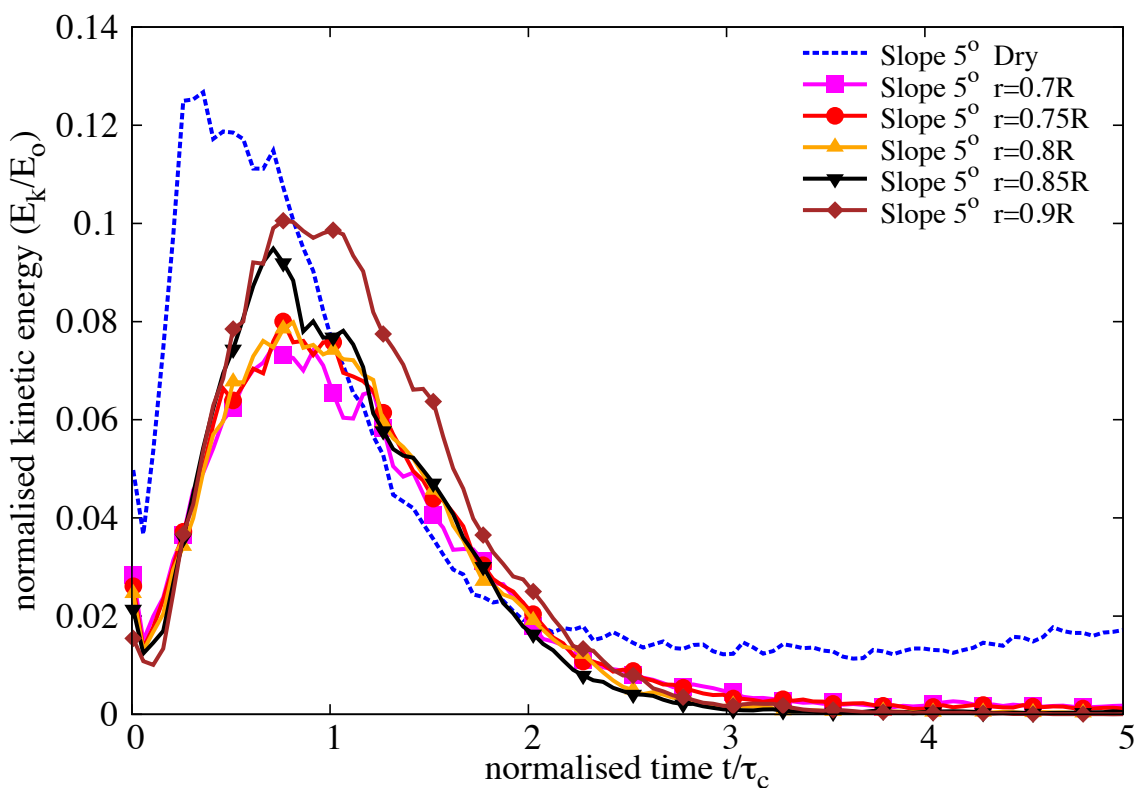


Figure 5.45 Evolution of Kinetic Energy with time for different permeability (loose slope 5°)

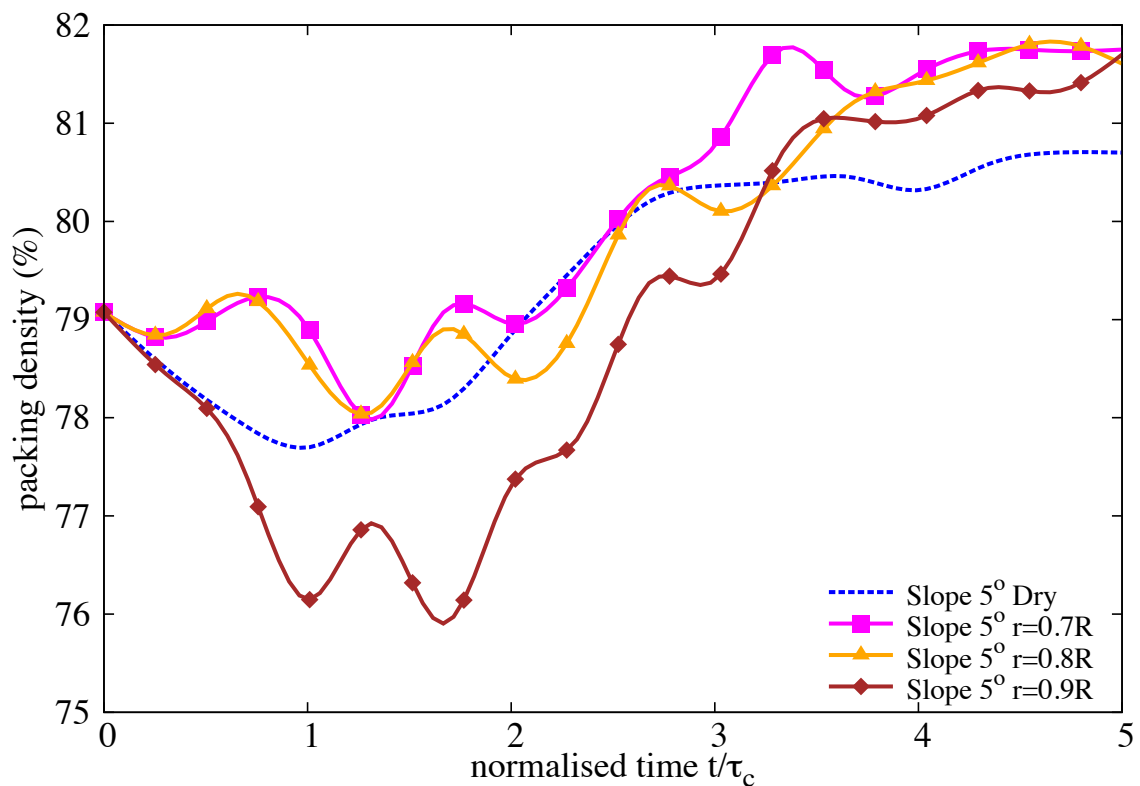
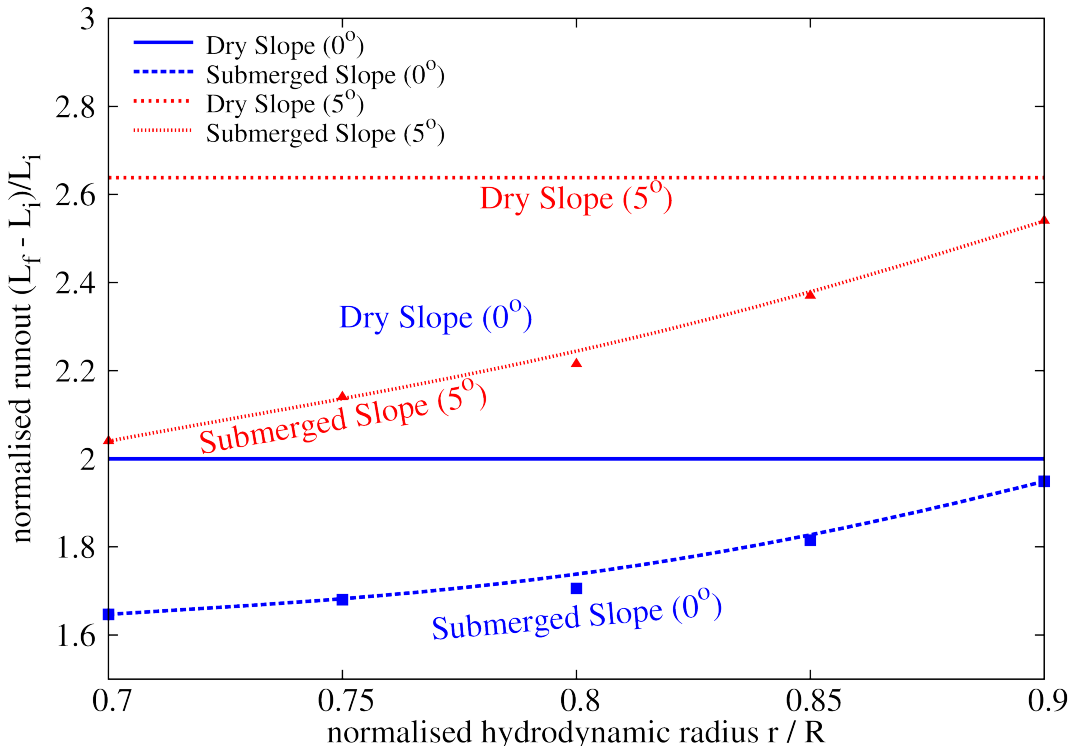
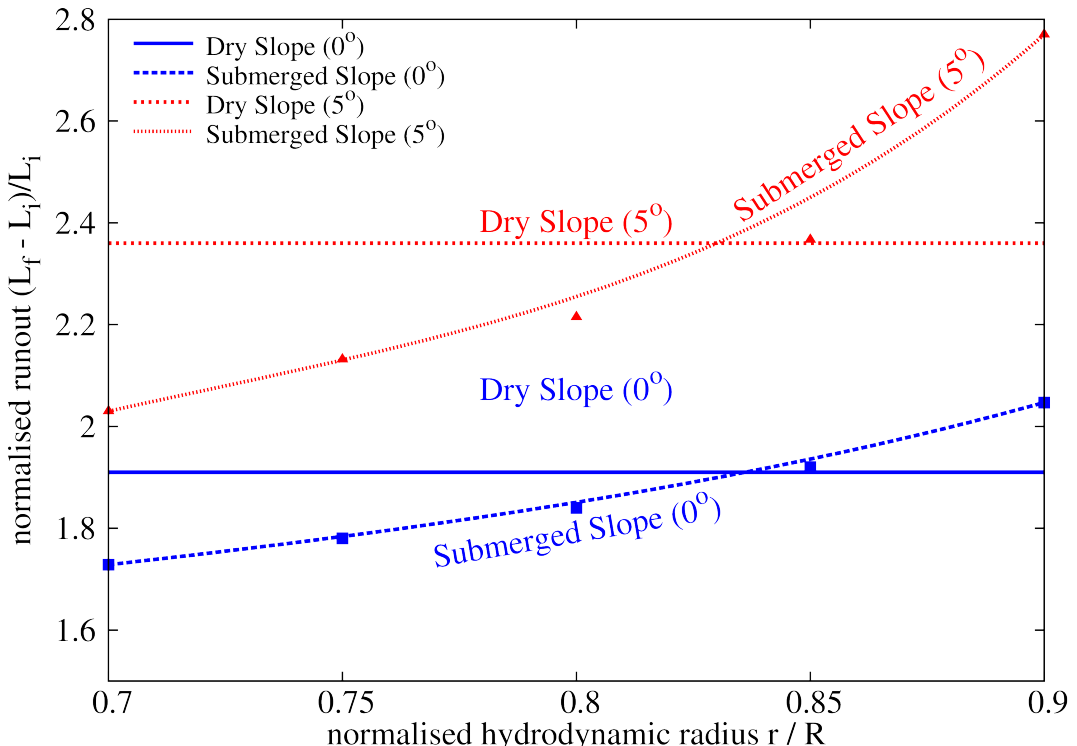


Figure 5.46 Evolution of packing density with time for different permeability (loose slope 5°)



(a) Effect of permeability on the run-out distance (Dense). Comparison between dry and submerged granular column for a slope angle of  $0^\circ$  and  $5^\circ$ .



(b) Effect of permeability on the run-out distance (Loose). Comparison between dry and submerged granular column for a slope angle of  $0^\circ$  and  $5^\circ$ .

Figure 5.47 Effect of permeability on the run-out distance (Dense and Loose). Comparison between dry and submerged granular column for a slope angle of  $0^\circ$  and  $5^\circ$ .

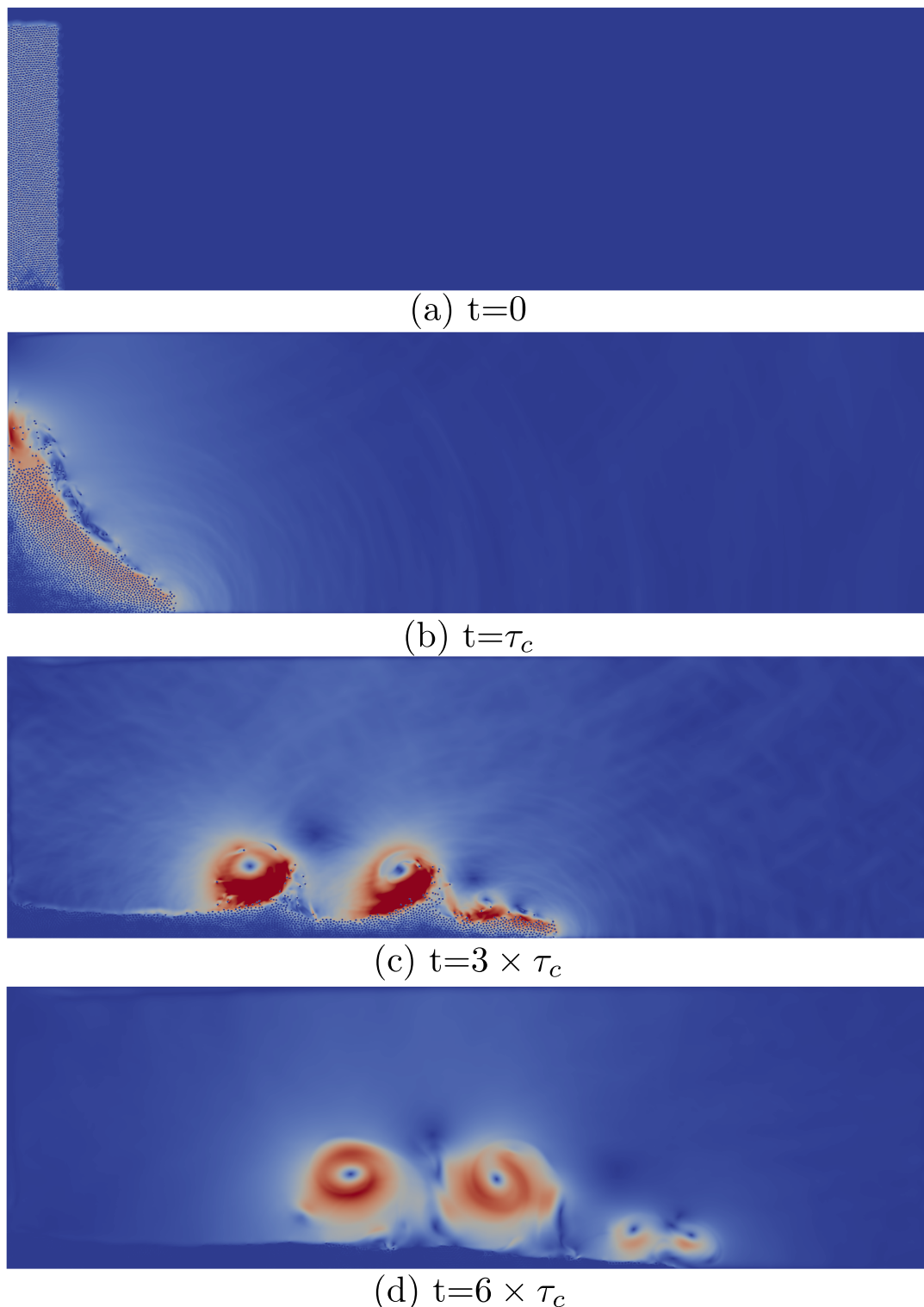
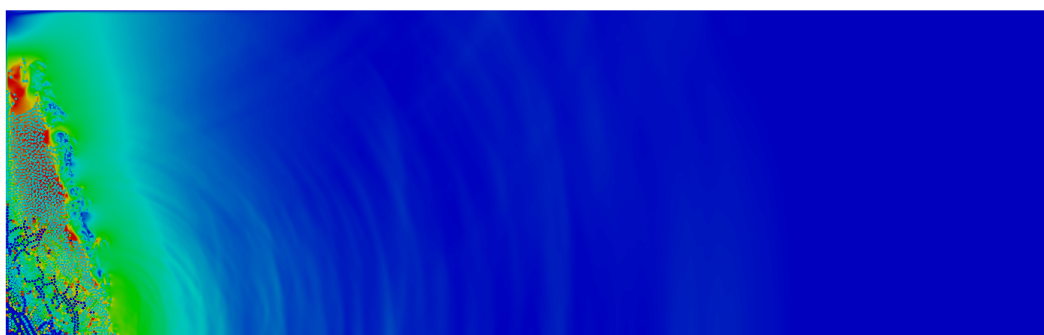
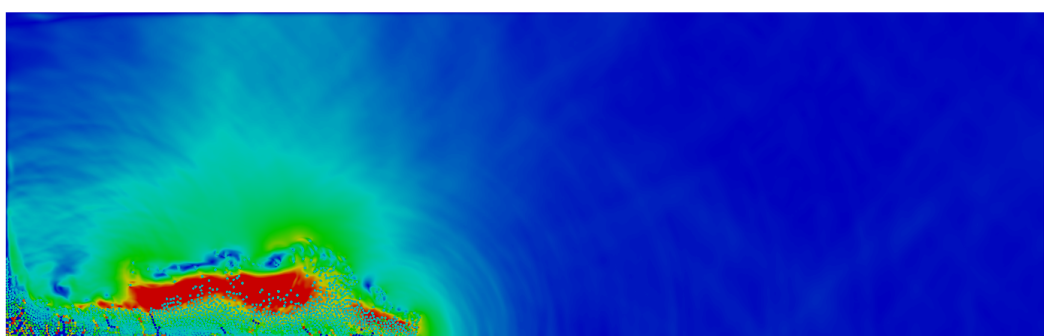


Figure 5.48 Flow evolution of a granular column collapse in fluid ( $a = 6$ ) on a horizontal surface

 $t = 0\tau_c$  $t = 1\tau_c$  $t = 3\tau_c$

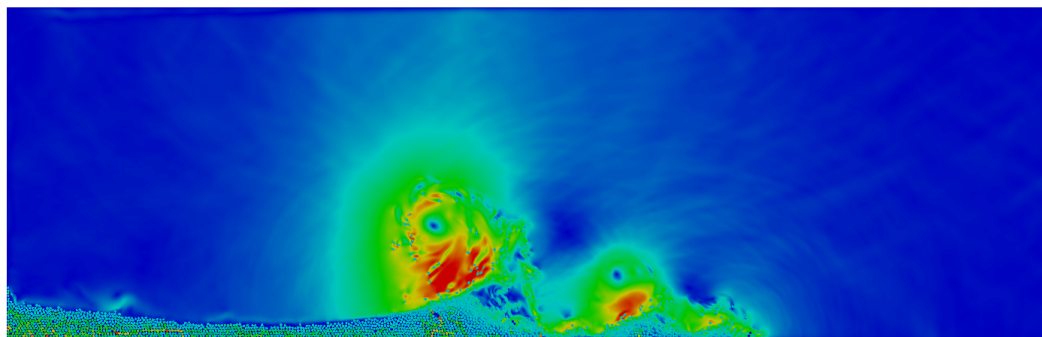
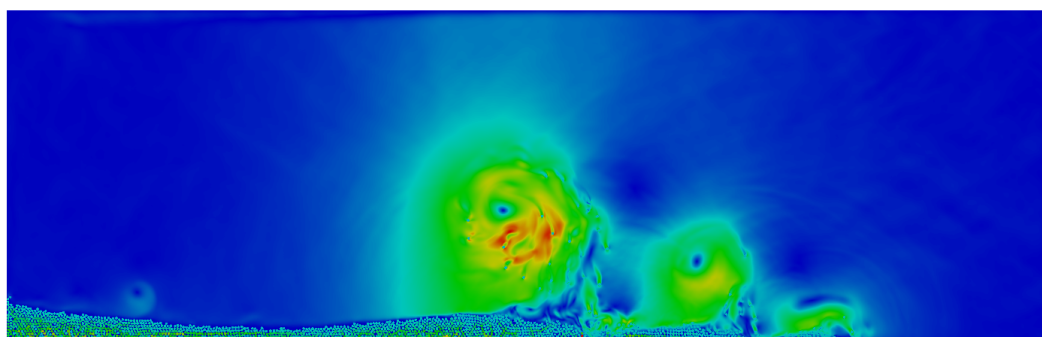
 $t = 6\tau_c$  $t = 8\tau_c$ 

Figure 5.49 Flow evolution of a granular column collapse in fluid ( $a = 6$ ) on a slope of  $5^\circ$ . Shows the velocity profile of fluid due to interaction with the grains (red - higher velocity).

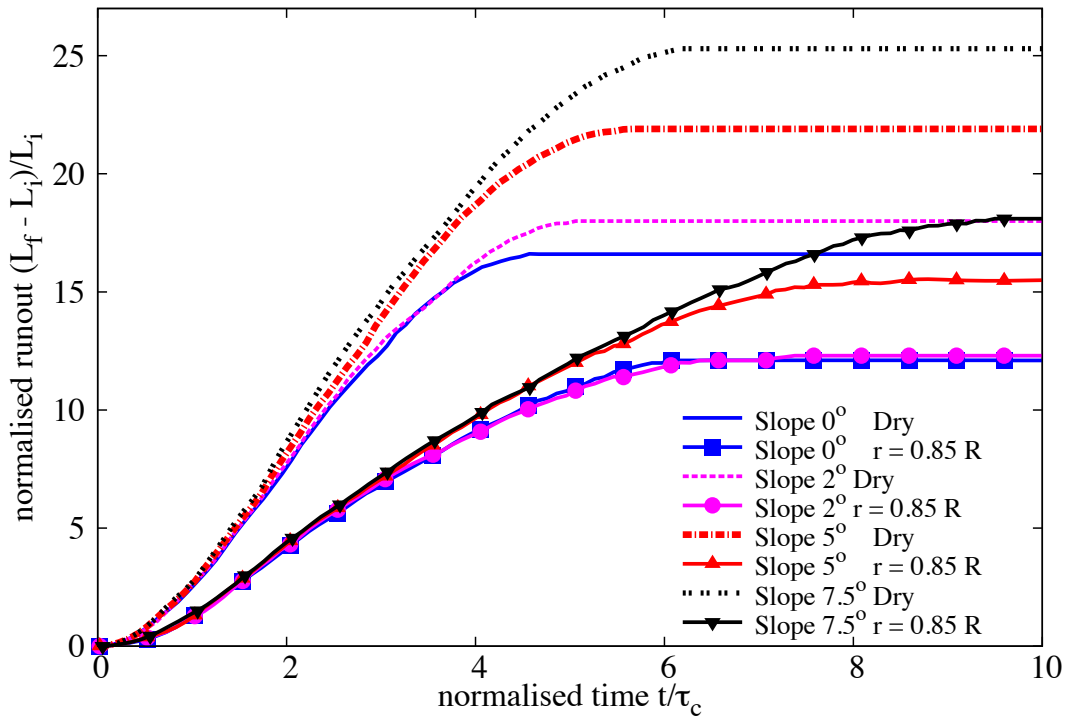


Figure 5.50 Evolution of run-out for a column collapse in fluid ( $a = 6$ ) on a slope of  $5^\circ$

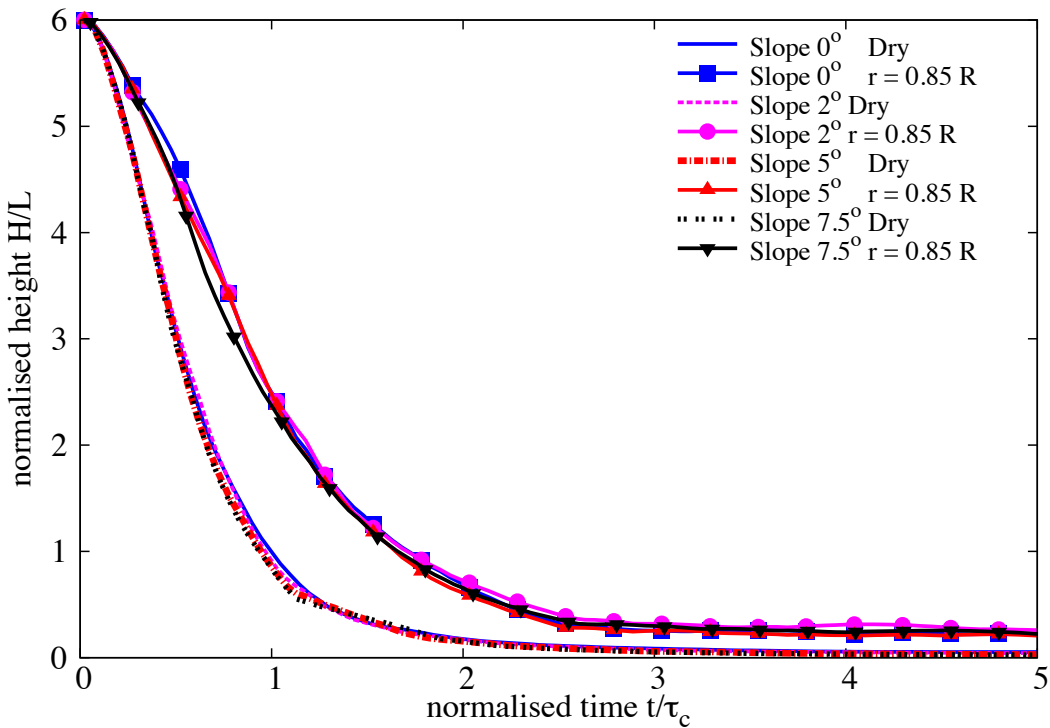
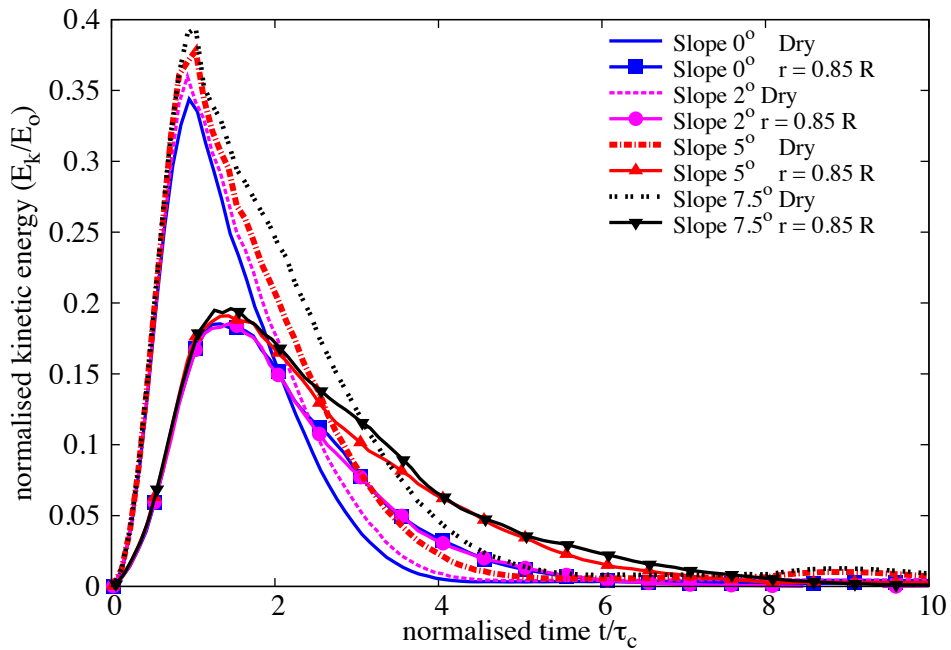
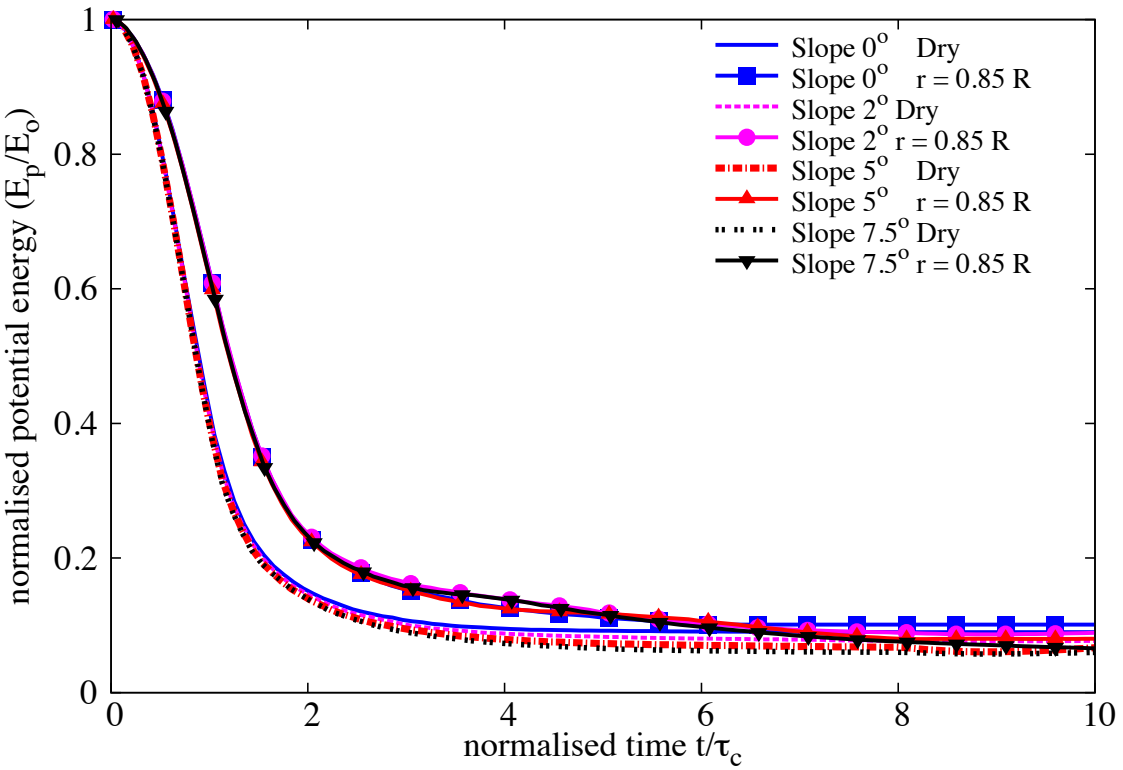


Figure 5.51 Evolution of height with time for a column collapse in fluid ( $a = 6$ ) on a slope of  $5^\circ$

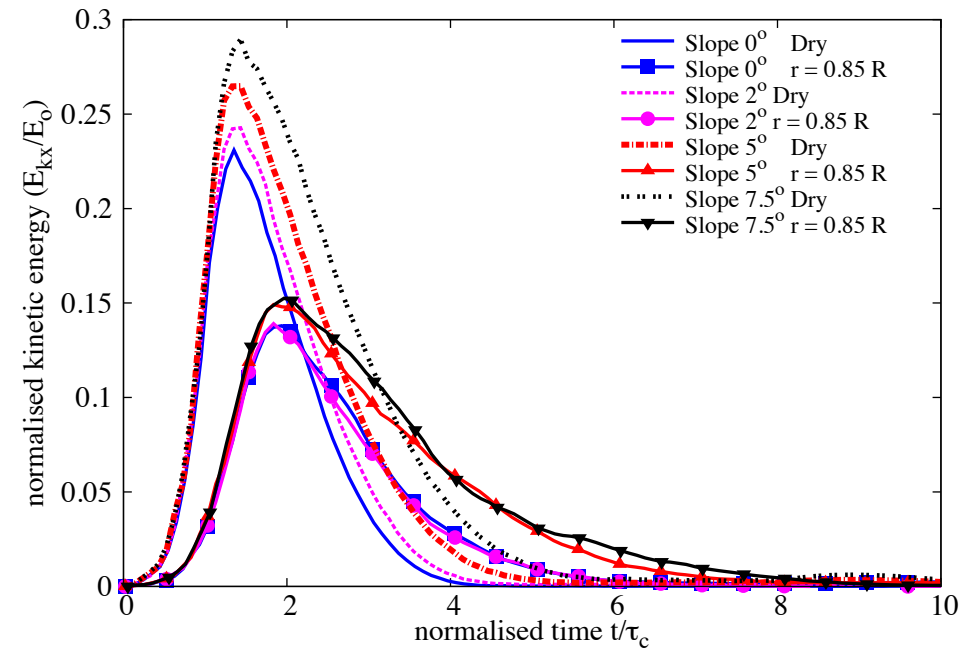


(a) Evolution of the total kinetic energy

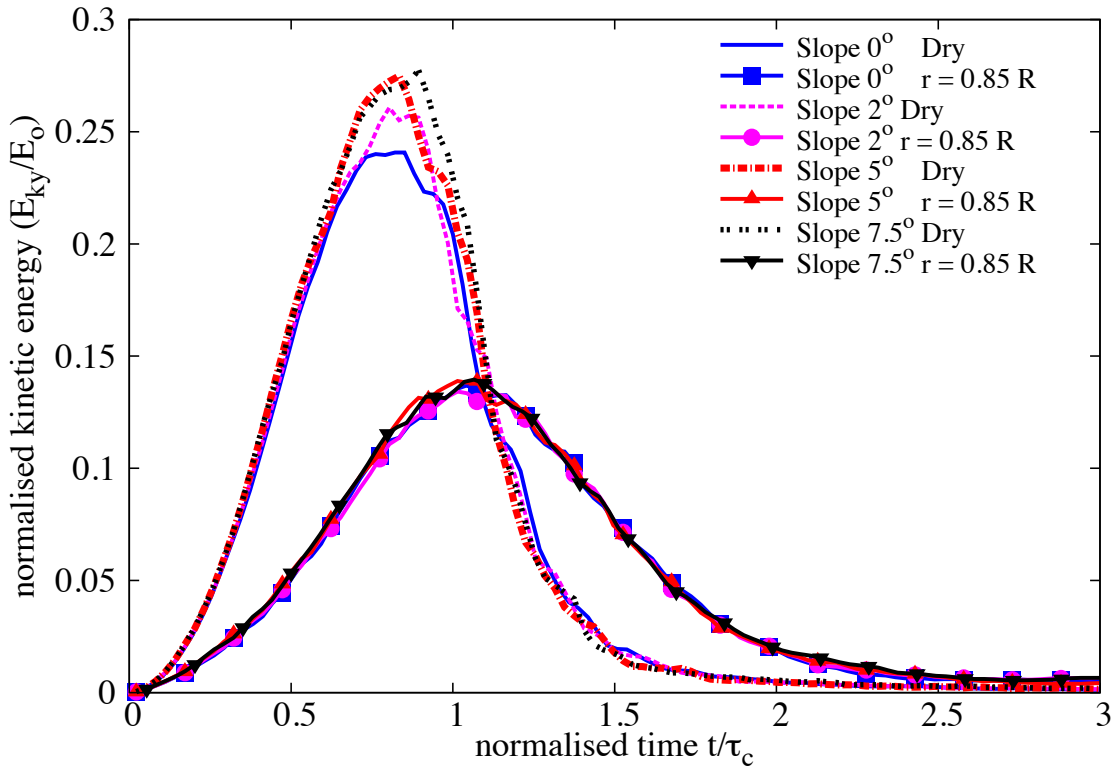


(b) Evolution of the total potential energy

Figure 5.52 Evolution of the kinetic and the potential energy with time for a granular column collapse in fluid (a = 6) on a slope of  $5^\circ$



(a) Evolution of the vertical kinetic energy



(b) Evolution of the horizontal kinetic energy

Figure 5.53 Evolution of the kinetic energies with time for a granular column collapse in fluid ( $a = 6$ ) on a slope of  $5^\circ$

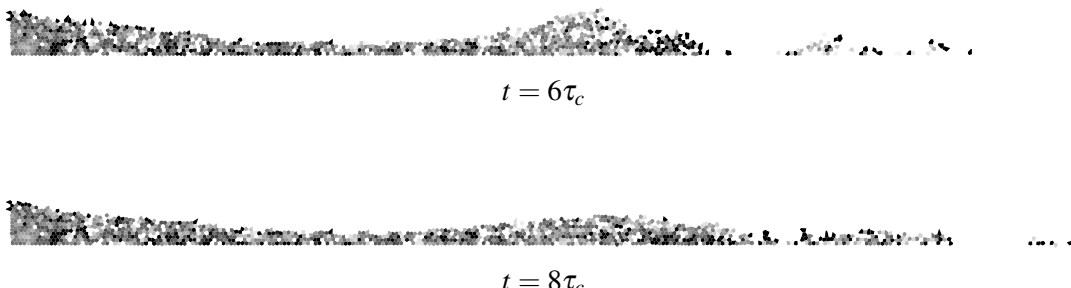


Figure 5.54 Packing density of a granular column collapse in fluid ( $a = 6$ ) on a slope of  $5^\circ$ .

in permeability. More research work is required to characterise the flow behaviour of granular materials, especially in submerged conditions.

25

26



# References

27

- 1 Abe, K., Soga, K., and Bandara, S. (2013). Material Point Method for Coupled Hydromechanical Problems. *Journal of Geotechnical and Geoenvironmental Engineering*, page 28  
04013033. 29
- 2 Balmforth, N. J. and Kerswell, R. R. (2005). Granular collapse in two dimensions. *Journal of Fluid Mechanics*, 538:399–428.
- 4 Bandara, S. (2013). *Material Point Method to simulate Large Deformation Problems in Fluid-saturated Granular Medium*. PhD thesis, University of Cambridge.
- 6 Bardenhagen, S. and Kober, E. (2004). The generalized interpolation material point method. 7 *Computer Modeling in Engineering and Sciences*, 5(6):477–496.
- 8 Bonnet, F., Richard, T., and Philippe, P. (2010). Sensitivity to solid volume fraction of 9 gravitational instability in a granular medium. *Granular Matter*.
- 10 Cambou, B., Jean, M., and Radjaï, F. (2009). *Micromechanics of granular materials*. Wiley- 11 ISTE.
- 12 Coetzee, C. J., Vermeer, P. A., and Basson, A. H. (2005). The modelling of anchors using 13 the material point method. *International Journal for Numerical and Analytical Methods in 14 Geomechanics*, 29(9):879–895.
- 15 Crosta, G. B., Imposimato, S., and Roddeman, D. (2009). Numerical modeling of 2-D granular 16 step collapse on erodible and nonerodible surface. *J. Geophys. Res.*, 114(F3):F03020.
- 17 Da Cruz, F., Emam, S., Prochnow, M., Roux, J. N., and Chevoir, F. (2005). Rheophysics of 18 dense granular materials: Discrete simulation of plane shear flows. *Physical Review E - Statistical, Nonlinear, and Soft Matter Physics*, 72(2):1–17.
- 20 Daerr, A. and Douady, S. (1999). Two types of avalanche behaviour in granular media. *Nature*, 21 399(6733):241–243.
- 22 Denlinger, R. and Iverson, R. (2001). Flow of variably fluidized granular masses across 23 three-dimensional terrain, ii: Numerical predictions and experimental tests. *J. Geophys. Res.*, 24 106(B1):553–566.
- 25 Estrada, N., Taboada, A., and Radjai, F. (2008). Shear strength and force transmission in 26 granular media with rolling resistance. *Physical Review E*, 78(2):021301.

- <sup>27</sup> Girolami, L., Hergault, V., Vinay, G., and Wachs, A. (2012). A three-dimensional discrete-grain  
<sup>28</sup> model for the simulation of dam-break rectangular collapses: comparison between numerical  
<sup>29</sup> results and experiments. *Granular Matter*, pages 1–12.
- <sup>30</sup> Guilkey, J., Harman, T., Xia, A., Kashiwa, B., and McMurtry, P. (2003). An Eulerian-  
<sup>31</sup> Lagrangian approach for large deformation fluid structure interaction problems, Part 1:  
<sup>32</sup> algorithm development. *Advances in Fluid Mechanics*, 36:143–156.
- <sup>33</sup> Harbitz, C. B. (2003). Hydroplaning of subaqueous debris flows and glide blocks: Analytical  
<sup>34</sup> solutions and discussion. *Journal of Geophysical Research*, 108(B7):2349.
- <sup>35</sup> Hogg, A. J. (2007). Two-dimensional granular slumps down slopes. *Physics of Fluids*, 19(9):9.
- Iverson, R. M. (1997). The physics of debris flows. *Rev. Geophys.*, 35(3):245–296. 1
- Iverson, R. M. (2000). Acute Sensitivity of Landslide Rates to Initial Soil Porosity. *Science*,  
290(5491):513–516. 2  
3
- Jean, M. (1999). The non-smooth contact dynamics method. *Computer Methods in Applied  
Mechanics and Engineering*, 177(3-4):235–257. 4  
5
- Kerswell, R. (2005). Dam break with Coulomb friction: A model for granular slumping?  
*Physics of Fluids*, 17:057101. 6  
7
- Lacaze, L. and Kerswell, R. R. (2009). Axisymmetric Granular Collapse: A Transient 3D Flow  
Test of Viscoplasticity. *Physical Review Letters*, 102(10):108305. 8  
9
- Lajeunesse, E., Mangeney-Castelnau, A., and Vilote, J. P. (2004). Spreading of a granular  
mass on a horizontal plane. *Physics of Fluids*, 16(7):2371. 10  
11
- Lajeunesse, E., Monnier, J. B., and Homsy, G. M. (2005). Granular slumping on a horizontal  
surface. *Physics of Fluids*, 17(10). 12  
13
- Larrieu, E., Staron, L., and Hinch, E. J. (2006). Raining into shallow water as a description of  
the collapse of a column of grains. *Journal of Fluid Mechanics*, 554:259–270. 14  
15
- Lo, C. Y., Bolton, M., and Cheng, Y. P. (2009). Discrete element simulation of granular column  
collapse. In *AIP Conf. Proc. Powders and Grains 2009*, volume 1145 of *6th International  
Conference on Micromechanics of Granular Media, Powders and Grains 2009*, pages 627–  
630. 16  
17  
18  
19
- Lube, G., Huppert, H. E., Sparks, R. S. J., and Freundt, A. (2005). Collapses of two-dimensional  
granular columns. *Physical Review E - Statistical, Nonlinear, and Soft Matter Physics*,  
72(4):1–10. 20  
21  
22
- Meruane, C., Tamburino, A., and Roche, O. (2010). On the role of the ambient fluid on  
gravitational granular flow dynamics. *Journal of Fluid Mechanics*, 648:381–404. 23  
24
- Midi, G. D. R. (2004). On dense granular flows. *European Physical Journal E*, 14(4):341–365. 25
- Mitchell, J. K. and Soga, K. (2005). *Fundamentals of soil behavior*. John Wiley & Sons. 26

- Mohrig, D. and Ellis, C. (1998). Hydroplaning of subaqueous debris flows. ... *Society of America* .... 27  
28
- Moreau, J. J. (1993). New computation methods in granular dynamics. In Thornton, C., editor, *Powders and Grains*, page 227. A. A. Balkema. 29  
30
- Mutabaruka, P. (2013). *Modelisation numerique des milieux granulaires immergés : initiation et propagation des avalanches dans un fluide*. Phd thesis, University of Montpellier 2. 31  
32
- Pailha, M., Pouliquen, O., and Nicolas, M. (2008). Initiation of Submarine Granular Avalanches: Role of the Initial Volume Fraction. *AIP Conference Proceedings*, 1027(1):935–937. 33  
34
- Peker, S. and Helvacı, S. (2007). *Solid-liquid two phase flow*. Elsevier. 35
- Radjai, F. and Dubois, F. (2011). *Discrete-element modeling of granular materials*. ISTE Wiley, London; Hoboken, N.J. 36  
37
- <sup>1</sup> Radjai, F. and Richefeu, V. (2009). Contact dynamics as a nonsmooth discrete element method. <sup>2</sup> *Mechanics of Materials*, 41(6):715–728.
- <sup>3</sup> Radjai, F., Schafer, J., Dipple, S., and Wolf, D. (1997). Collective Friction of an Array of <sup>4</sup> Particles: A Crucial Test for Numerical Algorithms. *Journal de Physique I*, 7(9):1053–1070.
- <sup>5</sup> Rondon, L., Pouliquen, O., and Aussillous, P. (2011). Granular collapse in a fluid: Role of the <sup>6</sup> initial volume fraction. *Physics of Fluids*, 23(7):073301–073301–7.
- <sup>7</sup> Rycroft, C. H., Orpe, A. V., and Kudrolli, A. (2009). Physical test of a particle simulation <sup>8</sup> model in a sheared granular system. *Physical Review E*, 80(3):031305.
- <sup>9</sup> Schaefer, D. G. (1990). Instability and ill-posedness in the deformation of granular materials. <sup>10</sup> *International Journal for Numerical and Analytical Methods in Geomechanics*, 14(4):253–278. 1393
- Staron, L. and Hinch, E. J. (2005). Study of the collapse of granular columns using two- <sup>1394</sup> dimensional discrete-grain simulation. *Journal of Fluid Mechanics*, 545:1–27. 1395
- Staron, L. and Hinch, E. J. (2007). The spreading of a granular mass: Role of grain properties <sup>1396</sup> and initial conditions. *Granular Matter*, 9(3–4):205–217. 1397
- Staron, L., Radjai, F., and Vilote, J. P. (2005). Multi-scale analysis of the stress state in <sup>1398</sup> a granular slope in transition to failure. *The European physical journal. E, Soft matter*, 18(3):311–20. 1399  
1400
- Staron, L., Radjai, F., and Vilote, J.-P. (2006). Granular micro-structure and avalanche <sup>1401</sup> precursors. *Journal of Statistical Mechanics: Theory and Experiment*, 2006(07):P07014– <sup>1402</sup> P07014. 1403
- Thompson, E. L. and Hupper, H. E. (2007). Granular column collapses: Further experimental <sup>1404</sup> results. *Journal of Fluid Mechanics*, 575:177–186. 1405
- Topin, V., Dubois, F., Monerie, Y., Perales, F., and Wachs, A. (2011). Micro-rheology of dense <sup>1406</sup> particulate flows: Application to immersed avalanches. *Journal of Non-Newtonian Fluid <sup>1407</sup> Mechanics*, 166(1–2):63–72. 1408

- Topin, V., Monerie, Y., Perales, F., and Radjaï, F. (2012). Collapse Dynamics and Runout of <sup>1409</sup>  
Dense Granular Materials in a Fluid. *Physical Review Letters*, 109(18):188001. <sup>1410</sup>
- Utili, S., Zhao, T., and Housby, G. (2014). 3D DEM investigation of granular column collapse: <sup>1411</sup>  
Evaluation of debris motion and its destructive power. *Engineering Geology*. <sup>1412</sup>
- Warnett, J. M., Denissenko, P., Thomas, P. J., Kiraci, E., and Williams, M. A. (2013). Scalings <sup>1413</sup>  
of axisymmetric granular column collapse. *Granular Matter*, 16(1):115–124. <sup>1414</sup>
- Yazdchi, K., Srivastava, S., and Luding, S. (2011). Microstructural effects on the permeability <sup>1415</sup>  
of periodic fibrous porous media. *International Journal of Multiphase Flow*. <sup>1416</sup>
- Zenit, R. (2005). Computer simulations of the collapse of a granular column. *Physics of Fluids*, <sup>1417</sup>  
17(Compendex):031703–1–031703–4. <sup>1418</sup>